

**A SIZING AND VEHICLE MATCHING METHODOLOGY
FOR BOUNDARY LAYER INGESTING PROPULSION
SYSTEMS**

A Thesis
Presented to
The Academic Faculty

by

Jonathan C. Gladin

In Partial Fulfillment
of the Requirements for the Degree
Doctor of Philosophy in the
Daniel Guggenheim School of Aerospace Engineering

Georgia Institute of Technology
December 2015

Copyright © 2015 by Jonathan C. Gladin

A SIZING AND VEHICLE MATCHING METHODOLOGY FOR BOUNDARY LAYER INGESTING PROPULSION SYSTEMS

Approved by:

Dr. Dimitri N. Mavris, Advisor
Daniel Guggenheim School of
Aerospace Engineering
Georgia Institute of Technology

Dr. Brian German
Daniel Guggenheim School of
Aerospace Engineering
Georgia Institute of Technology

Dr. Jechiel I. Jagoda
Daniel Guggenheim School of
Aerospace Engineering
Georgia Institute of Technology

Dr. Jimmy Tai
Daniel Guggenheim School of
Aerospace Engineering
Georgia Institute of Technology

Dr. Brian K. Kestner
Aerospace Engineer
General Electric Aviation

Mr. James Felder
Aerospace Engineer
NASA Glenn Research Center

Date Approved: October 2, 2015

To my family,

John, Janice, and Christopher Gladin,

without whom I would not have come this far.

ACKNOWLEDGEMENTS

My time at ASDL under Professor Dimitri Mavris has so far been an amazing adventure. I have learned so much from him and the wonderful organization he has built around him that I have called home for so long. I would like to thank him, first and foremost, for lending me this opportunity 6 years ago, in the midst of a very difficult time in my life, and for helping me towards where I am today. He serves as an inspiring role model for all those around him.

I would also like to thank Dr. Jimmy Tai, first for explaining to me the difference between combustion and propulsion on my first day in the lab, and second for taking a chance on someone who (obviously) knew very little about propulsion at the time. He has always been a great advocate for me and has helped me immensely in the final push to finish this thesis.

I must also especially thank Dr. Brian Kestner, who was essentially my mentor within ASDL for several years and taught me all that I know about engine modeling. He has always pushed me to do more than I thought possible, and expected the highest quality work. He is also single handedly responsible for dropping the BLI problem in my lap 4 years ago, and for that I thank him.

I would like to thank the rest of my committee, especially Dr. German for his insightful comments and advise which really helped set the direction of the thesis. Also many thanks to Dr. Jagoda and Mr. Jim Felder for coming on very late in the game and providing useful insights and helpful comments.

I would like to give a special thanks to Jon Sands, Metin Ozcan, and Adam Siegel, who have been great friends, sources of information, and necessary distractions at the right time in our lab. Special thanks to Jon for helping to co-author several papers

and taking away time from working on his thesis to help with mine. Also to Mr. Russ Denney, from whom I have learned so much about engines and who is always available to discuss propulsion related topics. Thanks to Dr. Jeff Schutte and Chris Perullo for making fun of me until I graduated, and for always being helpful in discussing the topic.

Finally, I would like to thank the many other students from ASDL and Georgia Tech generally who have shown me the way, and kept me company there. These include, but are not limited to: Ceara Byrne, Angela Lowe, Martin Levihn, Jonathan Scholz, Baris Akgun, Tushar Kumar, and Jeswanth Sreeram.

TABLE OF CONTENTS

DEDICATION	iii
ACKNOWLEDGEMENTS	iv
LIST OF TABLES	x
LIST OF FIGURES	xi
LIST OF SYMBOLS OR ABBREVIATIONS	xii
SUMMARY	xiii
I INTRODUCTION	1
1.1 Environmental Pressures and Aviation Technology	1
1.2 Boundary Layer Ingestion	2
1.2.1 BLI Benefits	4
1.2.2 BLI Risks	5
1.3 Design Methodologies	6
1.4 Need for an Improved System Analysis	8
II LITERATURE REVIEW	10
2.1 BLI System Level Literature Review	10
2.1.1 General Studies	10
2.1.2 HWB with Hi-Bypass Turbofan Studies	12
2.1.3 NASA N3X: Felder et. al.	16
2.1.4 Double Bubble: MIT N+3	17
2.2 Modeling Approaches for BLI	17
2.2.1 Airframe Aerodynamics and Boundary Layer	19
2.2.2 BLI Inlet Modeling	20
2.2.3 Fan Modeling	21
2.2.4 BLI Engine Off-Design	22
2.3 The Subsonic Airframe Integration Process	22

2.3.1	BLI as a Paradigm Shift	25
2.4	Research Objective Formulation	27
2.5	Towards A Solution	28
III	A METHOD FOR BLI PROPULSION SYSTEM SIZING AND VEHICLE MATCHING (BLIPSS)	32
3.1	BLIPSS Methodology Overview	32
3.1.1	BLI Modeling Phase Overview	33
3.1.2	Architecture Integration Phase Overview	35
3.1.3	Vehicle Matching Phase Overview	35
3.2	Methodology Development: Research Questions and Hypotheses	36
3.2.1	BLI Modeling Phase	36
3.2.2	Architecture Integration Phase	74
3.2.3	Vehicle Matching Phase	87
IV	BLI MODELING PHASE	97
4.1	Baseline Vehicle	97
4.2	Baseline Propulsion System	101
4.3	BLI Component Models	109
4.3.1	Modeling Domain	109
4.3.2	Airframe Aerodynamics Model	110
4.3.3	Power Balance Model	114
4.3.4	Inlet Model	118
4.3.5	Fan Model	126
4.4	Experiment 1	138
4.4.1	Experimental Setup	141
4.4.2	Experiment 1.a Results	143
4.4.3	Experiment 1.b Results	151
4.4.4	Experiment 1.c Results	159
4.4.5	Experiment 1.d Results	168
4.5	Experiment 2	171

4.5.1	Experimental Setup	172
4.5.2	Experiment 2.a Results	173
4.5.3	Experiment 2.b Results	179
4.6	Summary of Chapter 4	185
4.6.1	Experiment 1 Summary	186
4.6.2	Experiment 2 Summary	187
V	ARCHITECTURE INTEGRATION PHASE	188
5.1	AI Phase Overview	188
5.2	Implementation	189
5.3	Experiment 3	189
5.3.1	Experiment 3 Design Specifications	189
5.3.2	Wake Correction Method	191
5.3.3	Experimental Setup	192
5.3.4	Experiment 3 Results	192
5.3.5	Comparison of Wake Correction and BLIPSS	205
5.3.6	Off-Design Evaluation	206
5.4	Experiment 4	207
5.4.1	Implementation	208
5.4.2	Results	209
5.4.3	Geometric Compatibility	218
5.5	Summary of Chapter 5	220
VI	VEHICLE MATCHING PHASE	221
6.1	Methodology Implementation	221
6.1.1	Baseline Flight Envelope Requirements	223
6.1.2	Propulsion System Schedules, Ratings, Limits, and Technol- ogy Parameters	228
6.1.3	Initial MDP Setup	230
6.2	Experiment 5	231
6.2.1	Screening Test Setup	231

6.2.2	Baseline MDP Results	232
6.2.3	Off-Design Screening Test Results	233
6.2.4	Screening Case Summary	243
6.2.5	Vehicle Re-match	245
6.2.6	On Hypothesis 5	249
6.3	Summary of Chapter 6	250
VII SUMMARY AND CONCLUSIONS		251
7.1	Review of Hypotheses	252
7.2	Summary of Contributions	256
7.3	Notes on the Methodology	258
7.3.1	On Convergence and Initial Iterates	258
7.3.2	Regarding Other Architectures	258
7.3.3	Other Use Cases	259
7.4	Recommendations for Future Work	260
7.4.1	Higher Fidelity Component Modeling	260
7.4.2	Integrated Vehicle Design Tools	261
7.4.3	Robust Design Methods	261
7.5	Final Thoughts	262
APPENDIX A — MODEL SOLVER SETUP		263
APPENDIX B — INTEGRAL BOUNDARY LAYER INLET MODEL		
268		
REFERENCES		291
VITA		298

LIST OF TABLES

1	NASA fuel burn targets for the next generation of aviation vehicles. [43]	2
2	Summary of the two prominent methods for boundary layer characterization and their pros and cons for system level conceptual design studies with BLI.	19
3	Fan efficiency assumption used for several system studies.	21
4	Table showing inlet shapes, $y(x)$, and r^*	58
5	Distortion Example Parameters	70
6	Design point mapping matrix for the 3 engine architecture highlighting the available design rules.	83
7	Key design parameters for the baseline HWB vehicle.	96
8	Engine thrust requirements for the baseline vehicle.	98
9	Baseline component efficiencies	99
10	Baseline duct pressure drops	99
11	Baseline technology parameters and design variables	101
12	Initial baseline design points for the MDP setup	105
13	Parameters for the SDP cycle analysis setup for experiment 1.	140
14	Table showing independent variables for experiments 1.a-1.d	140
15	Table showing independent variables for experiments 2.a and 2.b	171
16	Design point mapping matrix for the 3 engine architecture for experiment 3.	188
17	Design point mapping matrix for the 3 engine architecture for experiment 4.	206
18	Technology parameters which define the engine constraints at different design points.	227
19	Initial baseline design points for the MDP setup	228
20	Summary of the cases run for experiment 5.	242
21	Initial baseline design points for the MDP setup	243
22	Table showing flow area ratio-MN solver independents and dependents for experiments 1-4 (SDP)	261

23	Table showing design point solver independents and dependents for all experiments	262
24	Solver independents and dependents for general “off-design” continuity point	263
25	Solver independents and dependents for the thrust matching and cycle design relations in experiments 3 and 4.	263
26	Solver independents and dependents for the thrust matching and cycle design relations in experiments 3 and 4.	264
27	Solver independents and dependents for the cooling flow relations in experiments 5.	264
28	Solver independents and dependents for the thrust matching relations and constraint relations for the rematch runs in experiments 5.	265

LIST OF FIGURES

1	Notional diagram of podded vs. BLI engine design	4
2	Notional diagram of the aerodynamic and propulsive interactions scheme.	7
3	Boundary layer ingestion system study estimates	15
4	Notional system level design process for a BLI propulsion system. . .	18
5	Notional cycle analysis for a BLI propulsion system. Boxes outlined in red show the components which need modification for BLI.	18
6	Notional picture of the regions of the flow field before the fan face. . .	20
7	Notional inlet diagrams showing different conditions for which there are high inlet incidence angles [67]	24
8	Notional inlet incidence angle requirements vs. freestream Mach number [67]	25
9	Simultaneous multi-design point cycle analysis equation setup [83] . .	29
10	MDP Methodology Data Flow Chart	30
11	BLIPSS Methodology Data Flow Chart	34
12	Diagram of the podded case illustrating the various components of the power balance equation.	40
13	Diagram of the podded case illustrating the various components of the power balance equation.	42
14	Diagram of a class 1 geometry type with trailing edge boundary layer shown. The dissipation integral is performed along the z-direction. . .	49
15	Illustration of a class 1 geometry aerodynamic wake for the isolated airfoil and case with a BLI propulsor.	49
16	Illustration of the distribution of the kinetic energy defect over the length of a notional “class 1” aerodynamic body.	50
17	Illustration of the distribution of the kinetic energy defect over the length of a notional “class 1” aerodynamic body.	52
18	Illustration of the the wake defect for a class 2 body with BLI.	53
19	General cross-section diagram.	54
20	Influence of mass flow on the cross-section width solution.	56
21	Influence of inlet aspect ratio on inlet width sizing.	57

22	Influence of inlet aperture shape on inlet width sizing.	57
23	Plot showing trend of boundary layer thicknesses vs. airfoil angle of attack for a NACA 2012 airfoil at Mach = 0.7, Re = 10 ⁶ as predicted by XFOIL	63
24	Standard ARP 1420 test rig showing static and total pressure probe locations	66
25	Illustration of a one-per-rev distortion type for a single probe ring (adapted from [16]).	67
26	Illustration of the definition of delta PRS with distortion (adapted from [57])	68
27	Illustration of the Notional Fan Face AIP	70
28	Example fan face ring total pressure distribution.	70
29	DC(θ) descriptor plotted vs. boundary layer thickness ratio.)	71
30	Examples of potential propulsion system architectures for an HWB aircraft.	74
31	Illustration of Sequential Single Point Design	76
32	Illustration of Multi-Design Point Process	76
33	Illustration of Multi-Engine Multi-Design Point Process	77
34	Illustration of 3-Engine Boeing N2A.	82
35	Turbofan specific thrust vs. Mach number for different altitudes.	88
36	Commercial turbofan variation in fan operating line with flight condition. Trends show that SLS hot day is critical and is worse at higher BPR.	91
37	Option 1 of 3 for determining the flight conditions where all off-design conditions are checked and iterated with the MDP sizing procedure.	93
38	Option 2 of 3 for determining the flight conditions where all off-design conditions are included as constraint points within the MDP.	93
39	Option 3 of 3 for determining the flight conditions where a subset of critical conditions are identified using a screening design of experiments; all subsequent cases do not run off-design iteration checks.	94
40	HWB baseline key design dimensions.	97
41	HWB baseline airfoil stackup.	97
42	HWB baseline vehicle drag polars; Altitude = 35,000 ft	98

43	Baseline propulsion system block diagram.	100
44	Baseline propulsion system fan map generated by CMPGEN	103
45	Baseline cycle design space showing contours of cruise TSFC vs. FPR and EXT.	105
46	Plot showing optimal extraction ratio as a function of chosen fan pressure ratio.	106
47	Baseline power hooks for several flight conditions in the mission profile.	106
48	Modeling domain for the BLI Models.	107
49	Boundary layer CFD data for the Boeing N2A at vehicle fuselage centerline showing multiple axial locations.	108
50	Boundary layer CFD data normalized by edge velocity and boundary layer thickness and showing change in shape at vehicle aft end.	108
51	Comparison of XFOIL predicted θ values vs. those predicted by CFD of Boeing [47].	110
52	Comparison of XFOIL predicted δ^* values vs. those predicted by CFD of Boeing [47].	111
53	Comparison of XFOIL predicted edge velocity values vs. those predicted by CFD of Boeing [47].	111
54	Plot of 1-D kinetic energy defect vs. vehicle angle of attack for centerline airfoil and for multiple flight conditions.	113
55	Upper surface defect percentage vs. angle of attack for the centerline airfoil and for multiple flight conditions.	114
56	Plot of boundary layer drag recovery per unit width vs. angle of attack for the centerline airfoil for many flight conditions.	115
57	Coupled inlet/airframe model data flow diagram.	117
58	NASA inlet A area distribution [7].	119
59	Comparison of inlet recovery vs. Mach trends from IBLT inlet model and experimental data of Berrier et. al. [8].	120
60	Trends of inlet recovery with mass flow.	121
61	Comparison of flow trends and μ^3 variation least squares fit.	121
62	Thickness variation for several different Mach numbers as predicted by the IBLT model	122

63	Normalized inlet duct total pressure loss caused by lip separation for an elliptical subsonic inlet at several throat Mach and flow ratio values (adapted from [84]).	123
64	Diagram illustrating the parallel compressor concept (adapted from Greitzer et. al. [57])	125
65	Parallel compressor engine model schematic.	126
66	Parallel compressor map scalar production process.	129
67	Parallel compressor sample results	131
68	Stall margin at constant speed for varying inlet recoveries for the basic parallel compressor model as applied to the baseline engine model . .	132
69	Pressure ratio loss for the fan using the basic parallel compressor model as applied to the baseline engine model	132
70	Mass flow loss for the fan using the basic parallel compressor model as applied to the baseline engine model	133
71	Parallel compressor map definition process including rematch for distortion related losses	135
72	Plot of thrust loss as a function of total average inlet recovery (blue line) and the required area increase to re-match the thrust with the parallel compressor model (green line)	136
73	Description of the components of experiment 1 and their relation to the model hierarchy created	138
74	Plot showing trends of inlet recovery (top left), fan efficiency (top right), thrust saving coefficient (bottom left), and fan area (bottom right) for each of the models in the model hierarchy	141
75	Plot showing trends of TSFC vs. inlet aspect ratio for different models in the hierarchy	142
76	Plot showing trends of inlet recovery (top left), fan efficiency (top right), thrust saving coefficient (bottom left), and fan area (bottom right) for several different values of angle of attack at the cruise condition	143
77	Contour plots showing level curves of TSFC as a function of FPR and extraction ratio for different models in the hierarchy	145
78	Plots showing TSFC at optimum extraction vs. fan pressure ratio for each of the models in the model hierarchy	146

79	Plots showing TSFC at optimum extraction vs. fan pressure ratio for increasing angle of attack at the design point	147
80	TSFC for different number of engines for each model in the hierarchy	148
81	TSFC for different number of engines for a range of angle of attacks with the full parallel compressor model	149
82	Plot showing trends of design mass flow ratio at the cruise point for the inlet vs recovery (left) and fan face mach number (right); Inlet aspect ratio = 1; $\alpha = 2^\circ$	150
83	Plot showing sensitivity of inlet recovery with respect to the pre-entry zone length	151
84	Plot showing sensitivity of inlet recovery with respect to the design mass flow ratio for different angles of attack	152
85	Plot showing sensitivity of inlet recovery with respect to the design mass flow ratio for fixed width and fixed aspect ratio assumption and 2 different angles of attack	154
86	Inlet aspect ratio sensitivities comparing the “fixed width” and “fixed AR” stream-tube models	155
87	Throttle sensitivities of recovery, fan efficiency, thrust saving coefficient, and TSFC for “fixed AR” and “fixed width” stream-tube models	156
88	Plots of baseline thrust over the flight envelope (top left) and difference between the thrust predicted by each of the models in the model hierarchy and the baseline	158
89	Plots of baseline TSFC variation over the flight envelope (top left) and difference between TSFC predicted by each of the models in the model hierarchy and the baseline	159
90	Throttle hooks for different models in the model hierarchy and for normal flight sizing conditions TOC (Top), cruise (middle), TKO (bottom)	161
91	Variation in thrust saving coefficient at different speeds and for increasing inlet aspect ratio for the clean model (no losses)	162
92	Variation of the deviation from baseline thrust and TSFC for the BLI system for a range of inlet aspect ratios for the clean model (no losses)	162
93	TSFC difference in percentage of the baseline at 75% speed for the clean, mixed, and parallel compressor models as a function of the inlet aspect ratio	163

94	Trends of the system losses, thrust saving coefficient, and aggregate performance for a range of angle of attack at cruise with a design α of 2 degrees	165
95	Trends of the system losses, thrust saving coefficient, and aggregate performance for a range of angle of attack at take-off (MN = 0.25, Altitude = 0 ft)	167
96	Percent difference of thrust (top) and TSFC (bottom) between the fixed and variable boundary layer models at different Mach numbers and a fixed angle of attack of 2 degrees	168
97	Percent difference of thrust (top) and TSFC (bottom) between the fixed and variable boundary layer models at different angles of attack at cruise	169
98	Contour plot of TSFC vs. thrust and AR with constraints shown assuming a minimum SMN loss of 9%	172
99	Plot of SMN vs. height for the data generated by varying inlet aspect ratio and the number of engines	173
100	Plot of SMN vs. TSC for the data generated by varying inlet aspect ratio and the number of engines	173
101	Constrained TSFC plot showing that the height/SMN relationship can be used to constrain the TSFC. Feasible space is shown for progressively thicker angles of attack.	174
102	Contour plot of distorted sector stall margin for different inlet aspect ratio values	175
103	Contour plot of distorted sector stall margin for different inlet aspect ratio values	176
104	Take-off stall margin vs. vehicle angle of attack for several angles of attack (3 engine configuration)	177
105	Correlation of circumferential distortion against inlet jet flow ratio (% of inlet flow)	178
106	Plot of stall margin (primary y-axis) and TSFC (secondary y-axis) for increasing core bleed extraction ratio. FPR = 1.4, EXT = 1.21. . . .	179
107	Contour plot showing the stall margin with a SMN constraint of 22 applied with the re-match solver logic	181
108	Contour plot showing the effect of engine rematch on area increase in the design space region which is height/stall constrained	182

109	Plot showing the effect of engine rematch in the region which height/stall constrained. The relative change in area is shown (green) along with relative change in TSFC (blue).	183
110	Boundary layer displacement thickness variation with engine outboard location.	191
111	Boundary layer momentum thickness variation with engine outboard location.	192
112	Engine BLI wake recovery per unit stream-tube width variation with engine outboard location.	192
113	Boundary layer edge velocity variation with engine outboard location.	193
114	Boundary layer shape parameter variation with engine outboard location.	193
115	Inlet recovery for the single inlet case as the engine location is moved outboard.	194
116	Fan efficiency loss for the single inlet case as the engine location is moved outboard.	195
117	Thrust saving coefficient for the single inlet case as the engine location is moved outboard.	195
118	% Change in thrust specific fuel consumption for the single inlet case as the engine location is moved outboard.	196
119	Difference between the wake correction and the single inlet TSFC. . .	197
120	Change in thrust for the inboard, outboard, and total system and also total mass flow relative to the single inlet case for an $\alpha = 0.5^\circ$	199
121	Change in thrust for the inboard, outboard, and total system and also total mass flow relative to the single inlet case for an $\alpha = 2^\circ$	200
122	Change in thrust for the inboard, outboard, and total system and also total mass flow relative to the single inlet case for an $\alpha = 4^\circ$	201
123	Change in fuel flow for the inboard, outboard, and total system for an $\alpha = 0.5^\circ$	201
124	Change in fuel flow for the inboard, outboard, and total system for an $\alpha = 2^\circ$	202
125	Change in fuel flow for the inboard, outboard, and total system for an $\alpha = 4^\circ$	202
126	Change in TSFC for the inboard, outboard, and total system for several angles of attack.	203

127	Difference between the single inlet case and the BLIPSS method vs. thrust saving coefficient of the system.	204
128	Difference between the BLIPSS method and the single inlet approach for different throttle settings in terms of TSFC. The data is shown for an $\alpha = 0.5^\circ$	205
129	Inboard, outboard, and total system thrust saving coefficient vs. the mass flow ratio of the system. Results are for an α of 0.5 degrees. . .	208
130	Inboard, outboard, and total system component efficiencies vs. the mass flow ratio of the system. Results are for an α of 0.5 degrees. . .	208
131	Inboard, outboard, and total system TSFC vs. the mass flow ratio of the system. Results are for an α of 0.5 degrees.	209
132	Inboard, outboard, and total system TSFC vs. the mass flow ratio of the system. Results are shown for the baseline and several BLI designs with different angles of attack.	210
133	Inboard, outboard, and total system TSFC vs. the mass flow ratio of the system. Results are for an α of 0.5 degrees and for the outboard core aerodynamic design point.	211
134	Inboard, outboard, and total system TSFC vs. the mass flow ratio of the system. Results are shown for the baseline and several BLI designs with different angles of attack.	211
135	Inboard, outboard, and total system TSC vs. the mass flow ratio of the system with angle of attack of 0.5 degrees.	212
136	Inboard, outboard, and average system component efficiencies vs. the mass flow ratio of the system with angle of attack of 0.5 degrees. . . .	213
137	Inboard, outboard, and average system component TSFC vs. the mass flow ratio of the system with angle of attack of 0.5 degrees.	214
138	Inboard, outboard, and average system component TSFC vs. the mass flow ratio of the system with angles of attack of 0.5, 2, and 4 degrees.	214
139	Stall margin variation for different angles of attack showing the inboard and outboard stall margin. Bottom right shows the minimum stall margin at each MFR for the 3 angles of attack.	215
140	High level algorithm for the “Vehicle Matching Phase” methodology.	220
141	Take-off angle of attack and thrust requirements	222
142	Lift coefficient vs. angle of attack take from the experiment of [32] at a Mach of 0.2 with zero elevon deflection (clean configuration).	223

143	Climb envelope showing Mach number vs. altitude, lift coefficient, angle of attack and thrust requirement.	224
144	Alpha schedule of the baseline vehicle for take-off, climb-out, and cruise. Also shown are the alpha envelope scenarios to be tested. . . .	225
145	Screening DoE Case Description	230
146	Figure showing the converged and failed cases in the screening doe for the initial BLI MDP setup.	231
147	Figure showing effect of increasing the thrust saving coefficient on the MDP design solutions with BLI.	232
148	Excess thrust vs. flight Mach number for the baseline scenario without the variable area nozzle and a constant ADP FPR of 1.4.	233
149	Distortion related stall margin loss vs. flight Mach number for the baseline scenario without the variable area nozzle and a constant ADP FPR of 1.4.	234
150	Excess thrust near TOC vs. flight Mach number for the baseline scenario without the variable area nozzle and a constant ADP FPR of 1.4.	234
151	Distortion related stall margin loss vs. inlet capture area aspect ratio for the baseline scenario screening cases without VAN.	235
152	Take-off excess thrust (negative means thrust loss) vs. inlet capture area aspect ratio at different TKO angles of attack.	236
153	Excess thrust vs. flight Mach number for the baseline scenario with the variable area nozzle and a constant ADP FPR of 1.4.	237
154	Distortion related stall margin loss vs. flight Mach number for the baseline scenario with the variable area nozzle and a constant ADP FPR of 1.4.	237
155	Van area schedule for the baseline flight envelope scenario.	238
156	Take-off excess thrust (negative means thrust loss) vs. inlet capture area aspect ratio at different TKO angles of attack with VAN.	239
157	Distortion related stall margin loss vs. flight Mach number for the baseline scenario without the variable area nozzle and a constant ADP FPR of 1.4.	240
158	Distortion related stall margin loss vs. flight Mach number for the baseline scenario without the variable area nozzle and a constant ADP FPR of 1.4.	241

159	Diagram of the re-matching procedure for the baseline scenario. . . .	244
160	Plot showing the % excess thrust at each point in the flight envelope for all of the converged cases using the re-match process	245
161	Plot showing the excess SMN at each point in the flight envelope for all of the converged cases using the re-match process.	245
162	Plot showing the capture area solution for each point run in the re-match experiment.	246
163	Plot showing the inlet aspect ratio vs. fuel burn trends and comparing the rematch MDP with the original setup.	247

LIST OF SYMBOLS OR ABBREVIATIONS

$0 - D$	Zero dimensional.
A_c	Capture area of the inlet hi-lite.
ADP	Aerodynamic design point.
A_i	Local flow capture area.
A_∞	Free-stream mass flow equivalent area (also A_o).
AIP	Aerodynamic interface plane.
α	Angle of attack.
A_o	Free-stream equivalent flow area.
AR	Inlet width to height ratio.
$A_{th,max}$	Maximum throat area.
B	Blockage parameter.
β	The percentage of the wake which is recovered by BLI.
BLI	Boundary layer ingestion.
$BLIPSS$	Boundary layer ingesting propulsion system sizing.
K	Kinetic energy defect.
M	Mass flow defect.
P	Momentum defect.
BPR	Bypass ratio of the engine.
BWB	Blended Wing Body.
C_d	Vehicle drag coefficient.
C_{fa}	Duct averaged pre-entry skin friction coefficient.
CFD	Computational Fluid Dynamics.
$CMPGEN$	NASA compressor performance tool.
C_p	Specific heat at constant pressure.
CV	Control Volume.

D	Total drag of the vehicle.
D_{BLI}	Drag recovery term related to BLI.
$DC(\theta)$	DC theta distortion descriptor.
δ	Boundary layer thickness or reference pressure correction factor.
δ^*	Boundary layer displacement thickness.
Δ^{**}	Boundary layer density thickness.
ΔPRS	Stall margin loss at constant flow due to distortion.
$\frac{\Delta PC}{P}$	Ratio of ring pressure loss to average ring pressure.
$\frac{\Delta PR}{P}$	Radial distortion descriptor.
D_i	Induced drag of the vehicle.
DoE	Design of Experiments.
\dot{E}_v	Rate of flow of wake transverse kinetic energy deposition.
\dot{h}	The climb rate of the vehicle.
\dot{m}	Mass flow rate.
\dot{m}_c	Corrected flow.
dS_{TP}	Differential area at the trefftz plane cross section.
EPR	Engine pressure ratio.
η_{BLI}	Propulsive efficiency of the BLI propulsor.
η_{Podded}	Propulsive efficiency of the podded propulsor.
FAA	Federal Aviation Administration.
F_n	Net thrust provided by the propulsor.
$F_{n,BLI}$	Net thrust provided by the BLI propulsor.
$F_{n,Podded}$	Net thrust provided by the podded propulsor.
FPR	Fan pressure ratio of the engine.
γ	Ratio of specific heats or the ratio of the surface dissipation ingested to the total surface dissipation.
\hat{n}	Normal vector to the inlet and outlet of the control volume.

<i>HPC</i>	High pressure compressor.
<i>HPCPR</i>	High pressure compressor ratio.
<i>HPT</i>	High pressure turbine.
<i>HWB</i>	Hybrid wing body aircraft.
<i>I</i>	Duct equivalent circumference integral.
<i>J</i>	Average pre-entry skin friction area integral.
K_c	Linear distortion correlation coefficient.
K_L	Kinetic energy defect on the lower surface.
K_U	Kinetic energy defect on the upper surface.
<i>L</i>	Aircraft lift.
<i>LPC</i>	Low pressure compressor.
M_e	Nozzle exit Mach number.
<i>MFP</i>	Mass flow parameter.
<i>MFR</i>	Mass flow ratio between outboard and inboard engines.
M_∞	Free-stream Mach Number.
<i>MN</i>	Free-stream Mach number.
M_o	Free-stream Mach Number.
M_t	Maximum throat Mach number.
μ	Mass flow ratio.
<i>n</i>	Total number of propulsors.
<i>N1</i>	Speed of the LP Spool or fan.
<i>NASA</i>	National Aeronautics and Space Administration.
N_{cMap}	Compressor map corrected flow.
N_{comp}	Number of aerodynamic design points.
n_{eng}	Number of engines.
N_p	Number of design points.
N_{pm}	Number of power management rules.

ν	Ratio of trailing edge kinetic energy defect which is re-energized to the whole defect.
OPR	Overall pressure ratio of the engine.
P_{av}	Average pressure of the entire fan annulus.
P_{av}	Average pressure of the fan low pressure sector.
PC	Parallel Compressor.
P_e	Boundary layer edge static pressure.
$PFAV$	Average radial pressure distortion summed over all of the rings.
ϕ_{Inlet}	Inlet loss coefficient.
ϕ_{Nozzle}	Nozzle loss coefficient.
π_d	Inlet diffuser pressure ratio.
π_r	Diffuser pressure ratio parameter.
P_k	The net flow of propulsor mechanical energy into the CV.
$P_{k,inl}$	Kinetic energy defect flowing into the control volume.
$P_{k,out}$	Kinetic energy defect flowing out of the control volume.
P_s	Net propulsor shaft power or static pressure in a flow.
P_v	The net pressure-volume power provided by the fluid expanding against atmospheric pressure.
q_∞	Free-stream dynamic pressure.
R	Universal gas constant.
Re	Reynold's number of the flow.
r_h	Hub radius of the fan.
ρ_e	Density at the edge of the boundary layer.
r_t	Tip radius of the fan.
SLS	Sea-level static.
$SLSU$	Sea-level static un-installed.
ST_c	Specific corrected thrust.
T	Uninstalled engine thrust.

T_3	Compressor exit total temperature.
T_4	Turbine inlet total temperature.
TE	Trailing of the edge of the vehicle airfoil.
θ^*	Boundary layer kinetic energy thickness (either area or height averaged).
θ_i^-	Circumferential extent of the distorted fan sector.
TKO	Take-off.
TOC	Top of climb.
TSC	Thrust Saving Coefficient.
$TSFC$	Thrust specific fuel consumption.
u_e	Axial velocity at the edge of the boundary layer.
U_{tip}	Compressor tip speed.
V_∞	Free-stream velocity.
V_{jw}	Jet velocity for the notional BLI propulsor.
V_w	Wake velocity.
W	Instantaneous weight of the vehicle.

SUMMARY

The current trend in aviation technology is towards radically more fuel efficient and quieter vehicles, which is being driven by a need for more environmentally responsible aviation. One concept which has been used to much success in marine propulsion applications, and has been identified for potential fuel burn savings in aviation is the "Boundary Layer Ingesting" (BLI) propulsion system. A BLI propulsion system is one in which the "boundary layer" or "wake" of an upstream aerodynamic body is ingested into and re-energized by the propulsor. This technology has been investigated at the theoretical level for aviation applications by many authors and has been the subject of much recent research in academia, industry, and government. This is, in part, because of the innate synergy of BLI with new advanced vehicle concepts such as the hybrid wing body.

The benefit of the BLI propulsion configuration arises from the basic fact that ingesting low velocity boundary layer flow increases the propulsive efficiency of the system. However, the benefit is potentially counteracted by the fact that propulsion system compression components tend to operate with reduced efficiency and stability when subject to heavily distorted flow conditions. The design challenge for BLI, then, is to maximize the amount of boundary layer which can be ingested while minimizing the negative impact of distortion on the system. From a design perspective, this task is a difficult one due to the strong aero-propulsive interaction and complex turbulent flow physics which drive the system. There is necessarily a degree of cross-fertilization which must occur between the propulsion and aerodynamic disciplines very early in the design process.

For the engine designer, BLI poses a problem during conceptual design because there are many new aerodynamic interaction effects for which empirical data may not be available. The cycle analyst therefore has the difficult task of quantifying these effects to understand the impact on the design space of the system. Methods used to date have employed simple approaches for cycle analysis whereby the boundary layer is characterized using data from a single CFD solution or from closed form boundary layer approximations. The losses are sometimes ignored, or are modeled parametrically with independent efficiency parameters in the cycle model. Conceptual level approaches also typically ignore the impact of system operability on the design choices made, which could impact the viability of the system. Additionally, BLI cycle analyses typically employ a single design point, single engine/propulsor sizing methodology, which ignores the impacts of BLI at important off-design conditions like high angle of attack take-off, climb, or landing. This also ignores the fact that engines often operate at different points on the airframe, depending on the choice of architecture. The research objective for this thesis was to develop a methodology which can account for both design and off-design performance impacts of BLI systems, including operability analysis, which can simultaneously size the entire system for all performance requirements.

To satisfy the research objective, three major areas of the problem were investigated. First, the necessary conceptual level modeling requirements were investigated for BLI systems, and an inquiry into the impact of operability on the BLI system design space is performed. Second, a methodology for the integration of various propulsion architecture types is derived which makes use of the existing multi-design point methodology. Finally, an investigation into the critical flight conditions required for sizing and constraining the system design is performed. A process for matching a given propulsion system architecture to a specific vehicle is defined which determines the critical flight conditions for the system and ensures that the system meets all of

the requirements and constraints.

The first area of investigation was into the necessary criteria for BLI modeling at the conceptual level. Theoretical investigations found that the impact of boundary layer ingestion on the propulsive efficiency is a function of the amount of boundary layer related drag that is ingested into the propulsion system in proportion to the total thrust required to propel the vehicle. Two types of systems were discussed: those with laterally distributed wakes (type 1) and those with circumferentially distributed wakes (type 2). For the former, the amount of boundary layer ingested is a function of the stream tube width, while for the latter it is a function of the stream-tube radius. For type 1, the distortion pattern is primarily circumferential while for type 2 it is mostly radial distortion induced by the boundary layer velocity profile. It was found that the system losses also depended on the amount of boundary layer that is ingested in relation to the height of the propulsor, as they typically scale with the proportion of clean to dirty flow. From these observations, hypothesis 1 was formed and states that the relationship between the vehicle boundary layer, the engine stream-tube, and system losses and power balance benefit must be captured during conceptual design in order to properly capture performance trends. A simple algebraic example showed that the stall margin loss of a fan would scale up as the propulsor height is decreased relative to the boundary layer thickness parameter. Hypothesis 2 states that this trend would place a constraint on the height of the propulsor achievable, which has implications for the level to which a BLI propulsion system can be made more distributed.

The second area of investigation was related to the integration of unique architecture types into a unified methodology for analysis. It was found that the multi-design point approach could be modified to account for differences in the aero-propulsive interaction between the propulsors at each flight condition to conduct the analysis. This required the implementation of potentially two new sets of rules: power management

and design rules. These rules are the mathematical relationships which govern how the power output of the propulsors are related at off-design and design points respectively. A process for setting up these rules was defined and mathematical relations for the required number of rules are presented, giving the user some guidance into how the multi-engine MDP process is executed. A third hypothesis was formulated which postulated that this approach is feasible, that solutions could be found, and that the difference between this approach and other potential approaches would be greater as the difference between the engines became larger. Since this new approach allows for the inclusion of design rules, it may sometimes lead to the inclusion of new design degrees of freedom. One such degree of freedom is the design mass flows of each propulsor – which is to say that each location could have a unique design instead of having a single propulsor designed for all locations. For the hybrid wing body example problem, a new cycle variable was defined as the mass flow ratio which represented the ratio between the outboard and inboard engines. A fourth hypothesis was formed which stated that the mass flow ratio variable could be used to further improve the fuel consumption performance of a 3-engine HWB system.

The third and final area of investigation was into the critical flight conditions for BLI systems which are required to include in a multi-design point sizing procedure. A theoretical analysis showed that installation effects could also impact the thrust of a system differently over a range of altitudes through the installed benefit to loss ratio coefficient. Furthermore, the inlet sizing point will depend on the size of the boundary layer, since choking induced by flow blockage can increase the required capture area. Finally, the impact of the distortion on stall margin was found to vary over the flight envelope along with the natural decline in stall margin as the engine moves to lower speed. Since this is also a function of the boundary layer which is strongly impacted by the angle of attack, and since angle of attack varies significantly over the flight envelope, there may be a critical condition for the stall margin constraint which is

very different from the design point and which is not known prior to analysis. All of this taken together implies that with an installed BLI engine, the necessary flight conditions to include are not precisely known prior to running the MDP. To check the off-design conditions, a screening process is proposed to check potential off-design conditions for criticality and the fifth hypothesis states that a sub-set of all potential conditions can be found that are the most critical, which would allow the critical conditions to be known prior to MDP execution.

The above areas of investigation led to the formulation of the “Boundary layer ingesting propulsion system sizing (BLIPSS)” methodology. The methodology includes the original MDP methodology and sections pertaining to each of the areas of investigation: the BLI modeling phase, architecture integration phase, and the vehicle matching phase. The methodology not only sizes the system for multiple design conditions, but also ensures that the system architecture impacts and operability constraints are included, which satisfies the stated research objective. Therefore, the thesis of this work is that the BLIPSS methodology is a useful approach which improves upon current BLI system analysis state of the art techniques.

To test the validity of this thesis and the related hypotheses, an implementation was conducted for a hybrid wing body vehicle with flush mounted turbofan engines. The modeling environment was constructed in the NPSS program developed by NASA which was used as a back end programming tool and for the thermodynamic modeling. The aerodynamic analysis of the vehicle airfoil stack was conducted using XFOIL, which is a low Reynolds number aerodynamic analysis tool. A custom inlet modeling tool was created in C++ which modeled the inlet pre-entry and duct diffusion losses prior to arriving at the fan face. Finally, a novel parallel compressor model was used to predict fan performance and operability losses. This coupled modeling environment is capable of representing the BLI propulsive efficiency benefit and inlet/fan related losses over a range of operating conditions, angles of attack, and locations of the

engine on the vehicle. This allows for a parametric exploration of the propulsion system design space at the aerodynamic design point and also at other relevant off-design conditions.

For each hypothesis, an experiment was conducted to demonstrate its validity. For hypothesis 1, a modeling hierarchy was constructed, which allowed for loss components to be turned on and off during the experiment. A comparison of these various models was shown for variations in design variables and for off-design operating conditions. The key result from this experiment is that the hypothesis was confirmed by showing that there were significant differences between the design spaces, both in terms of the shape, magnitude, and final optimum design depending on which loss model was used. This was true for a number of design space sensitivities including FPR, inlet aspect ratio, and the number of engines. Another important effect shown was that the angle of attack, which is a surrogate for boundary layer thickness, has a strong impact on the performance of the engine. At take-off, the boundary layer separation at high angles of attack produced significant blockage prior to entry into the engine, which can lead to choking of the inlet at its capture area.

The second experiment was designed to test the validity of hypothesis 2 by varying the inlet capture height and measuring the stall margin loss as predicted by the parallel compressor model. Hypothesis 2 was found to be valid for the test case by showing that there was a strong correlation between the capture height of the propulsor and the stall margin of the engine, thereby imposing a minimum height constraint for the system. The stall margin analysis in experiment 2 was shown for the cruise design point, but off-design trends at TKO also showed that this point could potentially be more critical if high angle of attack is required. Several stall margin mitigation actions were also implemented, including fan re-match and recirculation bleed. Both of these proved relatively ineffective at restoring stall margin in relation to their costs.

The third experiment showed that the proposed multi-engine, multi-design point approach was successful in sizing the system for a total vehicle thrust and that the results differ significantly from the single engine method and a “wake correction” based approach. This occurs because the BLIPSS methodology accounts for differences in inlet recoveries between the engines. The fourth experiment showed that the mass flow ratio could be used to improve the efficiency of the 3 engine HWB system by making the outboard engines smaller relative to the inboard engine, which implies that a BLI system can tailor the size of each propulsor to the specific local boundary layer size and that the BLIPSS methodology is the proper method for this task. However, it was found that to do this, there should be minimal impact on the gas turbine core such as was the case for the fixed-core designs which did not show benefit.

The final experiment attempted to determine the critical flight conditions for the notional HWB vehicle. To do this, all of the flight conditions in the envelope of the vehicle were checked at their highest required angle of attack and at max power. A screening design of experiments was constructed to vary the thrust saving coefficient of the system during the screening process. The case without variable area nozzle showed that designs were generally stall margin constrained at the high angle of attack TKO point. The TOC point used for the baseline engine also proved to be less critical than a slightly different TOC point with a higher Mach number for the BLI systems with more thrust saving coefficient. For all of the screening cases, the most critical points for both thrust and stall margin were the high angle of attack TKO and the highest Mach climb point which confirms hypothesis 5 since the full set of potential critical conditions can be reduced to an additional two conditions. The 2 critical conditions were included in a set of re-match cases and the original screening DoE was executed to show the impact of the newly imposed criteria. Results showed that the inclusion of a choking constraint at the high angle of attack TKO point pushed the inlet to a larger capture area which penalizes the system during cruise.

This had a significant impact on the fuel burn of the system. Additionally, thrust requirements at these two points caused an increase in system size for some of the cases which would be associated with an increase in system weight.

Taken together, the results of experiments 1 through 5 give a justification for the structure and use of the BLIPSS methodology during conceptual design of BLI systems. This method is an improvement on current state of the art conceptual design processes for BLI systems. It provides better estimates of performance trends over the design space, includes operability constraints, is capable of dealing with different propulsion system architectures, and can size and match the system to a specific vehicle while satisfying all performance requirements at design and off-design conditions. Though the method was only tested for the specific case of the hybrid wing body with turbofan engines, the method is general enough to handle many different architectural layouts, vehicle configurations, and both types 1 and 2 BLI. Future work recommended includes defining the parameters for implementation of BLIPSS for other vehicle configurations, extending fan modeling to a higher fidelity regime, and potentially integrating robust and probabilistic design techniques into the cycle selection process.

CHAPTER I

INTRODUCTION

1.1 Environmental Pressures and Aviation Technology

The current trend in industry standards for aviation technology is towards more fuel efficient and less noisy vehicles and power systems. Many entities including government agencies such as NASA and the FAA are interested in studying the effects of specific technologies to assess the potential return on investment to properly appropriate scarce government research dollars. In this context, many technologies require reasonable assessments of improvements at the conceptual level, when much design information is utterly lacking. In many cases, the technologies of interest are new materials, which may simply require refinement of the manufacturing processes required to achieve the necessary material strengths and thermal properties. Other types of technologies are related to the design of specific components which improve efficiencies or operability and durability throughout the component lifetime. Another class of technologies are those which alter the aerodynamics of the vehicle, such as winglets, ribs, or boundary layer laminar flow control. Such technologies are more dependent on the design of the vehicle and require proper design as well. The environmental and economic benefits of these technologies thus rely upon having reasonable design methods to assess their potential improvements. One such technology which falls into the latter class and is the subject of this thesis is boundary layer ingestion or "BLI". Rather than being a "technology", it is instead a novel arrangement of the propulsion system such that it interacts positively with the aircraft wake to produce higher propulsive efficiencies. This is done by at least partially embedding the engine

into the aircraft surface and ingesting the low-momentum boundary layer flow into the propulsor. NASA has identified aggressive fuel burn targets for the next generation of aircraft and beyond as shown in figure 1. Boundary layer ingestion has been identified as a potential technology to help enable the achievement of these fuel burn targets.

Table 1: NASA fuel burn targets for the next generation of aviation vehicles. [43]

Corners of the trade space	N+1 (2015) (Relative to B737/CFM56)	N+2 (2020) (Relative to B777/GE90)	N+3 (2025) (Relative to B737/CFM56)
Noise	-32 dB	-42 dB	-55 dB
LTO NO _x Emissions	-60%	-75%	-80%
Cruise NO _x Emissions	-55%	-70%	-80%
Aircraft Fuel/Energy Consumption	-33%	-50%	-60%

1.2 Boundary Layer Ingestion

Boundary layer ingestion (BLI) has been practiced in maritime engineering for quite some time now [36]. The main effect comes from the propulsive efficiency gains from ingesting the low-momentum flow into the propulsor and re-energizing the flow to a velocity much higher than it would be otherwise. In aviation, the gains from BLI are theoretically plausible and have been studied at some length but have yet to come to fruition in civil applications due to the additional difficulty of designing a proper aerodynamic intake which can deliver reasonable levels of distortion to the fan and compression system at transonic flight speeds and Reynold’s numbers. However, the next generation of aircraft may have much better performance synergy with the

integrated propulsive systems such that the costs of designing to negate the impacts on the engine operation of BLI are offset by the reduction in fuel consumption. One such futuristic aircraft which synergizes well with the BLI concept is the hybrid wing body. The synergy with BLI arises from the large space on the upper surface of the aircraft which is available for the placement of engines within the airframe. There are other aircraft configurations for which BLI could be a plausible option, including the "double bubble" aircraft [37], which is an aircraft resembling a conventional tube and wing but with a significantly flatter and wider body on the upper surface allowing for 2 or 3 embedded BLI engines. In fact, the configuration is such that almost the entire upper fuselage boundary layer can be ingested into the engine, which is a relatively large percentage of the total vehicle drag.

There are multiple engine architectures which are possible for a BLI system, especially for the HWB vehicle, including traditional turbofan direct-drive engines, geared turbofans, single-core/multi-fan type systems (e.g. tri-fan), and distributed propulsion. The single-core/multi-fan type systems have the benefit of being able to ingest much more boundary layer while avoiding the negative impacts on the gas turbine core. A distributed propulsion system has many small propulsors "distributed" over the upper surface in an array type configuration. The system is synergistic with BLI because it allows a very large percentage of the aircraft boundary layer to be ingested. For each of these architectures, there are further options in terms of the inlet design used – high or low aspect ratio, embedded or flush mounted, long or short, etc. Any design method for BLI systems must be able to include the physical performance differences between these propulsion system configurations in order to properly trade between different options at the system level.

1.2.1 BLI Benefits

Figure 1 illustrates the basic difference between an ideal BLI engine and a podded engine [69]. Here V_∞ represents the free-stream velocity and V_w represents the averaged wake velocity in the podded case. From classical propulsion theory, the input power required is given by equation 1 for the podded case and by equation 3 for the BLI case, where V_j is the jet velocity exiting the nozzle.

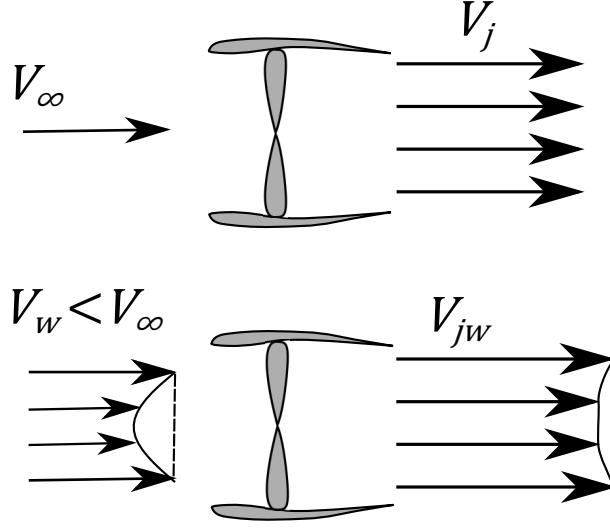


Figure 1: Notional diagram of podded vs. BLI engine design

$$P_{Podded} = \frac{\dot{m}}{2} (V_j^2 - V_\infty^2) = \frac{F_{nPodded}}{2} (V_j + V_\infty) \quad (1)$$

$$F_{nPodded} = \dot{m} (V_j - V_\infty) \quad (2)$$

$$P_{BLI} = \frac{\dot{m}}{2} (V_{jw}^2 - V_w^2) = \frac{F_{nBLI}}{2} (V_j + V_w) \quad (3)$$

$$F_{nBLI} = \dot{m} (V_{jw} - V_w) \quad (4)$$

Then, the propulsive efficiencies are:

$$\eta_{Podded} = \frac{2}{1 + \frac{V_j}{V_\infty}} \quad (5)$$

$$\eta_{BLI} = \frac{2}{\left(\frac{V_{jw} + V_w}{V_\infty}\right)} \quad (6)$$

Now, V_w is inherently less than the free-stream velocity, and for a constant mass flow and thrust, the jet velocity required for the BLI case is also reduced. By comparing equations 5 and 6, it is clear that the propulsive efficiency will be higher in the BLI case. The benefits of BLI can be described, then, as a reduction in the total power requirement of the vehicle due to an increase in propulsive efficiency.

Depending on the system configuration, there may be other ancillary benefits. For instance, the weight of the propulsion system is typically improved because of the elimination of the need for an engine pylon. There may also be a wetted drag reduction since the pylon and nacelle area can be reduced with properly embedded or flush mounted engines having some of their surface area contained within the aircraft and not wetted by the air, though this is possibly offset by aerodynamic interference or flow separation.

1.2.2 BLI Risks

Perhaps the most significant risk with regard to BLI is the performance of the inlet and fan system. The intake of an aircraft engine, while simple, is an absolutely essential component whose performance has a high impact on the specific fuel consumption of the engine. The intake must supply the necessary amount of air flow to the compression system to accommodate the required level of thrust without significant losses or flow distortion which can lead to performance degradation or compression stability concerns. Two risks arise from this problem: 1.) Engine performance degradation (related to inlet total pressure recovery and fan distortion); 2.) Compromised stability of the compression system due to the presence of both steady-state and dynamic inlet total pressure and swirl distortion. There is a therefore a risk that the BLI induced gains in propulsive efficiency may be offset by the presence of a poorly performing inlet configuration and also a risk that the engine, while more efficient, may not be operable over the required flight envelope of a civil air transport. Nichols, in

an evaluation of the Silent Aircraft Initiative, also identifies these risks as the primary factors of uncertainty for the concept [64].

There are other ancillary risks such as the effect of the distortion on component degradation and lifetime. Such factors can significantly impact operational costs and potentially offset some of the fuel burn savings. There is also the additional difficulty of designing a configuration which has a highly integrated airframe and propulsion system. This concern is exacerbated by the fact that these components are produced by separate companies requiring the need for inter-corporate cooperation to certify this new technology and provide for an economical design [15]. There are also other detailed factors such as the control of a system which is specifically designed to have steady-state and transient turbulent distortion present during operation or vibration which might arise from the same phenomenon. Significant research funding has gone into investigating the possibility of designing a "distortion tolerant fan" which can operate under the types of distortion related to BLI with improved efficiency and stall margin [29].

1.3 Design Methodologies

With the above discussion as pretext, we turn to the fundamental problem of designing BLI systems: to quantify the aero-propulsive interactions between the propulsion and airframe systems in a multi-disciplinary manner. Though several authors have constructed and implemented methodologies which seek to integrate high fidelity CFD tools with propulsion system analysis tools for coupled design (illustrated in fig. 2), the task is a daunting one. For example, both Rodriguez [72] and Lee [53] implemented a coupled optimization methodology for the propulsion system which used high fidelity aerodynamic tools. Though Rodriguez showed that inlet designs and propulsor orientation could be significantly improved using these methods, the run times are long, setup times are difficult, and ultimately requires a fixed configuration.

Lee found a similar result when trying to implement his Bayesian optimization method with a BLI system. Even with a theoretically better optimization routine, the run times were prohibitive for actually converging on an optimized solution. Again, both of these studies were performed on point designs in the configuration space. To

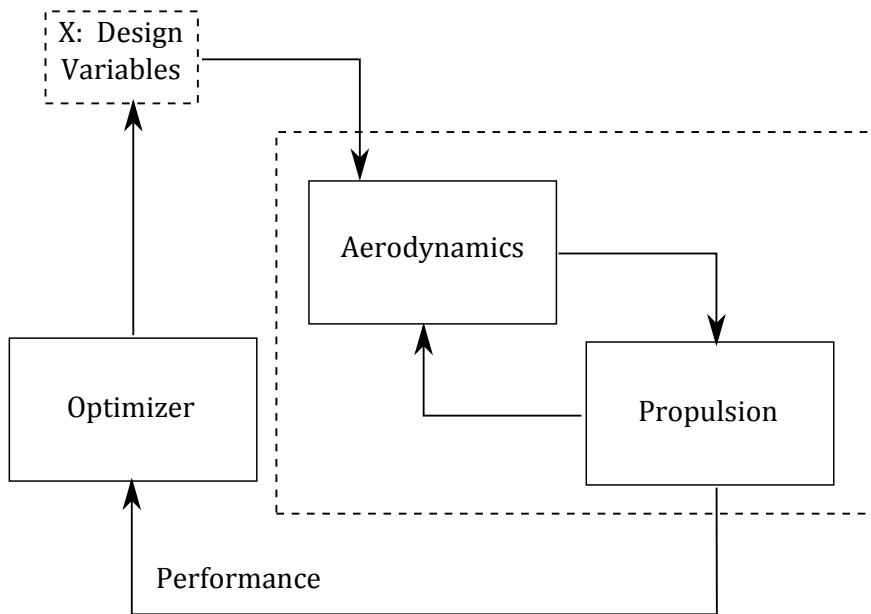


Figure 2: Notional diagram of the aerodynamic and propulsive interactions scheme.

get around this problem, entities researching BLI have essentially employed a multi-fidelity approach to the design problem, which is a bit more consistent with how industry operates. The cycle analysis is conducted for the propulsion system and configuration design studies. Promising candidate designs are selected and initial geometries are defined based on these which are then moved to the higher fidelity tools for evaluation and detailed optimization. Some experimentation has been conducted on specific inlets, fans, and existing engines to determine the impact of BLI, in general. This process, while perhaps not the most integrated, is a practical way of progressing through the phases of the integrated propulsion system design process.

There have been a number of conceptual, system level design studies performed on BLI propulsion systems in recent years which will be discussed in more detail in Chapter 2. The most common employ the thermodynamic cycle analysis while

also incorporating some method for quantifying the impact of BLI on the engine performance. Typically these are "0-D", axially symmetric analyses that aim to provide thermodynamic gas path properties, thrust, fuel flow, and expected fuel burn benefit. From this analysis, a propulsion system configuration, cycle design (typically fan pressure ratio) is selected, and some sensitivities to unknown parameters like inlet recovery and compression system efficiency are conducted to understand targets for component optimization. Being the first step in the integrated design process, this is arguably the most important step, since the selected architectures and cycle designs will be passed to more computationally expensive tools, consuming much of the engineering budget of the project. As such, making better decisions about the BLI propulsion system during the conceptual level analysis will pay dividends during the rest of the process.

1.4 Need for an Improved System Analysis

A cursory review of the existing system study literature will show that there is often significant disparity between the results of the system level studies and the higher fidelity results. For example, see Plas [69] who compared different modeling approaches and Rodriguez [72] who compared his CFD based method with simpler "back of the envelope" type approaches. Much of this arises from either deficiencies in the way that the BLI benefit or inlet losses are quantified and also from effects such as flow separation, excess nacelle/inlet drag, and other factors which only a high fidelity approach can truly capture. This highlights the difficulty with using these conceptual levels tools so early in the design process to make likely dubious decisions based on a poor understanding of their true aerodynamic consequences. Nevertheless, the higher fidelity analysis requires some system definition prior to execution, as well as a cycle model to link the analysis to for boundary condition purposes. Rather than have an

arbitrary configuration, some cycle analysis is necessary and may be useful in identifying trends which give insights into possible best configurations and also the impact of information needed from the higher fidelity tools. This thesis attempts to identify gaps in the current system design literature and outline an improved methodology for sizing and performance analysis of conceptual level BLI system studies which will allow for more accurate analysis and better system-level design decisions. The thesis will be structured as follows:

- Chapter 2 will discuss the past literature and identify gaps in previously used methods to establish the need for the methodology developed.
- Chapter 3 will discuss the theoretical justification for the methodology and establish a set of research questions and hypotheses to be investigated.
- Chapters 4-6 will present an implementation of the approach, and discuss the results of experiments conducted to validate the hypotheses and the use of the methodology.
- Chapter 7 will provide a summary of the work, conclusions, and recommendations for future work.

CHAPTER II

LITERATURE REVIEW

2.1 BLI System Level Literature Review

As discussed previously, the typical tool set for the engine designer at the conceptual level is engine thermodynamic cycle analysis. The point of the cycle analysis at the conceptual level is to establish an engine aerothermodynamic cycle which can satisfy all of the requirements of the engine while minimizing operational costs such as fuel burn. In the early years of cycle analysis, cycle trade studies were the primary tools for conducting the parametric engine cycle design studies, while the advent of the modern computer and computer aided design has enabled the integration of other aspects of the design process such as engine flowpath, aircraft mission and cost analyses. Additionally, modern design techniques enable broad trade space exploration and optimization within the context of these computational models. Along the same lines, engine and airframe integration, especially in the military realm, has had a similar history with increasing tendency towards integrated design processes to facilitate increasing design knowledge early in the design phase to eliminate costly design changes in the later phases. This section will look at the latest cycle analysis techniques for BLI.

2.1.1 General Studies

Classic Studies

Boundary layer ingestion really stems from considerable usage in marine propulsion where it is much easier to take advantage of the large ship wake that can be ingested by an aft mounted propeller. It has been researched somewhat in previous investigations

for aircraft applications however. The first investigation of BLI was conducted by A.M.O. Smith [85]. In 1946, Smith conducted an analysis of a turbojet engine and aircraft design with standard inlets and with BLI inlets. The BLI inlets were idealized as slots installed over the wing. Smith showed a 30% improvement in fuel efficiency and a 7% higher optimum cruise speed, though this is in comparison to designs of the time.

Lynch [60] performed a momentum analysis on an early turbofan engine design that ingested fuselage boundary layer and obtained a 3% improvement in propulsive efficiency accompanied by a 6-10% decrease in maximum engine thrust. Lynch's analysis also depended on the assumption of minimal inlet losses.

Douglass [19] performed an energy wake analysis on an aircraft with aft fuselage-mounted engines. The engines were assumed close enough to the fuselage to ingest the boundary layer. Douglass analysis suggests up to a 10% improvement in propulsive efficiency compared to an equivalent pylon mounted engine installation.

Smith

Smith [86] studied the impact of a wake ingesting unducted propeller. He conducted analysis very similar to that shown in Chapter 1 and in the marine propulsion literature. The analysis showed that the benefit was parametrically dependent both on the size of the wake ingested into the propulsor (the wake defect), the shape factor of the wake, and finally crucially dependent on a factor defined as the “recovery parameter” – essentially a measure of how of the wake is flattened by the propulsor. For this type of configuration, it was found that sizing the propeller just big enough to capture the boundary layer would be sufficient, since the benefit wasn't found to be as large for high mass flow (low thrust loading coefficient) propulsors.

2.1.2 HWB with Hi-Bypass Turbofan Studies

Boeing Studies

Dagget et. al. conducted a study for the Boeing company under the Ultra Efficient Engine Technology/Propulsion Airframe Integration Project. The study was designed to analyze the effect of BLI on the BWB aircraft with active flow control (AFC). The engine analysis was done using the "ram drag" approach, meaning that the ram drag term contained within the net thrust is reduced by a percentage which is calculated based upon the boundary layer characteristic averaged over its height. The analysis included 3 tasks: first the establishment of a baseline; second, the evaluation of embedded engines with BLI; third, evaluation of active flow control (AFC) to inlets. A podded engine based off of typical engine technology was established as the baseline engine. For the BLI configuration, a long S-Duct, highly off-set embedded inlet was used to establish the fuel burn benefits from the ram drag reduction. It was determined that the baseline BLI configuration would offer 3.1% fuel burn improvement, which is relatively substantial. With the addition of the AFC technology, the inlet duct can be shortened which has weight, wetted area, and total engine length benefits. This also allows the use of high aspect ratio inlets which allows for larger ingested boundary layer. The fuel burn benefit with the AFC technology and the shorter low-offset inlets was estimated as 5.5%.

Another study conducted by the Boeing company focused on the inlet configuration and the potential benefits offered by increasing the aspect ratio of the inlet. The approach and general vehicle configuration was very similar to that studied in ref. [42]. The study also refined the calculation for the nacelle viscous drag by "proper analyses of viscous changes where reductions in nacelle drag account for local Reynolds Number effects". This accounting difference led to a much greater estimate of the potential of BLI with AFC and flush mounted inlets which was estimated at 10%

maximum. It was determined that the lower aspect ratio inlet (higher height than width) resulted in a better net fuel burn than the larger width inlets due to the fact that the inlet pressure recovery was assumed to be 1% different. The result of this is therefore dependent on the validity of this assumption. If the lower and wider inlet (higher AR) can be kept at sufficiently similar levels of inlet recovery, it should offer larger benefit due to the increased amount of drag ingestion and improved ram drag effect.

Nickols

Nickols and McCullers conducted a configuration system study for the Hybrid Wing Body concept. This study was a relatively low fidelity study which did not truly employ engine design techniques or cycle analysis. Instead the study assumed a certain percentage drag reduction to be applied to the aircraft drag polar within the mission analysis, as well as a nacelle wetted area reduction factor, pylon weight structural factor, and SFC penalty due to the lower inlet pressure recovery. The final analysis showed an impact of 5.2% fuel burn benefit for the BLI technology.

Rodriguez

Rodriguez, as a part of his doctoral work, developed a method for multi-disciplinary inlet optimization which combined high fidelity CFD methods with a propulsion model. The method was applied to the BWB vehicle with 3 boundary layer ingesting high-bypass ratio engines. The method consisted of optimizing the inlet and external cowl shape such that the fuel burn rate is minimized while maintaining an acceptable level of inlet distortion. The method itself did show significant improvement from the baseline design, which highlights the importance of higher-order methods in the detail aerodynamic design phase. However, the work showed that the same optimization applied to the podded case yielded the result that BLI did not provide any benefit

(BLI was actually worse, in fact). This could have resulted from the fact that there were a limited number of design variables for the outboard engines, yielding excess and potentially removable wave drag from the outboard engines. Furthermore, the inlet pressure recovery was very low in comparison to recent studies which have shown potentially much higher values of inlet recovery using other optimization methods.

Plas

As part of NASA's silent aircraft initiative, Plas conducted a study of boundary layer ingesting engines in which the following 3 contributions were intended: Creation of a conceptual and theoretical framework for BLI in aircraft design; development of high fidelity models for representing an aircraft with BLI embedded engines; Quantification of the benefits of BLI. This work is the first of its kind that actually analyzes the impacts of BLI while including an actual model of the turbomachinery operating in non-uniform flow. The study assumed that the configuration of interest was a ducted fan type. The work included an assessment of three different degrees of fidelity within the fan modeling: a one-dimensional parallel compressor approach, an integral boundary layer approach, and a 3-D body force model. The highest fidelity of these approaches showed that BLI for the aircraft under consideration in the silent aircraft initiative gave power savings between 3-4%. The study also concluded that a principal feature required to estimate power saving for the propulsor is the distortion transfer across the fan (i.e. level of distortion downstream of the fan). It was also found that the power savings differed by 10-40% between the different fidelity fan models, although the trends remained roughly the same regardless of the modeling fidelity.

NASA and UTRC

Hardin et. al conducted an aircraft system study of a BLI propulsion configuration. The analysis included a detailed cycle model for an ultra-high-bypass propulsion

system with BLI. The system study employed lower order models for the different components of the BLI problem, including the BLI theoretical benefits; nacelle weight and drag; fan performance; and inlet pressure losses. Aircraft trade factors were used to estimate fuel burn based on the engine cycle calculations and weight estimates, and the results of the study showed that a 3-5% BLI fuel burn benefit could be achieved for the "N+2" generation aircraft relative to a pylon mounted baseline. Another key conclusion was that the inlet pressure recovery and fan efficiency have a strong impact on the level of fuel burn achieved with 1% pressure recovery loss translating to 3% fuel burn increase. This provides the motivation for low loss inlets and distortion tolerant fan configurations to maximize the potential benefit of the technology.

Summary of HWB-Turbofan BLI Configurations

A few trends arise from an analysis of the system study literature:

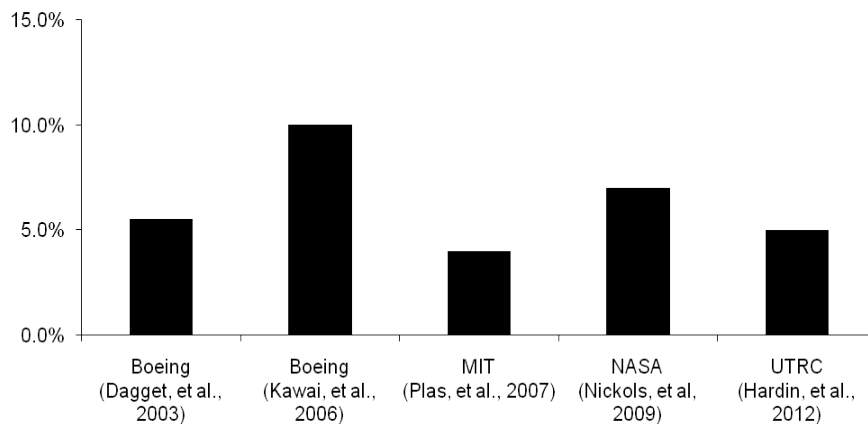


Figure 3: Boundary layer ingestion system study estimates

- The fuel burn analysis for BLI is a function of the trade-offs between propulsive efficiency gains obtained via drag ingestion, thermal efficiency penalty due to distorted inlet flow, propulsive efficiency changes due to changes in nacelle and interference drag, and the effect on the engine and support structure weight – all of which affect the aircraft fuel burn.

- There is a wide uncertainty on the potential benefit that BLI offers for the HWB aircraft, typically ranging from 0-10%. (See fig. 3)
- The quality of the inlet, level of inlet distortion, and impact on the fan efficiency have a strong impact on the potential benefits. This is shown by simple cycle analysis results, as well as by the study of Rodriguez, which predicted no benefit for BLI with very high loss inlets relative to studies with much improved assumptions.
- Configurations which can reasonably ingest more boundary layer across the upper surface of the aircraft stand to offer larger potential benefits.

2.1.3 NASA N3X: Felder et. al.

The NASA N3X is an airframe concept very similar to the Boeing HWB designs, except that it employs the turbo-electric distributed propulsion (TEDP) concept. This is where wing tip placed gas turbine cores provide power to electrically driven fans. The fans are distributed in an array along the upper surface of the N3X vehicle and ingest a substantial amount of the aircraft upper surface. Felder et. al. [47] conducted a propulsion system analysis and found a substantial benefit with BLI relative to a free-stream propulsor. It was found that for a 15 propulsor design, that the lowest possible design fan pressure ratio would give the best benefit for the system and that there was substantial difference between having a variable inlet model vs. a fixed inlet assumption. Finally, an off-design analysis was conducted which concluded that the BLI benefit effect increased as the system fan speed was decreased which substantially improves the part power performance of BLI systems.

2.1.4 Double Bubble: MIT N+3

Researchers at MIT have developed the so-called “double bubble” or D8 concept, which is a vehicle with very long, slender, high aspect ratio wings and BLI propulsors on the aft end of an unconventional fuselage with a relatively flat upper surface. Greitzer et. al. [37] demonstrated the use of the power balance approach developed by Drela [23] to analyze the system and found a substantial benefit with BLI as well. The approach taken approximated the BLI benefit by accounting for the BLI benefit term from the boundary layer and wake defect properties. This was used to estimate impacts on the engine cycle analysis.

2.2 Modeling Approaches for BLI

To summarize the previous studies, the system level studies essentially follow the process notionally outlined in fig. 4. The idea is that there is some competitive baseline design to which the BLI system is compared. The effect of the BLI on the system is then evaluated based on an estimate of the quality of the boundary layer at a specific inlet location. The system is sized at some condition and a notional cruise point is used to evaluate the specific fuel consumption of the engine. To conduct the cycle analysis, the initial baseline cycle model must be augmented to account for the BLI design. This is typically done in a way notionally described in fig. 5, where certain components of the propulsion system cycle analysis are augmented to account for some aspect of the aero-propulsive interaction. The rest of the section will focus on describing the state of the art system level approaches taken for each of the above components which require BLI impact modeling.

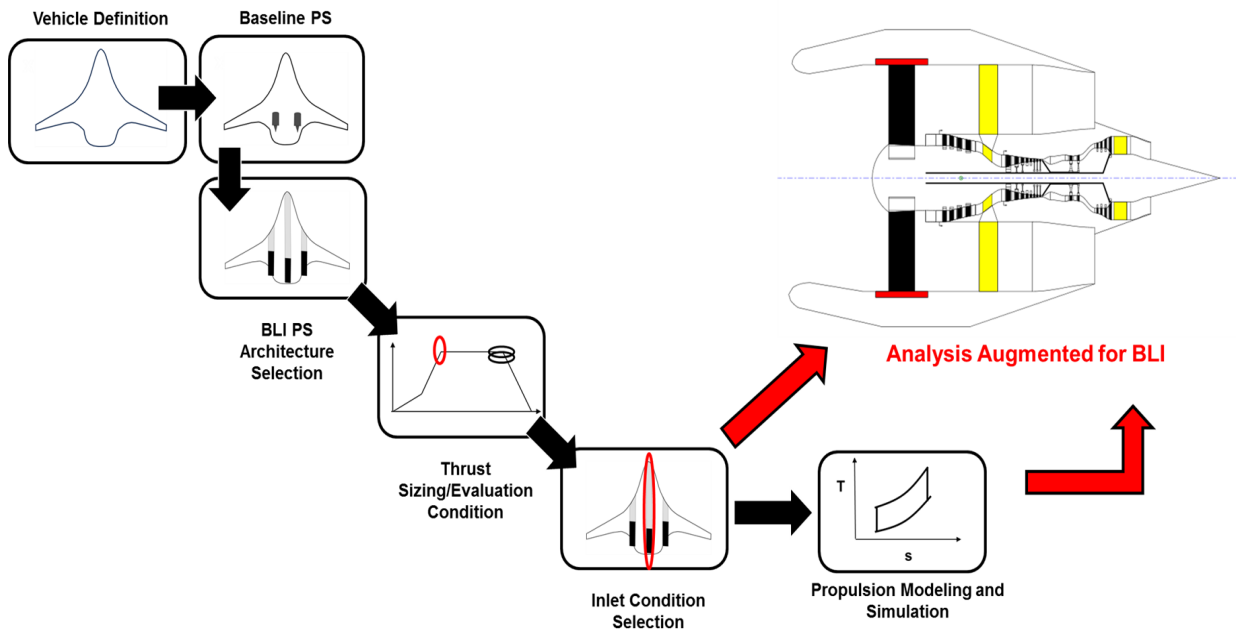


Figure 4: Notional system level design process for a BLI propulsion system.

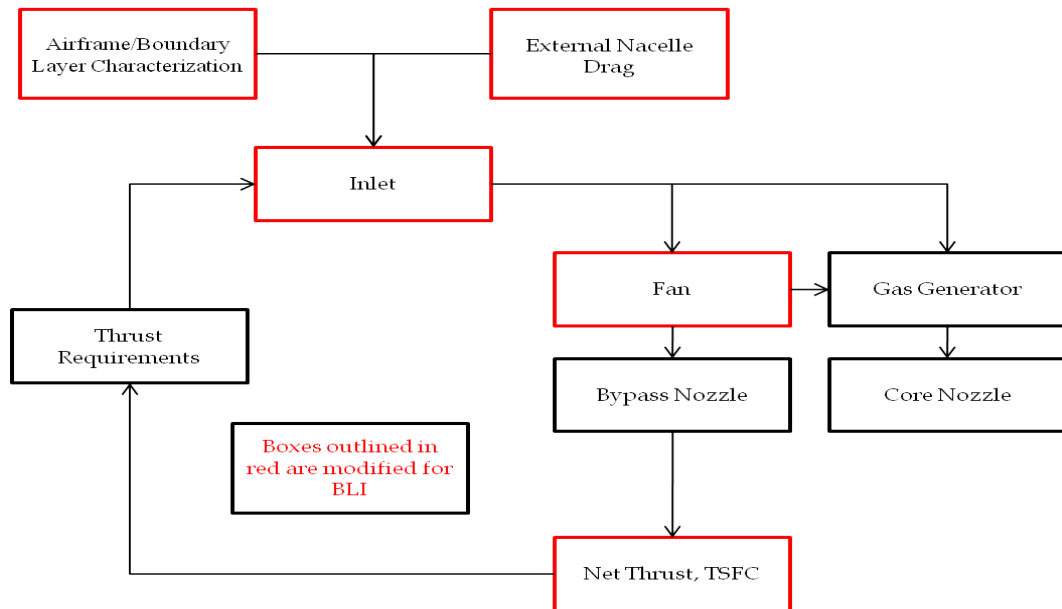


Figure 5: Notional cycle analysis for a BLI propulsion system. Boxes outlined in red show the components which need modification for BLI.

2.2.1 Airframe Aerodynamics and Boundary Layer

The previous section discussed the power balance method and the metrics by which BLI performance can be estimated. These turned out to be a function of the characteristics of the aerodynamics of the vehicle and specifically the boundary layer properties such as the momentum and kinetic energy thicknesses as well as the shape factors. This section will discuss the methods by which system studies have estimated the inviscid airframe properties as well as the boundary layer properties needed for the performance analysis.

There are a few general methods used to generate the airframe boundary layers. The two primary methods for conceptual level system studies are summarized in Table 2. Studies which use the first method include [79] [70], and studies which use the second method include [47] [40] [42]. The majority of system level studies avoid using CFD in the multi-disciplinary analysis loop, but rather assume

Approach	Pros	Cons
1-D Boundary Layer Profiles	<ul style="list-style-type: none"> • Simple • Fast • Closed form solution • Scalable with Reynolds 	<ul style="list-style-type: none"> • Can't capture 2-D/airframe effects • No angle of attack variation
CFD Based Boundary Layer Profiles	<ul style="list-style-type: none"> • Captures Airframe Effects 	<ul style="list-style-type: none"> • Not scalable • Data only at points where CFD is run • Expensive/time consuming

use the second type of method include [47] [40] [42]. The majority of system level studies avoid using CFD in the multi-disciplinary analysis loop, but rather assume

that the boundary layers do not change much from the cruise point and simply use those profiles as a starting point. From the first method, typical approaches are to assume a Coles wake profile or a $1/7^{th}$ power law profile which is typical of flat plate turbulent boundary layers.

2.2.2 BLI Inlet Modeling

Figure 6 outlines the various regions of the flow field leading up to the fan face of the embedded engine. The pre-entry boundary layer region was described in the previous section along with the models that are typically employed for conceptual level studies. Additionally, there is the "pre-compression" region which is described by Plas in [69]. This is the region in which the streamtube is affected by the presence of the engine and the flow is compressed into the inlet capture area. Flow that is not ingested into the engine passes over the external cowl region which may typically induce some drag due to wall pressure or shock wave generation. Inside the inlet, the Mach number

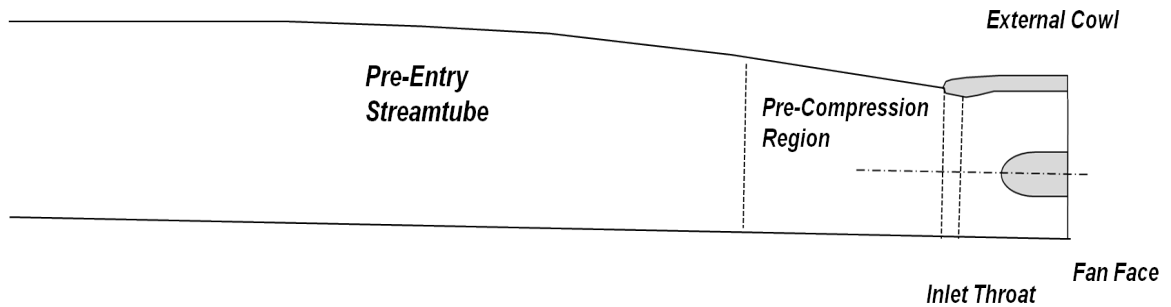


Figure 6: Notional picture of the regions of the flow field before the fan face.

decreases as the flow is diffused inside the inlet until it reaches the fan face. The fan face Mach number is typically a function of the fan design specific flow capability.

Finally, the last component of the aerodynamic analysis prior to the fan face is the performance of the inlet duct. The necessary output of this analysis depends upon the fidelity of the fan model used. If the fan model requires more detailed fan face profiles, then a higher fidelity analysis must be used. If the fan model requires

only a characterization of the "dirty" or distorted region, then a simple 1-D type analysis might suffice, such as the integral boundary layer method [69]. By far the most common approach, however, is the use of a simple inlet recovery parameter or inlet efficiency as is used in standard cycle analysis techniques. This means that the BLI losses are essentially passed as a lower mass averaged pressure recovery to the standard fan analysis. This approach is used in [47] [79] [40] [65] with various values assumed for the pressure loss, which tends to have a significant impact on BLI performance.

2.2.3 Fan Modeling

At the conceptual, system study level, the fan modeling approach taken is typically a simple efficiency hit. This approach was used in [47] [79] [40] [65] . Although simple, it does provide a basic parametric way to understand the impact of the fan performance relative to the BLI propulsive efficiency benefits to understand technology targets for a BLI fan design. Table 3 shows the differences in assumptions used for the fan efficiency for some of the important system studies mentioned earlier. It is common to assume that the efficiency penalty will be small, however recent work conducted by Pratt and Whitney [29] shows that there is a likely efficiency penalty relative to a clean fan on the order of 0-1.5%.

Table 3: Fan efficiency assumption used for several system studies.

Reference	η duct
Dagget, 2003	0%
Kawai, 2006	0%
Nickols, 2009	0%
Felder, 2011	1%
Hardin, 2012	0-8%

As discussed previously, Plas [70] conducted a study on 3 different levels of modeling fidelity for a ducted fan. For brevity, the details of each model will not be discussed here, but rather some of the key conclusions from the study will be summarized and some observations will be made that are relevant for the current work.

2.2.4 BLI Engine Off-Design

For engine off-design, only a few authors have addressed many of the potential issues. In a relatively recent review paper, [26] discusses some of the issues, including the increased influence of the BLI savings at part power as shown by Felder et. al. Ferrar also mentions that BLI has a feature of tending to have favorable variation of the capture area at low flight speed because the equivalent area is increased with the thinner boundary layer. Other than this, not many authors have considered the off-design influences during system level analyses. This is an important observation moving forward in this thesis.

2.3 The Subsonic Airframe Integration Process

Since this thesis primarily will focus on BLI for reduction in civil aviation fuel burn, it is worth looking at the current inlet and engine integration processes and requirements which are typical and to also consider how the BLI concept might change this paradigm. Firstly, civil transports of the kind to be considered for BLI will spend the vast majority of their time at the cruise condition. For that reason, cruise fuel burn is typically considered the metric of interest in most studies. However, of course it is worth mentioning that cruise does not take place at a fixed altitude, but rather a range of altitudes and Mach numbers during flight, with the vehicle lift, angle of attack, and pressure distribution changing as fuel is burned. Typically the engine is sized for some value of thrust at the top-of-climb condition where corrected mass flow is a maximum. Additionally, there is typically some maximum specified turbine inlet

temperature at take-off where the engine is running at its hottest, and the engine has to be able to supply the necessary thrust to achieve a particular take-off field length and climb rate. The point is that there are a large range of operating conditions from take-off through climb, cruise, and descent which the inlet must supply sufficiently clean air for the propulsion system to supply the necessary thrust power to fly the vehicle. At each of these flight conditions, there is a different interaction between the airframe boundary layer and the engine than at the cruise condition. This difference will have an impact on performance through the BLI effects discussed in previous sections, but also on the ability of the propulsion system to meet the requirements. Uncertainty in these interactions could lead to mistakes in design choices or fundamentally overestimated benefit of the technology, leading to a totally inferior aircraft relative to the state of the art podded engines. Such mistakes could have catastrophic consequences considering the modern economic climate.

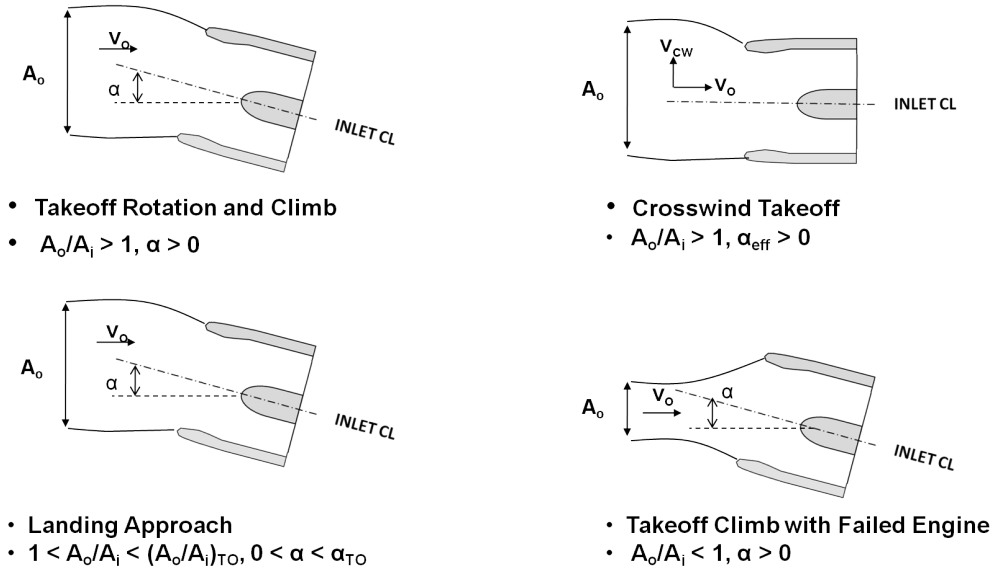
Subsonic Flow Incidence Requirements

Although the inlet and airframe integration process is somewhat less tedious than for the military case, since civil transports clearly do not have as many critical maneuvers as military planes, the point still remains that there are multiple conditions in which the geometric orientation of the airframe causes potential problems for an engine inlet. Perhaps most important among these are conditions such as take-off, climb, and landing where the vehicle and engine might be at an increased angle of incidence relative to the free-stream. The inlet mass flow ratio is the parameter that best describes the approaching flow and is given by equation 7.

$$\frac{A_o}{A_i} = \frac{\left(\dot{m}_2\sqrt{\theta_2}/\delta_2\right)\left(\delta_2/\delta_o\right)}{\left(\dot{m}\sqrt{\theta}/\delta A\right)_o\left(A_i\right)} = \frac{\left(\dot{m}\sqrt{\theta}/\delta\right)_2\left(\pi_d\right)}{\left(\dot{m}\sqrt{\theta}/\delta A\right)_o\left(A_i\right)} \quad (7)$$

Oates states that: "For subsonic inlets, the numerical value of A_o/A_i is a direct indication of the general incidence of the flow approaching the inlet. A value of unity

means that the inlet is capturing its projection in the freestream and the stagnation point will occur at the inlet highlight for level flight. A value less than unity indicates flow is pre-diffusing in the freestream, such that an outward flow incidence occurs; this is generally the case for cruise flight speeds. Conversely, A_o/A_i will exceed unity at low flight speeds and moderate to high power settings, such that an inward flow incidence develops with the stagnation point on the outer portion of the lip.” Furthermore, other flight conditions in which flow incidence is induced produce a velocity component normal to the freestream on top of the basic mass flow effect. Figure 7 illustrates these issues for different flight conditions. For each of these flight conditions, there



35

Figure 7: Notional inlet diagrams showing different conditions for which there are high inlet incidence angles [67]

is a danger that the flow could separate as it passes over the lower inlet lip, thus producing potentially unacceptable distortion levels. The engine must still be able to supply relatively low distortion flow to the inlet such that the engine maintains thrust and does not surge. Furthermore, this condition must be satisfied over a range of free-stream Mach numbers, since the aircraft is accelerating during climb and decelerating during landing. Typical engine incidence requirements are shown

plotted vs. freestream Mach number in figure 8.

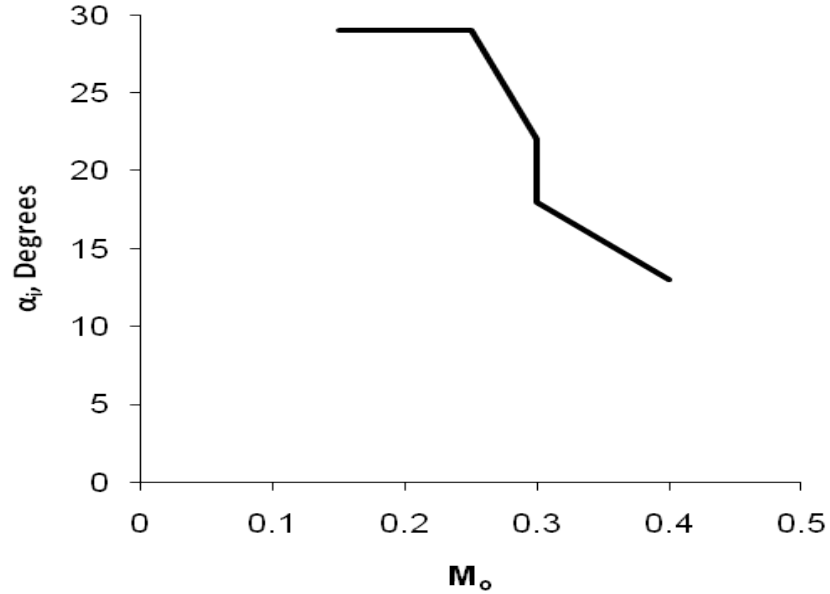


Figure 8: Notional inlet incidence angle requirements vs. freestream Mach number [67]

Finally, it is worth discussing the take-off with engine out condition. This is critical since the engine is operating at peak temperature during take-off meaning that a failure is likely to happen at that condition since the majority of the damage to the components occurs there. If an engine goes out, the ingested mass flow ratio is significantly less than unity since the engine is windmilling. At this condition, the external cowl can produce significant drag due to the flow accelerating rapidly over the cowl lip. The remaining operating engines must be able to overcome this drag on it's own with sufficient climb rate.

2.3.1 BLI as a Paradigm Shift

With the preceding understanding of the limiting flight conditions for typical subsonic inlet integration, it is now necessary to consider how the above might change if there is some base level of distortion being ingested into the engine. Firstly, the

fundamental difference between the embedded engine and the podded engine is that the danger due to separation is coming from the airframe itself rather than the inlet lip. This means that the level of distortion is inherently greater and the consequence of flow separation potentially greater as well. It is logical to speculate then, that the BLI engines will struggle to meet the vehicle incidence requirements. Indeed, the angle of attack envelope of the vehicle may need to be limited by the distortion limits of the engine as a function of Mach number. All of this has hitherto been unaddressed in the analysis literature, even with computational fluids tools, much less in the system study literature. Since these concerns may ultimately limit the possible engine configurations and also impact the cycle designs, there is a need to integrate these design conditions into conceptual design cycle analysis framework to at minimum understand their impact.

Another level of complexity generated by the boundary layer ingesting engine has to do with the placement of the engines on the airframe. First, the placement of each engine (or array of engines in the case of distributed propulsion) is now a design variable, although it is certainly subject to key constraints such as stability and control and similar practical concerns. Furthermore, since preceding sections have substantiated that having smaller engines distributed across the airframe suction surface potentially offers higher BLI propulsive efficiency gains, there is a problem of having different airframe-engine interference for different sets of engines. For instance, if there are three engines such as in the work of Rodriguez [72], then the centerline engine may have quite different inlet flow properties – primarily boundary layer thickness – and subsequent performance impacts. As a corollary to this, Rodriguez showed that a proper inlet aerodynamic optimization might yield different inlet designs and slightly different inlet orientation for the inboard and outboard. This would then mean that the recoveries and distortion levels between the engines are different even though each engine is subject to the same operability constraints. To date, one

system study has looked at the possibility of quantifying the impact of this [79] effect in terms of the BLI propulsive efficiency benefit. This study determined that if one does not consider the effect in the fuel burn calculations, then BLI benefit is rather significantly over predicted (which for BLI could mean 1 or 2%). Another computational fluids study [45] which showed this effect was done for the Boeing N2B design, in which the boundary layer thickness was found to differ by as much as a factor or two between inboard and outboard propulsors.

2.4 Research Objective Formulation

Now that the essential literature for BLI system studies has been laid out, the next task is to identify potential gaps in the existing approaches in order to develop a method which might improve upon the existing analysis tools. The claim made in this thesis is that there are essentially 4 deficient areas in the current system level methodologies: first, that the BLI component loss modeling (fan efficiency and inlet recovery specifically) are not parametric with respect to conceptual design decisions; second, that the operability issue is generally not modeled at the system level, but ultimately may constrain the design space; third, that doing the cycle analysis using a single engine with a single inlet condition is not compatible with the diversity of BLI architectures; and finally, that off-design performance – and specifically variation in the BLI impacts at off-design – is not considered when actually sizing these systems. From the above considerations, a research objective has been formulated and is stated as follows:

Research Objective: Develop a methodology for conceptual system level sizing and analysis of BLI propulsion systems which can quantify BLI performance and operability impacts over a range of system operating conditions, determine the impact of architecture and cycle choices on performance and operability, determine critical design conditions for the system, and allow for simultaneous satisfaction of system requirements and constraints at multiple design conditions.

2.5 Towards A Solution

The preceding section established that although cruise is the primary condition where the performance of the engine is most consequential in terms of fuel burn, that there are several other "off-design" conditions where the engine thrust capability must be sufficient and might therefore be candidates for inclusion into the engine cycle selection process. The traditional engine design process has been performed at a single design point to set the cycle. Performance at other operating conditions is then evaluated in off-design analysis. Though this standard approach provides a good basis for understanding the trends of gas turbine performance, it does not provide a practical approach for a designer to match an engine and performance requirements for a particular airframe.

Schutte [83] designed and analyzed a methodology called simultaneous "multi-point design", in which modern computational tools are used in an engine sizing process which simultaneously satisfies engine requirements and constraints at multiple flight conditions. This is done by linking engine "On-Design" and "Off-Design" within a modified Newton-Raphson solver to satisfy the thrust constraints at all conditions. The process is necessary because it allows the formation of an engine cycle design space where each candidate cycle design is inherently feasible so long as the technology assumptions are physically achievable. This eliminates needless manual iteration between the single point engine "On-Design" solutions and other off-design solutions.

The MDP concept is shown graphically in figure 9. The design points are linked via the simultaneous solution of a system of equations. The MDP process is broken down

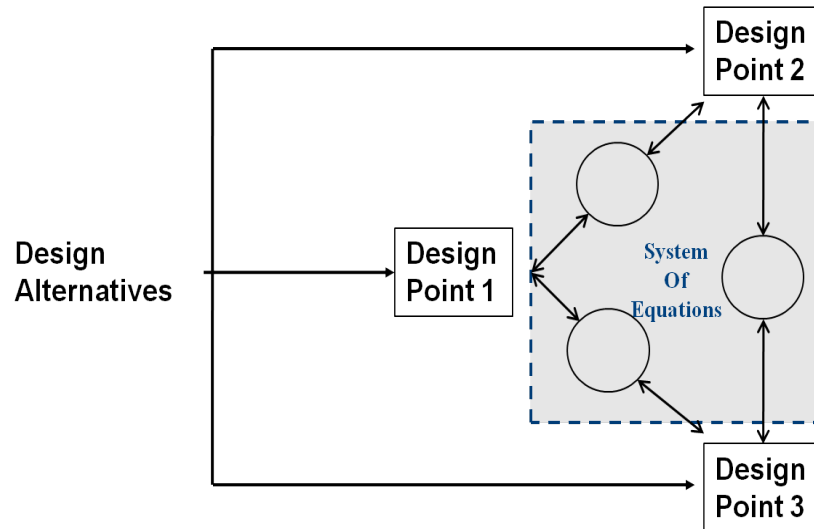


Figure 9: Simultaneous multi-design point cycle analysis equation setup [83]

into 3 parts: the requirements and technology definition phase; the MDP setup phase; and the MDP execution phase. The data flow chart for this process is shown in figure 10. The requirements and technology definition phase is general enough to handle any arbitrary operating (design) condition, which is one of the fundamental gaps in the current BLI literature. Furthermore, it is also able to impose certain flight conditions as a cycle "constraint" condition. If a condition is a critical distortion pinch point in the flight envelope, it could be used as a cycle constraint condition within an MDP analysis. Technology rules for how the distortion is handled or how much is allowable can then be specified to affect the operating point of the engine to move sufficiently away from the fan stall line. Impacts of the distortion related technology rules on the performance of the engine at the other sizing conditions would then be automatically known to the designer. For these reasons, the MDP design process will be the starting point for moving towards a new paradigm for BLI cycle analysis.

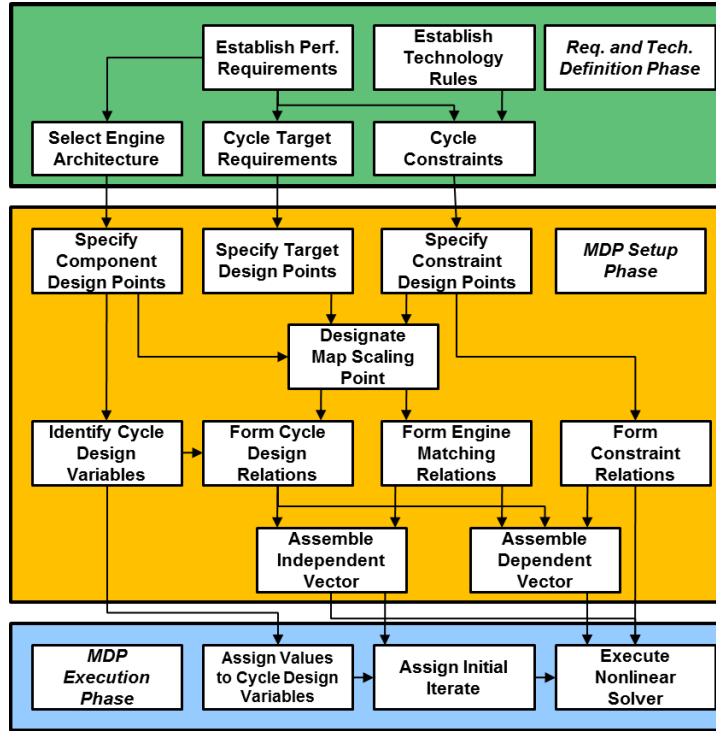


Figure 10: MDP Methodology Data Flow Chart

Short-Comings of the MDP Process for BLI

Though the MDP process is an appealing starting point for moving towards a proper BLI propulsion system sizing approach, there are a few areas where doing MDP alone is not sufficient for filling in the gaps described above.

- MDP does not describe how the installation effects of BLI are to be modeled or mapped across the different flight conditions. It merely assumes that the designer has constructed a proper mapping of the installation effects a-priori. The same goes for the modeling of distortion and how that is achieved.
- MDP does not deal with the problem of distributed architectures, in which the inlet conditions are different across a propulsor array. Rather, it is designed specifically for typical gas turbine arrangement on current tube and wing aircraft.

- The designer using an MDP may not know the flight conditions which are most critical for new concepts such as BLI, where installation effects could have a significant impact on the location of the critical sizing and operability conditions in the flight envelope.

CHAPTER III

A METHOD FOR BLI PROPULSION SYSTEM SIZING AND VEHICLE MATCHING (BLIPSS)

THE gap analysis of the BLI cycle design literature from the previous chapter highlighted some key areas within this domain that are in need of further investigation. The subject of this chapter is to outline and describe, in detail, an overall methodology for resolving these issues for establishing a proper design space for a boundary layer ingesting propulsion system. The chapter will first give an introduction to the method and will show the overall logic behind the development of the method, a brief introduction to the prior work from which it is derived, and a description of its parts and their intended function. The rest of the chapter will be devoted to identifying key research questions and hypotheses related to each part of the method which will be investigated in later chapters to further develop an understanding of how to use the method in the context of a BLI sizing problem.

3.1 BLIPSS Methodology Overview

The BLIPSS methodology is developed out of a need to fill in the gaps for a propulsion system sizing method described in chapter 2. For reasons stated there, the "Multi-Design Point" method is used as a starting point. There are three main areas which need to be added to the MDP method in order to achieve the stated research objective. First, the proper method for modeling boundary layer ingestion, including both benefits, losses, and operability needs to be included. This will be done in an additional phase added on to the MDP method called the BLI Modeling Phase. The second part of the method addresses the fact that different architectures may have

differing non-symmetric intake conditions at the entrance point of the engine. This leads to disparities in inlet recovery, fan losses, and the amount of boundary layer ingested and recovered by the system. This phase is called the vehicle matching phase, and attempts to modify MDP in order to allow for the use of different inlet conditions, and potentially different propulsor sizes to optimize the amount of BLI that is ingested. The third part of the method deals with the fact that the BLI critical flight conditions may not be known prior to the propulsion system analysis – meaning that they may, in fact, be system dependent variables and would change within the design space. This phase is intended to provide a framework for determining the flight conditions prior to running a design optimization or design of experiments, in order to reduce the run time of the BLIPSS method.

The data flow chart for the methodology is shown in figure 11. Again, this methodology is not intended to represent an entire propulsion system development framework, but rather it is a piece of the puzzle for highly integrated BLI systems which allows for propulsion system sizing of different architectures and the matching of that system to a specific airframe.

3.1.1 BLI Modeling Phase Overview

The BLI modeling phase is the phase of analysis in which the components of the engine cycle analysis which are impacted by BLI – in terms of both performance and operability – are modified to account for these affects. It is clear that this at least requires the definition of a baseline vehicle and engine for a point comparison. The baseline engine can either be defined in terms of an already design fixed engine or it could be a competitive architecture, such as a standard podded turbofan engine. The vehicle definition should be sufficient to define the boundary layer models required in this phase. This could be given in terms of boundary layer data at necessary flight conditions or vehicle geometry on which analysis is to be conducted in the BLI

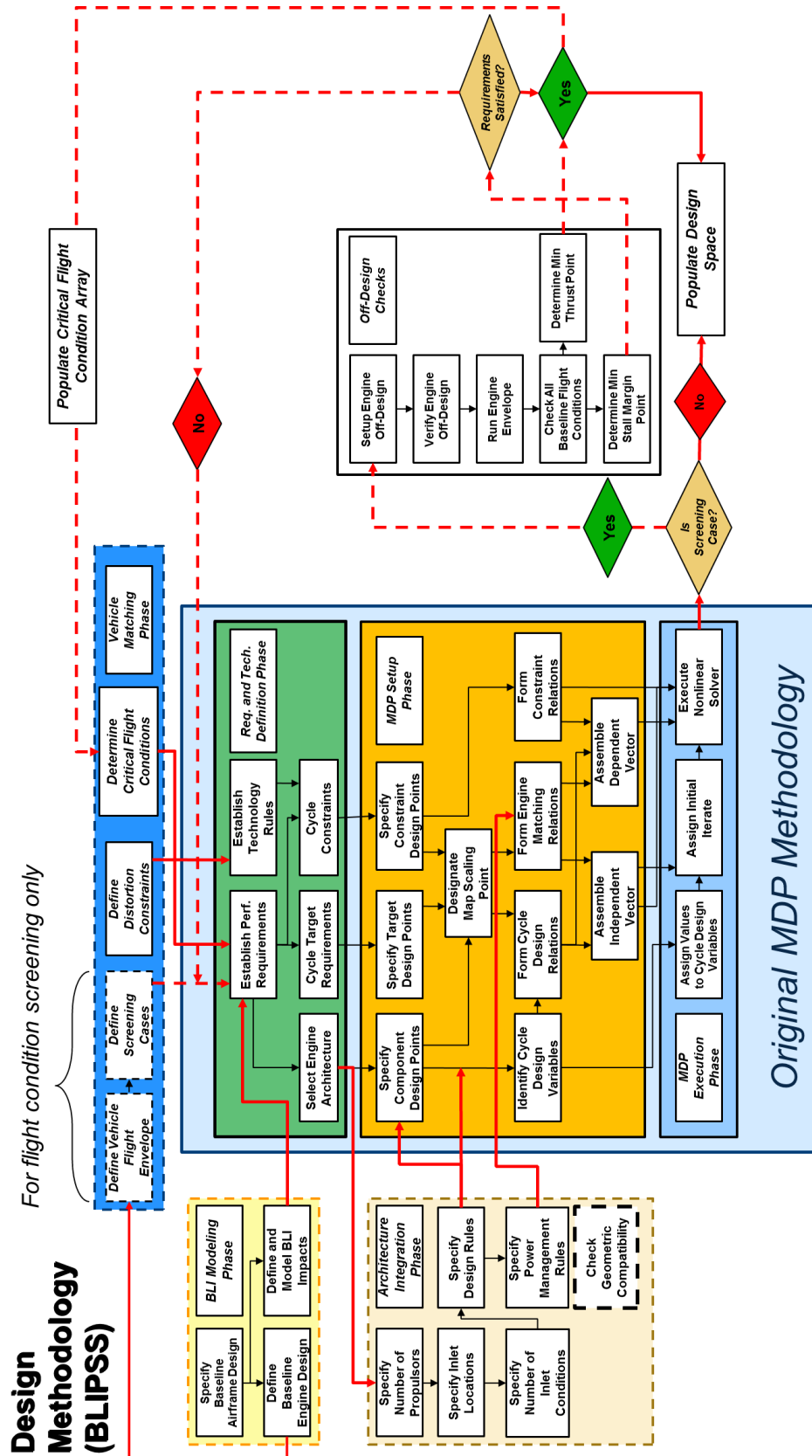


Figure 11: BLIPSS Methodology Data Flow Chart

modeling phase.

3.1.2 Architecture Integration Phase Overview

The architecture integration phase is the phase of the analysis in which the particular architecture which is chosen during the requirements and technology definition phase is defined in terms of the number of propulsors and their locations on the vehicle. The phase requires the specification of a number of propulsors and a location of each propulsor. From this, the number of unique inlet conditions and propulsors can be determined and a model for each unique propulsor can be defined within the MDP setup phase. The design strategy choices made during the architecture integration phase affects the number of turbo-machinery design points and the flight conditions which are chosen for them. The power management strategy are choices made by the designer to determine how different propulsors are power managed. These choices, as well as the architecture itself, determines the overall engine matching relation for the system, which will be different than for a traditional, single-inlet, MDP setup phase.

3.1.3 Vehicle Matching Phase Overview

The vehicle matching phase is the phase in which the critical flight conditions for which the system must be sized are determined for the BLIPSS process. A set of requirements for the distortion constraint must be specified in this phase, along with a series of flight conditions which are to be evaluated. In order to reduce the run-time of the design study, an initial screening exercise is conducted to determine which flight conditions are most critical. This is done for a sub-set of the overall design space, and the results are used to determine the most likely flight conditions which will dominate the sizing of the engine. The flight conditions which are determined to be critical are then included for all non-screening cases going forward within the DoE. This is done to both limit the amount of cases for which a full off-design check must

be done and also limiting the amount of flight conditions which are added to the MDP requirements definitions phase, since adding too many points can make convergence more difficult and also makes programming the MDP process much more difficult.

3.2 Methodology Development: Research Questions and Hypotheses

3.2.1 BLI Modeling Phase

The history of the analysis of boundary layer ingesting engines, much as the history of any analysis, is littered with varying levels of modeling fidelity and assumptions with often quite disparate results. The complicated nature of the question – viscous and turbulent airframe-propulsion interaction – often lends itself to convenient simplifications for the sake of expediency in order to draw some initial conclusion about potential net benefits and viable configurations. Once such decisions have been made, engineers are free to move on to the difficult work of determining the validity of the assumptions and analysis via higher order toolsets such as modern Navier-Stokes codes and the like. This is all very typical of a usual design process, in which conceptual design begins with some crude assumption and is refined by later analysis and optimization. However, the point of this thesis is to try to get closer to a feasible answer – at least for the basic propulsion system cycle design and sizing – before the aerodynamicists embark on refining the assumptions that went into making that decision. Furthermore, it is intended to guide the aerodynamicist and experimentalist in appropriately directing finite resources for their efforts in the most productive directions (correct flight conditions, configurations, initial geometry, etc), and providing sufficient data back to the propulsion engineer in an iterative process which eventually converges on a solution. It is with this basic project in mind that research question 1 is formulated and stated simply as follows:

Research Question 1: What are the minimum requirements for conceptual level modeling of a boundary layer ingesting cycle model in order to reasonably construct the architecture and cycle design space of a BLI propulsion system?

Note that the question asks for the "minimum" modeling requirements for conceptual design. In a sense, this is asking "what can we get away with" or "what is good enough" at the conceptual level, since obviously the best case scenario is to build a complicated fluid dynamics model, allow it to run on an infinitely powerful computer, and come back with a high-fidelity answer. Unfortunately, no such computer exists and even if it did, the designer would still have to know which design to model.

In attempting to answer this question, we first take on some components of the answer as being trivial and therefore not worth further investigation; one needs a reasonable engine cycle model to begin with, as well as thermodynamic component models for the constituent machinery and ducting; one also needs some approximation of the vehicle flow field at the points where it interacts with the engine and a total clean vehicle drag which translates to a thrust requirement. These are the first few blocks of the "BLI modeling phase" and it is somewhat obvious that they must be known to complete any analysis of the system.

The component of the question which is far more interesting, however, is in quantifying the interaction between the flow field and propulsion system and its impact on system performance. These interactions can broadly be classified into 3 regimes: power balance (or thrust balance), turbo-machinery performance and efficiency, and engine stability. The first two have been looked at by almost every author on the subject, while the latter has been studied by some component designers, aerodynamic engineers, and a few others [29]. Stability, though it is certainly a dominant concern among technologists and planners [10], has tended to take a "back seat" at the cycle analysis level, in part because it is a difficult subject to analyze, but also because

it is often assumed that modern aerodynamic methods will solve the problem after the fact [29]. For this reason, we will begin the analysis by ignoring the stall margin question and returning to it later to analyze this dubious partitioning of the problem.

On Design Analysis with BLI

In order to conduct engine sizing during on-design analysis, it is necessary to augment the basic thrust or power balance relations which match the vehicle requirement with the propulsion system. For example, the basic textbook thrust equation for a podded engine $F = \dot{m}(U_j - U_\infty)$ must be modified to include the effect of BLI on the system. The following analysis establishes the basic power balance relations for boundary layer ingesting according to the most current literature, predominantly produced by MIT in theoretical form [23] [78].

We begin with defining the basic power balance equation for any vehicle in an aerodynamic flow which follows from the analysis of Drela:

$$P_s + P_v + P_k = W\dot{h} + \dot{E} + \Phi \quad (8)$$

Here, the term P_s represents the net propulsor shaft power or wing flapping power input to the control volume. Since here we are only considering the case where the turbomachinery are outside of the CV, the P_s is considered to be 0, and the effect of the work done by the turbomachinery is included in the net flow of propulsor mechanical energy into the CV represented by P_k . The P_v term represents the net pressure-volume power provided by the fluid expanding to atmospheric pressure and can be non-zero in this case, depending on the character of the nozzles.

The terms on the right hand-side of the equation represent the potential energy change due to climbing ($W\dot{h}$), the total flow-rate of mechanical energy out of the control volume (\dot{E}), and the total rate at which kinetic energy is converted into heat inside of the CV (Φ). The \dot{E} term can be decomposed into various components, but

the primary term to consider for subsonic transports of the type considered here is the rate of wake transverse kinetic energy deposition \dot{E}_v . For the case of a relatively close Trefftz-plane, where trailing vortices have not dissipated, this term is essentially the equivalent of V_∞ times the induced drag D_i [23].

The dissipation rate Φ can be broken down into three components: surface and wake dissipation due to the presence of the boundary layer, and dissipation in the jet stream aft of the propulsors. Re-writing Eq. 8 according to this decomposition and the assumptions described above, we have the following:

$$P_k + P_v = W\dot{h} + \dot{E}_v + \Phi_{surf} + \Phi_{wake} + \Phi_{jet} \quad (9)$$

This equation describes the basic power balance relation for the case of an aircraft with a propulsor whose internal volume is not considered part of the control volume analysis and for the case of a subsonic transport aircraft. It is valid for both isolated propulsors and the BLI case. The following sections will describe both of these cases, their differences, and identify key observations from the analysis that are relevant to the research question.

Podded Case

The basic configuration for the podded case – shown in figure 12 – illustrates the fact that the propulsor is (at least to first order) separated from the airframe. Equation 9 can therefore be simplified into terms that are more familiar to an aerodynamicist using standard momentum-based techniques. First, the drag of the aircraft is

normally divided broadly into profile drag (due to friction) and "lift-dependent drag" (due to trailing vortices). The first is manifested in the dissipation terms (Φ_{surf} and Φ_{wake}) and is the sum of the surface and wake dissipation, and the second is represented by \dot{E}_v . These power based terms can be translated into an equivalent drag by dividing them by the free-stream velocity V_∞ . The left-hand side of the

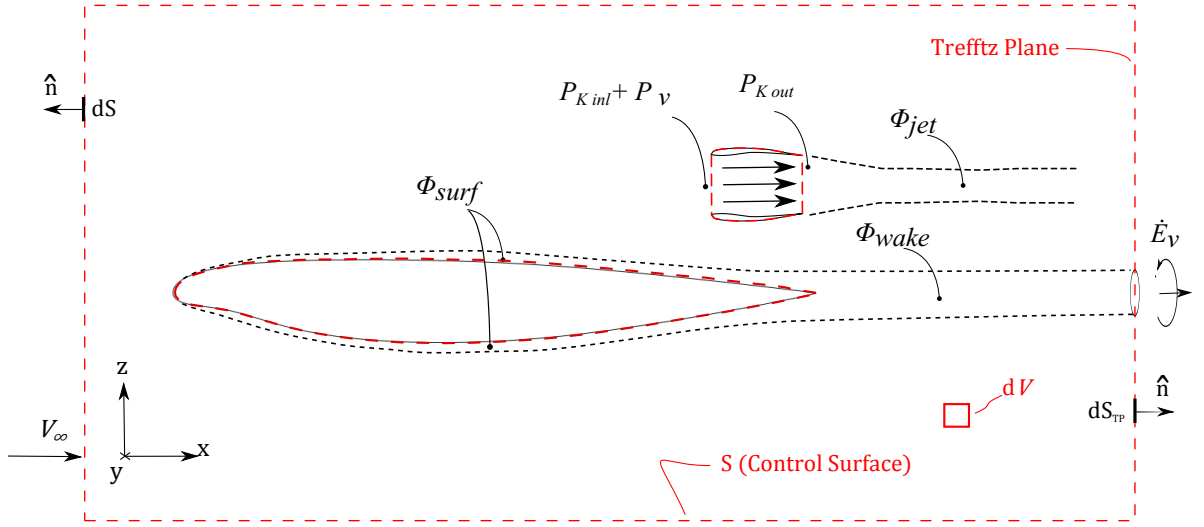


Figure 12: Diagram of the podded case illustrating the various components of the power balance equation.

equation has to do with the engine kinetic energy flux into and out of the control volume and the volumetric mechanical power integral P_v . Writing the equation for P_k :

$$P_k = \oint - \left[(p - p_\infty) + \frac{1}{2} \rho (V^2 - V_\infty^2) \right] V \cdot \hat{n} dA \quad (10)$$

Taking this equation and separating out the integral into that over the inlet and exit as shown in figure 12 and also assuming that the nozzle is not significantly over or under expanded ($p \simeq p_\infty$) gives:

$$P_{k_{out}} = \oint - \left[\frac{1}{2} \rho (V_j^2 - V_\infty^2) \right] V \cdot \hat{n} dA_{nozzle} \quad (11)$$

simplifying, we get:

$$P_{k_{out}} = \frac{1}{2} F_n (V_j + V_\infty) \quad (12)$$

Where the net thrust, F_n is as normally defined from the simple jet equation. From the same assumptions as above,

$$P_{k_{inl}} + P_v = 0 \quad (13)$$

Now, the dissipation in the jet stream Φ_{jet} is essentially the wasted kinetic energy of the stream which is eventually converted back into heat after it has been dissipated

in the jet. This can be calculated as follows:

$$\begin{aligned}\Phi_{jet} &= \iint \frac{1}{2}(V_\infty - V_j)^2 \rho V_j dA_{nozzle} \\ &= -\frac{1}{2}F_n(V_\infty - V_j)\end{aligned}\tag{14}$$

From 12 and 14, we get:

$$P_{kout} - \Phi_{jet} = V_\infty F_n\tag{15}$$

So, the power contribution of the propulsor is essentially the net kinetic energy flux that the propulsor provides to the total aircraft control volume minus the rate at which energy is dissipated in the jet stream wake. Now that all of the terms of the power balance equation have been defined, we can re-write the equation to be in terms more familiar to the aerodynamicist:

$$\begin{aligned}V_\infty F_n &= W\dot{h} + V_\infty D_i + V_\infty D_p \\ &= W\dot{h} + V_\infty D\end{aligned}\tag{16}$$

Other terms, such as an acceleration term or friction forces during ground roll could be added, but this is sufficient for steady-state flight with a constant climb or descent rate.

BLI Case

The BLI case, illustrated in figure 13, is clearly different in two ways: first, there is an inlet defect due to the presence of the boundary layer, such that P_{kinl} is non-zero; second, there is a component of the wake dissipation which is not present since it is ingested into the propulsor and replaced by the jet stream. The following analysis will develop a mathematical comparison between this case and the original podded case. First, it is necessary to define a relationship between the podded (clean vehicle) case and the BLI case. This is done by defining a parameter β , which represents the ratio of the wake dissipation in the BLI case to the podded case:

$$\Phi_{wake_{BLI}} = (1 - \beta)\Phi_{wake} = (1 - \beta)(\Phi_\infty - \Phi_{TE})\tag{17}$$

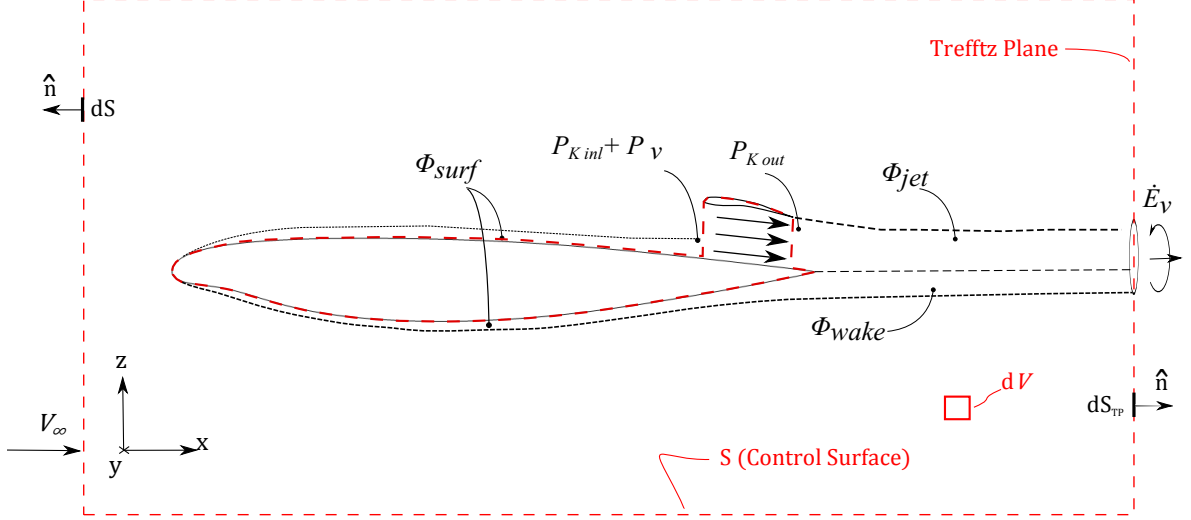


Figure 13: Diagram of the podded case illustrating the various components of the power balance equation.

The inlet defect P_{kinl} is equivalent to the surface dissipation ingested into the propulsor at the inlet location of the propulsor:

$$P_{kinl} = \Phi_{Inl} = \gamma \Phi_{surf} = \gamma \Phi_{TE} \quad (18)$$

The parameter γ is defined in Eq. 18 as the ratio of the surface defect at the point of ingestion as normalized by the defect in the podded case at the trailing edge.

In general the surface dissipation is not changed much by the presence of the propulsor, except for the fact that the wetted area of the fuselage upper surface is decreased. Given the parameters defined above, the following derivation for the surface dissipation in the BLI case is made:

$$\Phi_{surf,BLI} = \Phi_{surf} - \beta \Phi_{surf} + \gamma \Phi_{surf} \quad (19)$$

The assumption being made here is that the proportion of the wake kinetic energy which is recovered is the same as the proportion of the trailing edge dissipation in the BLI case to the total TE (surface) dissipation in the podded case. Equation 19 then states that the total surface dissipation in the case of BLI is the podded value, minus the trailing edge ingested value, plus the value of the dissipation at the inlet.

Therefore, the term $(\beta - \gamma)$ represents the percent change in the surface dissipation integral.

$$\Phi_{surf_{BLI}} = (1 - \beta + \gamma)\Phi_{surf} \quad (20)$$

In the case where the propulsor is assumed mounted on the trailing edge of the vehicle, γ and β are equal and the surface dissipation between the two cases is assumed identical unless the propulsor affects the upstream dissipation in the pre-entry region. Moving the propulsor far forward would tend γ and $P_{k_{inl}}$ towards zero and would also have an impact on the actual value of β , as it would be unclear how the jet stream would interact with the surface aerodynamics. In any case, this would be undesirable and so the case is not considered.

Finally, we define a similar ratio between the induced drag in the BLI case and the podded case:

$$\dot{E}_{v_{BLI}} = \zeta \dot{E}_v \quad (21)$$

The above definitions can be used in conjunction with Eq. 8 to write the final power balance equation for the BLI case:

$$(P_{kout} - \Phi_{jet}) + \gamma\Phi_{surf} = (1 - \beta + \gamma)\Phi_{surf} + (1 - \beta)\Phi_{wake} + \zeta\dot{E}_v + W\dot{h} \quad (22)$$

Rearranging and simplifying:

$$(P_{kout} - \Phi_{jet}) + \beta(\Phi_{surf} + \Phi_{wake}) = \Phi_{surf} + \Phi_{wake} + \zeta\dot{E}_v + W\dot{h} \quad (23)$$

Using the results from the podded analysis, we get:

$$\underbrace{V_\infty F_n + \beta\Phi - \zeta\dot{E}_v}_{\text{Total Net Thrust}} = \underbrace{V_\infty D + W\dot{h}}_{\text{Podded Vehicle Drag}} \quad (24)$$

Here, the term β represents all changes to the viscous wake profile in relation to the podded case for an aft-mounted propulsor. This includes the recovery of the wake dissipation, which is now replaced with the jet stream, and another term that essentially represents a reduction in the flux of kinetic energy into the propulsor

control volume (ram drag reduction). This equation is generally simplified, at this level of analysis, by assuming that ζ is also zero and therefore the vortex drag is not altered in the case of BLI. We will see in later sections that this is most likely an inappropriate assumption for very high or low engine power levels, where the surface static pressure distribution is modified significantly by the pre-entry flow. This creates an awkward scenario where the actual drag polar, lift, and pitching moment of the vehicle would be throttle dependent, totally throwing asunder all notions of the book-keeping separability of thrust and drag. At the level of conceptual design and cycle analysis, it is essentially necessary to ignore the effect of the engine on the lift distribution since to model this would be cumbersome and is unlikely to have much effect on the sizing of the engine, which is typically done at normal power levels where pre-entry flow pressure gradients are small.

Performance Parameters

It is now useful to define some performance parameters based on this analysis to determine how this might affect the system in relation to the podded case. The thrust saving coefficient is defined as the proportion of the total net thrust of the propulsor which is related to the BLI wake-recovery effect.

$$TSC = \frac{\beta \cdot \Phi}{\left(V_\infty F_n + \beta \Phi - \zeta \dot{E}_v\right)} = \frac{\beta \cdot \Phi}{\left(V_\infty D + Wh\right)} \quad (25)$$

Where again, F_n is defined as above. At times, others define the slightly less useful parameter (%BLI) is used and defined as the ratio of the wake recovery term to the total drag (ratio of ingested drag to uningested drag). Assuming that ζ is zero and that there is no excess power required for climb or acceleration, the thrust saving coefficient and %BLI are the same for the vehicle as a whole.

The "BLI" efficiency was defined by Sato [78] and includes the contribution from both the wake recovery and the propulsive efficiency increase of the engine due to the

kinetic energy defect at its inlet.

$$\eta_{BLI} = \frac{\left(T \cdot V_\infty\right)_{Podded}}{\left(\Delta KE\right)_{BLI}} = C_{BLI} \cdot \eta_{pr,BLI} \quad (26)$$

With C_{BLI} defined as the ratio of the dissipation and vortex loss terms (rhs of power balance):

$$C_{BLI} = \frac{\dot{E}_v + \Phi}{\dot{E}_v + (1 - \beta)\Phi + \gamma\Phi_{surf}} \quad (27)$$

C_{BLI} is generally greater than unity for non-zero BLI so that it has the effect of increasing the overall value of η_{BLI} . Higher values of β obviously tend to give more benefit.

The propulsive efficiency for a BLI propulsor is calculated according to its definition:

$$\eta_{pr} = \frac{P_k - \Phi_{jet}}{P_k} = \frac{P_{k,out} - \Phi_{jet} + P_{k,inl}}{P_{k,out} + P_{k,inl}} \quad (28)$$

This can be rewritten by using Eq. 18 to compute the inlet defect.

$$\eta_{pr} = \frac{P_{k,out} - \Phi_{jet} + \gamma\Phi_{surf}}{P_{k,out} + \gamma\Phi_{surf}} \quad (29)$$

In the case of no BLI (no $P_{k,inl}$), then Eq. 29 simplifies to the normal Froude propulsive efficiency equation. With ($\gamma > 0$), $\eta_{pr,BLI} > \eta_{pr,Podded}$, meaning there is a propulsive efficiency benefit for ingesting BLI, along with the general reduction in the amount of power required to propel the aircraft (represented by C_{BLI}).

The overall efficiency of the podded (non-BLI) propulsion system is defined as follows:

$$\eta_o = \frac{F_n \cdot V_\infty}{\dot{m}_f \cdot h_{LHV}} = \frac{V_\infty}{TSFC \cdot h_{lhv}} \quad (30)$$

For the BLI case,

$$\eta_o = \underbrace{\left[\frac{\left(F_n \cdot V_\infty\right)_{Podded}}{\left(F_n \cdot V_\infty\right)_{BLI}} \right]}_{C_{BLI}} \underbrace{\left[\frac{\left(F_n \cdot V_\infty\right)_{BLI}}{\left(\Delta KE\right)_{BLI}} \right]}_{Prop.Efficiency} \underbrace{\left[\frac{\left(\Delta KE\right)_{BLI}}{\left(\dot{m}_f \cdot h_{lhv}\right)} \right]}_{Thermal.Efficiency} \quad (31)$$

Therefore, the benefit is seen to be a function of two phenomena: 1.) the reduction in the wake dissipation which is no longer present; 2.) An increase in the propulsive efficiency because of the non-zero kinetic energy defect entering the propulsor (ram drag reduction). Both of these are also found to be strong functions of the amount of BLI ingested, with the final power balance being mainly a function of β . This standard observation from the BLI literature is therefore formulated as follows:

Observation 1: The performance benefit of boundary layer ingestion systems is generally a function of the ratio of the amount of equivalent viscous drag ingested by the propulsor to the total drag in the podded case.

Finally, the use of the thrust saving coefficient can combine the above effects into the thrust specific fuel consumption variable:

$$TSFC = \frac{\dot{m}_f \cdot (1 - TSC)}{F_n} \quad (32)$$

Changes in propulsive efficiency are then wrapped up into the calculation of the thrust saving coefficient and any changes in thermal efficiency would arise from the calculation of the fuel flow \dot{m}_f from the thermodynamic cycle model. For this reason, the modified TSFC metric described in Eq. 32 will be used to describe the benefit of the system going forward.

Calculation of BLI Benefit

Now that the basic power balance equations for a vehicle with BLI have been established as well as the important parameters contributing to the overall benefit of the system, it is now necessary to define how these quantities can, in theory, be computed. First, some useful boundary layer quantities are defined [78]:

Mass Defect:

$$\mathbf{M} \equiv \rho_e u_e \delta^* = \int_0^{\delta} (\rho_e u_e - \rho u) dz \quad (33)$$

Momentum Defect:

$$\mathbf{P} \equiv \rho_e u_e^2 \theta = \int_0^\delta (u_e - u) \rho u \, dz \quad (34)$$

Kinetic Energy Defect:

$$\mathbf{K} \equiv \frac{1}{2} \rho_e u_e^3 \theta^* = \frac{1}{2} \int_0^\delta (u_e^2 - u^2) \rho u \, dz \quad (35)$$

Density-flux Defect:

$$\mathbf{D} \equiv \rho_e u_e \Delta^{**} = \int_0^\delta (\rho_e - \rho) u \, dz \quad (36)$$

The above equations relate the conditions in the boundary flow gradient region to the external inviscid flow (EIF) integrated in the “y-direction” normal to the wall. Note that in the case of turbulence, the definitions above apply only to the mean (time-averaged) quantities but the notation is kept the same for convenience and any reference to a flow-field quantity is referring to the mean value.

Sato [78] gives a derivation for the evolution of the kinetic energy defect in relation to the profile mechanical loss coefficient Φ_p shown in Eq. 37. This is effectively conservation of energy in integral form:

$$\int_{out} \mathbf{K} \cdot \hat{n} \, dl_{out} = \Phi_p - \Pi_V \quad (37)$$

The above equation is valid for a control volume which has its inlet and side planes sufficiently far from the vehicle such that the integral of the kinetic energy deficit is zero and the “out” plane is the location of the exiting plane which can be placed at some axial location along the aerodynamic body. The first term on the right-hand side of Eq. 37 is the viscous dissipation term:

$$\Phi_p = \iint D \, dS = \iint \rho_e u_e^3 c_D \, dS \quad (38)$$

The second term is the so-called “baroclinic” term (Eq. 39), which represents the change in mechanical energy flux due to the pressure gradient acting on the boundary

layer flow at a different density than the inviscid flow. The value of this typically scales with M_e^2 and is approximately 5% for high subsonic flows [78].

$$\Pi_V = \iint \mathbf{D} \cdot \nabla \frac{1}{2} u_e^2 dS = \iint \mathbf{D} \cdot u_e \frac{\partial u_e}{\partial x} dS \quad (39)$$

Placing this plane far down-stream of the body at the Trefftz plane (A_∞), the total mechanical dissipation coefficient is given in equation 40 and represents the total dissipative profile drag for the body on the right hand side of the general power balance (Eq. 8):

$$\Phi_p^* = \int_{A_\infty} \mathbf{K} \cdot \hat{n} dl_{out} = \Phi_p - \Pi_V \quad (40)$$

The dissipation term from the power balance equation is then computed by integrating the axial 2-D kinetic energy defect \mathbf{K} over the exit plane area. We now consider this integral for two types of aerodynamic wake profiles.

“Class 1” Aerodynamic Body

There are two fundamental aerodynamic body shapes, as defined by Kulfan [51]. The first is type “Class 1”, which represents wing airfoil type shapes with a distribution along a stacking axis (Fig. 14). Something like a hybrid wing body design falls into this class of aerodynamic bodies. Fig. 15 illustrates the type of wake which develops for a BLI propulsor on a class 1 type aerodynamic body. The wake dissipation factor for the isolated geometry case is:

$$\Phi_p^* = \int K_\infty \cdot \hat{n} dl = \underbrace{\int (K_L + K_u)}_{\text{Trailing Edge}} + \underbrace{\Phi_{wake}^*}_{\text{Wake dissipation}} \quad (41)$$

The wake for the ingesting propulsor case is $K_{\infty,BLI}$ and the parameter $\nu = K_{\infty,BLI}/K_\infty$ is defined to form a relation between the BLI and isolated case. For $\nu = 1$, there is no boundary layer ingested at that y-location, while $\nu = 0$ represents the case where all of the defect is ingested (lower and upper surface). An approximation for ν can

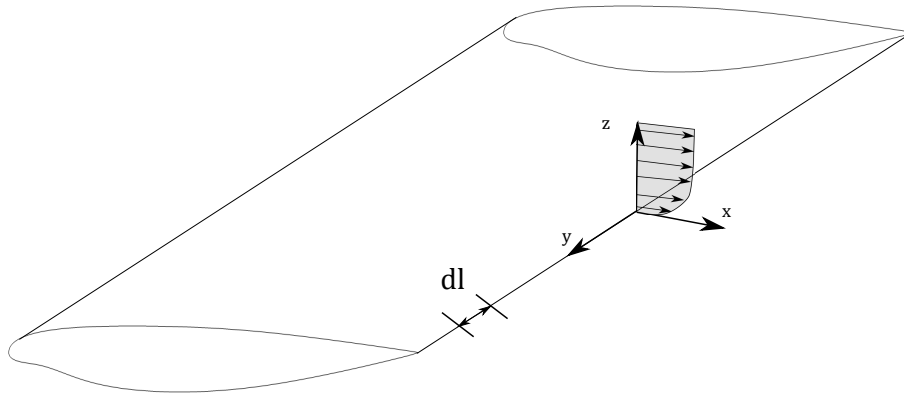


Figure 14: Diagram of a class 1 geometry type with trailing edge boundary layer shown. The dissipation integral is performed along the z-direction.

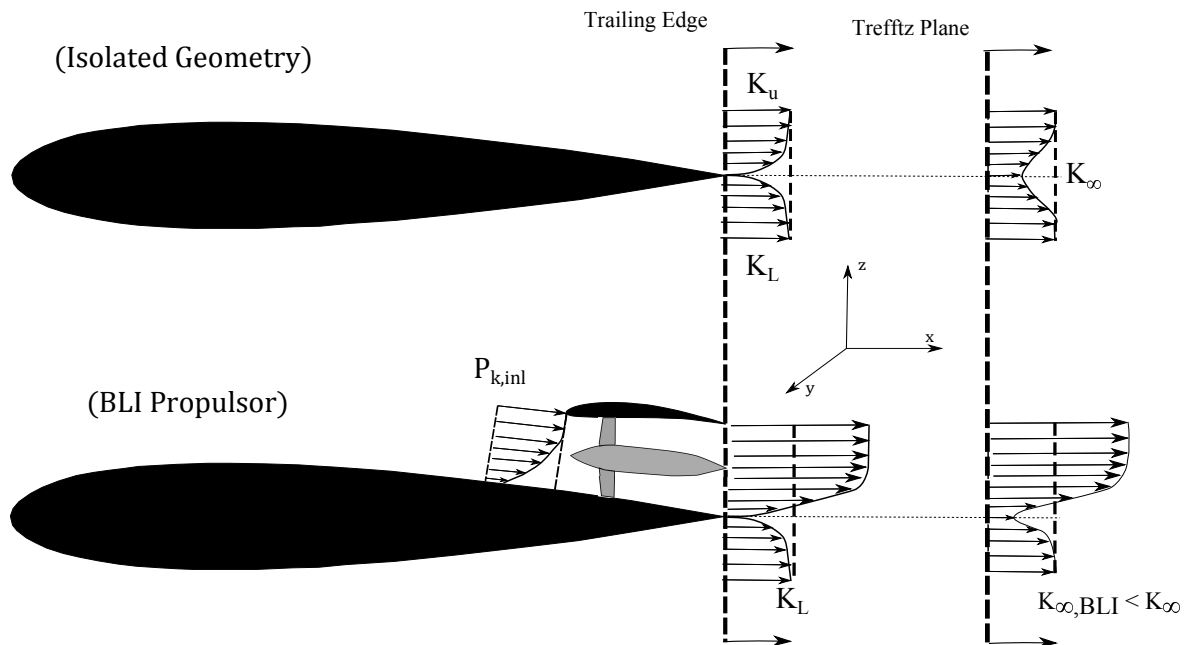


Figure 15: Illustration of a class 1 geometry aerodynamic wake for the isolated airfoil and case with a BLI propulsor.

be made by assuming that only the contribution of the upper portion of the wake is removed:

$$\Phi_{p,BLI}^* = \int \nu \mathbf{K}_\infty \cdot \hat{n} dl = \int \frac{K_L}{(K_L + K_u)_{TE}} \cdot (\mathbf{K}_\infty \cdot \hat{n}) dl \quad (42)$$

The next step is to carry out the integration over the length of the wake at the trefftz plane to compute the mechanical energy flux for the BLI case in relation to the isolated body case. Fig. 16 shows an example “Class 1” body with constant cross section and chord length.

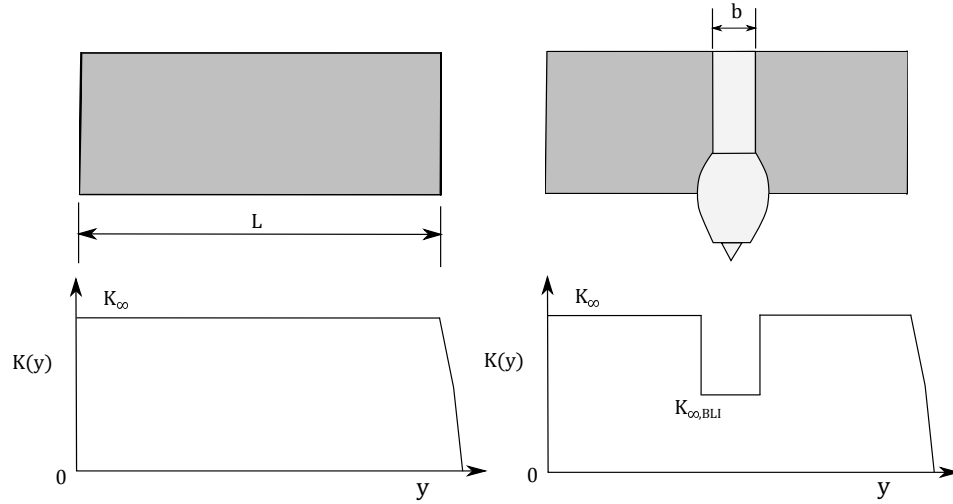


Figure 16: Illustration of the distribution of the kinetic energy defect over the length of a notional “class 1” aerodynamic body.

The variable “b” here is a term representing the “span”, or width, of the ingested boundary layer. The dissipation integral (Eq. 42) is the area under the curve of this distribution. From this, and by using the definition of β in Eq. 17, we get the following general relation for a class 1 vehicle:

$$1 - \beta = \frac{\Phi_{p,BLI}^*}{\Phi_p^*} = \frac{\int_{x=\infty} \nu(y) K_\infty(y) dy}{\int_{x=\infty} K_\infty(y) dy} \quad (43)$$

From fig. 16, and carrying out the integration for this notional class 1 body, an

approximation of β is thus:

$$1 - \beta = \frac{\Phi_{p,BLI}^*}{\Phi_p^*} = \frac{K_\infty(L - b) + b\nu K_\infty}{LK_\infty} \quad (44)$$

$$= \left(1 - (1 - \nu)\frac{b}{L}\right)$$

Again, Eq. 44 is an approximation, but is at least useful for simple cases and understanding the overall parameters involved in the analysis for the class 1 type. From Eq. 44, the relationship for the thrust saving coefficient is as follows:

$$TSC = \frac{\beta \cdot \Phi_p^*}{DV_\infty + W\dot{h}} = \frac{(1 - \nu)bK_\infty}{DV_\infty + W\dot{h}} \quad (45)$$

Observation 2: For class 1 aerodynamic bodies with BLI, the ratio of ingested drag to net thrust depends on both the value of the recovered boundary layer kinetic energy defect at the trefftz plane and the total span of the boundary layer defect ingested by the engine stream-tube.

“Class 2” Aerodynamic Body

The “class 2” aerodynamic body, as defined by Kulfan [51], is the type where the cross-sectional stacking axis is along the “x-axis”. These types of bodies are generally things like fuselages, nacelles, missile or payload pods, etc. These can generally be specified by either having a set of cross-sections which are rotated around some center-line axis or can also be represented by stacking along a vehicle station-line. For BLI, the important aspect of the class 2 type problem is that the trailing edge and downstream wakes are of a fundamentally different character. An illustration of this is shown in fig. 17 with a notional tube and wing aircraft. The fuselage tail-cone has a wake at the trailing edge of the vehicle with a circumferential distribution around the body which is roughly uniform. The gradient in the boundary layer is in the radial or “y” direction.

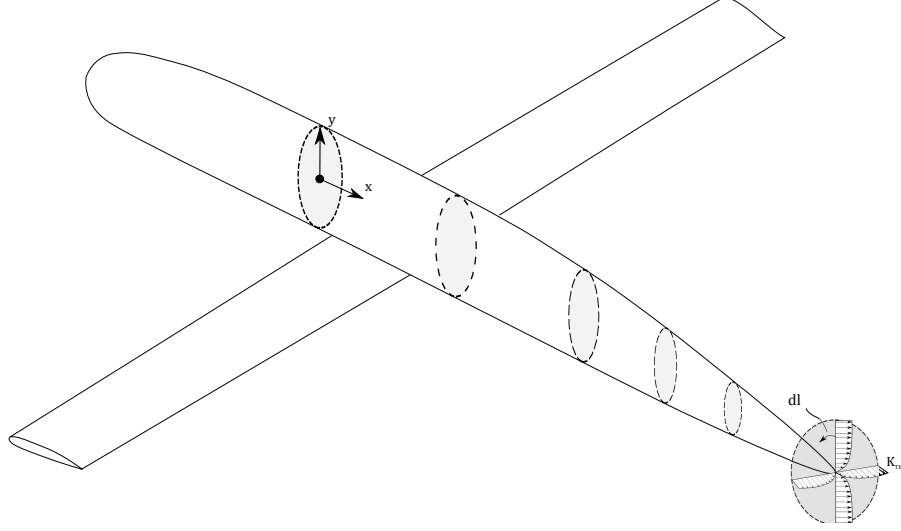


Figure 17: Illustration of the distribution of the kinetic energy defect over the length of a notional “class 1” aerodynamic body.

The wake integral from equation 40 can be computed by integrating the boundary layer kinetic energy defect over the circumference of the wake and assuming $dl = \delta d\theta$, where δ is the boundary layer thickness (distance from wall to “edge”).

$$\Phi_p^* = \int_{T_{refftz}} K_\infty(\theta) \delta d\theta \quad (46)$$

and the equation for β , similar to Eq. 43, is the following:

$$1 - \beta = \frac{\int_0^{2\pi} K_\infty(\theta) \nu(\theta) \delta(\theta) d\theta}{\int_0^{2\pi} K_\infty(\theta) \delta(\theta) d\theta} \quad (47)$$

If we assume circumferential uniformity, then the K_∞ and δ can be pulled out of the integration. The BLI benefit term (β), then, is only a function of the fraction (ν) of the isolated wake which is recovered in the BLI case. For most aerodynamic bodies of practical concern, the wake will be small enough to entirely ingest it inside of an aft mounted propulsor so that $\nu(\theta) = 0$ at every θ and the wake is entirely recovered, as shown in fig. 18. With ν everywhere zero at the trefftz plane, then β is precisely equal to one, unless the wake from other bodies, such as a wing, is included. It is likely that the entire wake will not be recovered, as illustrated in fig.

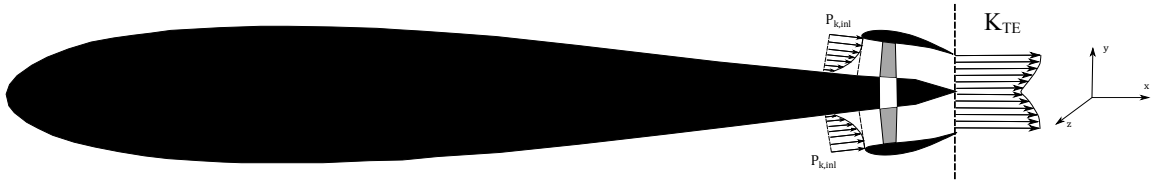


Figure 18: Illustration of the the wake defect for a class 2 body with BLI.

18, and that there will be some residual kinetic energy defect in the jet stream of the BLI propulsor. This can be captured either by modeling the jet stream with an overall gross-thrust coefficient or by including a recovery factor, such as that defined by Smith [86], and include the defect in the calculation of $P_{k,out}$ in the power balance equation (Eq. 23). These approaches are equivalent assuming the nozzle gross thrust coefficient is calculated accordingly.

The primary difference between the “Class 1” and “Class 2” type vehicle with boundary layer ingestion is that a single propulsor can be designed to ingest the entire trailing edge wake defect for the class 2 designs. As such, observation 2 does not apply for these types of designs. Furthermore, if the entire wake is ingested by a propulsor which surrounds a class 2 type body, then the distortion will be primarily radial, rather than being a combined radial/circumferential complex distortion profile. This leads to a natural classification for BLI propulsion systems:

- Class 1 BLI Systems: Laterally distributed boundary layer, for which the calculation of the dissipation integral (wake recovery term) is dependent on the width of the engine ingested stream-tube.
- Class 2 BLI Systems: Circumferentially distributed boundary layer, for which the dissipation integral is not dependent on the width of the ingested stream-tube, but only on the radius.

Propulsor Sizing: Class 1 BLI

Consider the case of a general cross-section with area “A” (fig. 19) with some velocity distribution over its surface. The general equation for the mass flux through this cross section is from Eq. 48.

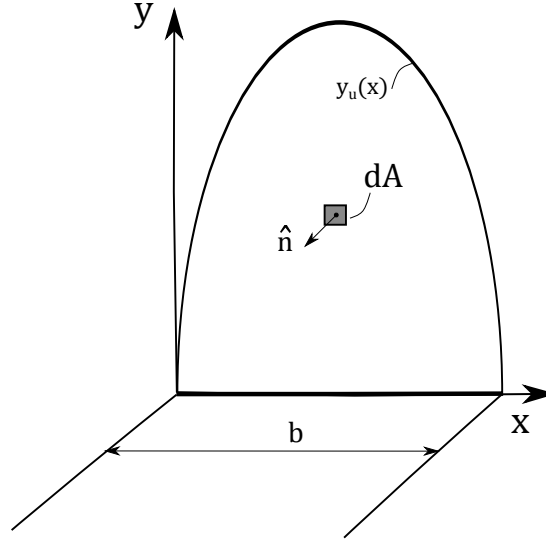


Figure 19: General cross-section diagram.

$$\dot{m} = \iint_A \rho(\mathbf{u} \cdot \hat{\mathbf{n}}) dA = \int_0^b \int_0^{y_u(x)} \rho u_x dy dx \quad (48)$$

From Eq. 33,

$$\int \rho u dy = \int \rho_e u_e dy - \mathbf{M} \quad (49)$$

Then:

$$\begin{aligned} \dot{m} &= \int_0^b \left[\rho_e u_e y_u(x) - \mathbf{M}(\mathbf{x}) \right] dx \\ &= \int_0^b \rho_e u_e \left(y_u(x) - \delta^*(x) \right) dx \end{aligned} \quad (50)$$

Here, the edge velocity and density are set by the incoming local properties which are a function of the vehicle aerodynamic shape and free-stream conditions. Therefore, if the designer desires a specified mass flow, then the width or height of the inlet can be adjusted to achieve the desired mass flow, and the integration of Eq. 50 is computed to do so. If the cross-section shape is known (fixed b and h), the mass

flow through that cross-section can be calculated from this relation. To demonstrate this in a simple way, the assumption is made that the 1-D mass defect δ^* and edge velocity and density are constant in the x-direction over the length of the inlet. From this assumption,

$$\dot{m} = \rho_e u_e \int_0^b y_u(x) dx - \rho_e u_e \delta^* b \quad (51)$$

Defining $h = \max(y(x))$, and recognizing that $\int y(x) dx = A$, the following definition is useful:

$$r^* = \frac{A}{b \cdot h} \quad (52)$$

Here, r^* is a measure of how closely the inlet shape matches to a rectangular shape, with a value of unity representing a rectangle with width “b” and height “h”. Defining the inlet aspect ratio to be $AR = b/h$, then Eq. 51 becomes:

$$\dot{m} = \rho_e u_e \frac{r^* b^2}{AR} - \rho_e u_e \delta^* b \quad (53)$$

Then, the above quadratic equation can be solved for the cross-section width, which directly multiplies the thrust saving coefficient from Eq. 45.

$$b = \frac{\delta^* AR}{2r^*} + \sqrt{\left(\frac{\delta^* AR}{2r^*}\right)^2 + \frac{\dot{m}}{\rho_e u_e} \frac{AR}{r^*}} \quad (54)$$

It is now worth considering what design choices are available to the designer to affect the size of the ingested engine stream-tube and therefore the overall amount of ingested boundary layer (drag). In general, anything that affects the engine mass flow demand will affect the ingested stream-tube size. The first obvious choice is the selection of the engine fan pressure ratio, which will have a very large impact on the bypass-ratio of the engine and the ingested mass flow. For architectures without traditional turbofan engines, such as a distributed propulsion system, the fan pressure ratio will still have a large impact on the sizing of the fan and the required ingested mass flow ([47]).

Secondary cycle variables and technology factors additionally affect the mass flow demand of the engine. For instance, the maximum temperature that the engine can

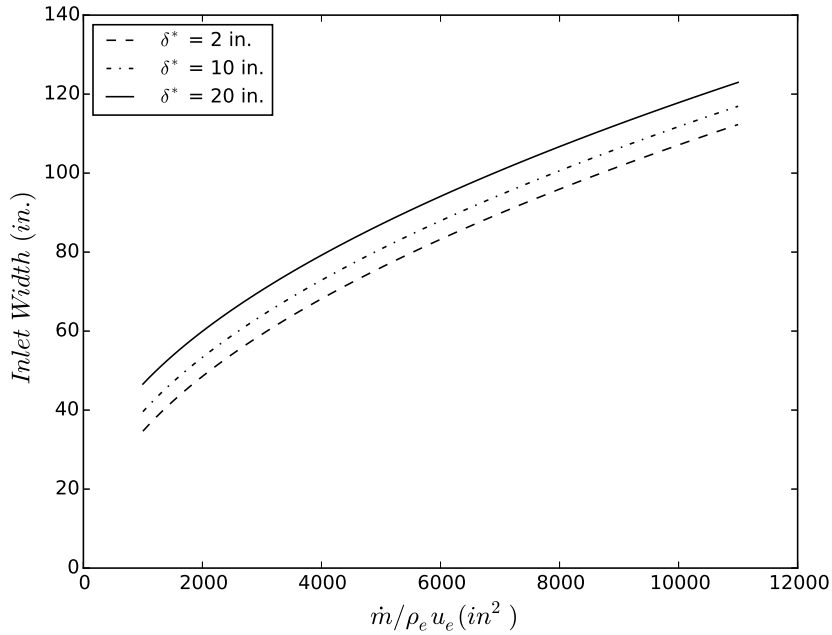


Figure 20: Influence of mass flow on the cross-section width solution.

burn at, typically limited by the turbine materials and cooling requirements, will have a significant impact on the available thrust of the propulsion system. Other less important factors are things like the component efficiencies of the fan, low and high pressure compressors, and the burner efficiency and pressure drop of the combustor. Anything that ultimately affects the ideal or actual cycle of the engine will have some impact on the desired mass flow and therefore the width of the ingested stream-tube.

Another design feature which has a significant impact on the ingested stream-tube width is the aspect ratio of the inlet aperture area. If the inlet's width is much larger than it's height, then the amount of captured boundary layer will be greater than the case where the width is equal to the height (aspect ratio = 1), as shown in fig. 21. The designer can therefore increase the aspect ratio of the inlet shape in order to achieve higher levels of ingested boundary layer. Higher mass flows make the inlet width even more sensitive to the aspect ratio of the inlet for a fixed boundary layer size, as demonstrated in fig. 21.

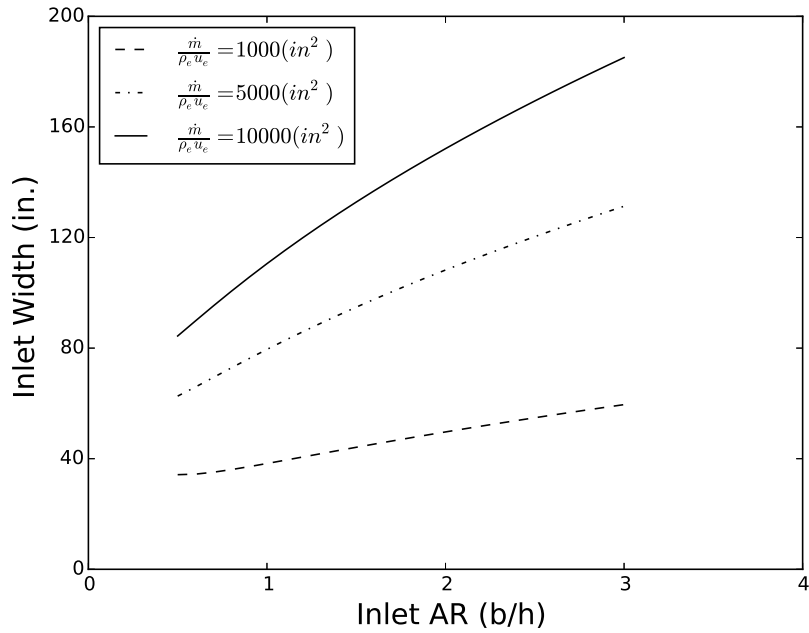


Figure 21: Influence of inlet aspect ratio on inlet width sizing.

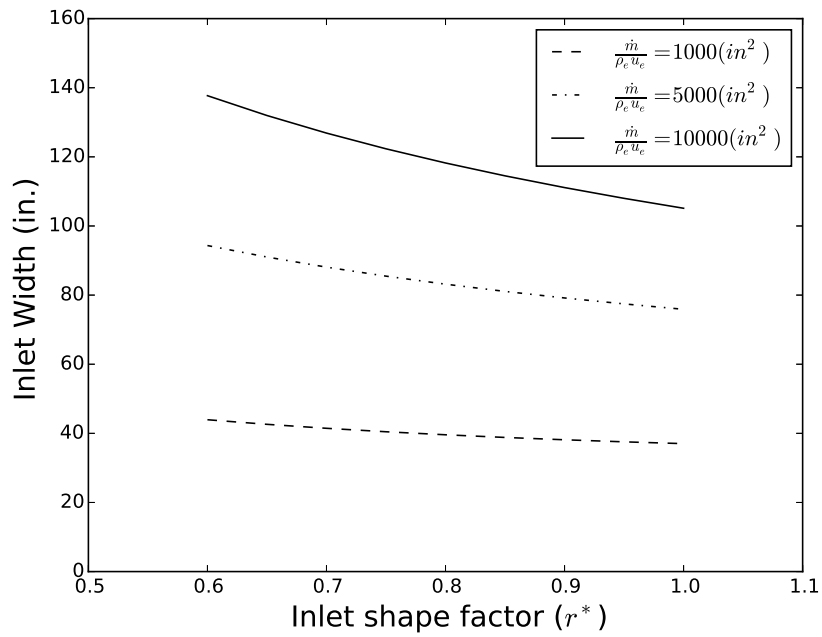

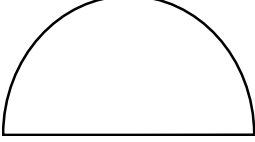
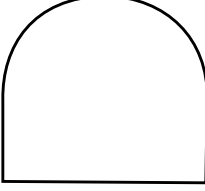


Figure 22: Influence of inlet aperture shape on inlet width sizing.

Table 4: Table showing inlet shapes, $y(x)$, and r^*

Shape	$y(x)$	r^*
	$y(x) = h$	$r^* = 1$
	$y(x) = h \cdot \sqrt{1 - 4 \frac{(x - b/2)^2}{b^2}}$	$r^* = \pi/4$
	$y(x) = \frac{h}{2} + \frac{h}{2} \cdot \sqrt{1 - 4 \frac{(x - b/2)^2}{b^2}}$	$r^* = 1/2 + \pi/8$

The choice of inlet aperture shape also has a relatively weak influence on the inlet width sizing as shown in fig. 22. As the inlet is tapered at the top, the width at the bottom of the inlet near the boundary layer must increase to capture more flow. Table 4 shows several typical BLI inlet shapes for class 2 type BLI with values of r^* and $y(x)$ shown.

Finally, a fundamental choice with regard to determining the overall system β is the location of each propulsor on the upper surface of the airframe. This involves both the selection of the number of propulsors (something that would effect the engine stream-tube size) and the location of each propulsor both span-wise and chord-wise. This last choice will affect the size of the boundary layer thickness, as well as the local velocity and static pressure at the inlet. This has an impact on both the total amount of drag ingested and the overall losses in the inlet and fan due to distortion. All of the above discussion leads to the following observation 3:

Observation 3: The engine mass flow size, inlet aperture shape, and location on the vehicle affect the ratio of the ingested drag to uningested drag for class 1 BLI systems.

Propulsor Sizing: Class 2 BLI

For class 2 BLI systems, the distortion is primarily radial, but the fundamental equation still applies from Eq. 50, except that the integration is different because of the way that the boundary layer is distributed. Furthermore, the calculation of the stream-tube width is irrelevant (even meaningless). Rather, the primary variable is the radius of the propulsor which determines how much mass is ingested. Consider a general flow annulus for a class 2 BLI problem with inner radius r_i and outer radius r_o . The equation for mass flow is then:

$$\dot{m} = \int_0^{2\pi} \int_{r_i}^{r_o} \rho u_x r dr d\theta \quad (55)$$

The definition of \mathbf{M} here is slightly different than Eq. 33, since it must account for the effect of radius on the area averaging of the velocity:

$$M_r(\theta) = \int_{r_i}^{r_o} (\rho_e u_e - \rho u) r dr \quad (56)$$

From Eq. 56, the final equation for the mass flow of a class 2 BLI propulsor is:

$$\dot{m} = \int_0^{2\pi} \left[\frac{r_o^2 - r_i^2}{2} \rho_e u_e - M_r(\theta) \right] = \rho_e u_e A - \int_0^{2\pi} M_r(\theta) d\theta \quad (57)$$

With the second part of Eq. 57 recognizing $A = \pi(r_o^2 - r_i^2)$. If the propulsor is sized with a radius greater than the boundary layer thickness, then the above can be simplified to solve for the required outer radius for a given desired mass flow. The net result is that the propulsor has to be a little bit bigger for a specified mass flow, however if the amount of BLI ingested is large, then the propulsive efficiency improves and the specific thrust increases requiring less mass flow.

The analysis of Smith [86] showed that a wake ingesting propeller with class 2 BLI will have significantly improved propulsive efficiency if the wake comprises a large portion of the total vehicle required drag. In general, for better propulsive efficiency, larger mass flow designs are desirable, since they require less jet velocity to produce the same thrust. However, Smith notes:

...when a large part of the craft's wake is ingested by the propulsor, there is much less incentive to keep the propulsor large. The message here is that, for best efficiency the propulsor should be positioned and sized to ingest as much wake fluid as possible (increase D/T), but after that, making it still larger does not pay off in propulsive efficiency and would have other adverse effects such as increased weight.

For the case of class 2 BLI, this amounts to sizing the propulsor with a large enough radius to consume the entire wake, while for class 1 BLI, there is a more significant design trade-off since larger mass flows imply larger levels of BLI.

Distortion Effects on the Engine

We now turn to the question of how the losses induced by the boundary layer ingestion are developed and also the question of model fidelity requirement with respect to these losses. Generally, the primary determining factor for the losses of the engine will come from the loss of total pressure due to the presence of the distortion. This pressure drop can be approximated by integrating the boundary layer velocity profile over the fan face area. Appendix B describes a mathematical development of the inlet model to be used later in this thesis but also contains an integral formulation showing that the total pressure loss can be approximated by using the kinetic energy defect property defined in Eq. 35, assuming that the density thickness is negligible and a uniform

static pressure.

$$\bar{P}_t = P_s + \frac{1}{2} \rho_e u_e^2 \frac{(A - \delta^* - \theta^*)}{(A - \delta^*)} \quad (58)$$

Equation 58 shows that the total pressure loss is proportional to the size of both the boundary layer blockage represented by δ^*/A and the kinetic energy thickness to area ratio θ^*/A . This means that a bigger ratio of boundary layer to "clean" flow yields a worse total pressure recovery. Note that this is in direct contradiction to the analysis developed previously for the BLI benefit, which dictates that ingesting a larger percentage of the boundary layer into the inlet is more beneficial. The fraction of boundary layer to total flow area is a function of the amount of boundary layer ingested, the value of the 2-D "height averaged" boundary layer thickness and shape, and also the edge velocity of the boundary layer itself – implying faster flows will tend to produce more losses in a shear layer. This observation is also corroborated in several experimental sets of data including that of Berrier et. al. [8]. These results show that bigger percentages of boundary layer to total flow area yield worse inlet recoveries implying an essential trade-off involved in designing the amount of BLI to be ingested into a system and the subsequent engine size required. Observation 4 comes the pre-ceeding analysis:

Observation 4: The boundary layer thickness does not scale directly with the propulsor mass flow, but the stream tube does change. Therefore boundary layer related losses will be different for changes in engine stream tube size, since the total inlet recovery is a function of the ratio of the boundary layer flow to the total flow.

Off-Design Analysis

The off-design analysis of BLI engines is something that has not been very extensively researched in the system study literature. Typically, the focus is on the cruise point efficiency and therefore variations in flight Mach and altitude are not considered

especially important for the sizing of the vehicle. However, the aerodynamic design point of an engine is not the only point of concern. In fact, the BLIPSS methodology is specifically designed to account for the fact that performance at off-design conditions for highly integrated systems is important to capture. Therefore, understanding the fidelity requirements for a BLI engine model in off-design is nearly as important as quantifying it for the cruise condition.

μ Variation

Shedon [84] defines a simple model for an inlet, in which the inlet duct loss varies with the cube of the inverse of the mass flow ratio defined as follows:

$$\mu = \frac{A_c}{A_\infty} = \frac{\rho_\infty u_\infty}{\rho_c u_c} \quad (59)$$

The parameter μ is effectively a measure of how the stream-tube expands or contracts as it approaches the inlet hi-lite area. The μ^3 variation [84] is defined, in its simplest form, as follows:

$$\frac{\Delta P}{q_c} = IC_{Fd} + JC_{Fa} \cdot \mu^3 \quad (60)$$

Here there are two skin friction coefficients, one for the duct and the other for the region of the vehicle prior to entry (as often seen in military aircraft). The pre-entry flow is the region sensitive to the mass flow ratio variation and is of particular importance for boundary layer ingesting systems. Usually 60 is re-arranged in terms of the free-stream dynamic head rather than the local capture head as follows:

$$\frac{\Delta P}{q_\infty} = \frac{IC_{Fd}}{\mu^2} + JC_{Fa} \cdot \mu \quad (61)$$

An analysis of 61 shows that there are essentially two regimes over which a BLI intake can operate: one in which the flow accelerates prior to entry ($\mu \ll 1$), and one where the flow is retarded prior to entry ($\mu \gg 1$). At extremes of these two regimes, the actual intake recovery varies from 61 because of pre-entry separation

and lip flow separation, neither of which are included in the derivation of 61. Pre-entry separation occurs in regions of extreme flow retardation ($\frac{dP}{dx} > 0$, $\mu \gg 1$). This generally happens in very low mass flow demand regions at high-speeds, such as possibly end of cruise or descent. Lip separation occurs in the opposite extreme in the low μ regime where mass flow is very high and velocity is low, which would be of greater concern at the take-off maximum power condition.

The preceding analysis again shows that, fundamentally, the determination of inlet losses is a function of how the inlet stream-tube varies as it approaches the inlet.

Flight Condition Variation

There has been some experimental data defining variations in inlet recoveries at different flight Mach, Reynold's, and mass flow ratio [7] [8] for inlets designed specifically for BLI applications on large transports. This data showed that flight Mach number has a very strong influence on the overall recovery, with the mass flow into the inlet playing a significant secondary role which is in congruence with the μ^3 analysis. The theoretical development by [84] also stressed the importance of the skin friction coefficient which significantly increases with the Mach number of the flow. Furthermore, the 61 gives an expression for duct loss which is normalized by the free-stream head which increases significantly at higher Mach. The expectation, then, is that the size of the boundary layer relative to the size of a fixed capture height inlet will decrease as the free-stream Mach number is decreased along with both benefit and loss. This implies that the thrust saving coefficient at low altitude and speeds, especially at the take-off condition, should be relatively lower – for similar vehicle angles of attack – than that at high speeds, but that distortion concerns would not be as great.

Angle of Attack Variation

In general, subsonic pitot inlet based engines are not generally thought to have much variation in thrust or performance with the angle of attack of the vehicle. In cases where large angle of attack is required, the inlets can typically be scarfed to provide a favorable flow angle into the intake, thereby reducing any distortion and mitigating loss of pressure recovery. In the case of BLI, this is not possible, and we would

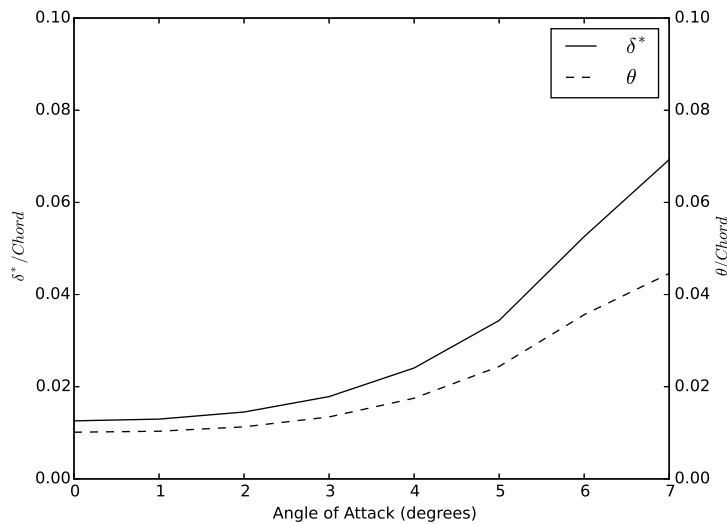


Figure 23: Plot showing trend of boundary layer thicknesses vs. airfoil angle of attack for a NACA 2012 airfoil at Mach = 0.7, $\text{Re} = 10^6$ as predicted by XFOIL

therefore expect to see significant variation in the performance of the engine as a function of the vehicle angle of attack. Figure 23 shows the variation of boundary layer properties for a NACA 2012 symmetric airfoil at a flight Mach of 0.7 with a Reynolds of 10^5 , as predicted by XFOIL [22].

Clearly the boundary layer thickness increases significantly, which will impact the thrust saving coefficient and inlet recovery. There is significant variation in the angle of attack of flight vehicles during their mission and therefore the variation in thrust, efficiency, and operability as a function of angle of attack, if found to be significant, would be necessary to include in a model at this level.

Hypothesis 1

Though the discussion above is barely touching the surface in terms of the complexity of an actual boundary layer ingesting flow field, there are some clear basic trends which have arisen from the analysis. First, the benefit of the system is ultimately a balance between drag recovery and distortion losses, which tend to both increase with the ratio of distorted boundary layer flow to clean flow. Second is that, at a given design point, any design choice which impacts the size of the ingested stream-tube will impact the amount of boundary layer that is ingested, though those choices will not have an impact on the vehicle boundary layer. Third, that the boundary layer thickness varies significantly with flight Mach number and angle of attack for a given vehicle. Fourth, that the losses in the inlet duct leading to the propulsor face will vary significantly with the free-stream mass ratio and the flight condition. Given that the BLIPSS methodology is intended to be able to account for multiple design conditions, it is therefore necessary, if it is to be used, to account for these fundamental variations in benefits and losses. Otherwise, changes in flight conditions and power settings will not appropriately match the actual variation in design point performance even at a first level approximation. From these observations, the following hypothesis is formed:

Hypothesis 1: BLI propulsion system cycle models need to include the physical coupling between the vehicle boundary layer profile, the ingested stream-tube, and system powerbalance and losses at critical sizing conditions. Without these effects, the model will not properly characterize performance trends at design and off-design conditions.

Stall Margin and Stall Constraint

Hypothesis 1 deals with the basic modeling requirements for any BLI system. It is formulated out of a need to appropriately size the system – based on requirements at multiple flight conditions – and thereby appropriately form a design space from which early design choices can be made. The hypothesis is developed in order to properly establish the trade-off between the propulsive efficiency benefit of ingesting more low momentum flow and the losses incurred by doing the same. The other major component of any boundary layer ingesting system, not addressed by Hypothesis 1, is the impact on the operability of the propulsion system incurred by the ingestion of distorted inflow. Clearly this is an important component of the problem, and yet it is not typically addressed at the level of conceptual design.

Operability is considered to be a constraint on a propulsion system, meaning that adding more is not necessarily desirable beyond that which is required. The major tool for meeting this constraint is the stall margin stack-up [67]. A fan stall margin stack-up typically comprises some percentage which is dedicated to account for possible distortion exiting the inlet at the fan face. If ingesting boundary layer produces levels or types of distortion which are fundamentally worse than that of typical fan designs, then something must be done in the design to restore normal levels of safe operability. While it is difficult to determine the efficacy of various distortion mitigating actions in the conceptual design phase, it is worth investigating how conceptual design choices – the kinds of which the BLIPSS methodology is intended to facilitate – affect the likely level of stall margin loss due to distortion and therefore the likelihood of being able to restore it to normal levels. Research question 2 is formulated accordingly:

Research Question 2: How does the stall margin constraint affect the BLI propulsion system design space?

Distortion Stall Margin Loss

The stall margin stack-up percentage which is included to account for distortion is usually estimated in design based on prior requirements for existing designs. Testing of fans and compressors then occurs after detail design of the fan is carried out and a test rig can be constructed. The ARP 1420 [13] guidelines have developed over the years to guide this experimental process to fruition by giving the operability analyst a standard set of tools and experimental setup to appropriately estimate and measure stall margin loss for specific designs. The standard rig setup dictated by ARP 1420 is

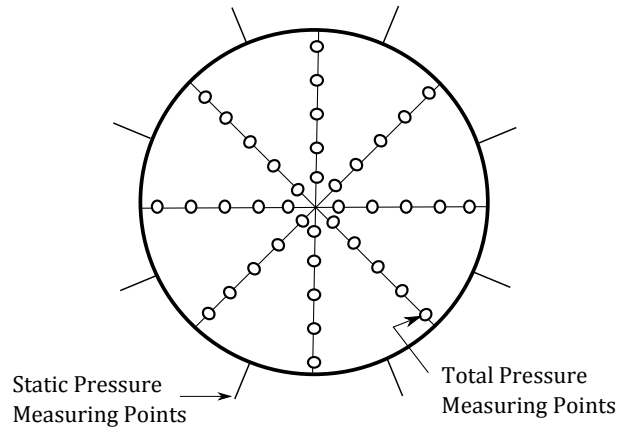


Figure 24: Standard ARP 1420 test rig showing static and total pressure probe locations

shown in figure 24 and consists of a set of pressure probes and rings at which the total pressure of the flow is measured. Typical distortion types can be described in terms of per-rev, which gives measurement of how many low pressure circumferential sections is the blade passing through. For BLI systems which ingest boundary layer from the upper surface of a vehicle, such as that for the typical HWB type configurations, the distortion usually takes on a 1-per-rev circumferential distortion type. This type is illustrated for in figure 25. The extent is defined as in Eq. 62 and is representative of the circumferential extent over which the total pressure is lower than the average.

$$\theta_i^- = \theta_{2i} - \theta_{1i} \quad (62)$$

The circumferential intensity is defined as:

$$\left(\frac{\Delta PC}{P}\right)_i = \frac{(P_{av})_i - (P_{avlow})_i}{(P_{av})_i} \quad (63)$$

$$(P_{AV})_i = \frac{1}{360} \int_0^{360} P(\theta)_i d\theta \quad (64)$$

$$(P_{AVLOW})_i = \frac{1}{\theta_i^-} \int_{\theta_{1i}}^{\theta_{2i}} P(\theta)_i d\theta \quad (65)$$

Then, the total circumferential intensity is the sum of each of the rings.

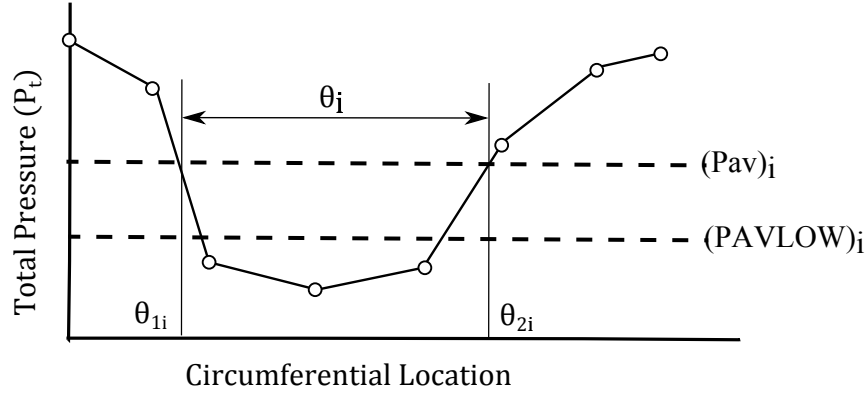


Figure 25: Illustration of a one-per-rev distortion type for a single probe ring (adapted from [16]).

$$DPCP_{avg} = \frac{1}{N} \sum_{i=1}^N \left(\frac{\Delta PC}{P}\right)_i \quad (66)$$

The stall margin loss is typically defined in terms of ΔPRS defined, which is the difference between the clean and distorted stall pressure ratio at constant flow in percentage of the clean stall pressure ratio which is illustrated also in figure 26.

$$\Delta PRS = \frac{PRS_{Clean} - PRS_{Distorted}}{PRS_{Clean}} \quad (67)$$

Typically the ΔPRS is quantified by correlating it with the intensity defined in Eq. 63. An example for classical one-per-rev distortion type would be described in 68 and is represented with a simple linear correlation.

$$\Delta PRS = K_c \cdot DPCP_{avg} \quad (68)$$

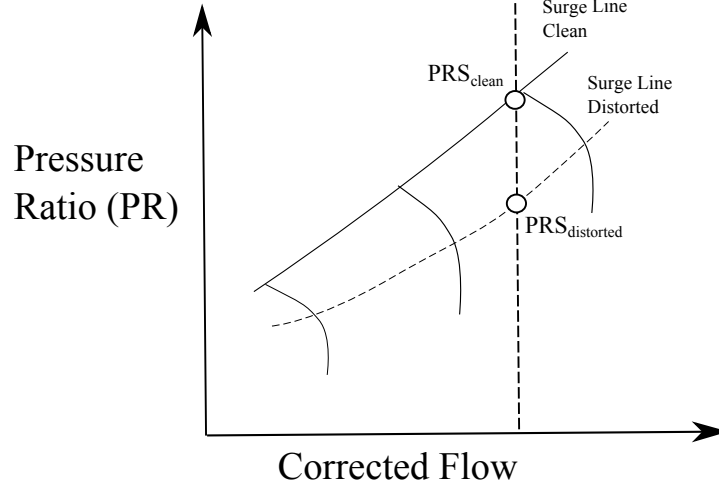


Figure 26: Illustration of the definition of delta PRS with distortion (adapted from [57])

The other type of distortion common to BLI systems is radial pressure distortion, which represents a gradient of the total pressure in the radial direction as is common within a viscous boundary layer. Radial pressure gradients can significantly affect the compressor characteristic and the pressure ratio at which stall occurs. The ARP 1420 radial descriptor is defined by Eqs. 69 and 70.

$$\left(\frac{\Delta PR}{P}\right)_i = \frac{PFAV - (P_{AV})_i}{PFAV} \quad (69)$$

Where,

$$PFAV = \frac{1}{N} \sum_{i=1}^N (P_{AV})_i \quad (70)$$

The standard $DC(\theta)$ which represents a descriptor for complex distortion types containing both circumferential and radial is then defined as follows:

$$DC(\theta_E) = \frac{1}{N} \sum_{i=1}^N \left[\left(1 - \frac{\Delta PR}{P}\right)_i \cdot \left(\frac{\theta_i}{\theta_E}\right) \cdot \left(\frac{\Delta PC}{P}\right)_i \right] \cdot PFAV/q_{avg} \quad (71)$$

This descriptor, which combines the types of distortion which can be represent various complex patterns can also be correlated with ΔPRS , which is standard practice for experimental testing and quantification of distortion stall margin loss [13].

Simple Example

Consider now the case of a circular fan aerodynamic interface plane defined in terms of polar coordinates (r, θ) and with a standard ARP 1420 set of rakes applied to it. The hub-to-tip ratio of the fan is fixed at 0.45. The centerline ($\theta = 0$) is represented by a $1/7^th$ power law velocity distribution typical of turbulent flat-plate boundary layer profiles with a 99% thickness defined as δ . The ratio of the boundary layer thickness to fan blade span is δ/h .

$$\frac{u}{u_e} = \left(\frac{y}{\delta}\right)^{1/7} \quad (72)$$

The circumferential variation in the velocity distribution is assumed to be defined as follows [72]:

$$p_t(r, \theta) = p_{t_l}(r) \cos^{10}(\theta) + p_{t_h}(r) \left[1 - \cos^{10}(\theta)\right] \quad (73)$$

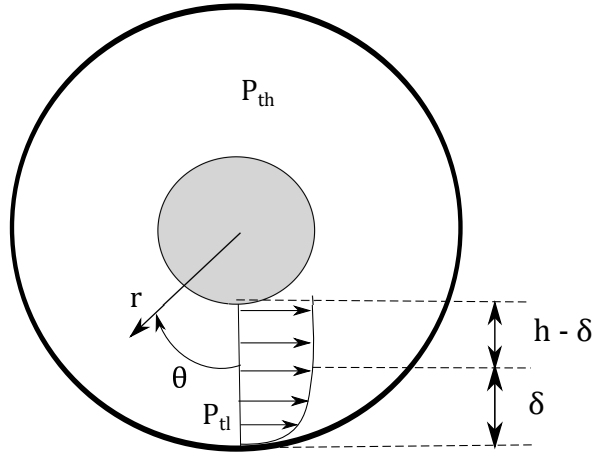


Figure 27: Illustration of the Notional Fan Face AIP

Applying the above parameterizations and assumptions in velocity profile, a 2-D fan face representation can be constructed and the distortion descriptor $DC(\theta_E)$ can be calculated. Some values for the pressures and temperatures assumed in this case are shown in table 5. Figure 28 shows the AIP pressure distributions for 5 typical rakes generated for a boundary layer thickness to blade height ratio of unity. From

Table 5: Distortion Example Parameters

Parameter	Value
P_{th}	15 psia
M_e	0.65
r_h/r_t	0.45
r_t	56 in.

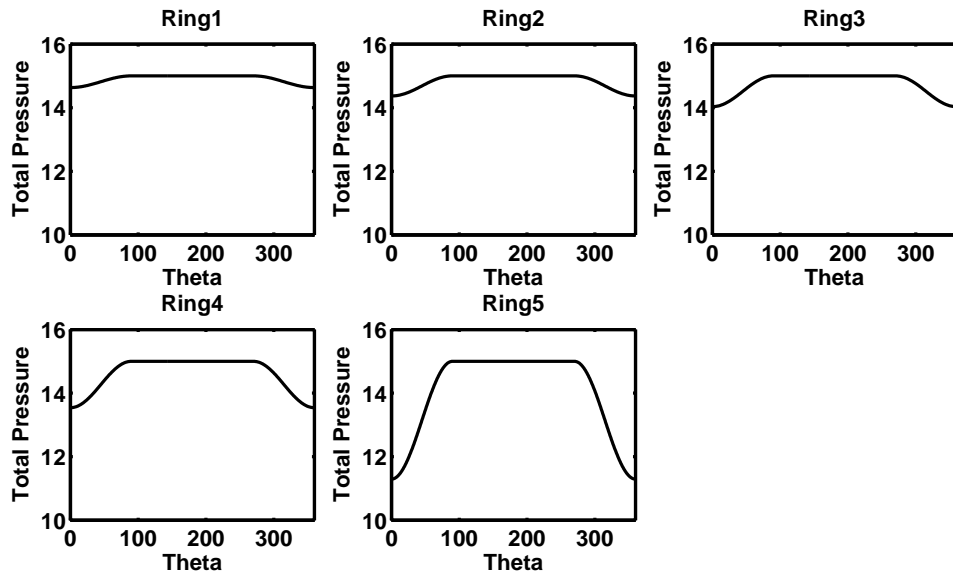


Figure 28: Example fan face ring total pressure distribution.

these distributions, the rake data can be used to calculate the distortion descriptors. The boundary layer height to blade height ratio was varied from 0.1 to 2 and the distortion descriptors are calculated. The results – shown in figure 29 illustrate what happens when the thickness of the boundary is increased relative to the size of the clean flow area.

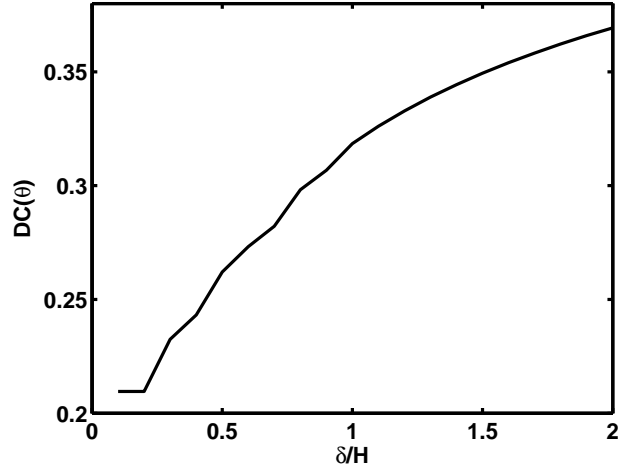


Figure 29: $DC(\theta)$ descriptor plotted vs. boundary layer thickness ratio.)

Hypothesis 2

Since $DC(\theta)$ generally correlates directly with ΔPRS , it stands to reason that increasing the boundary layer thickness to height ratio will harm the stability margin of the fan substantially. This could, in theory, place limits on the size of the propulsor in relation to the size of the boundary layer in order to maintain operability. From observation 2, it has been established that the benefit of BLI is a strong function of the same ratio, implying that operability may limit the cycle designer’s ability to ingest more drag within imposing an operability problem on the system. If the cycle designer is given a hard target on what the allowable stall margin loss (ΔPRS) is at the conceptual phase, then this would limit the possible benefit that a BLI propulsion system would give. Hypothesis 2 is therefore derived from this simplified analysis and

is stated as follows:

Hypothesis 2: The operability constraint limits the size of a propulsor in relation to the amount of boundary layer that it ingests.

There are a few caveats worth mentioning to clarify the statement of Hypothesis 2. It does not necessarily say that the constraint will be an active constraint on the system. For instance, if something else, such as engine core "size-effect" losses or other practical concerns limit the available amount of ingestion, then the constraint would still be present in the design space but would not affect the design choice made. Also note that the hypothesis is made in terms of a single propulsor, not necessarily an entire system. There may, in fact, be system configurations in which part of the propulsion system ingests boundary layer while another part does not. In this case, increasing the thrust saving coefficient of the BLI propulsor would not necessarily increase the overall β of the system, but it would decrease operability via distortion increase.

BLI Modeling Phase Process

Hypotheses 1 and 2, if substantiated, imply a partial solution to research question 1: namely that the BLI modeling phase should consist of building models which accurately represent the relationship between the major conceptual design variables determining the level of BLI ingested and losses in performance and operability of the system. The following modeling algorithm for the BLI modeling phase is thus developed from this understanding and the preceding theoretical analysis:

Prior to Analysis

- ① Establish vehicle airframe geometry

- ② Identify BLI propulsor type: Class 1 or 2
- ③ Establish aerodynamic cross-section stack-up (based on step 1): Lateral for C1; rotational for C2

For each flight condition and propulsor location:

- ④ Compute BL defect property from “clean” airfoil analysis ($\delta^*, \theta, \theta^*$) at $(x, y)_{inl}$, $(x, y)_{TE}$, and $(x, y)_{treftz}$
- ⑤ Approximate $\nu = K_{\infty_{BLI}}/K_{\infty}$ based on BLI type.

For each cycle analysis iteration

- ⑥ Compute BLI thrust term ($\beta \cdot \Phi_p^*$) based on BLI type (Eq. 44 for C1, Eq. 47 for C2)
- ⑦ Compute $\frac{A_o}{A_c}$ and inlet losses based on inlet BL properties.
- ⑧ Estimate inlet distortion and compute propulsor operating line
- ⑨ Estimate ΔPRS and $\Delta \eta_F$

3.2.2 Architecture Integration Phase

With advances in aerospace concepts toward more fuel efficient, revolutionary aircraft, such as the HWB, there are many possible types of architectures that could potentially become viable. Varying numbers of BLI engines could be used, such as 2, 3, 4, or 5 engine BLI turbofans [40]. The concept of turbo-electric distributed propulsion has also been investigated as a possible architecture, in which there are turbo-generators which do not ingest boundary layer but transfer power, via an electrical distribution system, to a propulsor array which spans the upper surface of the vehicle [47] [44]. Each of these architectures can take advantage of boundary layer ingestion, with some of them ingesting more overall stream-tube than others. Figure 30 shows several of

these possible architectures, with varying propulsor numbers and locations on the upper surface of the HWB. All of these potential propulsion system architectures need to be evaluated in comparison to each other, but also need to be properly sized at the conceptual level in order to make legitimate comparisons of overall fuel burn and weight between the systems.

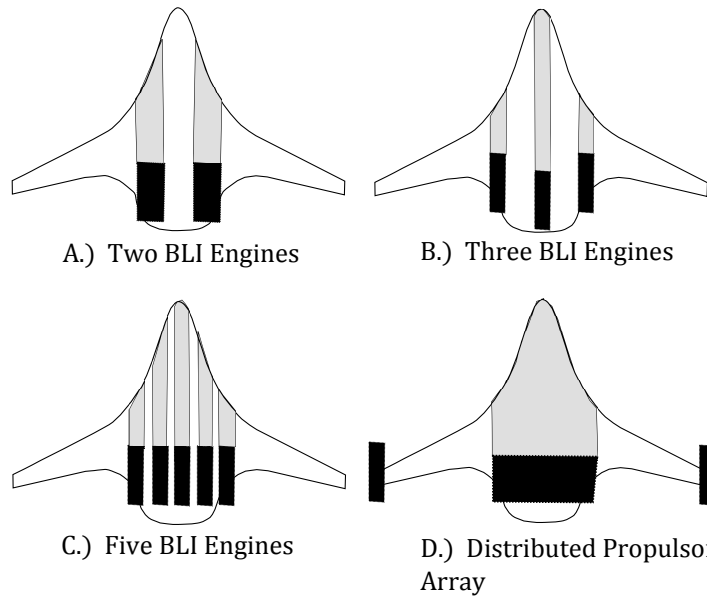


Figure 30: Examples of potential propulsion system architectures for an HWB aircraft.

Observations and Research Question 3

As noted in chapter 2, the problem of integration for BLI systems in relation to the MDP sizing process is that the airframe can impact each propulsor/gas generator in different ways depending on the location of the propulsor on the airframe. This relates to both the nature of the boundary layer at the inlet location, which will significantly impact the recovery, and the overall amount of boundary layer ingested and recovered by the engine. Factors which impact this are mostly related to the airframe geometry, including things such as the airframe airfoil design (thickness-to-chord, camber, etc) and the overall chord length. For example, in general the boundary layer thickness will

increase as a function of the axial location along a surface. A simple demonstration is seen in Eq. 74 for a turbulent flat-plate boundary layer – assuming a 1/7th power law – which represents the increase of the boundary layer thickness with axial position [9].

$$\frac{\delta}{x} = \frac{0.3747}{(Re_x)^{0.2}} \quad (74)$$

This means that if chord length of the airfoils tapers, as it clearly does for the HWB, then the boundary layer will decrease as a function of the %Chord, and the amount of wake recovery generated by ingesting the boundary layer will be less. This is also saying that the inner portion of the HWB center body, which is much longer and therefore thicker, will generate more viscous profile drag. Thus, choices of where the propulsors are placed will have an impact on the overall thrust saving coefficient, inlet recovery, and the stall margin loss of the system. To further corroborate the idea that this will significantly impact the system, one need only read reference [45] here, in which the boundary layers of the outboard sections of an HWB design (Boeing N2B) were found to be significantly smaller than the outboard (factor of 1/2). Furthermore, the engine aerodynamic interface planes had significantly different levels of distortion and overall recovery between them. The above considerations illustrate the nature of the integration problem vis a vis the propulsion system cycle analysis, and research question 3 is formulated as a result:

Research Question 3: How can multiple design points, different BLI propulsion system architectures, and variations in inlet properties between propulsors/engines at a given flight condition be accounted for in BLI propulsion system conceptual design?

Methodology Development

To establish a way of dealing with the above research question, it is first necessary to understand how the MDP methodology operates in practice. Figure 31 shows the sequential SDP process. This process is designed for a single engine and design point. The idea is to iterate between the desired off-design conditions to check that the requirements at those conditions are met. The operating thrust at the design condition can be altered to then satisfy the off-design conditions.

Sequential SDP: Single Engine, Single Design Point

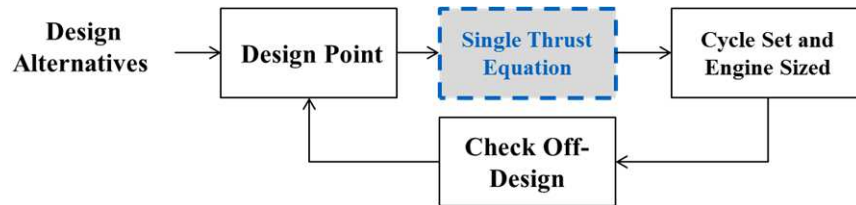


Figure 31: Illustration of Sequential Single Point Design

By comparison, the multi-design point process, illustrated in figure 32, is intended to remove the iteration with the off-design conditions in order to automate the design process to produce a design space with off-design conditions automatically satisfied.

Multi-Design Point: Single Engine, Multiple Design Points

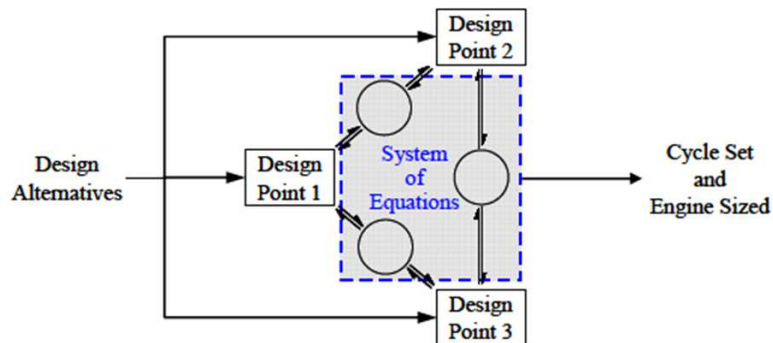


Figure 32: Illustration of Multi-Design Point Process

To account for the performance of the engine/propulsor at different inlet conditions, the MDP process from 32 could be iterated with an off-design condition where the inlet conditions are changed. Then, the engine could be rematched according to the change in performance that is calculated. Instead of this manual process, which is analogous to the SDP process, the inlet conditions can be included as "Design Points" in the MDP analysis. To extend this even further, the possibility of having different sized propulsors can be included in this, which would mean that each unique propulsor/inlet combination at each flight condition would be considered a "Design Point" in the automated MDP process. This process is illustrated in figure 33.

There are two major changes which occur from this view of the multi-engine/propulsor MDP process: first there needs to be some set of rules which relate the design and operation of the propulsor at each flight condition; second is that the thrust calculated is now the sum of the separate propulsor thrusts from each "design point" times the number of propulsors included in that design point (since it is possible to have multiple propulsors represented by a single design point). The rules required for the completion of the ME-MDP process are classified into two categories: design rules, and power management rules. These are discussed in more detail in the following section.

Design Rules

Design rules are defined as a mathematical relationship that relates the size of a propulsor or propulsor components at its aerodynamic design point to another uniquely different propulsor at the aerodynamic design original propulsor. If there is only a single engine/propulsor designed, then there is no need to have additional design rules. If "k" unique propulsors are designed, then there can be as many as $\sum_{i=1}^k N_{comp} - 1$ design rules, where N_{comp} is the number of aerodynamic design points for propulsor "i". For example, if 2 different turbo-fan engines were sized for a 3-Engine HWB with

BLIPSS : Multi-Engine, Multi-Design Point

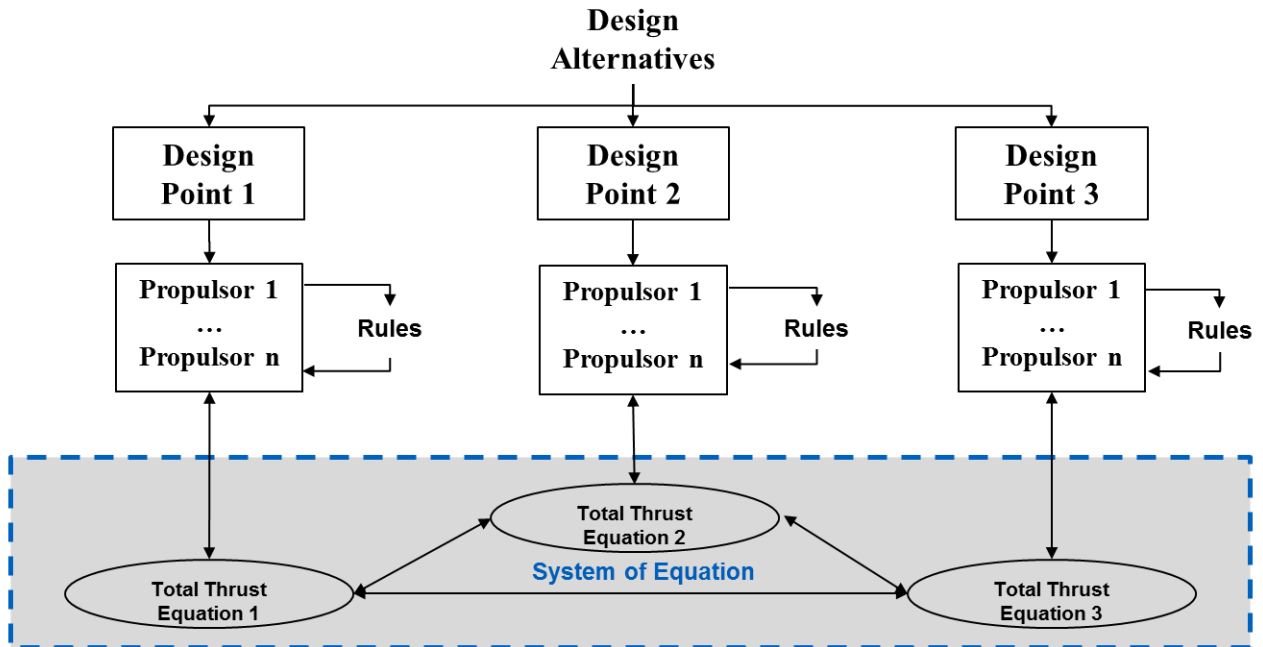


Figure 33: Illustration of Multi-Engine Multi-Design Point Process

BLI (a case to be considered in detail later in this document), then the number of design rules is exactly 1. If there is only a single aerodynamic design point (only 1 propulsor designed), then there is no required design rule. Another interesting aspect of the creation of design rules is that it creates additional cycle design variables for the system, which may have a significant impact on the amount of BLI ingested by each propulsor and potentially the system as a whole.

Power Management Rules

Power management rules are mathematical relationships that relate the power output of one propulsor **at each design point** to the power output of another. In general, the amount of power provided by a propulsor will be proportional to the speed, meaning the power management scheme will pertain to the speeds of the fans/propellers. Some engine manufacturers use the fan speed (N_1) as the primary power management variable which is measured in the engine, while others use engine pressure ratio

(EPR) to correlate thrust [87].

Power management rules are specified at each flight condition, except for the aerodynamic design points of the propulsors, since turbo-machinery components are, by definition, at 100% speed at their ADP. If one propulsor is at its aerodynamic design point, and another is not, then the power management rule and the design rule are the same thing at that point, since setting the size of the propulsor will also set the relationship between the power output of the propulsors. Therefore, the number of additional power management rules (on top of the design rules) required can be computed by Eq. 75, where k is the number of unique propulsor/inlet combinations, " N_p " is the number of design points, and N_{comp} is the number of ADPs for each propulsor.

$$N_{pm} = \underbrace{N_p(k-1)}_{\text{Design + PM Rules}} - \underbrace{\left(\sum_{i=1}^k N_{comp}\right) - 1}_{\text{Design Rules}} \quad (75)$$

Engine Matching Relations

The normal engine matching relations are a set of independent variables and dependent relations that are solved by the Newton-Raphson solver in the MDP method. The independent variables in the engine matching relations are typically the fuel-to-air ratios of the burner, while the dependent relations are equations which set the thrust to a desired level of thrust or the speed of the engine/propulsor to a desired fraction of the design speed (which correlates with thrust). As such, the MEMDP method must necessarily modify the engine matching relations to accommodate the new architectural arrangement.

If a propulsion system has k uniquely defined propulsor/inlet condition combinations and the i^{th} combination contains m_i propulsors, then the total number of

propulsors is defined by:

$$n = \sum_{i=1}^k m_i \quad (76)$$

and the total thrust, in the case of BLI is defined by:

$$F_{n_{BLI}} = \sum_{i=1}^k m_i (F_{n_{BLI}})_i \quad (77)$$

As such, the thrust saving coefficient and thrust specific fuel consumption are also computed as the sum.

$$TSC = 1 - \frac{\sum_{i=1}^k m_i F_{n_i}}{\sum_{i=1}^k m_i \frac{F_{n_i}}{(1 - TSC_i)}} \quad (78)$$

$$TSFC = \frac{W_f}{F_{n_{BLI}}} = \frac{\sum_{i=1}^k W_{f_i}}{\sum_{i=1}^k (F_{n_{BLI}})_i} \quad (79)$$

Finally, the total amount of engine matching relations is precisely equal to $N_p + N_{pm}$. These engine matching relations comprise the vector of independent variables which affects the power output of each propulsor and the vector of dependent thrust or power balance relations (power management rules plus P total thrust relations). If k is greater than unity, and the additional (k-1) unique propulsors are allowed their own design points, then the number of engine matching relations is reduced and each replaced with a single cycle design relation for the uniquely designed propulsor.

Alternative Approaches and Hypothesis 3

The major alternative approach to dealing with the problem of inlet condition variation is to add an augmentation term to the boundary layer ingestion term in the power balance. This approach will be called the "wake correction method". This would work by sizing a single propulsor in a traditional manner, but with the wake recovery term for that single propulsor augmented to reflect the difference in wake-recovery between the different propulsors on the vehicle. This approach has the difficulty of not always knowing "a-priori" exactly how much wake recovery will be lost or gained due to that

variation and it also does not capture differences in inlet recovery between the propulsors induced by the boundary layer disparity. It also does not allow the new degrees of freedom appropriated by the additional design rules and power management rules in the ME-MDP method. This alternative approach was used in an example system level study of a distributed propulsion architecture by MIT [79]. A comparison of this approach will be shown in later sections.

With the above description of the proposed ME-MDP approach to be used within the BLIPSS design method, the following hypothesis has been formed in relation to research question 3.

Hypothesis 3: Differing inlet conditions for BLI propulsion systems can be accounted for by using a modified simultaneous MDP approach where design points are considered on a per-propulsor basis and sizing to a total vehicle thrust. If the difference in the local inlet properties are large, this approach will yield increasingly different performance predictions than if the traditional single engine or the wake correction method is used.

Canonical Problem and Research Question 4

The test problem for hypotheses 1-3 chosen for this thesis is the N2A boeing HWB design. The selected propulsion architecture to test hypothesis 3 is a 3-engine turbofan based architectures. As such, this section will define the architecture integration phase and pose a relevant research question for this canonical problem with regard to the power management and design rules. A diagram of the 3-engine configuration is shown below in figure 34 with some key parameters for the system defined. The propulsion system will, in order to maintain symmetry, always have one "inboard" engine at the aircraft centerline (thicker boundary layer) and an outboard engine

which is at some parametric location value. This value will be used to test hypothesis 3 and to determine engineering trades on the system overall.

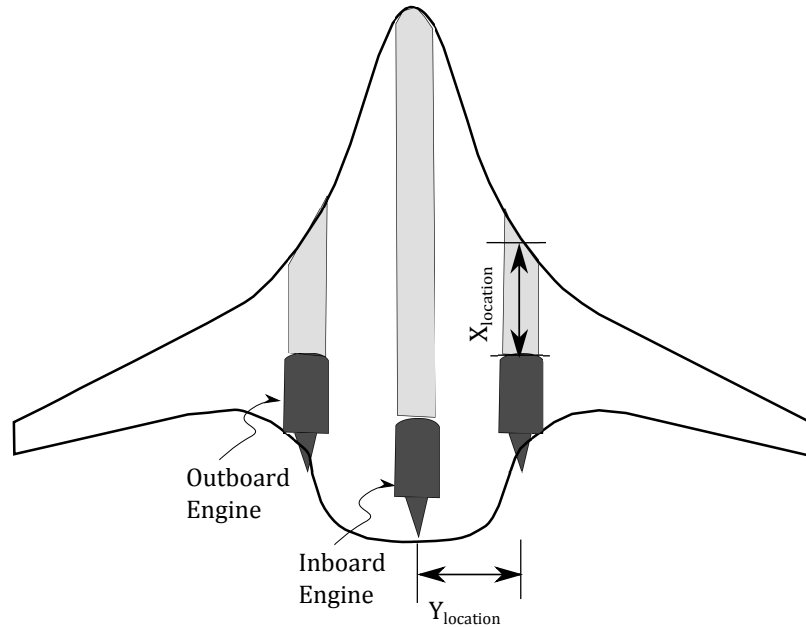


Figure 34: Illustration of 3-Engine Boeing N2A.

Design Options for 3 Engine HWB

The design options for any propulsion system can be specified by showing the design point mapping matrix as defined by Schutte for the MDP process. Different design potential rules can be specified for each design option. These are shown in table 6. The single inlet case is the condition where only the single inlet condition is considered. This case will be used to test hypothesis 3 and is representative of the standard cycle analysis where only a single propulsor/inlet condition combination is considered. The single engine is the case where there is only a single design point (one-engine designed). For this case, there are two options, either inboard core design point or outboard core design point, which raises the question of which is better to choose. Finally, there are the two design options where the inboard and outboard propulsors are sized independently. The fixed core design assumes that only the bypass and LP spool are re-designed for each, while the core/HP spool are designed

Table 6: Design point mapping matrix for the 3 engine architecture highlighting the available design rules.

	X = Not used	D = On-Design	O = Off-Design
Design Option	Core/HP Spool		Fan/LP Spool
			Design Rule
Single Inlet	Inboard	D	D
	Outboard	X	X
	Inboard	X	X
	Outboard	D	D
Single Engine	Inboard	D	D
	Outboard	O	O
	Inboard	O	O
	Outboard	D	D
Fixed Core	Inboard	D	D
	Outboard	O	D
Double Engine	Inboard	D	D
	Outboard	D	D

at either inboard or outboard and held constant. The double engine is the case where a new engine is sized for both conditions. In each of these cases, there is a design rule required for the analysis because the size of the propulsors with respect to each other are not fixed. Therefore, a new variable is defined and called the "mass flow ratio" or MFR, which is not to be confused with the ratio of free-stream tube area to capture which is sometimes called the mass flow ratio. The MFR is defined as the ratio of the mass flow of the outboard engine to the inboard engine and is considered a cycle parameter.

$$MFR = \frac{\dot{m}_{outboard}}{\dot{m}_{inboard}} \quad (80)$$

It is worth noting that other design rules could be used, such as the ratio of the thrusts, which would effectively represent the same thing, but it is easier from a practical standpoint to fix the mass flows of the engine, since mass flow demand is typically an independent parameter while thrust is a dependent result of the cycle analysis. By using the MFR as the design rule, the mass flow of one engine can be varied to satisfy the thrust matching relation, and the other engine mass flow can be set to a value for each pass through the model based on the MFR.

The research question for this section of the thesis pertains to which of the above options is preferable for this application. Chapter 5 will discuss the modeling setup and implementation of the 3-Engine N2A cycle analysis, as well as the architecture integration phase setup. From this analysis, general conclusions about choices of design options and design rules for other systems will also be made.

Research Question 4: For BLI propulsion systems, which design options provides the largest benefit?

Observations and Hypothesis 4

A hypothesis in regard to research question 4 can be made by reiterating the conclusion from : namely that the performance of the engine changes significantly with the ratio of the boundary layer to inlet height, and that this can be controlled for each propulsor by varying the mass flow ratio. Having the extra independent mass flow ratio variable allows the designer to match each propulsor to the appropriate boundary layer to height ratio. However, as discussed previously, there may be countervailing factors that prevent one or more of the propulsors from being sized to a particular level.

One such potential factor is the existence of significant size effects for gas turbine engines, and specifically the gas turbine core. Scaling down the core size can tend to exacerbate tip clearance losses and Reynold's effects. Thus, making the gas turbine core very small at its design point by varying the mass flow ratio will have a significant impact on the performance of the core.

Another potential factor which can effect the gas turbine core is flow mis-match which could happen in the case of the fixed core design option. If the outboard and inboard engines are designed to the same bypass ratio, then the core will need to be "over" or "under" sped in relation to the design point. This can have a significant impact on the efficiency of the core and the pressure ratio at which it operates. As such, the following hypothesis is developed based on the above reasoning.

Hypothesis 4: The mass flow ratio degree of freedom can improve the performance benefit of the canonical BLI propulsion system.

3.2.3 Vehicle Matching Phase

The point of the vehicle matching phase is to determine the flight conditions for which the propulsion system need to be designed and which therefore need to be included in the MDP analysis. This section will outline the basic requirements for including a flight condition within the MDP analysis, and also outline a method for finding the flight conditions in the most efficient way for a given set of requirements. Research question five is formulated with respect to this phase of the analysis:

Research Question 5: What flight conditions are necessary to include for sizing BLI systems in a MDP cycle analysis?

In general, sizing points need to be included in the MDP analysis if some aspect of the design at that point will constrain or place more demand on the system. For instance, it is common to include both top-of-climb (TOC) and take-off (TKO) conditions in an MDP, since TOC places a significant mass flow demand on the system while TKO (especially for a hot day) is the hottest point of operation and therefore sizes the cooling flow which impacts the overall required mass flow and fuel consumption rate. Looking at the MDP analysis, there are two ways to include flight conditions in the analysis: constraint points or target points. For the latter, thrust or cycle targets are precisely met, while constraint points merely constrain some aspect of the system at that point. For BLI, the thrust or power balance requirement is precisely the same as for a podded system, though the thrust target point may not necessarily be the same as the typical top-of-climb position. While distortion concerns can be important for podded subsonic inlets, it is not often considered to impact the choice of propulsion system design, but rather impacts the final stall margin stack-up of the fan. The increased inherent distortion for a BLI system places an additional requirement for a BLI system which must be included in the MDP analysis.

Thrust Sizing Condition

Consider the un-installed thrust of an isolated, ducted fan propulsor:

$$T = P_k - \phi_{jet} = \dot{m}(V_j - V_\infty) \quad (81)$$

Now, define the installation losses of a propulsor in relation to the un-installed thrust value:

$$\phi_{inlet} = \frac{F_{loss,inlet}}{T} = \frac{\Phi_{Inlet}}{T \cdot V_\infty} \quad (82)$$

$$\phi_{Nozzle} = \frac{F_{loss,Nozzle}}{T} = \frac{\Phi_{Nozzle}}{T \cdot V_\infty} \quad (83)$$

The installed net thrust of the propulsor is then:

$$F_n = T \cdot (1 - \phi_{Nozzle} - \phi_{Inlet}) = \dot{m}(V_j - V_\infty) \cdot (1 - \phi) \quad (84)$$

Where ϕ is the sum of the inlet and nozzle loss percentages. For a given fan pressure ratio, increased inlet and fan losses will required a larger propulsor mass flow. Setting Eq. 84 equal to the net thrust required of the vehicle, we get:

$$TV_\infty \cdot (1 - \phi) = (DV_\infty + Wh) \quad (85)$$

and the mass flow required for the engine is then:

$$\dot{m} = \frac{D + Wh/V_\infty}{(F_n/\dot{m})(1 - \phi)} \quad (86)$$

This can be corrected to sea-level by using the parameter $\delta = P_t/P_{sl}$ and $\theta = T_t/T_{sl}$.

$$\dot{m}_c = \dot{m} \cdot \frac{\sqrt{\theta}}{\delta} = \left(\frac{D + Wh/V_\infty}{\delta} \right) \cdot \left(\frac{1}{1 - \phi} \right) \cdot \left(\frac{1}{ST_c} \right) \quad (87)$$

Where ST_c is the corrected specific thrust given by:

$$ST_c = \frac{F_n}{\dot{m}\sqrt{\theta}} \quad (88)$$

The corrected specific thrust is mainly a function of the engine/propulsor type, cycle parameter choices, and flight condition. The general trend of specific corrected

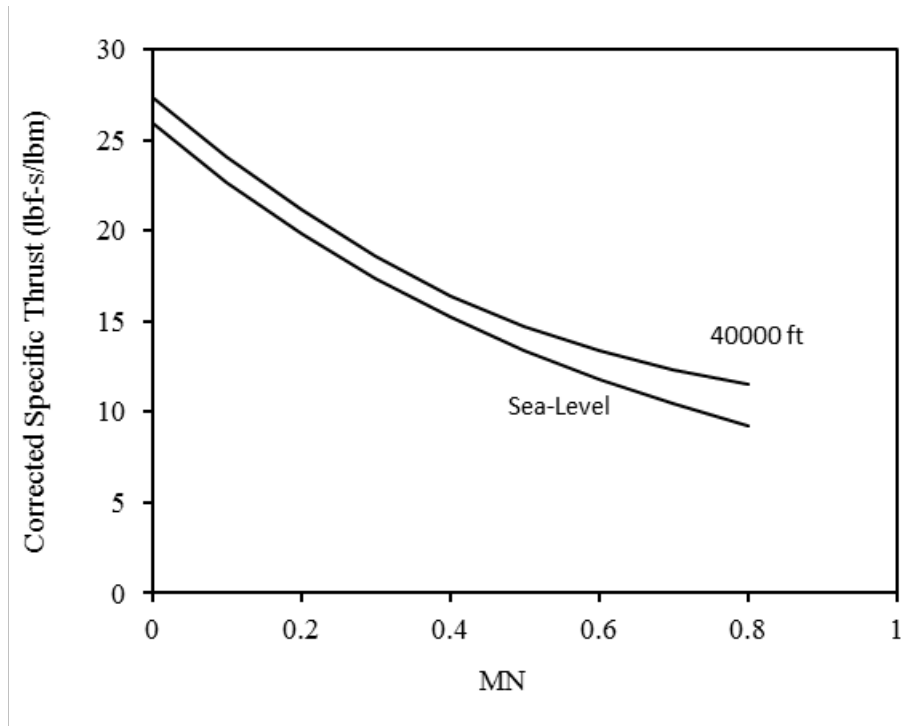


Figure 35: Turbofan specific thrust vs. Mach number for different altitudes.

thrust for a commercial turbo-fan engine is shown in figure 35 showing a significant fall at very high Mach numbers such as at the top-of-climb flight condition. The first term in Eq. 87 represents the corrected thrust required to power the vehicle. Through the course of the mission of a typical commercial vehicle, the Mach number will obviously increase significantly at cruise flight speeds and the lift coefficient will decline significantly as the weight and lift required is decreased. The net result is that the corrected thrust required changes over the course of the mission and is generally decreased as the engine moves to top-of-climb. However, this is not enough to offset the significant decrease in the thrust per unit mass flow delivered at higher flight velocities. The top of climb condition is therefore typically used to size the mass flow of typical turbofan engines.

The loss term $\frac{1}{1-\phi}$ can also influence this balance. If the losses are significant enough at any flight condition, it's possible that this could offset the loss in specific corrected thrust in the final term.

BLI Case

For BLI, the primary difference is that there is now a benefit term represented by the thrust saving coefficient, as derived previously.

$$F_n = T \frac{(1 - \phi)}{1 - TSC} \quad (89)$$

From the previous analysis, Eq. 87 can be updated to include the thrust saving coefficient due to the boundary layer ingestion.

$$\dot{m}_o = \left(\frac{D + Wh/V_\infty}{\delta} \right) \cdot \left(\frac{1 - TSC}{1 - \phi} \right) \cdot \left(\frac{1}{ST_c} \right) \quad (90)$$

This means that the critical flight condition may potentially change depending on the ratio of the boundary layer benefit to losses represented by the second term of Eq. 90. It also potentially means that the critical mass flow sizing condition could be dependent the amount of boundary layer ingested, which was seen previously to have a significant impact on the system TSC and losses.

Futhermore, this shows that the BLI engine will have a fundamentally different lapse profile with respect to a podded engine to the change in the amount of wake recovery that occurs as the Mach and Reynolds number is changed during the flight. This could potentially have an impact on the optimal flight path that the vehicle might take, implying that a much tighter coupling between vehicle and propulsion system designers must take place for commercial BLI systems which ingest significant amounts of boundary layer.

Inlet Sizing

In order to meet the thrust demand for the vehicle, the engine intake must be sized so as to supply adequate flow capacity. For subsonic inlets, this must be done while maintaining a reasonably low Mach number at the throat of the inlet to prevent transonic effects and lip separation. The maximum inlet throat area required for a

podded subsonic engine (from Mattingly [63]) is as follows:

$$A_{th,max} = \left(\frac{\dot{m}_o \sqrt{T_{to}}}{P_{to}} \right) \left(\frac{1}{MFP@M_t} \right) \quad (91)$$

The first term in the above equation on the right hand side is the maximum corrected flow requirement, and the second term is the mass flow parameter, given by eq. 92.

$$MFP(M) = \sqrt{\frac{\gamma}{R}} M \left(1 + \frac{\gamma - 1}{2} M^2 \right)^{-\frac{\gamma + 1}{2(\gamma - 1)}} \quad (92)$$

The free-stream to capture area ratio is then as follows, taking into account the contraction ratio of the inlet lip from capture to throat:

$$\left(\frac{A_c}{A_\infty} \right) = \left(\frac{A_{th}}{A_\infty} \right) \left(\frac{A_c}{A_{th}} \right) = \frac{MFP(M_\infty)}{MFP(M_t)} \left(\frac{A_c}{A_{th}} \right) \quad (93)$$

With BLI, there is some blockage in the inlet which must be accounted for, and the equation becomes:

$$\left(\frac{A_c}{A_\infty} \right) = \frac{MFP(M_\infty)}{MFP(M_t)} \left(\frac{A_c}{A_{th}} \right) \left(\frac{1}{1 - B} \right) \quad (94)$$

The blockage here obviously depends on the character of the boundary layer coming in and its relative size to the inlet height. There are then two important points to make: first, that the critical sizing condition is blockage dependent, with more blockage requiring a larger throat area to prevent boundary layer induced choking; second, that this depends on the flight condition and the sizing method used therefore needs to account for the fact that the capture area must be sized properly for all conditions.

Stall Margin Condition

Consider a fan operating at some pressure ratio (PR) and corrected flow ($W_c = W \cdot \frac{\sqrt{\theta}}{\delta}$) and exhaust area A_e . As the ambient conditions and throttle change, the area must necessarily remain constant. Given this, Eq. 95 shows a relationship between the constant area, the ambient conditions, and the nozzle exit velocity.

$$A_e = constant = \frac{W}{\rho_e u_e} = W \cdot \frac{\sqrt{\theta}}{\delta} \cdot \frac{1}{M_e} \quad (95)$$

From Mattingly [62], the equation for the fan exhaust stream is given by:

$$M_e = \sqrt{\frac{2}{\gamma - 1} \left(\pi_r \pi_d \pi_f \pi_{fn} - 1.0 \right)} \quad (96)$$

Where π_d is the diffuser pressure recovery, π_f is the fan pressure ratio (a.k.a FPR), π_{fn} is the fan nozzle duct pressure drop, π_r is the ram recovery term given in Eq. 97, and γ is the ratio of specific heats.

$$\pi_r = \left(1 + \frac{\gamma - 1}{2} M_o^2 \right)^{\frac{\gamma}{\gamma - 1}} \quad (97)$$

Clearly, two factors are of major importance in determining the flow required for a given nozzle exhaust area, which are the fan operating pressure ratio and the flight Mach number. At hot day TKO, the flight Mach number is substantially reduced relative to cruise or TOC, and the nozzle becomes unchoked ($M_e < 1$). This forces a decrease in flow (and therefore RPM) for a fixed fan pressure ratio. For a fixed corrected speed ($N/\sqrt{\theta}$), there is an increase in pressure ratio and decrease in flow. This necessarily moves the fan closer to the stall line.

The other major factor is the design pressure ratio of the fan, which substantially increases the BPR of the engine – something typically desirable for efficiency. From Eq. 96, the Mach number at the nozzle exit will decline significantly for lower π_f (higher BPR). The impact of both flight condition and choice of engine BPR for a typical turbofan engine is shown in figure 36, where the operating line at hot day TKO and higher bypass ratio is much more stall critical.

BLI Case

For BLI, the limiting stall condition will be that flight point where the fan operating line moves closest to the stability line after modification from the BLI related distortion. If any point is predicted to have a lacking stability margin after distortion is accounted for, then additional margin must be added to compensate. This must be

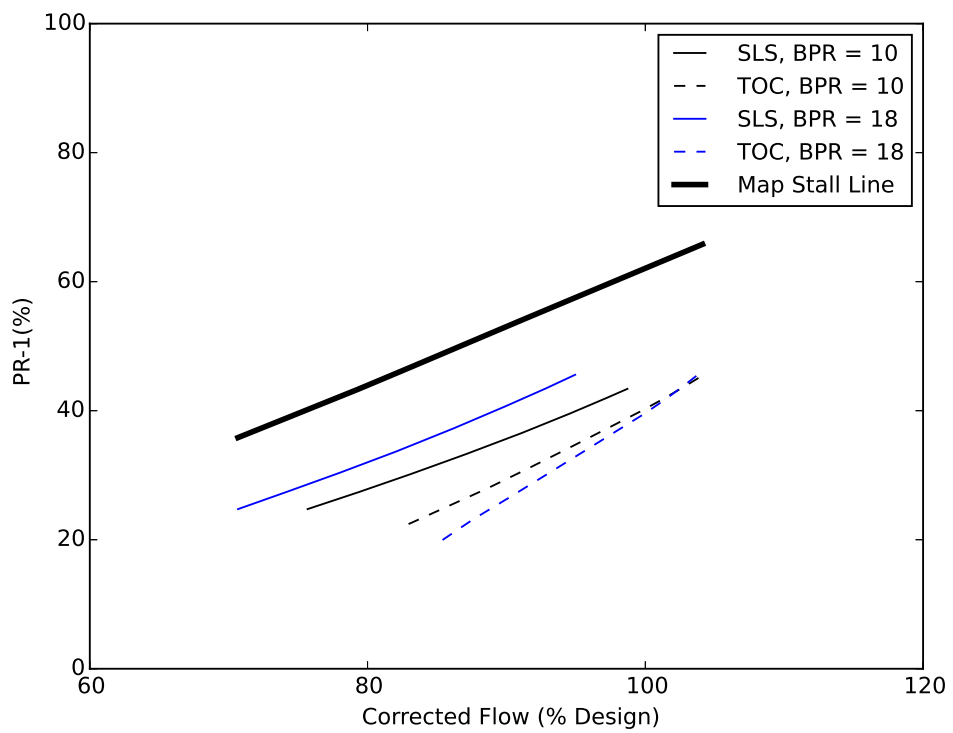


Figure 36: Commercial turbofan variation in fan operating line with flight condition. Trends show that SLS hot day is critical and is worse at higher BPR.

done by either mitigating the effects of the distortion on the system or by modifying the fan exhaust area to move the operating line farther from the stability limit.

So, while the basic trend for a turbofan engine is that stall is generally much more critical at sea-level TKO conditions, the increased distortion at higher Mach numbers could make flight speeds at high power more critical. Conditions which require very high angles of attack should also be considered such as take-off and landing where large amounts of lift is required and the engines are generally at worse stall margin anyway. Cycle choices, such as the fan pressure and bypass ratios, will have also a significant impact on both the stall margin variation over the flight envelope, the amount of distortion ingested, and the stall margin loss due to distortion. As such, one major claim of this thesis is that the most critical stall condition for a given vehicle and requirements set cannot necessarily be assumed known prior to conducting the analysis. The following section discusses the potential ways this problem might be dealt with and discusses the reasoning for choosing the method implemented in the BLIPSS methodology.

Options for Determining Flight Conditions

The analysis from the previous sections showed that both the thrust target point and stall margin (distortion) constraint point for a BLI system might vary significantly depending on the choice of cycle design, the level of boundary layer ingested, and the flight requirements imposed on the system. One option for finding these conditions would be to check every single off-design flight condition within the mission flight envelope – illustrated in figure 37. The problem with this is that it violates the purpose of the MDP methodology to begin with: to reduce the amount of design iterations needed to converge on the required engine size. Depending on the complexity of the cycle model, it may take many iterations and off-design cycle analysis runs to finish this process.

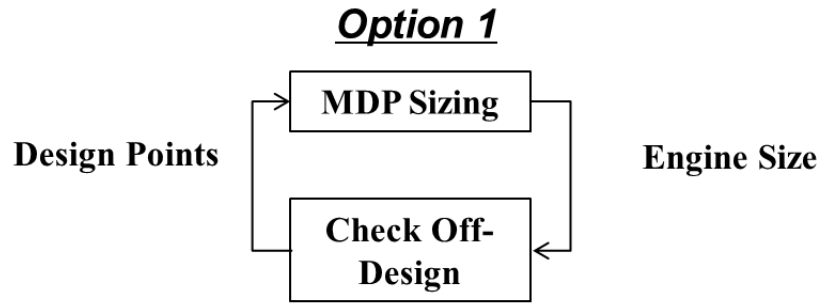


Figure 37: Option 1 of 3 for determining the flight conditions where all off-design conditions are checked and iterated with the MDP sizing procedure.

The second option for determining the flight conditions would be to include every condition in the multi-design point process as in figure 38. Given that there may be many conditions to check if the entire mission envelope is included, this would place an unmanageable level of program complexity on the cycle designer and may have convergence issues if a single initial iterate is used. The final option, as illustrated in

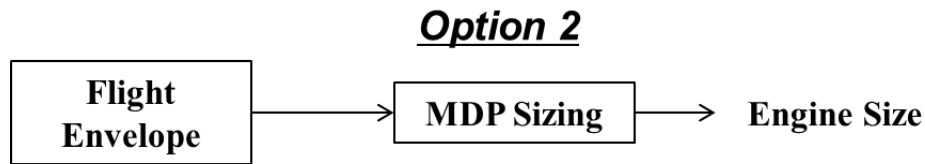


Figure 38: Option 2 of 3 for determining the flight conditions where all off-design conditions are included as constraint points within the MDP.

figure 39, is to assume that some subset of the total flight condition set will cover the majority of the critical conditions over the span of the design space. The process will then setup a screening design of experiments which represents a range of the design space to determine the likely critical flight conditions.

For screening cases, the first option is implemented and all off-design conditions are checked. For non-screening cases, off-design is not checked, and only the MDP sizing procedure is run. The final selected design can then also be run through the off-design check to ensure that it's critical sizing conditions were appropriate and that no off-design conditions have thrust or stall margin deficits. Obviously option 3 is the one

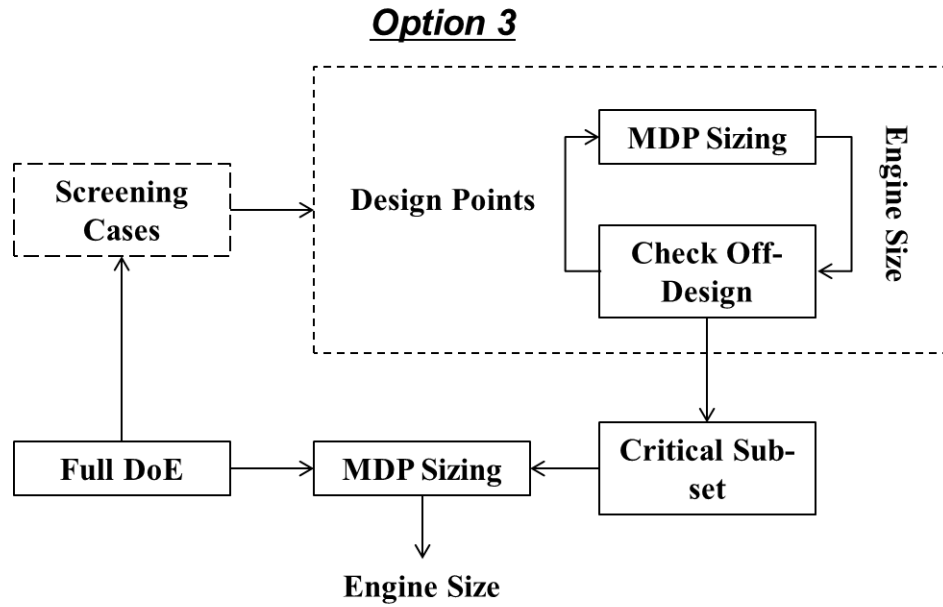


Figure 39: Option 3 of 3 for determining the flight conditions where a subset of critical conditions are identified using a screening design of experiments; all subsequent cases do not run off-design iteration checks.

that seems most viable given the above analysis and is therefore implemented in the BLIPSS methodology algorithm description in figure 11. To verify that this process is acceptable, the following hypothesis is made and will be tested thoroughly in chapter 6 with a numerical simulation and experiment on the canonical BLI problem.

Hypothesis 5: A sub-set of all thrust/stall margin flight conditions can be found that contain the most critical conditions for a large majority of the BLI conceptual design space.

CHAPTER IV

BLI MODELING PHASE

In the previous chapter, the overall BLIPSS methodology was developed and hypotheses 1 and 2 were made based on observations from past literature and additional theoretical analysis. This chapter will demonstrate the BLI modeling phase, as outlined in Chapter 3, for a canonical design problem involving a hybrid wing body vehicle with boundary layer ingesting turbofan engines. The chapter will proceed according to the outline of the BLI modeling phase and the BLI component modeling process defined in Chapter 3. Furthermore, experiments intended to validate hypotheses 1 and 2 will be defined and conducted in order to justify the need for each of the components of the method and to determine which physical effects are relatively important for this canonical problem.

The chapter will first outline the baseline vehicle design and geometry and thrust requirements for the propulsion system. The baseline propulsion system will also be specified and defined in detail for purposes of comparison with the BLI designs. The BLI modeling components for the propulsion system will be defined in detail and verification/validation data will be provided to substantiate the models. Experiments 1 and 2 will be defined and the results will then be shown to draw conclusions in relation to hypotheses 1 and 2.

4.1 Baseline Vehicle

The baseline vehicle used here is very similar to the Boeing N2A-EXTE design. The vehicle is intended to carry 300 passengers and would therefore be a future potential replacement for a Boeing 777 (double aisle) type airplane. Some overall assumed

parameters for the vehicle which are relevant to the BLI problem are shown below.

Table 7: Key design parameters for the baseline HWB vehicle.

Parameter	Value
Gross Weight	536,282 lbs
Wing Span	240 ft
Max Fuel	197,000 lbs
Cruise Mach	0.84
Initial Cruise Alt	35,917 ft
Final Cruise Alt	43,000 ft
Initial Cruise L/D	21.6
Final Cruise L/D	20.0
SLS Thrust/Engine	72,605
Design Range	7530 nm
Payload	64,000 lbs

The vehicle planform geometry is shown in fig. 40 outlining the major geometric quantities which define the vehicle boundary layer scales. Note the difference between the inboard and outboard chords which vary by a factor of nearly two. This will become relevant in the results for the architecture integration phase in chapter 5. The airfoil cross-section stack-up is shown in fig. 41 for a few different lateral location on the vehicle. The thickness-to-chord ratio decreases towards the outboard wing sections, while the inner cabin section is thicker.

Figure 42 shows the drag polar for the baseline vehicle at near top-of-climb altitude of 35,000 ft. The typical lift coefficient at this point is in the range 0.21-0.22, leaving the total thrust required at about 25,100 lbs. The thrust requirements for the baseline engine are shown in table 8. The lapse rate between SLS and TOC is chosen to provide the vehicle with enough thrust at both conditions, while not over-speeding the engine

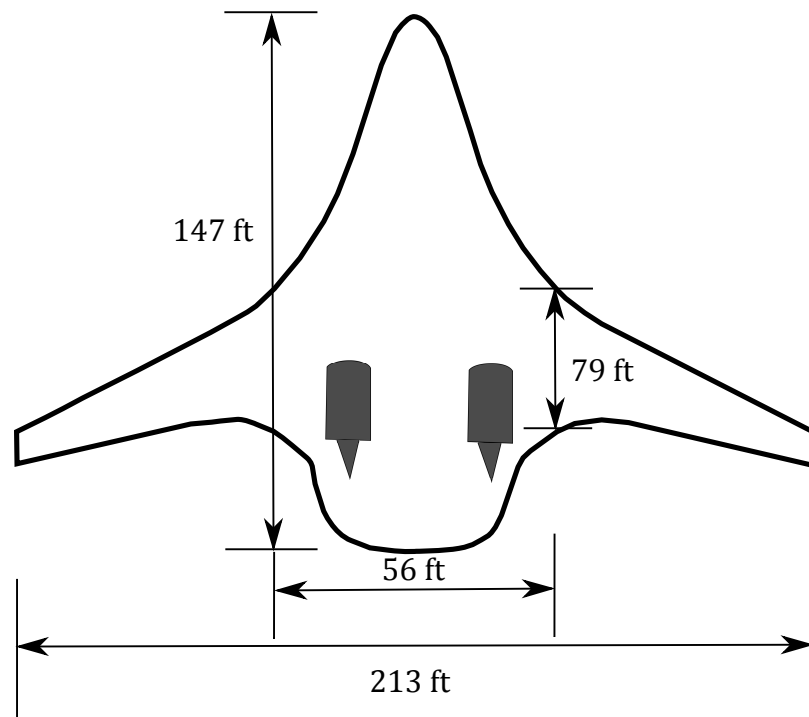


Figure 40: HWB baseline key design dimensions.

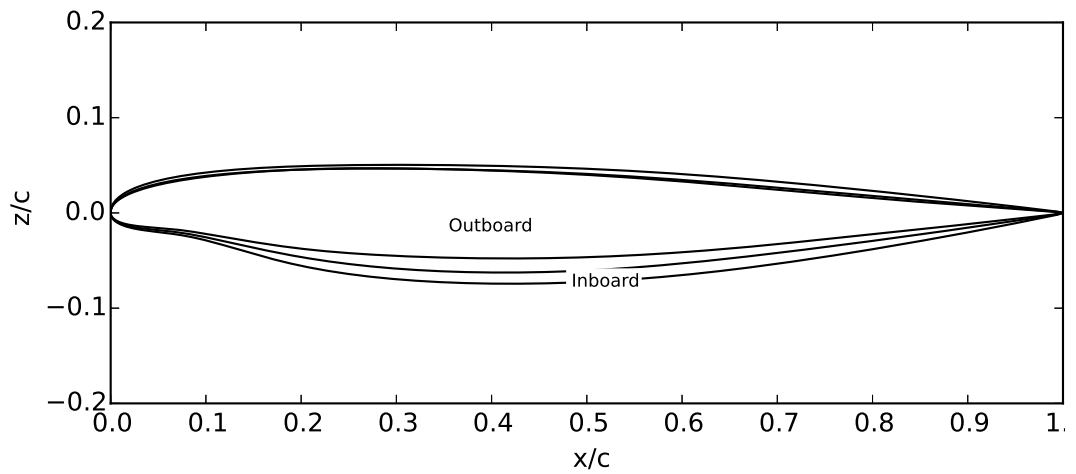


Figure 41: HWB baseline airfoil stackup.

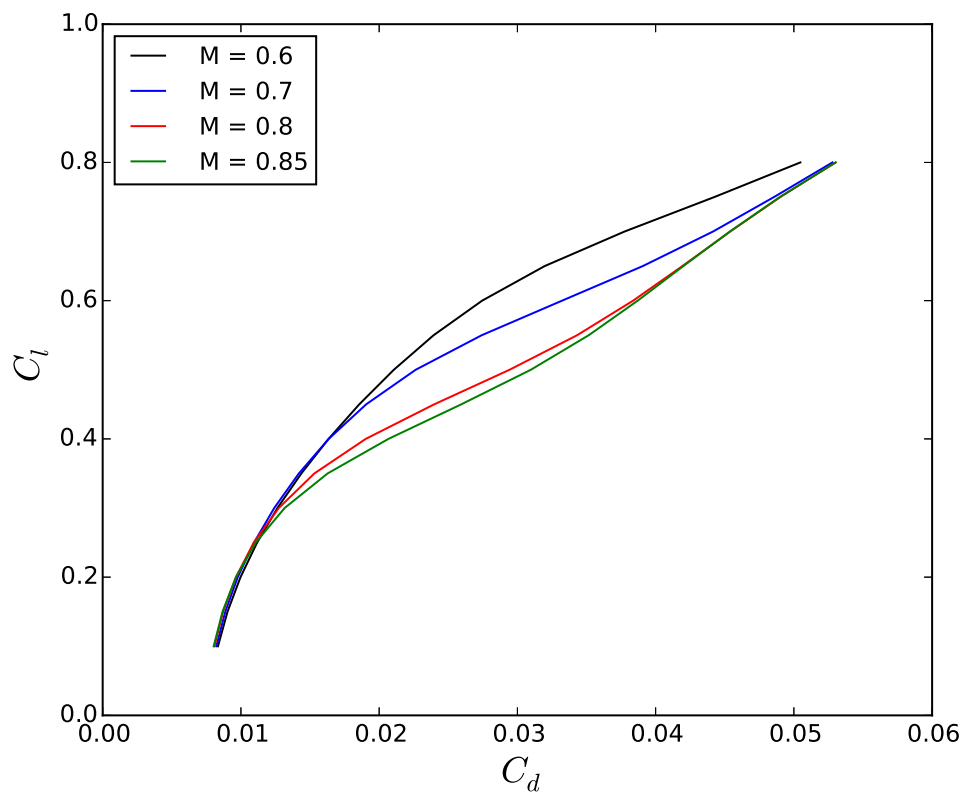


Figure 42: HWB baseline vehicle drag polars; Altitude = 35,000 ft

Table 8: Engine thrust requirements for the baseline vehicle.

Parameter	Value
TOC	15357 lbs
SLS	72605 lbs
SLS Hot Day	72605 lbs
TKO Hot Day	58502 lbs

too much at the TOC condition and meeting the TKO maximum temperature limit.

4.2 Baseline Propulsion System

The baseline propulsion system architecture comprises two typical high-bypass ratio geared turbo-fans mounted on engine pylons and are considered to be isolated engines (no BLI). The baseline engine architecture schematic is shown in figure 43.

The baseline model is built in the Numerical Propulsion Systems Simulation tool (NPSS) [2] [1] [41], originally developed by NASA and now sold commercially. This tool is the standard for the gas turbine industry for cycle analysis and is used widely within NASA as well. NPSS allows for the construction of generic architectures from simple “elements” which represent the basic thermodynamic components shown in fig 43.

The level of technology used for this engine is in the N+2 time-frame (2020) [81], and is therefore representative of expected future gas turbine technology within the next few decades. Parameters for the engine design point efficiencies and pressure drops at the design point are shown in tables 9 and 10 respectively.

Table 9: Baseline component efficiencies

Efficiency	Value
Fan	0.9345
LPC	0.8989
HPC	0.88
Burner	0.997
HPT	0.9251
LPT	0.9376

The baseline level of technology used relates to the allowable levels of temperatures and rotational speeds within the engine. The maximum T_4 – typically at HD TKO

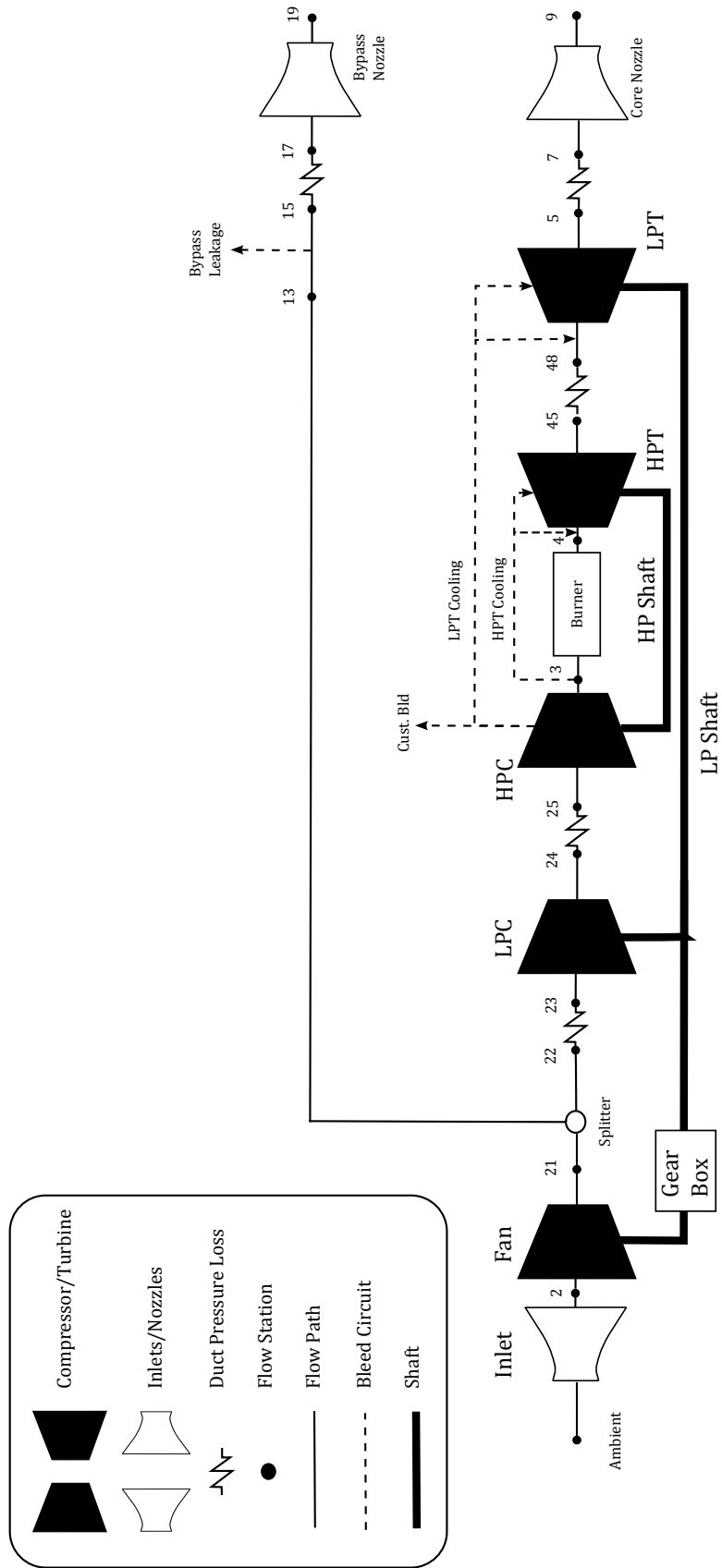


Figure 43: Baseline propulsion system block diagram.

Table 10: Baseline duct pressure drops

dP Norm	Value
LPC	0.0102
Burner	0.04
IC	0.0083
IT	0.0095
Bypass	0.0180
Core	0.007

condition – is assumed to be 3450(R) and likewise the T_{41} requirement is similarly set and generally sizes the cooling flows. The maximum allowable T_3 is based on current materials used for the latter stages of the HPC. The maximum allowable over-speed, typically used at TOC, is set at 109% speed and is selected with a desired ADP to TOC ratio of 103% corrected flow.

The primary cycle design variables for the system are the overall pressure ratio and the fan pressure ratio. The HPC pressure ratio is fixed to a constant value at design, and the LPC pressure ratio is varied to match the chosen OPR of 42.8 (chosen to maintain reasonable T_3 values).

Fan Design

The tool used to define the fan is the NASA program CMPGEN, which generates fan performance maps based on a set of design inputs [14]. The fan design inputs for the baseline propulsion system model are the design point efficiency, tip speed, and fan specific flow. The efficiency and tip speed are related to the design fan pressure ratio, since spinning the turbo-machinery faster generally increases the fan pressure ratio but also produces more tip losses due to higher speed aerodynamic losses.

For the set of experiments designed to test the hypotheses, the fan design point

Table 11: Baseline technology parameters and design variables

Name	Description	Value/Range
FPR	Fan Pressure Ratio (P_{21}/P_2)	1.25-1.65
OPR	Overall Pressure Ratio (P_3/P_2)	42.8
EXTR	Extraction Ratio (P_{18}/P_8)	0.9-1.6
HPCPR	HPC Pressure Ratio (P_3/P_{25})	29.4
Gear Ratio	Gear Ratio on the LP Spool	1-3
T_4 Max	Maximum turbine inlet temperature	3450 °R
T_3 Max	Maximum HPC exit temperature	1800 °R
Fan N_{cMap}	Maximum Fan Corrected Speed	1.09(% of Design)

efficiency will be assumed to be held constant and does not vary with the design pressure ratio. This is done to isolate the effects of the BLI models on the cycle performance by reducing variability due to other physical effects. For the final design study in chapter 7, the correlation below will be used to relate the fan pressure ratio to the design point efficiency :

$$U_{tip} = -508.1708 \cdot FPR^2 + 2968.65 \cdot FPR - 2243.749 + \Delta U_{tip} \quad (98)$$

$$\eta_p = (-1.67547 \cdot 10^{-8}) U_{tip}^2 - (4.58201 \cdot 10^{-6}) U_{tip} + 0.9505 + \Delta \eta_p \quad (99)$$

$$\eta_f = \frac{(FPR^{\frac{\gamma-1}{\gamma}} - 1)}{(FPR^{\frac{\gamma-1}{\eta_p \gamma}})} \quad (100)$$

The $\Delta \eta$ parameters in Eqs. 98-100 are included to calibrate the efficiencies – which tend to improve over time – to a given technology level. For a baseline FPR of 1.4, the design point efficiency calculation is 0.9345 for the assumed technology level here. This value will be used for the hypothesis tests in chapters 4-6. For the specific corrected flow of the fan – fan corrected flow normalized by the annulus area – a value of 44.0 lbm/sec-ft² will be used, which is typical for modern high bypass fans.

The fan specific flow will be held constant for all designs at this value throughout the thesis. With these parameters, the inputs to CMPGEN are specified and an unscaled base map can be generated which represents the fan compression process and its variation for different values of pressure ratio and flow. The base, un-scaled, fan map is shown in Figure 44 including efficiency rings and constant speed lines ranging from 30 to 115% of design speed. For each design, this map is scaled to meet the flow requirement and match the design point efficiency calculated from the FPR/tip speed correlations.

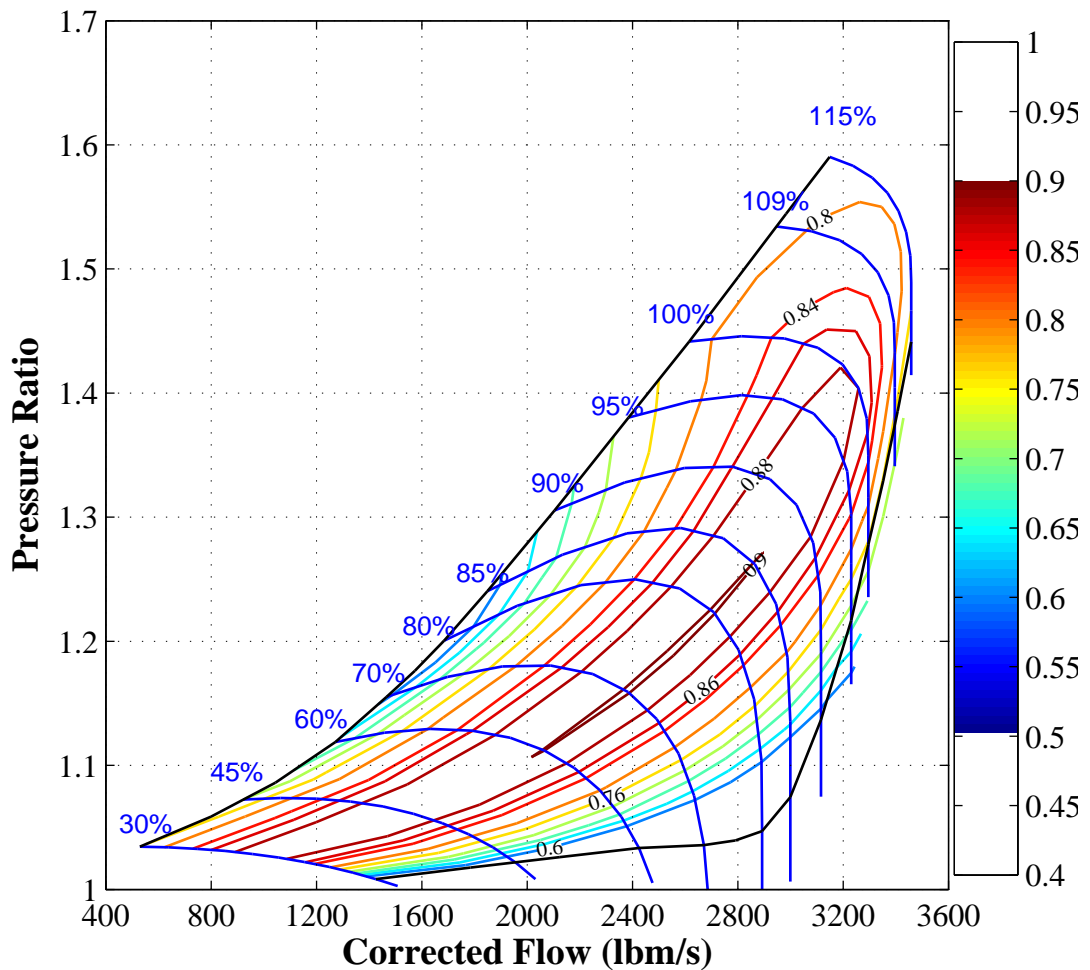


Figure 44: Baseline propulsion system fan map generated by CMPGEN

Other Component Models

Similar component models for the LPC and HPC are developed using the CMPGEN tool with other tip speed/efficiency correlations for those components. The turbine maps are notional designs for typical turbofan engines. The geared turbofan LPT has a different speed than the fan shaft, and so the efficiency calculation for the LPT is augmented using a Smith map. The remaining gas turbine baseline component models are not particularly relevant to the BLI problem or the hypothesis testing so the details are left out.

Baseline Design Points

The baseline MDP setup – shown in Table 12 – is a basic 5-point engine design. The two points which essentially size the system are the TOC and TKO design points, with the former sizing the fan flow and the latter sizing the core flow. Since the ADP is simply a reference point, but is by definition at 100% fan N_c , the W_C at TOC into the fan is specified to be at 103% of that at the cruise point. This will, in general, maintain the fan below the maximum corrected speed limit of 109%. At take-off, the engine is assumed to be at maximum rated turbine inlet temperature, and the SLS uninstalled point is similarly specified. The SLSI point includes installation penalties and must be able to produce the same amount of thrust as the uninstalled point for a hot day. The solver setup for this MDP and for the engine model is shown in appendix A.

Baseline Performance Evaluation

The cycle performance model for the baseline system was evaluated for varying cycle parameters as shown in table 11. The results in Fig. 45 show that an optimum occurs at the point $FPR = 1.37$ and extraction ratio of 1.38. These TSFC numbers were calculated assuming a constant cruise thrust evaluation point. As the FPR increases,

Table 12: Initial baseline design points for the MDP setup

Design Point	Mach	Altitude	Delta Temp.	Specification
ADP (Cruise)	0.8	35,000 ft	0	Fan $N_c = 100\%$
TOC	0.85	39,000 ft	0	$F_n = 15350$ lbs, $W_c/W_{c_{Des}} = 103\%$
TKO	0.25	0 ft	+27 ° F	$F_n = 58500$ lbs, $T_4 = T_4\text{-Max}$
SLSU	0	0 ft	0	$F_n = 72605$ lbs, No customer bleed, installation effects or HPX
SLSI	0	0 ft	+27 ° F	$F_n = \text{SLSU thrust}$, Includes customer bleed, installation effects and HPX, $T_4 < T_4 \text{ Max}$

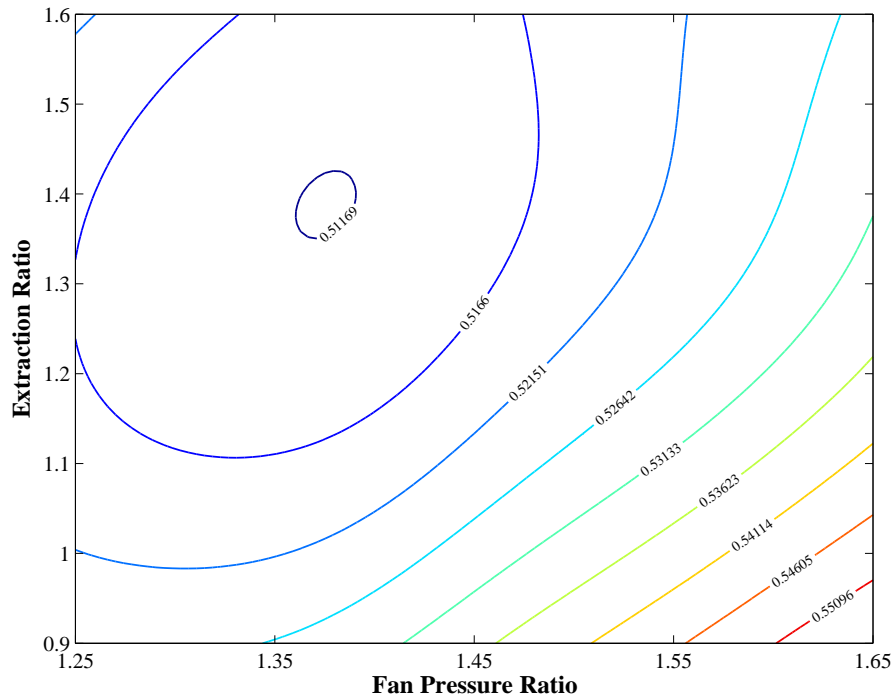


Figure 45: Baseline cycle design space showing contours of cruise TSFC vs. FPR and EXT.

the optimum extraction ratio (and bypass ratio) also decreases as shown in Fig. 46.

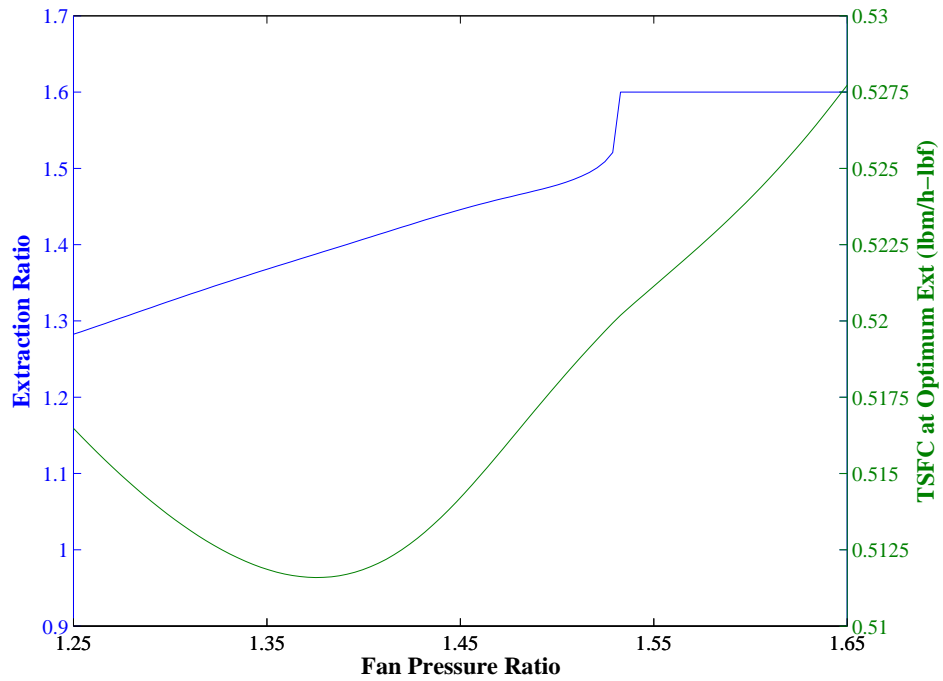


Figure 46: Plot showing optimal extraction ratio as a function of chosen fan pressure ratio.

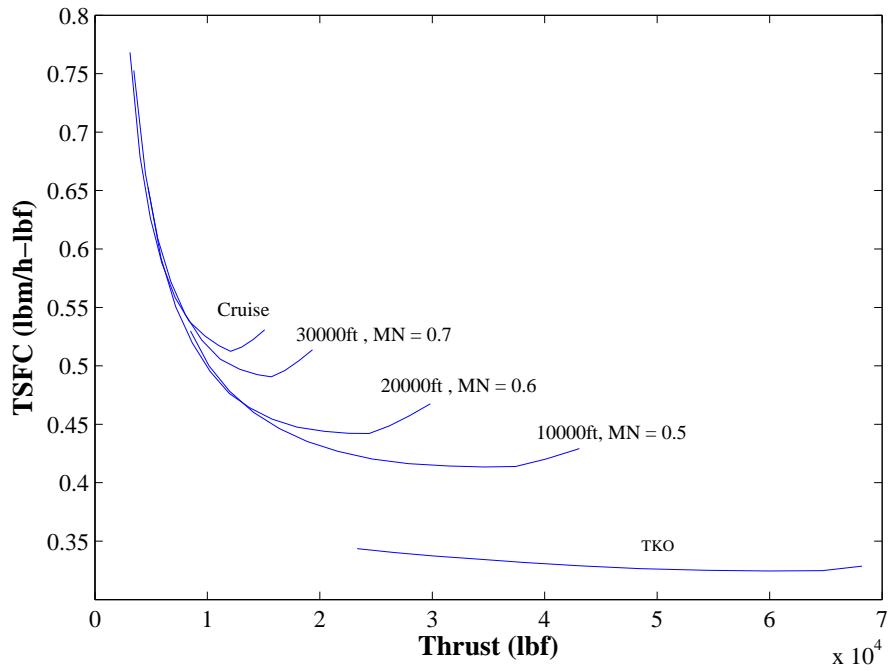


Figure 47: Baseline power hooks for several flight conditions in the mission profile.

Since Figs. 45 and 46 only show the TSFC at the nominal cruise point, it is worth showing the off-design characteristics at the baseline for performance evaluation. Typical power hook characteristics for the engine are shown with the TSFC increasing significantly at both very high and low powers.

4.3 BLI Component Models

4.3.1 Modeling Domain

Now that the baseline vehicle and engine, and their performance have been established, the next basic task in the modeling phase (steps 3-10) is to define the component models which augment the basic cycle model to account for the impact of BLI. For this, the aircraft/engine physical domain is broken down into regions as shown in the 48. The fan bypass and core are taken directly from the baseline model, which is to say that the assumption for this case is that the gas turbine core is not significantly harmed by any distortion transfer into the core. Models will be constructed for each of the other domain sections to provide an estimate of the impact on the engine performance.

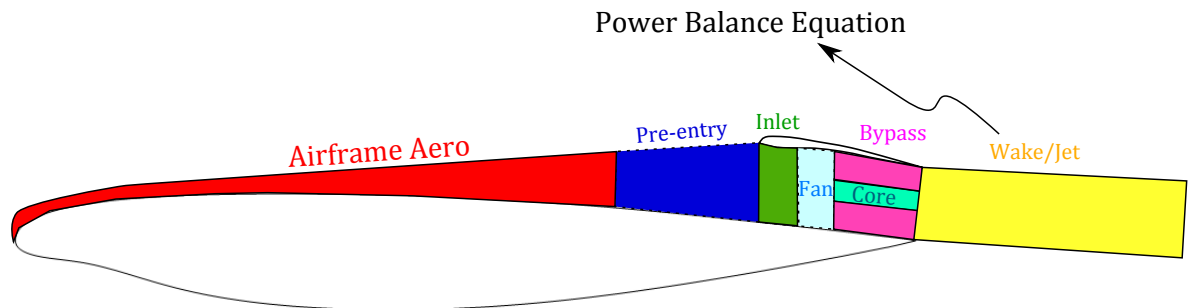


Figure 48: Modeling domain for the BLI Models.

BLI Propulsor Type

The next step of the BLI modeling phase process (step 3) is to establish the type of BLI propulsor. Clearly this vehicle is similar to a flying wing type and the BLI propulsion system type would be the C1 type (laterally distributed wake) with upper surface mounted propulsors. As such, it is necessary to carry forward the computation of the power balance terms according to the C1 equation set defined in chapter 3.

4.3.2 Airframe Aerodynamics Model

Step 4 in the BLI modeling process is to define the characteristics of the airframe aerodynamics up until the pre-entry region where the presence of the engine begins to affect the stream-tube and boundary layer. There are several approaches used within the previous literature to do this. Perhaps the most common is to use high-fidelity CFD data to define the boundary layer at various positions along the airframe. For example, Felder et. al. [47] used the curves in Fig. 49 to represent the boundary layer prior to pre-entry, which is based off of a Boeing CFD analysis of the N2A.

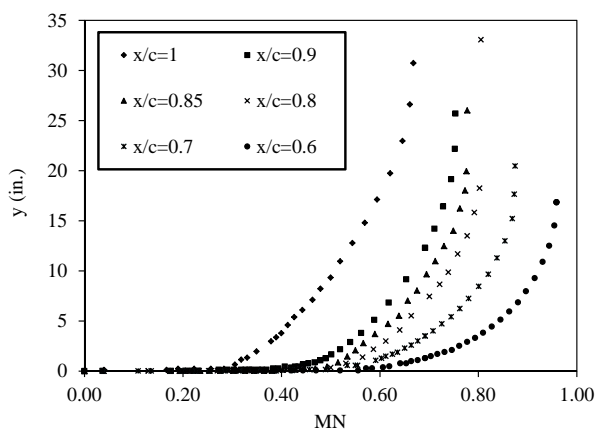


Figure 49: Boundary layer CFD data for the Boeing N2A at vehicle fuselage centerline showing multiple axial locations.

The data shows quite clearly that the edge velocity of the boundary layer in the inviscid region accelerates over the airfoil until the aft end of the vehicle when it

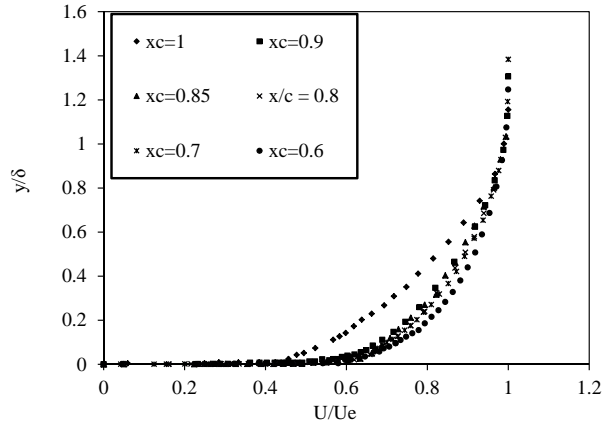


Figure 50: Boundary layer CFD data normalized by edge velocity and boundary layer thickness and showing change in shape at vehicle aft end.

significantly decelerates. The edge velocity passes the free-stream value of Mach 0.8 at the 80-85% of the centerline chord. The adverse pressure gradient associated with the fluid deceleration increases the thickness of the boundary layer and also changes its shape as shown in Fig. 50. Using this approach is appropriate for a single design point sizing or evaluation, but if one considers that the boundary layer varies as a function of the lateral location on the vehicle and with changes in flight condition, then another approach is required. However, it is expected that any tool used to predict the boundary layer properties should at least replicate the fundamental trends shown in the CFD analysis as well as a reasonable level of prediction accuracy.

Possible tools which would be useful and applicable for defining the airframe aero module would be any kind of 2-D viscous airfoil analysis code, which has some capacity to predict either detailed boundary layer profiles or overall BL properties. One such code is XFOIL [22], which is a low Reynolds number analysis tool for airfoil sections. The code predicts boundary layer properties and viscous edge velocity as a function of axial location. It can also perform the analysis for specified flight condition variation (Mach, altitude, angle of attack, etc.) and for different chord lengths, allowing for additional analysis beyond the single cruise point as required

by the BLIPSS methodology. It is also easy to implement simple interfacing with the code and to construct data tables from the output, since the BL properties are directly output. Its downfalls are that it performs poorly at predicting airfoil drag/lift at very high Reynolds number (such as the cruise/TOC points needed here), and it cannot operate when a point on the airfoil exceeds a sonic condition and therefore cannot model shockwave impacts. These deficiencies aside, it is a good choice for an initial implementation of the BLIPSS methodology because of its simplicity, and ease of use.

To show that XFOIL provides reasonable results relative to the CFD from Fig. 49, the boundary layer properties (δ^* , θ), and edge velocity have been computed for the CFD data and compared to an equivalent analysis using XFOIL. The results are shown in Figs. 51-53, and it is clear that the tool provides reasonable estimates for the vehicle boundary layer trend. The angle of attack for the CFD is unknown, but appears to be somewhere between 0-1°. The prediction of flow deceleration and boundary layer growth towards the trailing edge are present with this model and the results are accurate enough for this example problem and for the testing of the hypotheses related to the BLIPSS methodology.

The model therefore works by using a tabular data set constructed within the NPSS modeling language which is built from a huge amount of XFOIL runs over varying Mach and altitude combinations. The local conditions boundary layer properties and edge velocity are all that is required to represent the state of the inviscid and viscous flow at the point where the pre-entry domain begins.

A few further assumptions are made, such as constant total pressure in the inviscid stream. With this assumption, it is necessary to compute the edge static pressure and temperature. The specific heat at constant pressure is:

$$C_p = \frac{R\gamma}{\gamma - 1} \quad (101)$$

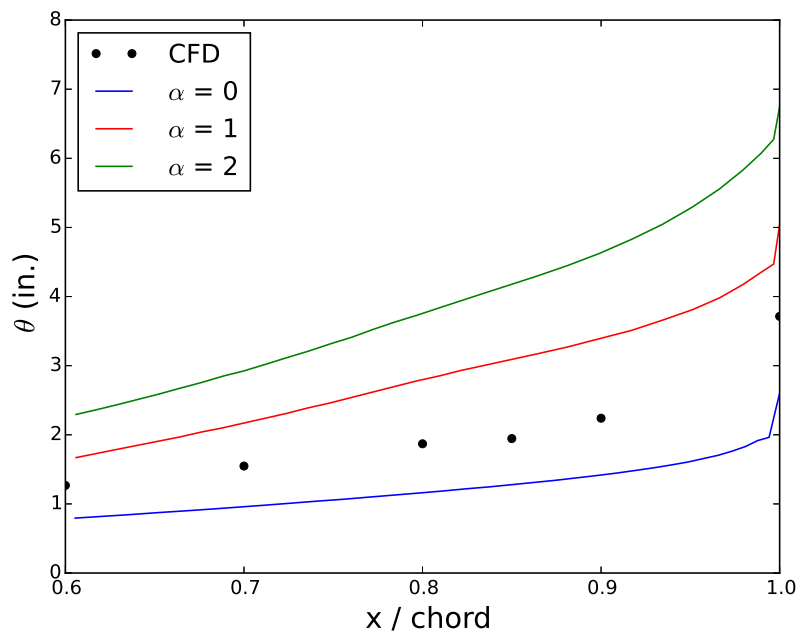


Figure 51: Comparison of XFOIL predicted θ values vs. those predicted by CFD of Boeing [47].

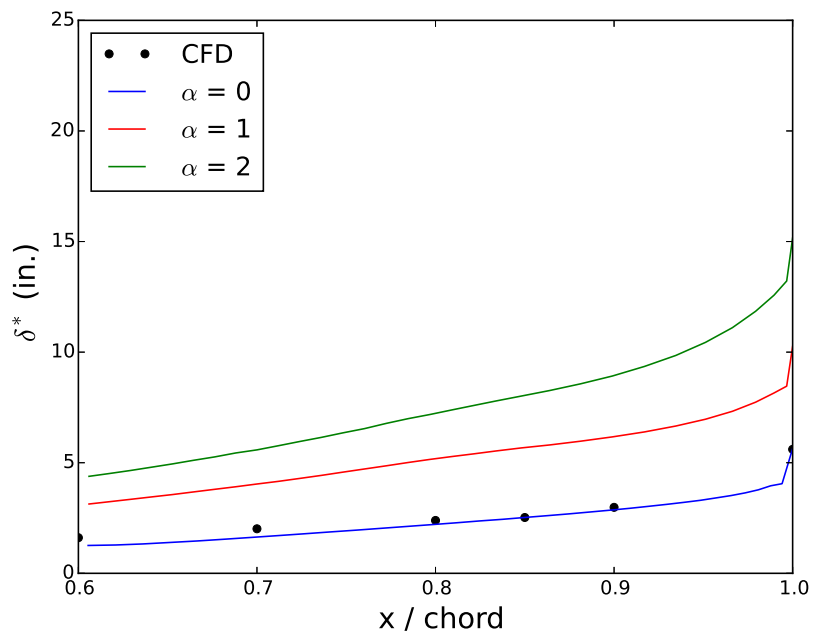


Figure 52: Comparison of XFOIL predicted δ^* values vs. those predicted by CFD of Boeing [47].

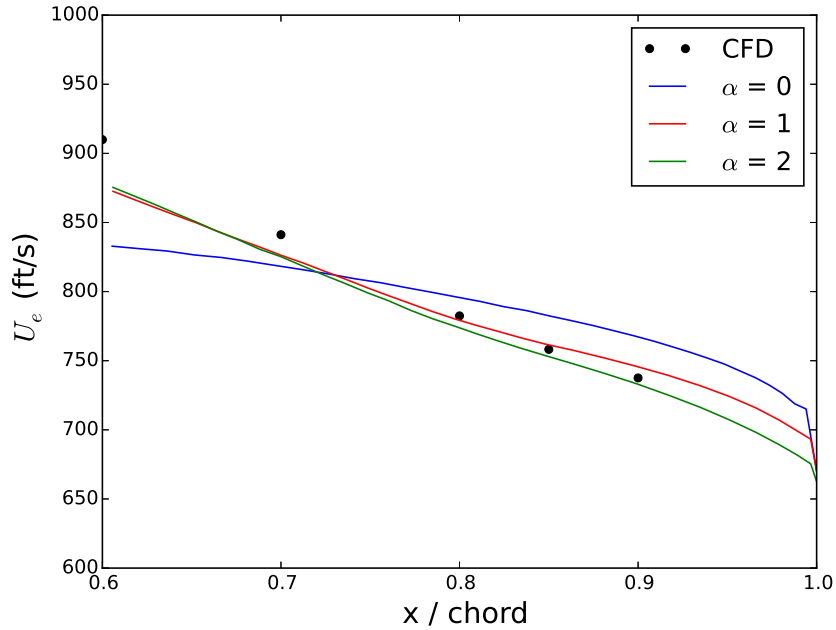


Figure 53: Comparison of XFOIL predicted edge velocity values vs. those predicted by CFD of Boeing [47].

and the local static edge temperature and resulting Mach number are:

$$T_e = T_{t\infty} - \frac{u_e^2}{2C_p} \quad (102)$$

$$M_e = \frac{u_e}{\sqrt{\gamma RT_e}} \quad (103)$$

and the edge static pressure is therefore:

$$P_e = \frac{P_{t\infty}}{\left(1 + \frac{\gamma - 1}{2} M_e^2\right)^{\frac{\gamma}{\gamma - 1}}} \quad (104)$$

Finally, the local density is computed from the state equation:

$$\rho_e = \frac{P_e}{RT_e} \quad (105)$$

The above state properties are used to compute the kinetic energy thickness factor from the local momentum and displacement thicknesses in combination with the turbulent closure relations in Appendix C. Together with the boundary layer properties and edge velocity, the assumption of constant free-stream total pressure is therefore

enough to entirely compute the state of the flow and boundary layer at the point where it enters the pre-entry region and begins to be affected by the presence of the propulsor.

4.3.3 Power Balance Model

It is now necessary to compute the power balance terms which augment the basic podded equation for the BLI case. Since this is a class 1 BLI with a laterally distributed wake, then equation 44 is useful for computing the BLI benefit term. It is necessary to estimate three parameters: the total wake KE defect at the trefftz plane “ K_∞ ”; the fraction of that defect which remains after ingestion “ ν ”; and the equivalent lateral width over which the dissipation integral is carried out “ b ”. The resulting estimate of the power balance reduction term is then:

$$\beta\Phi_p^* = (1 - \nu)K_\infty b \quad (106)$$

The total wake KE defect is computed using the XFOIL output at the Trefftz plane. The turbulent closure relations for a free-wake region are used to convert the edge velocity and BL properties (δ^* , θ) into the kinetic energy defect θ^* , and the value of K_∞ is computed from its definition (Eq. 35). Plots of the wake defect are shown for various flight conditions and angle of attacks in Fig. 54.

The parameter ν is computed by estimating the ratio of the upper surface wake to the lower wake at the trailing edge:

$$\nu = \left(\frac{K_L}{K_U + K_L} \right)_{TE} = \frac{\theta_L^*}{\theta_L^* + \theta_U^*} \quad (107)$$

Therefore ν effectively represents the proportion of the profile drag which comes from the lower surface and $(1 - \nu)$ is the upper surface proportion. Plots of $1 - \nu$ which result from XFOIL output are shown for various flight conditions and angle of attack in Fig. 55. An interesting trend is that the percentage of the Trefftz plane wake that is attributed to the upper surface doesn’t vary much over different flight conditions,

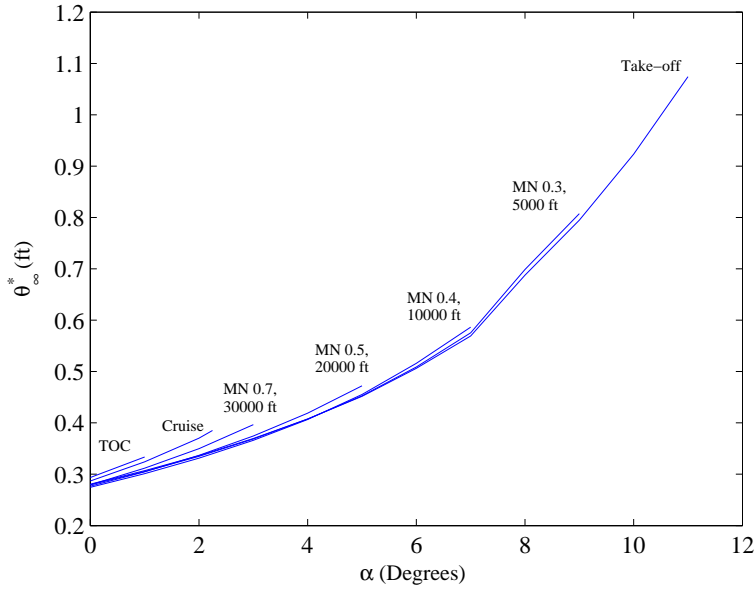


Figure 54: Plot of 1-D kinetic energy defect vs. vehicle angle of attack for centerline airfoil and for multiple flight conditions.

but varies significantly as a function of the angle of attack. This implies a large increase in the amount of available BLI for ingestion

The drag recovered from BLI per unit length is then computed according to Eq. 108.

$$\frac{D_{BLI}}{b} = \frac{\beta \Phi_p^*}{u_\infty} = (1 - \nu) \frac{K_\infty}{u_\infty} = \frac{\beta \Phi_p^*}{u_\infty} = \frac{1}{2} (1 - \nu) \rho \theta_\infty^* u_\infty^2 \quad (108)$$

This is computed for a vast array of flight conditions (Mach, altitude, α) and for several airfoils along the span-wise axis. This is kept in a data table within the NPSS model which is read and interpolated based on the input engine span-wise location and vehicle flight condition. Plots of D_{BLI}/b for many different flight conditions and angles of attack are shown below in Fig. 56. Clearly the change in free-stream dynamic pressure at cruise or TOC flight speeds has a significant impact on the amount of recoverable boundary layer. At the TKO condition, only very high angles of attack will provide substantial benefit from BLI, especially since thrust requirements at that point are quite high and therefore the benefit in percentage would be lower.

The width of the ingested stream-tube at the trefftz plane “b” is assumed to be the

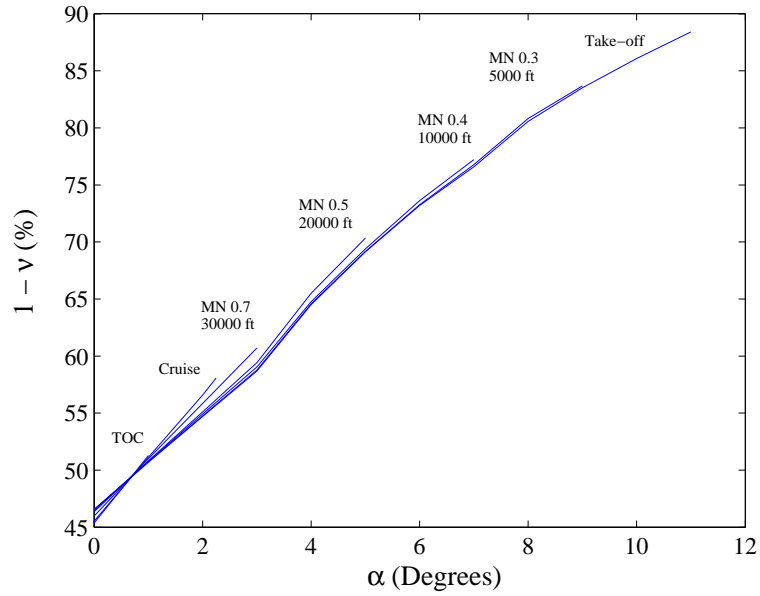


Figure 55: Upper surface defect percentage vs. angle of attack for the centerline airfoil and for multiple flight conditions.

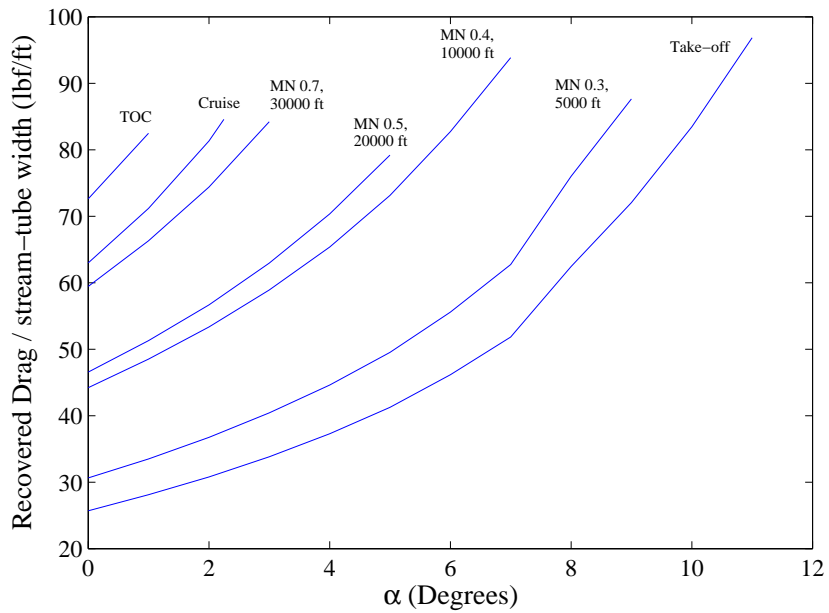


Figure 56: Plot of boundary layer drag recovery per unit width vs. angle of attack for the centerline airfoil for many flight conditions.

same as the width of the stream-tube prior to the pre-entry zone. This width is used to compute the total BLI recovery term D_{BLI} . Note that the assumption is made that over the width of the inlet, the boundary layer does not vary significantly. Strictly speaking then, this model would only be accurate for widths which are small relative to the lateral boundary layer gradient (small $\frac{\partial \theta^*}{\partial y} \cdot b$). This is an appropriate assumption for this canonical problem since inlet widths will generally be small relative to the size of the scale over which the vehicle chord changes and since centerline values will be chosen which will generally represent an average of the boundary layer over the inlet width anyway.

4.3.4 Inlet Model

The inlet model described here has two purposes: first to size or compute the required capture area for a given flow demand of the engine, and second to provide a total inlet recovery for the cycle model based on the above inlet size and definition. There have been several methods for doing this in the previous BLI system study literature. Perhaps the most relevant is the integral boundary layer method used by Plas [69]. This method allows for the computation of inlet recovery based on the progression of the boundary from some initial condition through an area change in the inlet duct. It captures the affect of both the skin friction of the inlet duct on the flow, viscid/inviscid interaction effects and influence of pressure gradient, and allows for things like the inlet length and other aspects of the design to be accounted for.

The method can also be included to account for the pre-entry zone – the region of the flow prior to entry of the inlet where the presence of the inlet forces a change in the flow. This region can have a significant impact on the character of the boundary layer change and also the inviscid flow velocity as shown by both Plas and also by the simpler model of Shedon discussed in Chapter 3. The following sections discuss the creation of a parametric integral boundary layer inlet model. This model will be

coupled to the airframe model to predict recovery as a function of the vehicle flight condition, engine power demand, and propulsion system design variable choices. This coupled model will be used to test hypothesis 1 later in this chapter.

Inlet Model Overview

A description of how the airframe and inlet model are coupled, as well as inputs and outputs are shown in fig. 57. The model is created as an NPSS "element", which is used in each representation of the inlet. The boundary layer properties from the XFOIL based vehicle model described above is used as a boundary condition to the installed inlet (IIBLT) model. This IIBLT model was created in C++ and compiled to an executable which is called by the NPSS element. The mathematical details and solution procedure are detailed in appendix C. Inputs to the IIBLT model are the inlet length, length of the pre-entry zone (in proportion to the height of capture area), and an area distribution as a function of axial length of the inlet. This area distribution defines the level of diffusion as the flow approaches the fan face.

Baseline Inlet Description

The baseline inlet used for the set of experiments in this thesis is the NASA Inlet A – or at least that area distribution will be used. The basic geometry of the inlet is shown in fig. 58 with area distribution and actual vertical coordinates vs. the normalized axial coordinate. The amount of area change from the lip to the fan face is about a 6% increase, which represents a somewhat small amount of diffusion. This is necessary to prevent excessive adverse pressure gradients and flow separation during the height transition portion. The inlet capture shape is assumed to be a D-inlet type, with an associated r^* value of 0.893 (see tab. 4 for more details). The effect of the off-set of the centerline and the curvature of the stream-lines is not modeled with the IIBLT tool since it does not capture wall curvature effects, but only area gradient effects.

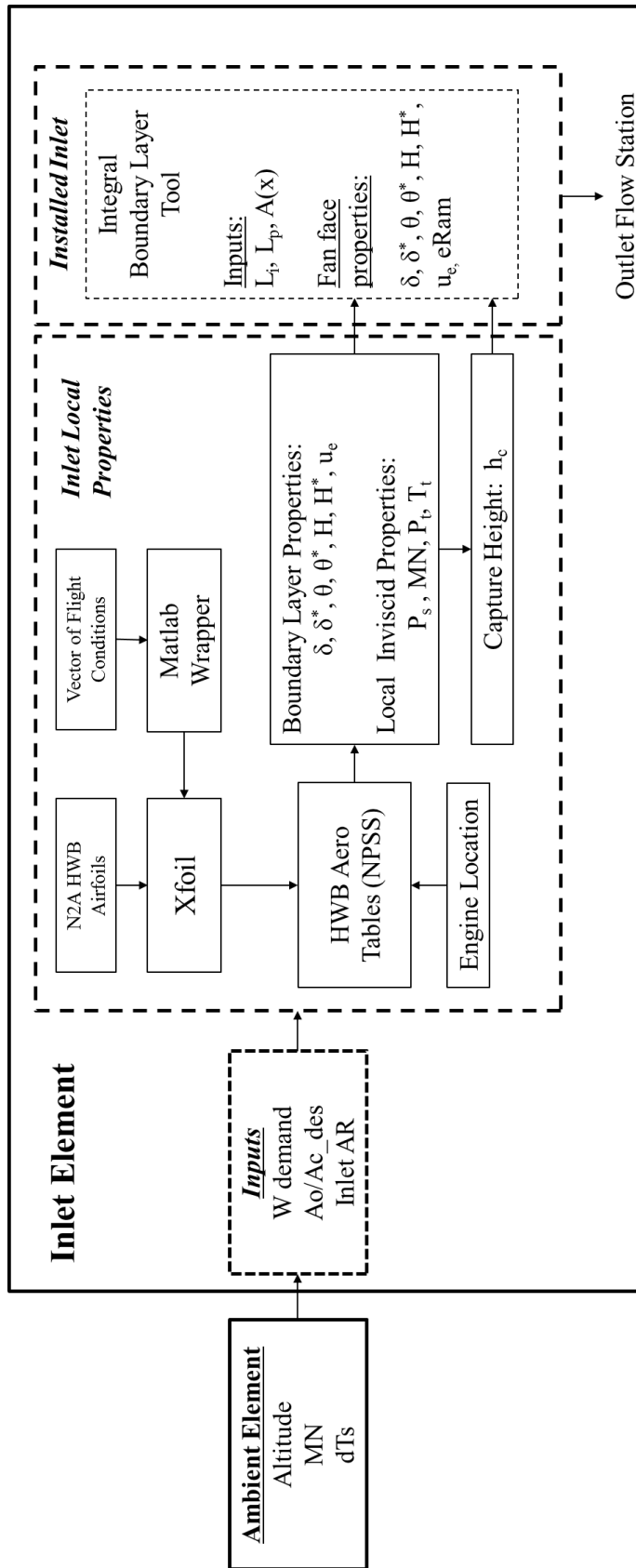


Figure 57: Coupled inlet/airframe model data flow diagram.

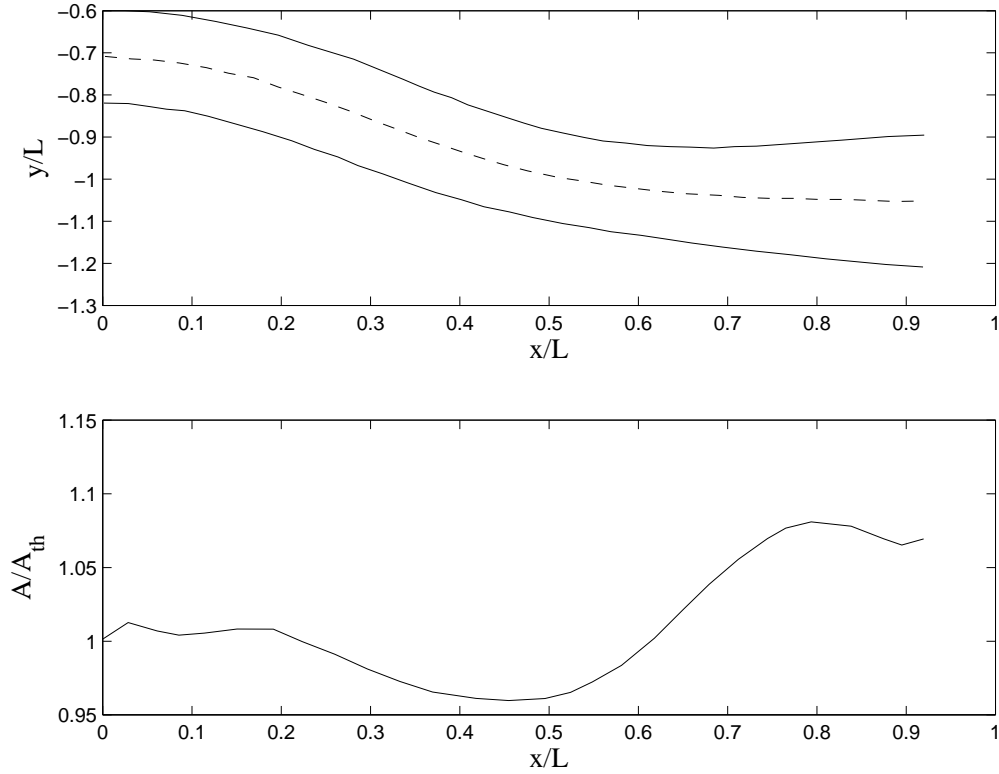


Figure 58: NASA inlet A area distribution [7].

This means that the inlet recovery estimates ought to be slightly conservative given that the secondary flow effects are not considered and included in the model.

Inlet Model Validation

A simple validation is now conducted for the IIBLT inlet model. The data to compare against for the NASA inlet A is from Berrier et. al. [8]. The conditions from each of the test cases listed in the experimental report were run through the inlet model with the exact area distribution taken from the same reference. Fig. 59 shows a comparison of the results from the IIBLT inlet model with the data for the cases of specific corrected fan flow equal to 124 and 165 $kg/s - m^2$. The results show that the trends are replicated by the IIBLT model, though there are some differences between the cases. The higher flow curve generally under predicts the experimental data. One possible cause of this is that the actual boundary layer thicknesses at the input to

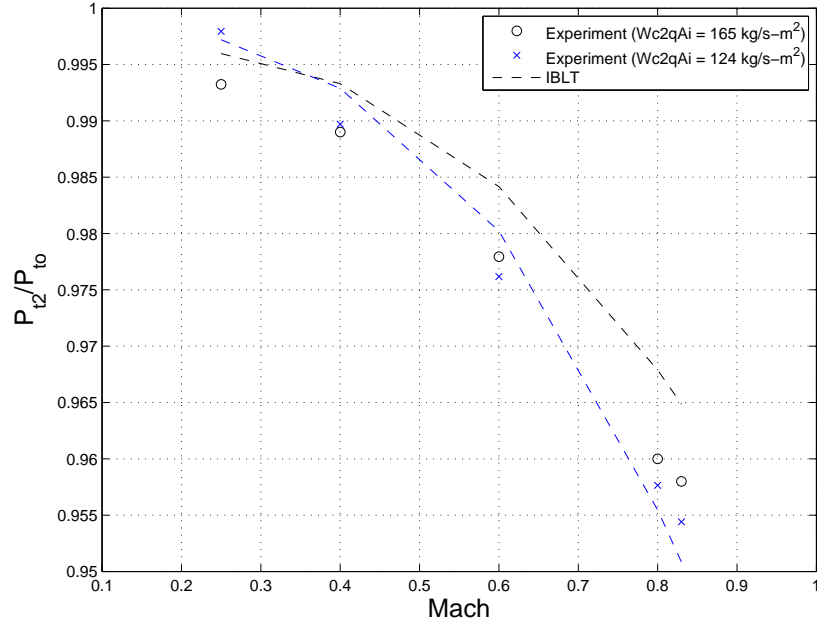


Figure 59: Comparison of inlet recovery vs. Mach trends from IBLT inlet model and experimental data of Berrier et. al. [8].

the IIBLT model domain are not known from the experiment, and only one value of nominal boundary layer thickness is given. This, however, generally changes with Mach number and therefore needs to be input specifically for each Mach number. A similar problem occurs for the lower flow points. Though again, this validation shows that the model is not by any means considered "high" fidelity, it does replicate the dominant trends in inlet recovery vs. Mach number. Furthermore, it also shows that the flow trends reverse at low vs. high Mach, with the curves crossing each other somewhere near Mach 0.4.

Fig. 60 shows trends of recovery vs. % of design flow for different fixed Mach numbers. As the flow is ramped down, the recovery falls off significantly at very high Mach, while at low speeds the trend is flattened out and nearly reversed. This happens because, at low speeds, the variation in the mass flow ratio over this range of corrected flows is significantly less than at higher speeds since the free-stream tube area A_o is much larger. Fig. 61 illustrates this by plotting the same data from fig.

60 against the inverse mass flow ratio μ . Furthermore, the data is fit using a non-negative least squares routine to the μ^3 model of Shedon for each Mach number. This chart illustrates the usefulness of the IIBLT approach, because it not only replicates trends from both theory and experiment, but is also able to provide these curves without needing input parameters – such as the skin friction coefficient – for the Shedon model.

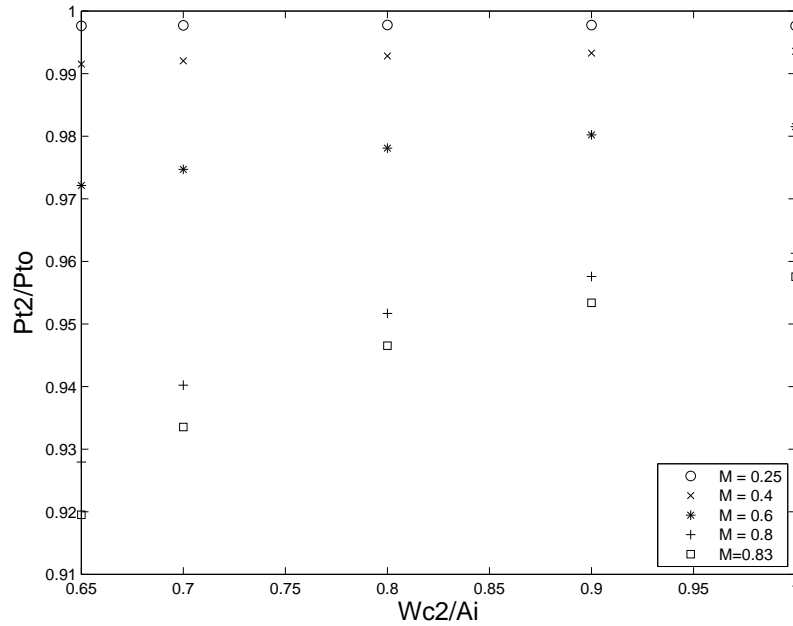


Figure 60: Trends of inlet recovery with mass flow.

Finally, we analyze the affect of the boundary layer thickness on the inlet recovery. Unfortunately, the data of Berrier – or any other study found by this author in the literature – does not provide a good basis for comparing variations of boundary layer thickness with the inlet recovery. However, we would expect that this should increase as the thickness increases from common sense and from the arguments made in Chapter 3 relating the inlet recovery at a cross-section to the kinetic energy thickness at that cross-section. Fig. 62 shows the results from the IIBLT inlet model by plotting the inlet exit recovery vs. the displacement area normalized by the inlet capture area. These trends show significantly decreased inlet recovery at higher BL thickness values

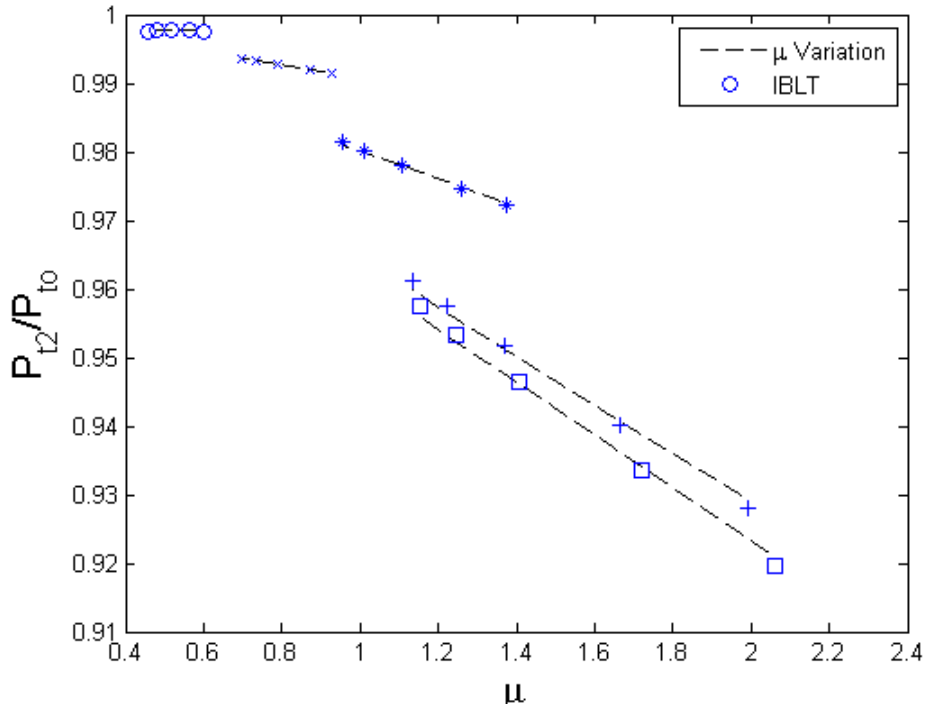


Figure 61: Comparison of flow trends and μ^3 variation least squares fit.

and that this effect is amplified significantly at higher Mach numbers (hence larger boundary layer edge velocities).

Lip Losses

In order to capture the effect of lip separation effects, especially at very high mass flow ratios, it is necessary to include a lip loss augmentation to the inlet recovery predicted by the IIBLT tool. A relatively simple approach will be used, which takes into account the experimental data in Shedon [84]. These curves give the lip loss as a function of the throat Mach number (estimated by the IBLT tool) and the mass flow ratio. These curves are shown in fig. 63, with increasing losses at higher throat Machs and mass flow ratios. The inlet lip essentially behaves like a fulcrum about which the flow pivots. The higher speed flows approach the lip with more energy and the higher flow ratios approach the lip at a greater flow angle since the engine is having to suck the air downwards toward the lip. These effects tend to produce a higher

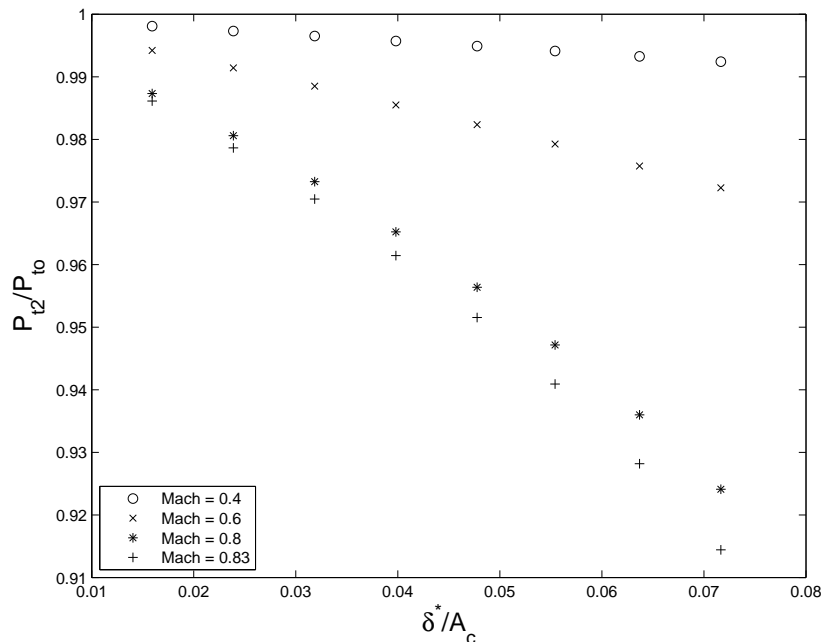


Figure 62: Thickness variation for several different Mach numbers as predicted by the IBLT model

propensity for boundary layer growth and lip separation at these conditions. This will most likely come into play at low speed/TKO conditions where there is likely to be a high flow ratio and blockage forcing the lip Mach to be higher.

4.3.5 Fan Model

The purpose of the fan model is two-fold: first to describe the influence of the distortion on the operating line of the fan and the associated loss in stall margin; second, to estimate an overall loss in pressure ratio and efficiency due to the distortion. The second aspect of this is difficult to do in practice, since any high fidelity model would need to include both radial and circumferential effects and changes in blade performance through some sort of loss model. These models are difficult to produce and often come with a high degree of computational burden for a single solution. Given that the point here is to be able to size a system with a multi-design point cycle model, it is necessary to have something that is computationally cheap, relatively

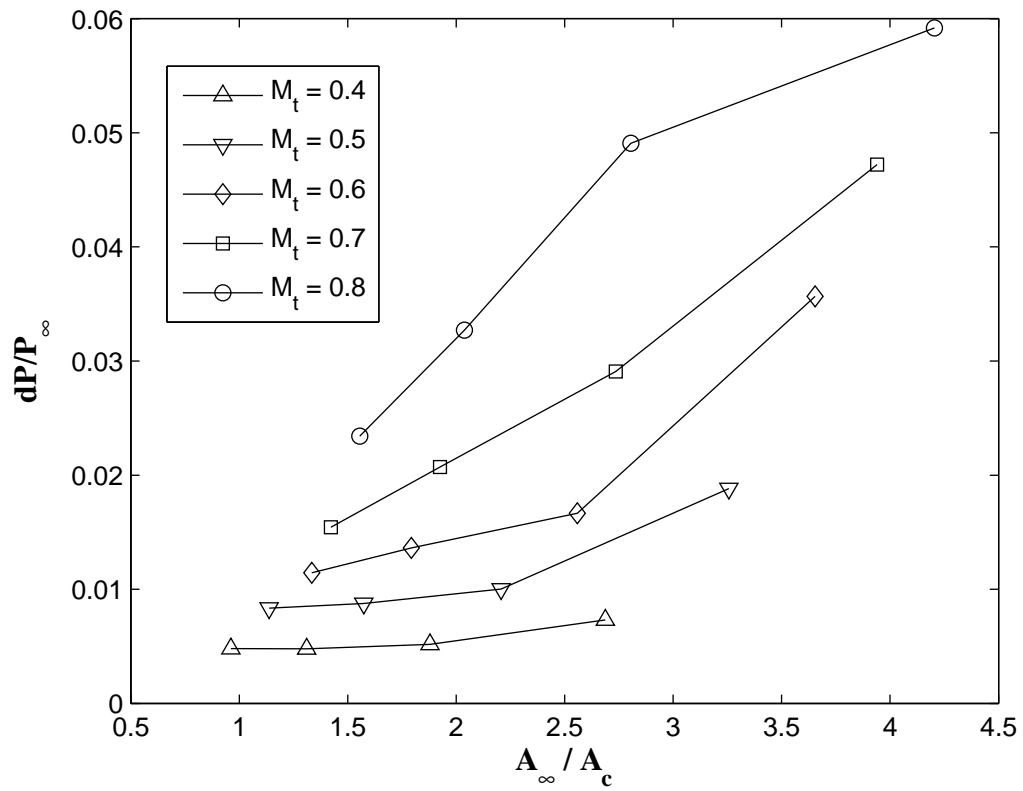


Figure 63: Normalized inlet duct total pressure loss caused by lip separation for an elliptical subsonic inlet at several throat Mach and flow ratio values (adapted from [84]).

robust, but also reflects general trends of distortion effects. These requirements are in line with the spirit of research question and hypothesis 1.

For this reason, the parallel compressor theory will be used to analyze the fan performance for the following experiments. The PC model is a standard “first approximation” for operability loss within the gas turbine industry when empirical or higher fidelity approaches are not possible or available [67] [16]. Recent studies have shown that modern gas turbine analysis tools can be integrated with a parallel compressor approach to yield reasonable and useful results for performance loss as well [52]. Furthermore, from an implementation stand-point, the only thing that is required is that the model needs to read two points from a compressor map, match the exit boundary conditions, and average the performance results. This can be done easily with the standard gas turbine tools, such as NPSS, and can be linked to the inlet tool which predicts the inlet recovery.

Parallel Compressor Basics

The essential concept of the parallel compressor theory is to treat the singular distorted compressor as two uniform compressors each operating at their own level of inlet total pressure [57]. The “low sector” is the distorted region and operates at a lower total inlet pressure, while the “high sector” is simply the opposite and operates at the free-stream pressure. Each of the streams assumes uniform operation at an individual point on the “clean” or uniform compressor map. Figure 64 shows what happens in each of the sectors in terms of the overall compressor map. The standard assumption is that both sectors exhaust to a uniform static pressure plenum, which acts as the boundary condition that the model must satisfy. Upstream of the compressor inlet, the presence of the compressor causes a redistribution of axial velocity and a change in static pressure, thus inducing static and total pressure distortion. The assumption that the exit static pressures are equal then requires that the low

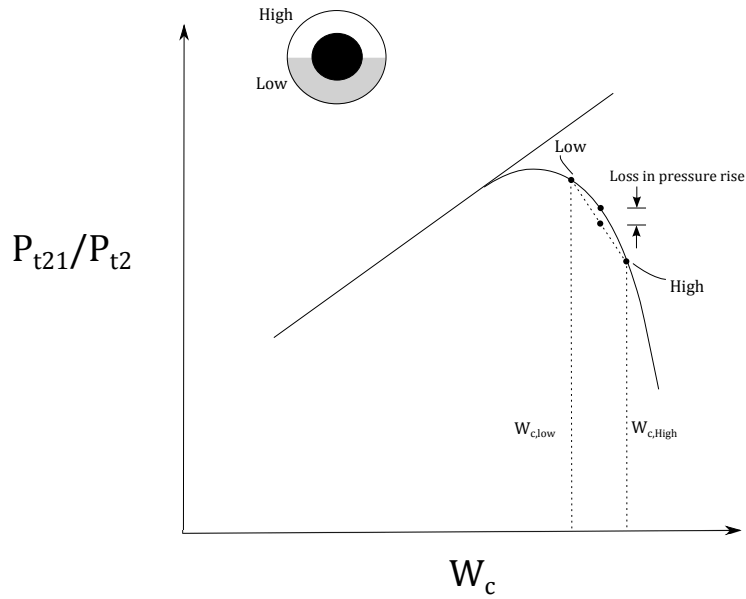


Figure 64: Diagram illustrating the parallel compressor concept (adapted from Greitzer et. al. [57])

pressure sector have a higher total pressure ratio than the high sector thus attenuating some of the pressure distortion.

The assumption of constant exit static pressure generally arises from the fact that the trailing edge flow angles after a compressor stage stator vane are roughly constant around the flow annulus, leading to a constant static pressure if the intermediate duct is straight and the flow is essentially 2-d. Implicit in this assumption is that there is no circumferential flow redistribution between the sectors within the machine. For multi-stage compressors, this is reasonable if the circumferential length scales are large in comparison to a typical rotor-stator stage gap. For single stage fans, this assumption is valid since there is no gap within the compressor where flow can travel between the sectors. However, the assumption of constant exit angle is not typically valid, since the fan stator is some distance downstream of the splitter location in the bypass stream. Typical BLI fan high-fidelity analyses [29] show some amount of static pressure distortion at the fan exit which likely forces flow redistribution in the splitter gap and bypass duct. In any case, whether the static pressure is assumed

exactly constant or not, this should not significantly impact the trends of experiments 1 and 2. Furthermore, many authors have used the assumption for constant exit static pressure when using the parallel compressor theory for fan analyses [69] [52] and the model used here will do the same for lack of a competitive assumption.

Model Architecture and Algorithm

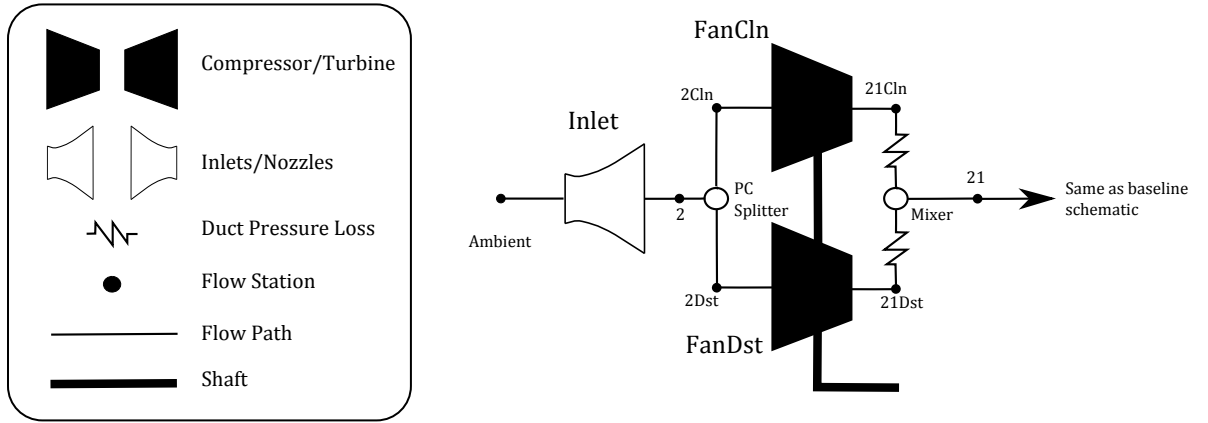


Figure 65: Parallel compressor engine model schematic.

The basic parallel compressor model is described schematically in fig. 65. The model architecture consists of a splitter dividing the flow between the high and low sectors, one compressor for each sector, two ducts aft of the compressors which allow for pressure balance, and a mixer which mixes out the pressure and temperature between the sectors. The model aft of this station is precisely the same as the original engine model. The following sections will describe the essential assumptions made in dividing the flow and computing the operating lines of each compressor.

The first step in implementation is to split the flow and annulus area A_2 between the high and low sectors. The low sector angle is an input to the PC splitter and the areas are split according to this input (eqs. 109 and 110). Setting the sector angle to π (180 degrees) means the area will be split equally between the sectors.

$$A_{2Cln} = \frac{A_2}{\left(1 + \frac{\theta/2\pi}{1 - \theta/2\pi}\right)} \quad (109)$$

The sum of the split areas has to equal the initial inlet out area.

$$A_{2Dst} = A_2 - A_{2Cln} \quad (110)$$

The second step is to define the necessary static pressures (or equivalently, flow velocity) for the different sectors at the inlet. This is done by assuming that the overall flow blockage (boundary layer displacement area) is kept constant but is all located within the dirty sector. The inlet exit discharge coefficient is computed by the basic definition of C_d and from the inlet exit flow velocity computed by the IIBLT model.

$$C_{d_2} = \frac{\dot{m}_{actual}}{\dot{m}_{ideal}} = \frac{\dot{m}_2}{(\rho Au_e)_2} \quad (111)$$

Since there is, by definition, no blockage in the clean sector, the discharge coefficient is unity in that sector. All of the flow blockage is therefore contained in the dirty sector and the discharge coefficient can be computed based on the sector mass flow definition.

$$C_{d_{2Dst}} = 1.0 - (1.0 - C_{d_2}) \frac{1.0 + BPR}{BPR} \quad (112)$$

Here, the bypass ratio (BPR) is not the typical engine bypass ratio, but rather the splitter specific BPR.

$$BPR = \frac{\dot{m}_{2Dst}}{\dot{m}_{2Cln}} \quad (113)$$

The total pressure in the low sector is then set by making a similar assumption that the recovery in the high sector is unity and all of the recovery loss computed by the inlet model is contained in the low sector. The distorted sector loss is then computed as follows assuming mass flow averaged pressure.

$$\frac{\Delta P_{t2Dst}}{P_{t\infty}} = 1.0 - \frac{\frac{P_{t2}}{P_{t\infty}}(1.0 + BPR) - 1.0}{BPR} \quad (114)$$

The assumption is then made that the area split between the sectors is the same at the fan outlet as the inlet. The total exit area is adjusted to achieve an overall

exit area ratio consistent with hi-bypass fans by adding the exit Mach number to the NPSS solver.

$$A_{21Cln} = \left(A_{21Cln} + A_{21Dst} \right) \frac{A_{2Cln}}{A_{2Cln} + A_{2Dst}} \quad (115)$$

The ducts in between the fan outlet stations and the mixing input stations are fixed area ducts which allow the static pressure to equilibrate at the exit. This is not any physical representation of a duct, but rather a numerical “trick” which deals with solver convergence issues related to directly linking the mixer inlet and fan outlet. It was found that having these “dummy” ducts in between the two allowed for a much more robust numerical procedure with the proper end result of constant static pressure.

The mixer is used to mix out the losses between the sectors. The dirty sector is generally at some lower total pressure than the clean sector, implying there is some distortion transfer (pressure not fully recovered). The NPSS mixer element requires that there be constant static pressure between the two mixer inlet stations, thus satisfying the constraint of the parallel compressor model. This is implemented in the solver, with the PC splitter bypass ratio used as the independent variable. This is to say that the corrected flow difference between the sectors is adjusted until the static pressure at mixer entrance is equal between the sectors.

Sector Map Treatment

The final piece of the puzzle for the PC model is the treatment of the compressor maps between the two fan sectors. In the traditional PC model, the map must first be defined by a clean or uniform design. In this case, the CMPGEN maps generated for the baseline model are used for both sectors. To define the scaled map for each design from the baseline map, an initial uniform pressure sizing case is run at the aerodynamic design point to set the map scalars. The map is defined by the clean sector, which is kept in “On-Design” mode during the clean ADP run, while the dirty

sector always necessarily inherits the map scalars from the clean in every run. It is therefore kept in “Off-Design” mode regardless of the run type or design point. This process is outlined in fig. 66 below.

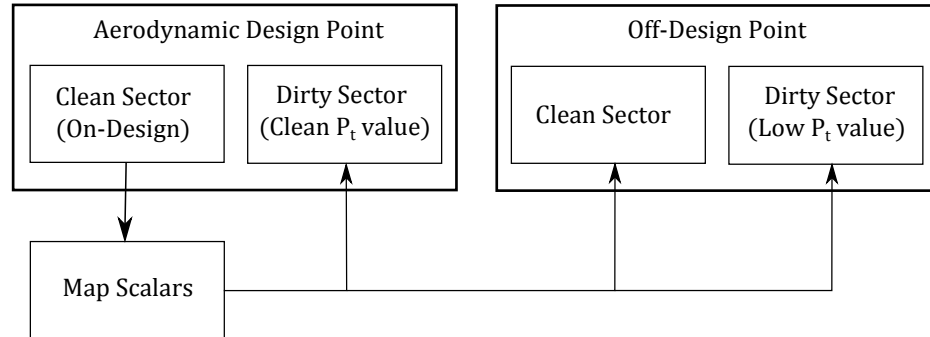


Figure 66: Parallel compressor map scalar production process.

PC Model Sample Results

The model was initially tested on the baseline engine model. To simplify the trends, a single design point model is used with a top-of-climb mass flow sizing point and a max turbine inlet temperatur – and cooling flows – similar to the baseline model. The design point is run with a zero inlet loss (recovery of unity), and the recovery is reduced to see how the operating lines – run from 80% to 110% corrected speeds – of the clean and dirty sector changes.

The results, shown in fig. 67 on the compressor map, show that the model qualitatively replicates the expected trends predicted by the parallel compressor theory. At an inlet recovery of one, the dirty and clean sectors are on precisely the same operating line at each speed (shown by the black dots on the graph). As the recovery is reduced, the clean sector moves farther right on each speed line towards compressor choke while the dirty sector moves closer to the stall line with lower corrected flow (higher PR).

For each of the parametric inlet recoveries used here, the stall margin at constant speed of the distorted sector is shown below in fig. 68. Clearly, the stall margin

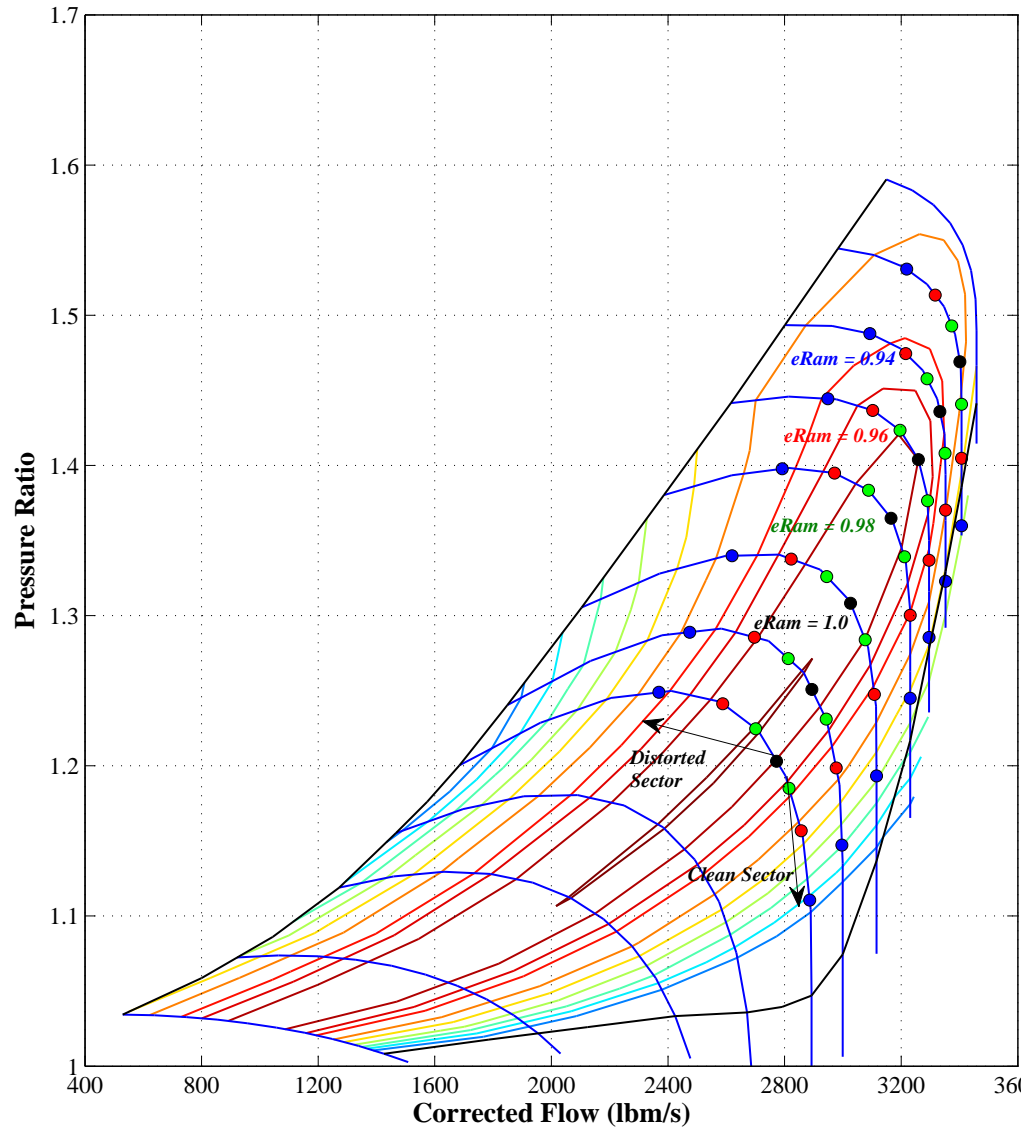


Figure 67: Parallel compressor sample results

declines for each progressively increasing inlet loss and has a more significant impact on the low speed operating conditions, although the stall margin is generally higher at those points naturally for this fan and operating line. The stall margin loss near cruise speeds (100%) and at NASA inlet A levels of distortion (recovery of 0.96-0.98) is quite large.

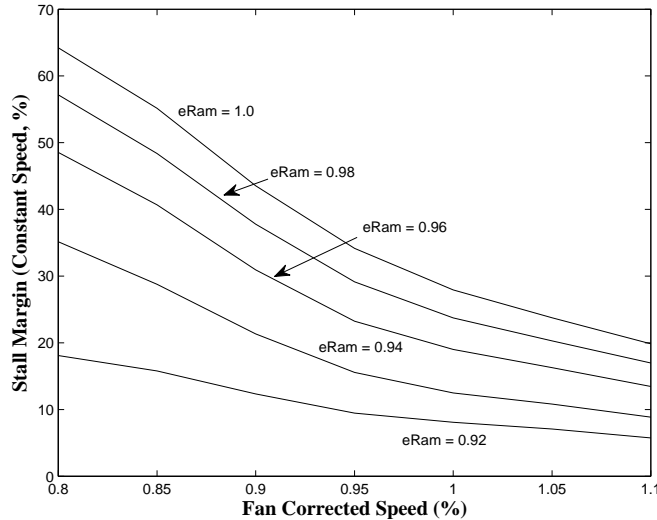


Figure 68: Stall margin at constant speed for varying inlet recoveries for the basic parallel compressor model as applied to the baseline engine model

A similar result is shown as that in fig. 68 for pressure ratio loss which was notionally illustrated in fig. 64. The results in fig. 69 show that the parallel compressor model described predicts increasing loss in pressure ratio as the difference between the sectors increases. The speed trend generally shows a “bucket”, with a maximum pressure loss at some intermediate speed and then relatively lower pressure losses at the extreme high and low speeds. This has to do with the change in the slopes and positioning of the speed lines which change substantially at different speeds. The mass flow loss exhibits a similar trend with increasing flow loss at part power and higher distortion levels.

Figures 69 and 70 show the factors which effect thrust loss in the gas turbine due to fan distortion. These losses would affect the thrust capacity of the propulsion system

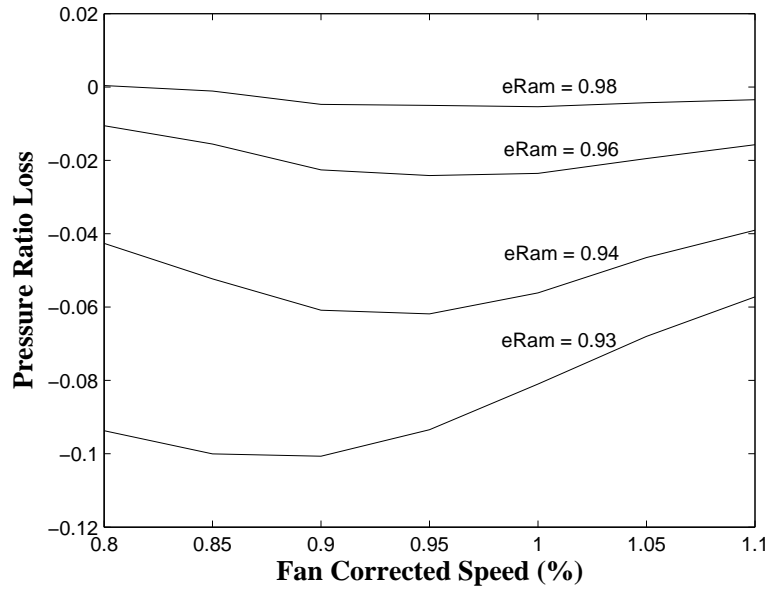


Figure 69: Pressure ratio loss for the fan using the basic parallel compressor model as applied to the baseline engine model

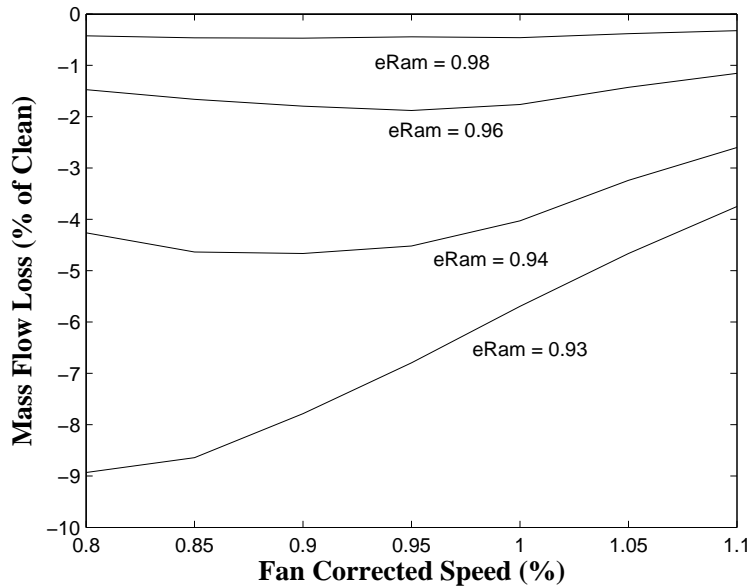


Figure 70: Mass flow loss for the fan using the basic parallel compressor model as applied to the baseline engine model

but also would increase the TSFC and overall fuel burn of the system. Generally, the parallel compressor model is not used to predict performance losses due to distortion, which are considered minimal for practical levels of pressure distortion. Kurzke [52] showed that the PC model can be used within the gas turbine simulation program (similar to that described above) to predict performance loss. Kurzke estimates a few percentage points of distortion loss for normal levels of DC60. The results here show that for the Inlet A levels of distortion ($e_{Ram} = 0.96-98$) at the cruise point, that the PR and mass flow losses are on the order of a few percent which is consistent with Kurtzke's findings. An experimental study on a low bypass turbo-fan with large amounts of BLI was recently conducted by Lucas [58] who showed that, for a BLI type distortion with a total inlet recovery of about 0.955, there was roughly 10% equivalent thrust loss in the engine, with much of that coming from downstream propagation of the distortion into the bypass duct. This estimate is on the same order as that predicted here by the parallel compressor model, except that the baseline engine used for these results employed a much lower fan pressure ratio which will typically have more distortion related losses and less attenuation. This model does not include a distortion propagation model in the bypass duct and its effect on thrust or entropy production, and so the model should be considered a bit conservative in terms of loss prediction.

Sizing with the PC Model

The performance loss considerations from the previous section now bring to light the question of sizing in the presence of distortion. Kurtzke mentions the possibility of rematching the engine to account for the distortion loss but does not mention how this process might occur or the proper method for conducting the analysis. The difficulty with doing the rematching process is that the parallel compressor model, which predicts the losses, is necessarily run in engine off-design mode after the map

aerodynamic design point has been executed.

To account for the distortion, the map flow capacity scalar must be adjusted to allow for additional thrust, but the design point of the map – design PR, N_c , and efficiency – must be kept consistent with the baseline map design. If the clean sector fan is used to define the map scalars while the parallel compressor model is active, then pressure ratio and efficiency will not be scaled properly since the map scaling point will be at an operating line which is different than the clean design operating line for which the original base map PR and efficiency was specified.

To accommodate this issue, a process has been developed to rematch the engine for distortion related losses predicted by the PC model which is illustrated in fig. 71. The first block is the same as in fig. 66 and the second part represents the rematch run execution. For the first run, the losses are uniformly mixed across both sectors, which represents a standard cycle model where a single inlet recovery is used. For this run, the clean sector is precisely at the specified design operating line (R-line) so that the pressure ratio and efficiency scalars are properly computed.

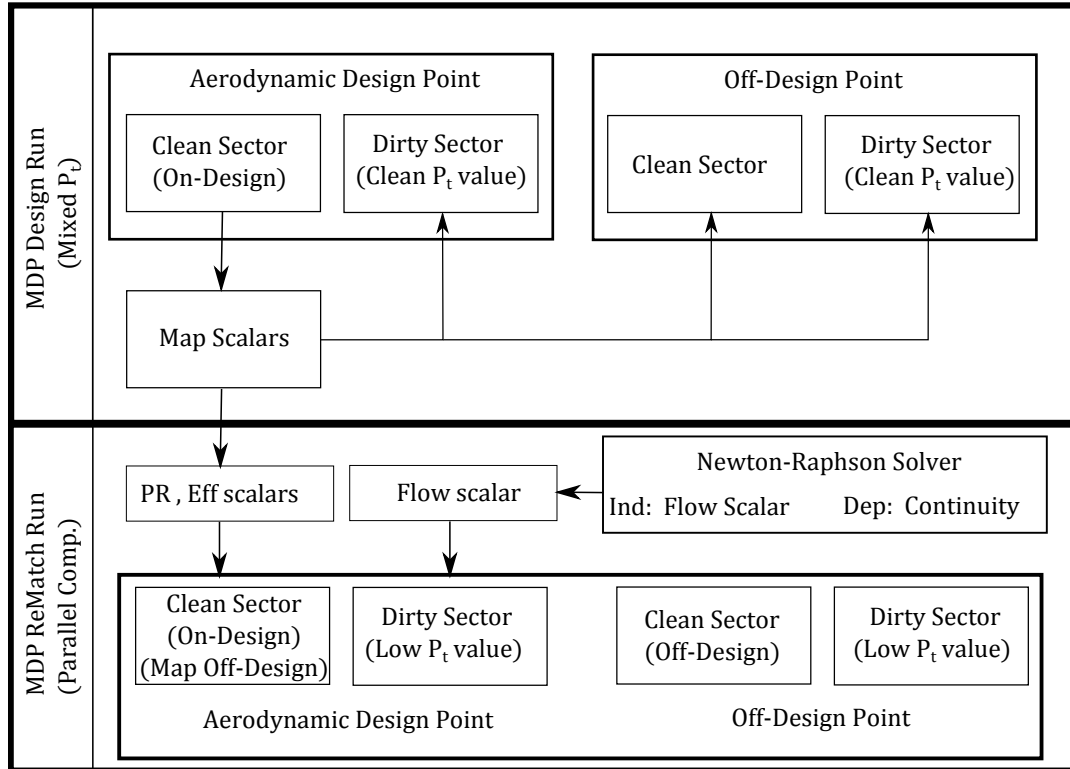


Figure 71: Parallel compressor map definition process including rematch for distortion related losses

In both the original and the rematch run, the clean sector of the fan at the aerodynamic design point is in design mode while the dirty sector is always in off-design mode. The main difference between the original map setting run and the re-match run is that the clean sector map is set to off-design for the latter case. This means that the map scalars are fixed to those set in the first design run with uniform total pressure. The pressure ratio and efficiency scalars are fixed at the mixed design run values as is desired. The flow scalar is controlled by the Newton-Raphson solver which also solves the general cycle model set of non-linear equations for the multi-design point execution. The independent variable is the flow scalar, and the dependent variable is the requirement of flow continuity between the required mass flow through the sector and the computed mass flow of the map. The flow is effectively scaled to match the required flow for the thrust demand at that point, except that

the distortion losses as described previously are accounted for in this case.

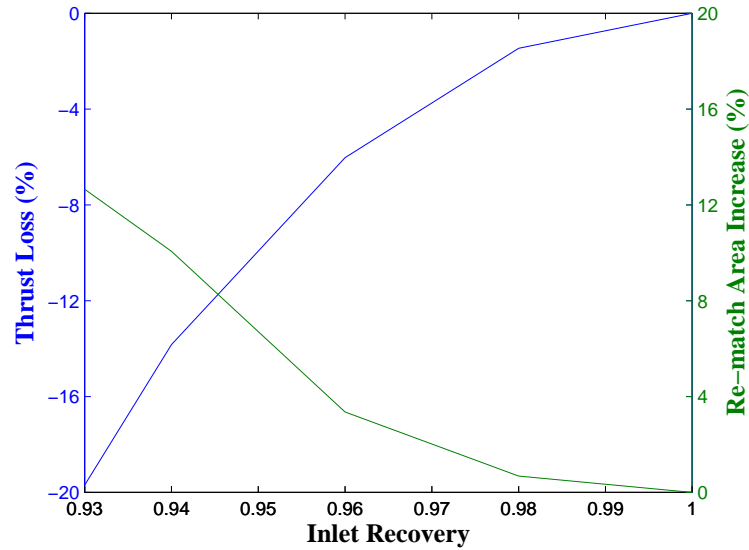


Figure 72: Plot of thrust loss as a function of total average inlet recovery (blue line) and the required area increase to re-match the thrust with the parallel compressor model (green line)

Fig. 72 shows the results from a sample test case for the parallel compressor model rematching process. The thrust loss and required fan area (also flow) increase to re-match the required thrust are shown to increase substantially as the total inlet recovery decreases and distortion increases. For the Inlet A levels at cruise, the distortion losses are not terribly significant (approximately 5-8%). However, there is a substantial non-linear region where the thrust loss and re-match area increase rapidly below a recovery of about 0.96. The model will not converge below a recovery of 0.93 because the clean sector enters the choked region where moving the operating line of the clean sector no longer increases the flow, making it impossible to satisfy the static pressure boundary condition at the fan exit.

4.4 Experiment 1

Now that the modeling environment for the test case has been described and developed in accord with the BLI modeling phase process, an experiment designed to test

hypothesis 1 will be conducted. As a reminder, hypothesis 1 claimed that there was a fundamental relationship between the vehicle boundary layer profile, the ingested stream-tube size, and the system performance. It implies the need to establish this relationship for both the On-Design and critical Off-Design conditions. The analysis and observations from chapter 3 established the plausibility of this hypothesis from a theoretical perspective. Experiment 1 is designed to test the following aspects related to but not directly addressed by hypothesis 1 and the analysis presented in chapter 3:

- The variation of design point performance with key design parameters that affect the ingested stream-tube
- Impact of various assumptions commonly made on propulsion system performance and design parameter optima
- The variation of performance with operating condition changes (off-design)
- Impact of boundary layer/stream-tube assumptions commonly made on off-design performance
- Impact of BLI on MDP setup and results

The goal is that the results of experiment 1 will establish the boundary layer stream-tube performance relations for the type of system chosen for the experiment and will highlight important factors and variations in BLI related performance as a function of design choices and operating conditions.

The experiment is therefore divided into 4 parts, each of which is designed to test aspects of the above list. In order to test the impact of various assumptions related to the stream-tube, boundary layer, and loss assumptions, the modeling environment has been separated into a hierarchy with different loss assumptions. The experiment is also divided into different assumptions pertaining to the stream-tube and vehicle

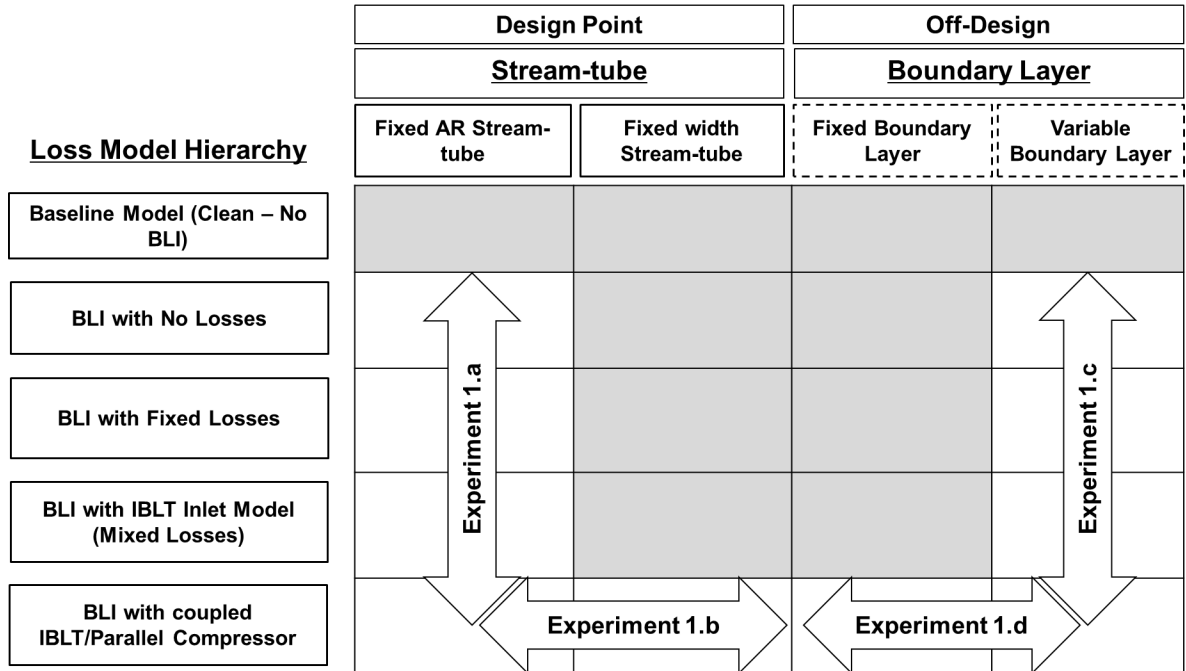


Figure 73: Description of the components of experiment 1 and their relation to the model hierarchy created

boundary layer. This division is shown in fig. 73 in matrix form and each of the 4 experiments represents a comparison of different models represented by blocks within the matrices.

The first model in the loss model hierarchy is the baseline model with no BLI effects at all. The second is the “clean” model which is the baseline model but with the added BLI benefit term in the power balance equation. The third is the “clean” model with additional fixed inlet losses that are uniformly distributed across the fan face. This is intended to represent the commonly used parametric method in which inlet recoveries are directly input to the model. The fourth model, called the “mixed” model, uses the IIBLT inlet tool to predict the inlet recovery losses as a function of the boundary layer and the other inputs to the inlet model. The final model in the hierarchy is the fully coupled model with the parallel compressor model added, which accounts for distortion effects on the fan performance.

4.4.1 Experimental Setup

The engine model used for the experiments is the baseline model with each of the associated BLI models progressively added on in the hierarchy. An SDP (single design point) sizing approach will be used for experiments 1-a through 1-d to isolate the impacts of the BLI effects on performance at design and off-design conditions. A final examination of the effects on a multi-design point model will be used to conclude the experiment, but for now the SDP model will be used for the analysis.

The main difference between the SDP and MDP method (that used for the baseline engine model, for instance) is that the engine is sized for a specific thrust lapse between the hot day take-off condition and the top-of-climb condition regardless of the cycle chosen during a given sizing run. For the SDP design, the engine is sized specifically for cruise to a fixed thrust. Some portion of the CDS will be infeasible by using this approach, but this is a better approach for isolating the effects of BLI at a single design condition. The maximum turbine inlet temperature is assumed to occur at take-off and the cooling flows are sized there. The approach for the SDP point is to use the baseline cruise T4 and the cooling flows calculated from the baseline MDP model, meaning that the baseline cycle has the same performance at take-off for the SDP sizing. Key parameters used for the SDP sizing are shown below in tab. 23 and were taken from the cruise point of the baseline MDP sizing model. The SDP sizing model very closely matches the cruise TSFC values for the MDP cruise point.

For each of the sub-experiments in experiment 1, comparison plots will be shown comparing the different models over a range of sets of independent variables. These variables will be either design space or operating condition related. Tab. 14 shows the independent variables for each set of experiments for each variable classification.

Table 13: Parameters for the SDP cycle analysis setup for experiment 1.

Parameter	value
TKO T4 Requirement	3450 °R
Cruise T4	2963 °R
Cruise OPR	42.8
Total Cruise Thrust	24482 lbf
HPT Bleed (NC)	0.0998
HPT Bleed (Charge)	0.0298
LPT Bleed (NC)	0.0292
LPT Bleed (Charge)	0.008
Total Cust Bleed	7.86 lbm/s
Total HPX	500 hp

Table 14: Table showing independent variables for experiments 1.a-1.d

Experiment	Design Independents	Operational Independents
1.a	FPR, BPR, Inlet AR, n_{eng}	Cruise α
1.b	Design A_o/A_c , s.PreEntry, Inlet AR	Fan % N_c , Cruise α
1.c	Inlet AR	Fan % N_c , α , MN, altitude
1.d	Inlet AR	α , MN, altitude

4.4.2 Experiment 1.a Results

For experiment 1.a, the independent design variables for the system will be varied to show the influence of the modeling assumptions on the propulsion system's performance for different vehicle angle of attacks. The actual vehicle angle of attack at the cruise point unknown, but should be somewhere between 0-4°. Each of the model comparisons will be shown for variations of angle of attack in this range.

Inlet AR Variation

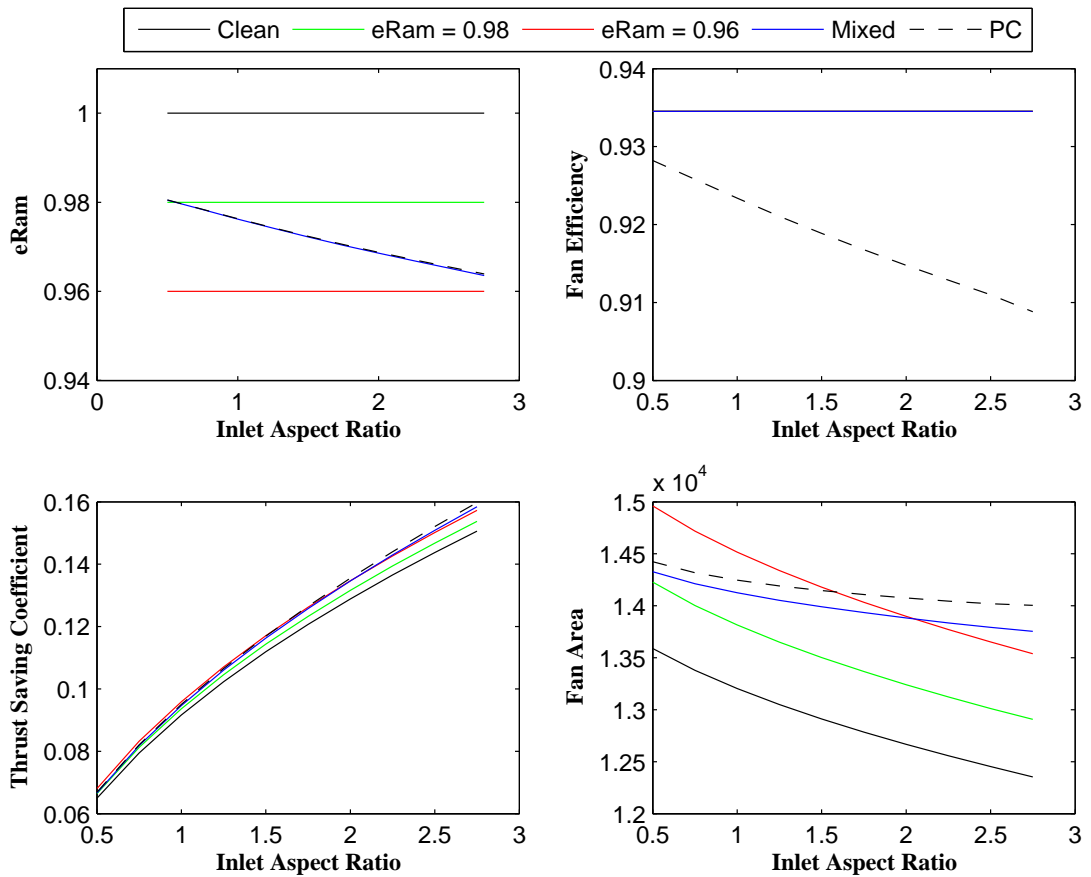


Figure 74: Plot showing trends of inlet recovery (top left), fan efficiency (top right), thrust saving coefficient (bottom left), and fan area (bottom right) for each of the models in the model hierarchy

The inlet aspect ratio is one of the most important design variables for determining

the performance of the BLI propulsion system since it effectively determines the width of the ingested stream-tube. Fig. 74 shows a sweep of the inlet aspect ratio variable for each of the different models in the model hierarchy. The thrust saving coefficient increases in a nearly linear way with AR and does not vary much between the models as expected. The primary difference between the models has to do with how the losses are predicted as a function of AR. The clean and fixed loss models have constant inlet recoveries while the inlet model predicts a steadily increasing loss as the height is lowered at higher inlet AR. The parallel compressor fan model further predicts a lowering of the average fan efficiency as the inlet recovery drops (distortion increase). The fan size trends essentially illustrate how this all plays out in terms of sizing. The constant loss models illustrate a strong downward trend in required engine size with inlet AR, which is being driven by the large increase in BLI thrust savings. For the large fixed loss model with recovery of 0.96, the performance is worse than

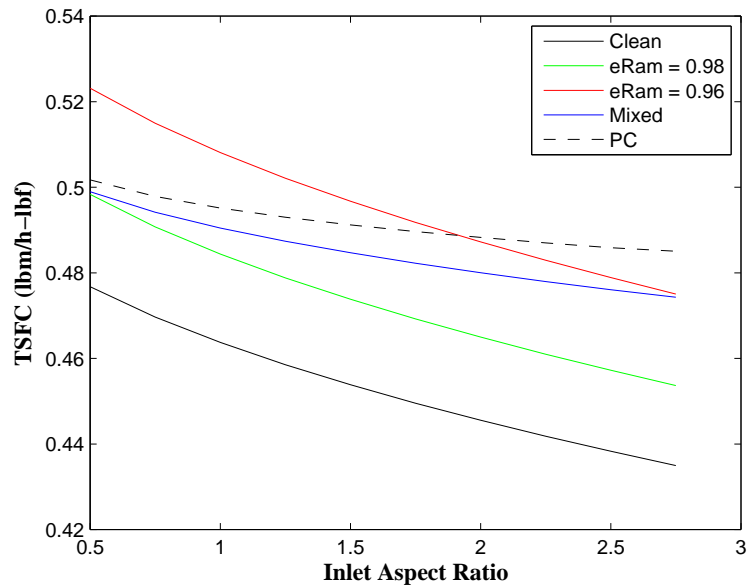


Figure 75: Plot showing trends of TSFC vs. inlet aspect ratio for different models in the hierarchy

the PC model at small inlet AR but better at higher inlet AR. The PC and mixed models exhibit similar trends, since they are largely driven by the variation in inlet

recovery with the stream-tube change, but the fan distortion penalties do a represent a non-negligible step change in performance.

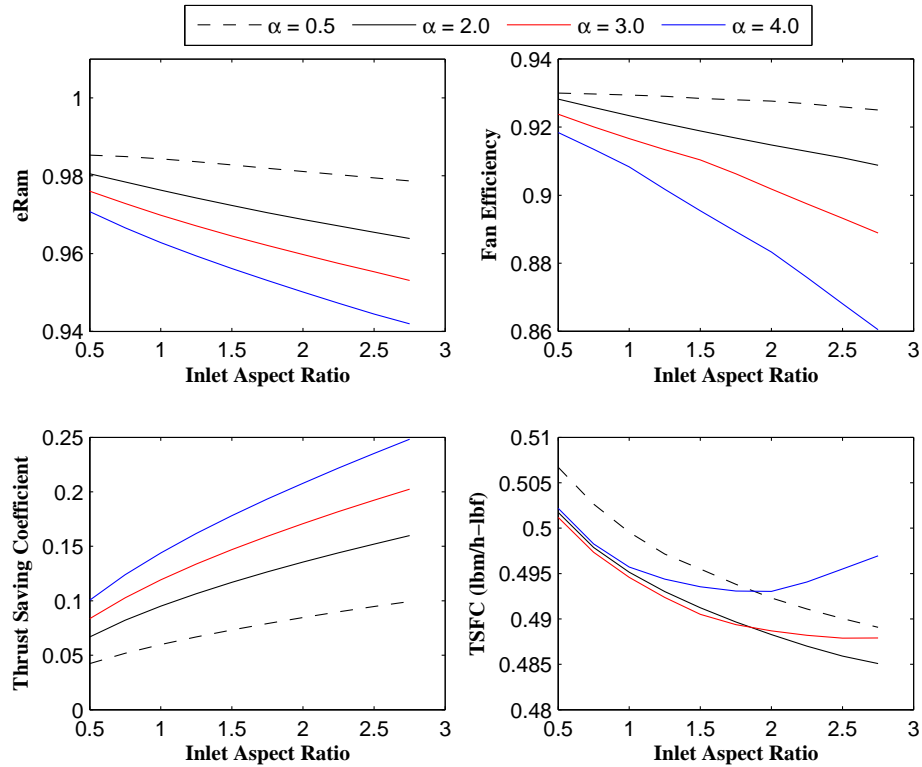


Figure 76: Plot showing trends of inlet recovery (top left), fan efficiency (top right), thrust saving coefficient (bottom left), and fan area (bottom right) for several different values of angle of attack at the cruise condition

The sensitivities of performance with inlet aspect ratio are shown again in fig. 76 with varying angle of attack. Here, the angle of attack is really a surrogate for increasing the boundary layer thickness. For each of these points, the sizing thrust remains fixed but we increase α and therefore the boundary layer thickness and thrust saving coefficient. The trends in TSC vs. AR are more or less the same for each of the angles of attack but are simply displaced to larger values for bigger boundary layer. One interesting trend which develops is that for very large cruise α of 4 degrees, the losses tend to dramatically impact the performance enough to counteract the increase in TSC as seen in the TSFC trends which exhibit a TSFC minimum somewhere near

an AR of 2. This is being driven by two factors: first the relative increase in the inlet losses at higher aspect ratio for lower α ; second, the non-linearity of fan losses with decreases in inlet recovery discussed earlier in the fan modeling section.

Cycle Variation

Another major variable selection for the propulsion system design space is the fan pressure ratio, which will directly effect the bypass ratio and mass flow of the system. This will be true whether or not you are using a turbofan engine with BLI or a distributed fan array. The fan pressure also significantly impacts the propulsive efficiency of the system in addition to determining the mass flow required and therefore the amount of boundary layer ingested. For separate flow turbofan engines, the bypass ratio is effected by the fan pressure ratio but is not uniquely defined by it as in mixed flow turbofans. For the current example problem, then, the additional variable of extraction ratio is used which represents the ratio of the bypass to the core total pressure. Fan pressure ratio and extraction ratio together determine the bypass ratio for the system. Fig. 77 shows the ext/FPR design spaces for each of the models in the model hierarchy. The clear trend here is that under a low or zero loss assumption, the presence of BLI tends to favor much higher bypass ratios, lower fan pressure ratios, and higher fan diameters to ingest more boundary layer flow. The optimum even extends beyond the range of FPR used here, which was limited for convergence purposes and practical limitations on the lower FPR limit. Adding on additional losses moves the optimum to higher values of FPR because the lower FPR designs are more sensitive to pressure loss in the inlet. Fig. 78 shows the TSFC for a range of fan pressure ratio at optimum extraction ratio. The interesting result is that the curve with the full parallel compressor model looks very similar to that of the original baseline model, which, to some degree is dominated by the balance of BLI driving to lower fan pressure ratios and inlet recovery loss driving it upward.

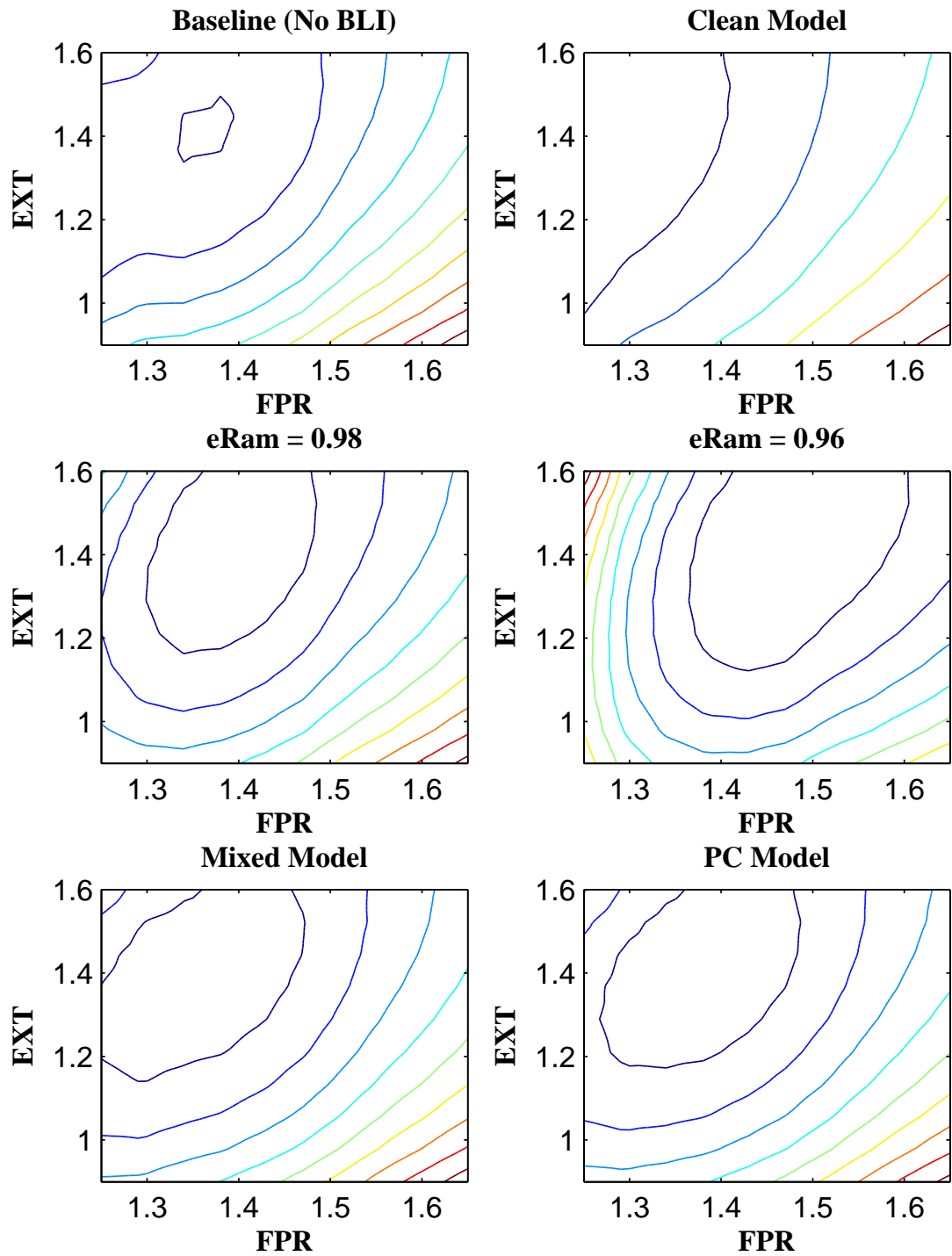


Figure 77: Contour plots showing level curves of TSFC as a function of FPR and extraction ratio for different models in the hierarchy

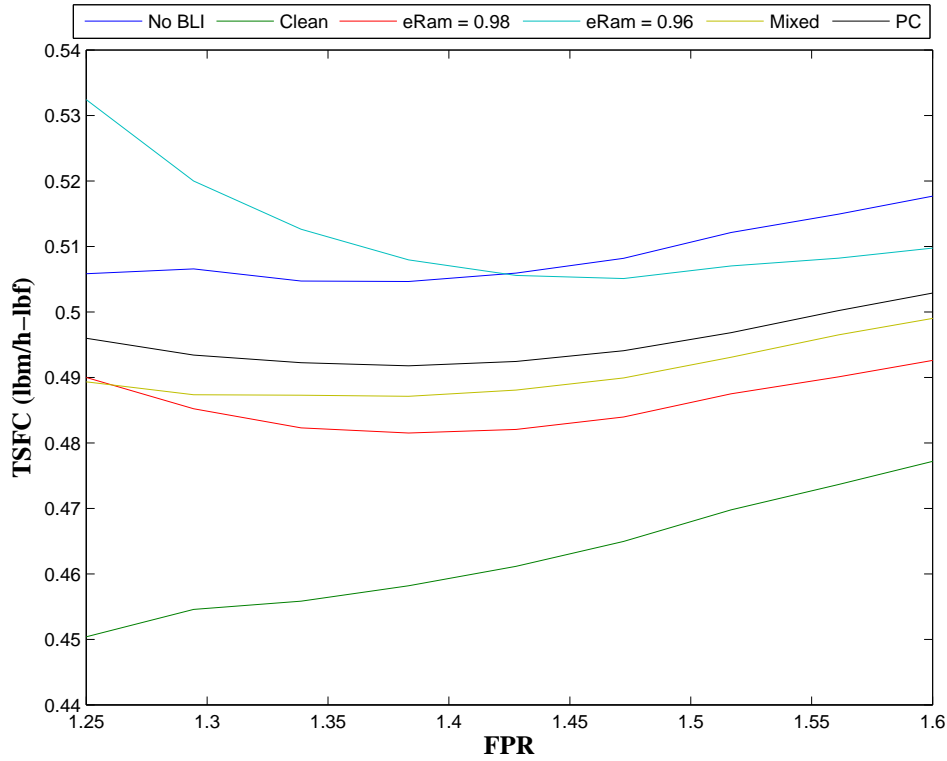


Figure 78: Plots showing TSFC at optimum extraction vs. fan pressure ratio for each of the models in the model hierarchy

Fig. 79 shows the FPR buckets for the full parallel compressor model for different angle of attacks. Again, the trends show that for low loss scenarios the fan pressure ratio optimum tends toward lower values to increase the overall BLI. At high losses, however, the lower fan pressure ratios are significantly penalized. Fig. 79 shows that, at higher FPR, increasing angle of attack at design directly improves the TSFC but at very low FPR, the system experiences an optimum α somewhere between 2 and 3 degrees.

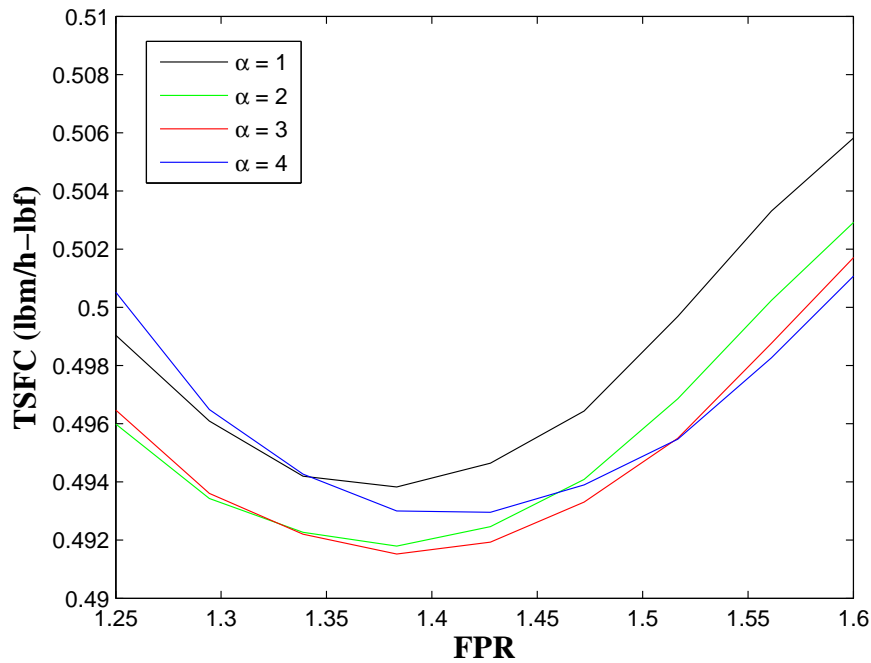


Figure 79: Plots showing TSFC at optimum extraction vs. fan pressure ratio for increasing angle of attack at the design point

Engine Number Variation

A major choice for the propulsion system, and one that is especially important in early phases of design, is the number of propulsors or engines. This impacts everything from performance to structures and sub-systems. In this context, we seek to simply determine the best case performance configuration with reasonable accuracy, realizing that the ultimate decision will be determined by weighted considerations of performance, weight, operating and purchasing cost, controls, and other practical concerns. In terms of BLI, increasing the number of propulsors generally has the effect of creating a more distributed system which ingests more boundary layer. It can be thought of as reducing the overall inlet height and therefore increasing the thrust saving coefficient for each propulsor. For the following experiment, the number of engines within the model is varied and the total thrust, power extraction, and the customer bleeds required are divided amongst the engines.

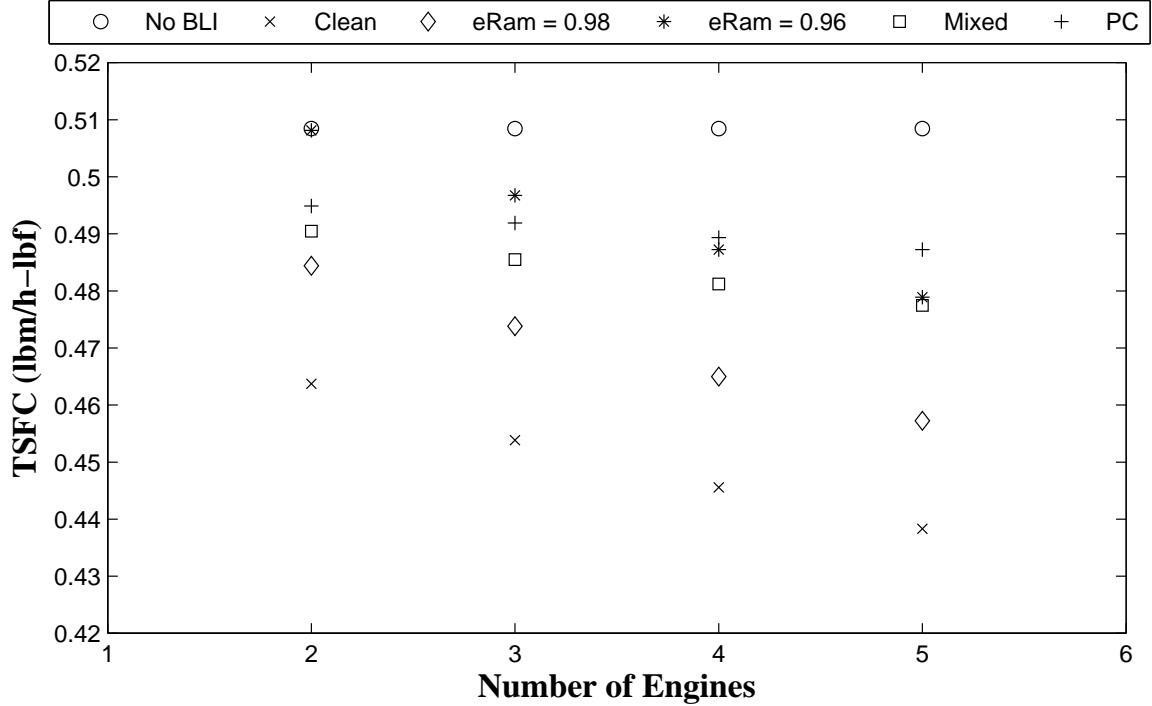


Figure 80: TSFC for different number of engines for each model in the hierarchy

Fig. 80 shows the basic trends of TSFC vs. engine number. The baseline does not show much variation with engine number since the cycle is not affected by any appreciable size effects in this case, as the exit corrected flow is still quite large even for the 5 engine case. For the clean BLI case, there is a clear trend toward a more distributed system with more engines. This is being directly driven by the increased BLI related thrust savings. As was the case for the inlet aspect ratio and fan pressure ratio trends, the trend of increasing TSC tends to be accompanied with a significant and increasing level of loss as the system capture height is decreased.

Similar trends as for the fan pressure α variation accompany the engine number trends. At large engine size (2 engines), the system is less sensitive to changes in losses due to the increase of boundary layer height, while at smaller engine numbers the increased angle of attack overcomes much of the thrust savings benefit.

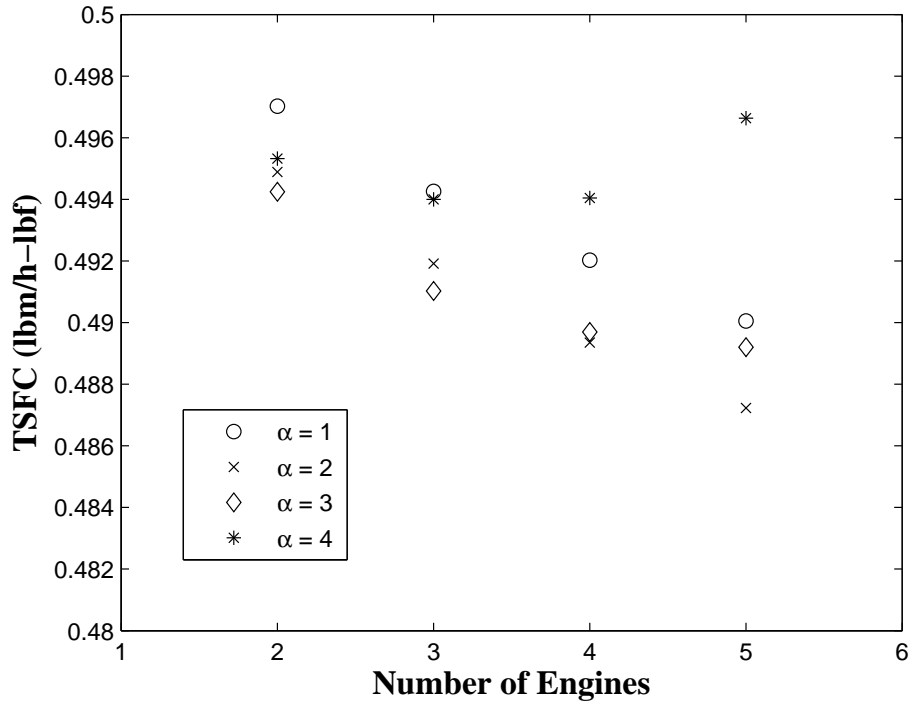


Figure 81: TSFC for different number of engines for a range of angle of attacks with the full parallel compressor model

4.4.3 Experiment 1.b Results

Mass Flow Ratio Variation

The mass flow ratio (or the inverse of μ as defined in chapter 3) is the ratio of the free-stream tube area to the capture area of the inlet. Since the capture area of the inlet is a free variable, the mass flow ratio at design sets the capture area of the inlet since the free-stream area A_o is set by the mass flow of the engine and free-stream flow conditions. This ratio determines the overall amount of diffusion that occurs within the pre-entry region. The inlet diffusion is defined by the inlet area ratio A_c/A_f which will be fixed at a value of 1.067 for the current study (based on the NASA inlet A value). The result of this assumption is that the fan Mach number will vary depending on the choice of the mass flow ratio at the design point as shown in fig. 82 in the plot on the right. Modern hi-bypass fans have a general range of design

point inlet mach numbers which can vary, but are generally in the range shown. The associated inlet recovery for this range of fan face Mach at the cruise design point is correspondingly shown in the left plot for the case of an inlet aspect ratio of unity and an α of 2 degrees.

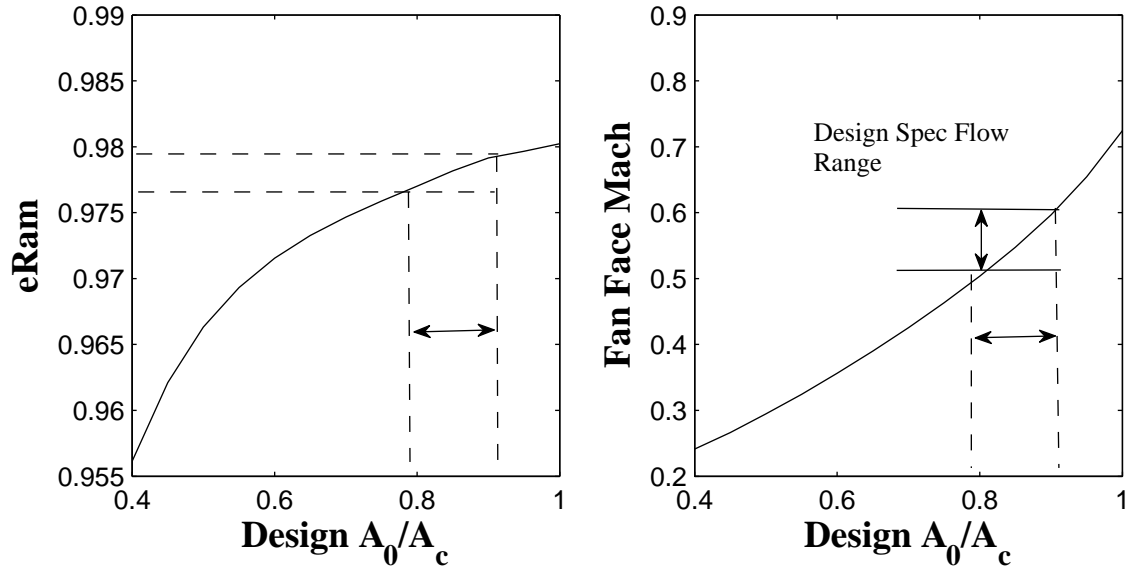


Figure 82: Plot showing trends of design mass flow ratio at the cruise point for the inlet vs recovery (left) and fan face mach number (right); Inlet aspect ratio = 1; $\alpha = 2^\circ$

The choice of the mass flow ratio at the design point is also important because it determines how the inlet will behave in off-design, where the mass flow may deviate significantly in either direction from the design point flow. At very high throttle, if the capture is too small the inlet will choke and not be able to accommodate the flow requirement. At low throttle setting, a capture area sized too large would mean that the pre-entry zone pressure gradients and associated boundary layer growth would overwhelmingly reduce the inlet recovery. Fig. 83 shows sensitivities of the mass flow ratio vs. recovery curves with respect to the pre-entry zone length multiplier. The pre-entry region length assumption matters much more for lower design flow ratios due to the pre-entry losses. There is a point where all of the curves intersect, which represents the point common point of zero pre-entry diffusion requirement, which

is contained within the acceptable region for the fan face Mach requirements. For these reasons, the design mass flow ratio will be kept near the 80% region. Fig. 83 also stresses the importance of understanding the nature of the pre-entry flow for determining part power performance (which will be discussed in more detail later).

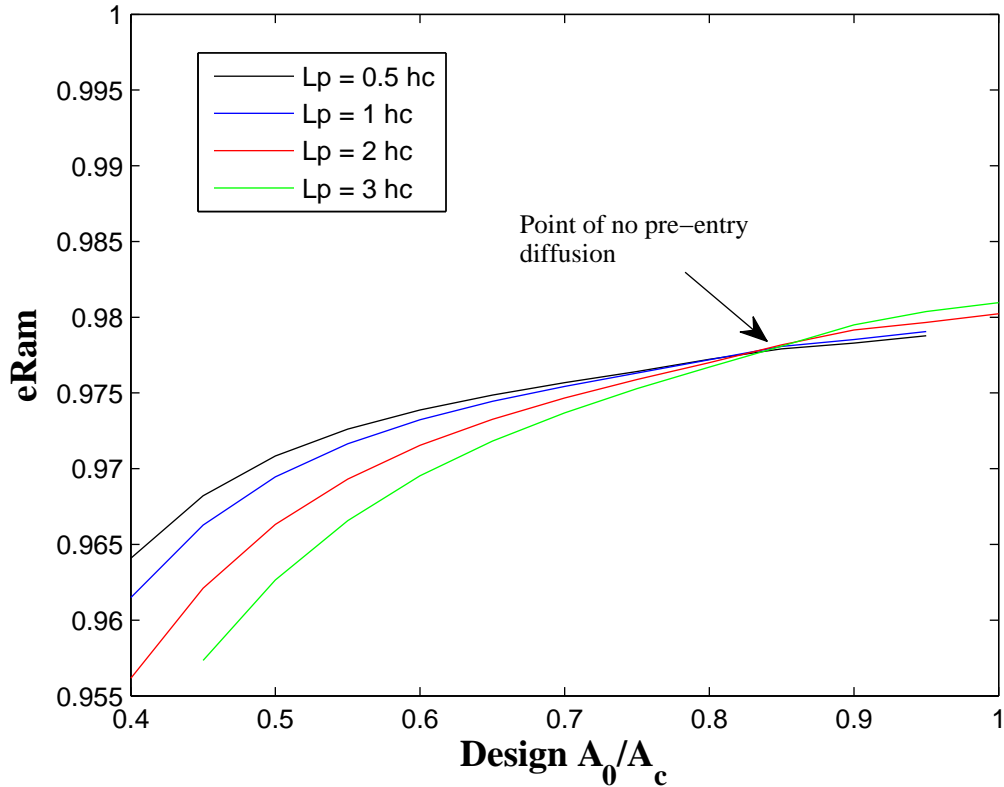


Figure 83: Plot showing sensitivity of inlet recovery with respect to the pre-entry zone length

The sensitivity of the design mass flow ratio curve with respect to the angle of attack (fig. 84) shows that the trends aren't changed much by the boundary layer thickness itself but are rather simply displaced to lower recovery values. This implies that a similar range of mass flow ratios as chosen for the $\alpha = 2$ case is reasonable regardless of the boundary layer thickness.

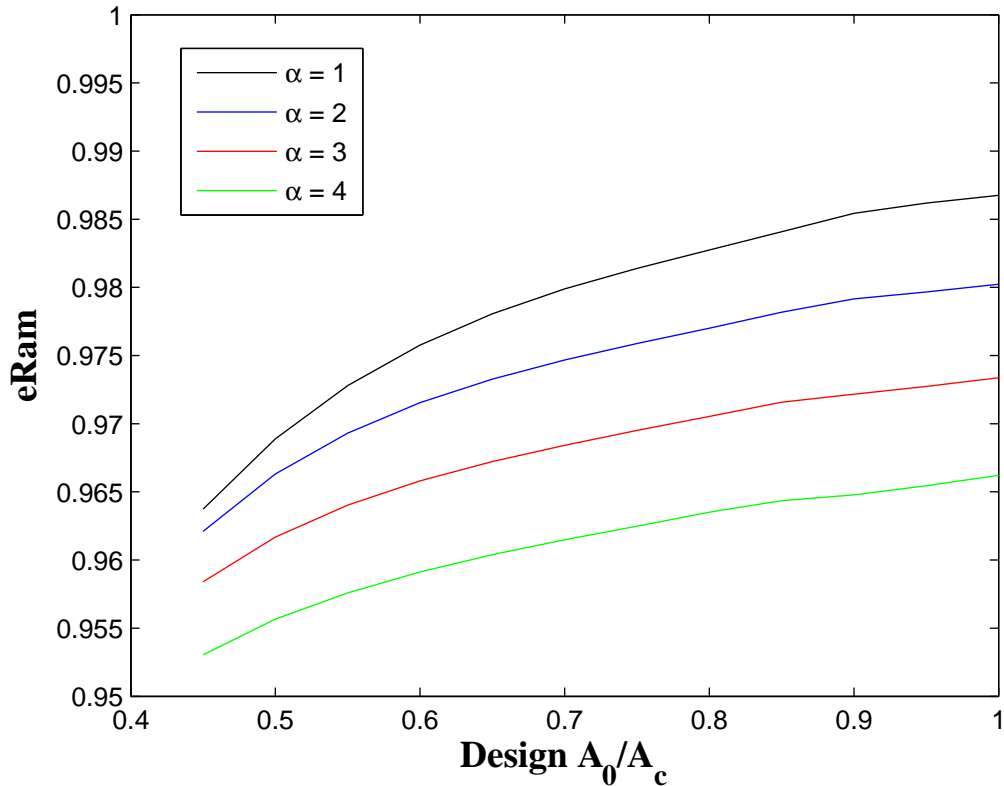


Figure 84: Plot showing sensitivity of inlet recovery with respect to the design mass flow ratio for different angles of attack

Fixed Width vs. Fixed AR

We now turn to the question of the evolution of the stream-tube as it progresses upstream from the capture location. There has been little work in determining the appropriate assumption for the type II BLI systems with regard to this issue. Ferrar [26] discusses the off-design performance of BLI systems very briefly in a review paper on the BLI literature. It is mentioned that the appropriate assumption is that the width of the stream-tube remains constant during the diffusion process though no physical logic is provided or associated reference. Shedon [84] does not seem to mention this issue in his text either. The computational fluids literature generally does not follow this theme in presenting their results. The other option opposed to

the fixed width assumption is to impose a “fixed AR” – implying the aspect ratio of the stream-tube is maintained throughout diffusion. Of course other intermediate linear combinations of these assumptions could be made, but for now we proceed with a parametric analysis of the impact of either assumption using the current modeling approach. We leave the determination of the appropriate assumption to future research.

The fixed width assumption presumes a constant width throughout pre-entry diffusion which implies that only the height may change to accommodate any necessary stream-tube area change. This has two consequences: for smaller mass flows it will yield a less conservative estimate for the boundary layer ingestion, since the stream-tube capture width will be larger; recovery predictions will also generally be worse since the inlet height to boundary layer thickness ratio is larger for a fixed width assumption. At mass flow ratios larger than unity, the trends are reversed, and the fixed width assumption provides a more conservative estimate of BL ingestion and inlet losses. These trends are shown in the mass flow ratio vs. recovery curve in fig. 85 for design mass flow ratios in the range of acceptable values and for several angles of attack. The fixed width assumption clearly implies inherently worse recoveries since the design mass flow ratio will generally be lower than unity.

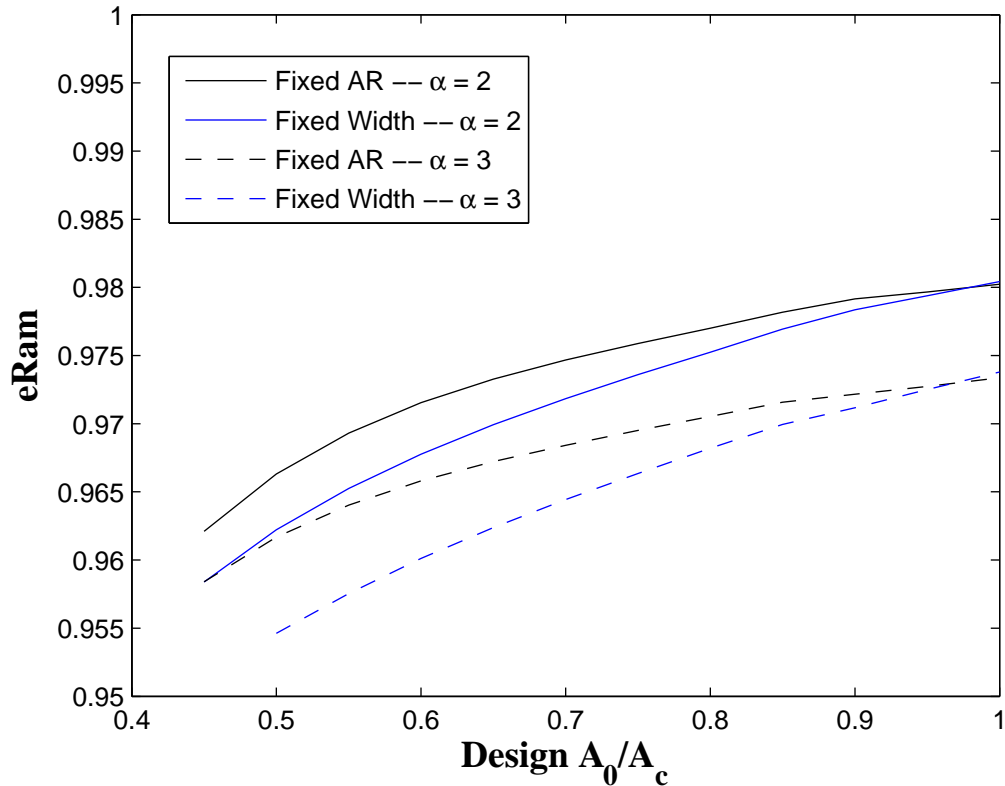


Figure 85: Plot showing sensitivity of inlet recovery with respect to the design mass flow ratio for fixed width and fixed aspect ratio assumption and 2 different angles of attack

The impact of the stream tube assumption on the inlet aspect ratio space is shown in fig. 86 and represents the same basic physics as described above. The fixed width assumption, at the design point, is less conservative for TSC but more conservative on the loss assumptions (greater loss). Furthermore, the separation between the models increases as the inlet aspect ratio is made larger (larger inlet width). In terms of the TSFC, these trends tend to somewhat cancel each other and the fixed width assumption seems to be shifted down by a roughly constant amount relative to the “fixed AR” curve (shown in bottom right plot).

The major impact of the stream-tube pre-entry assumption ought to be seen in the off-design comparisons and especially at low mass flow ratio values. Fig. 87 shows

these trends for several angles of attack and shows that the difference between the two assumptions becomes much larger at low mass flow ratio and at high angle of attacks. Specifically, the fan losses become quite substantial at an angle of attack of 4 degrees as compared to 2 degrees. Though there is some difference between the curves at over-speed values, the difference is essentially negligible in comparison to the part power trends. These trends highlight the importance of understanding how the stream-tube variation and BLI benefit change with off-design conditions especially for significant part power conditions such as end of cruise, descent, and flight idle.

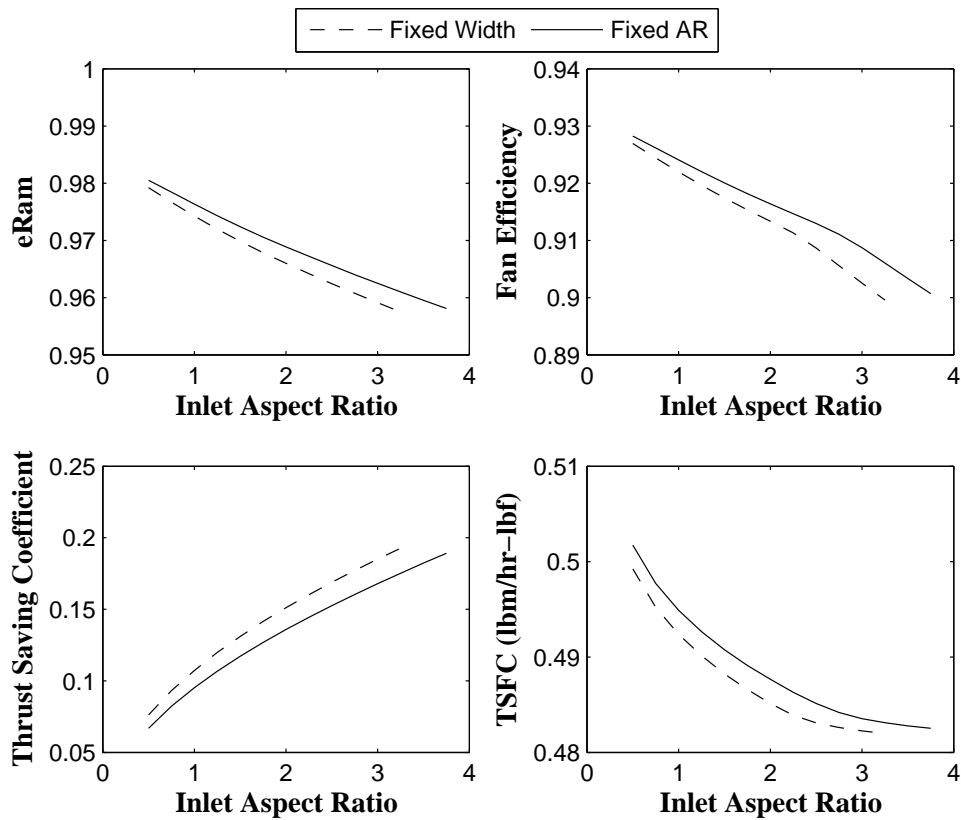


Figure 86: Inlet aspect ratio sensitivities comparing the “fixed width” and “fixed AR” stream-tube models

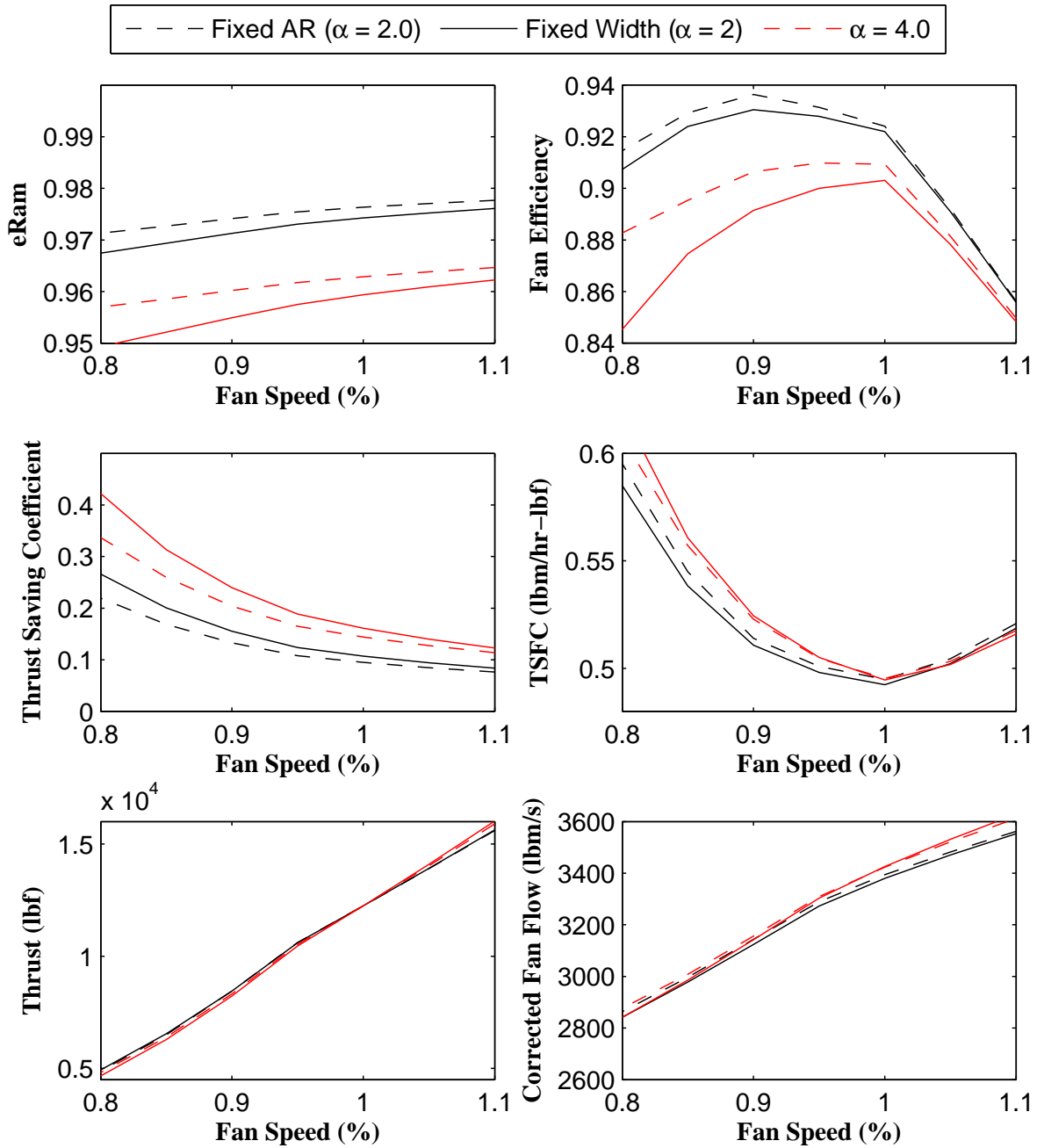


Figure 87: Throttle sensitivities of recovery, fan efficiency, thrust saving coefficient, and TSFC for “fixed AR” and “fixed width” stream-tube models

4.4.4 Experiment 1.c Results

Experiment 1.c is designed to test the validity of hypothesis 1 with respect to off-design conditions – changes in Mach, altitude, throttle, and angle of attack. The test will consist of determining the variability of distortion related losses and BLI related thrust savings over a range of vehicle operating condition, and will determine the impact of choosing fixed loss assumptions an engine model.

Flight Condition Variation

The results from the off-design flight condition variation at constant angle of attack are shown in fig. 88. The baseline thrust lapse is shown in the top left and the other plots show the difference between that baseline thrust and the different models in the model hierarchy. The results show significant difference between the modeling assumptions. First, the clean model is so optimistic at cruise that the system is undersized at low angle of attack take-off as indicated by the blue region near low Mach in the top right plot. The drag savings of BLI (thrust saving coefficient) are so small at low speed that undersizing at cruise under an optimistic loss scenario will yield an engine that does not lapse well to SLS or TKO. This would imply that for a multi-point design for BLI, the low speed points would need to be checked in order to properly size the engine for TKO thrust and that the propulsion system would need to be under-spiced at cruise and TOC relative to the baseline. For the designs with higher losses, this problem is less severe since the losses at the design point reduce specific thrust and force the engine to be larger.

Another trend worth noticing here is that the thrust at higher speeds falls off in the case where the losses increase with the boundary layer thickness. For a fixed loss assumption the opposite is true, since the TSC increases but the losses do not. This highlights the importance of off-design model scalability.

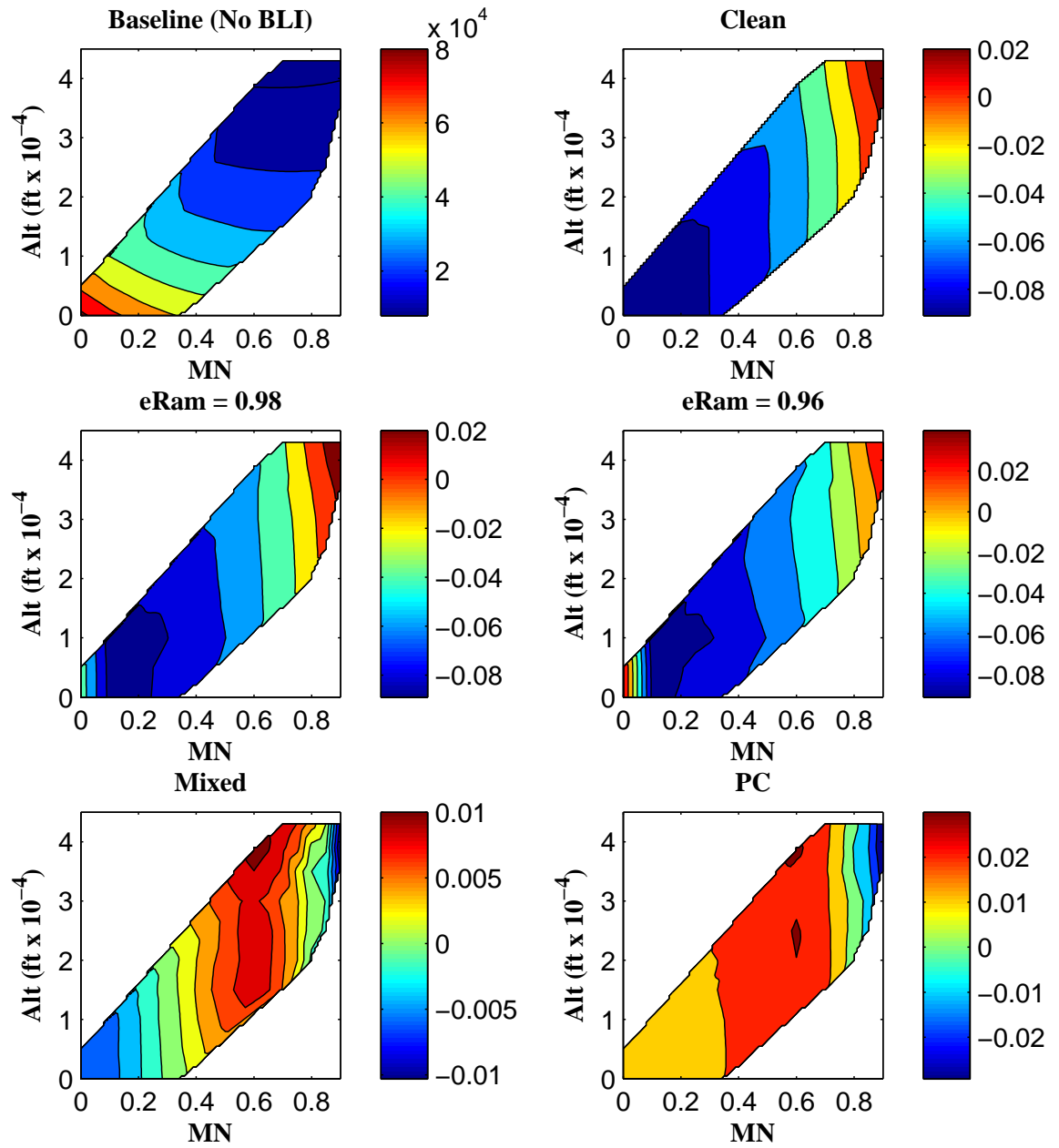


Figure 88: Plots of baseline thrust over the flight envelope (top left) and difference between the thrust predicted by each of the models in the model hierarchy and the baseline

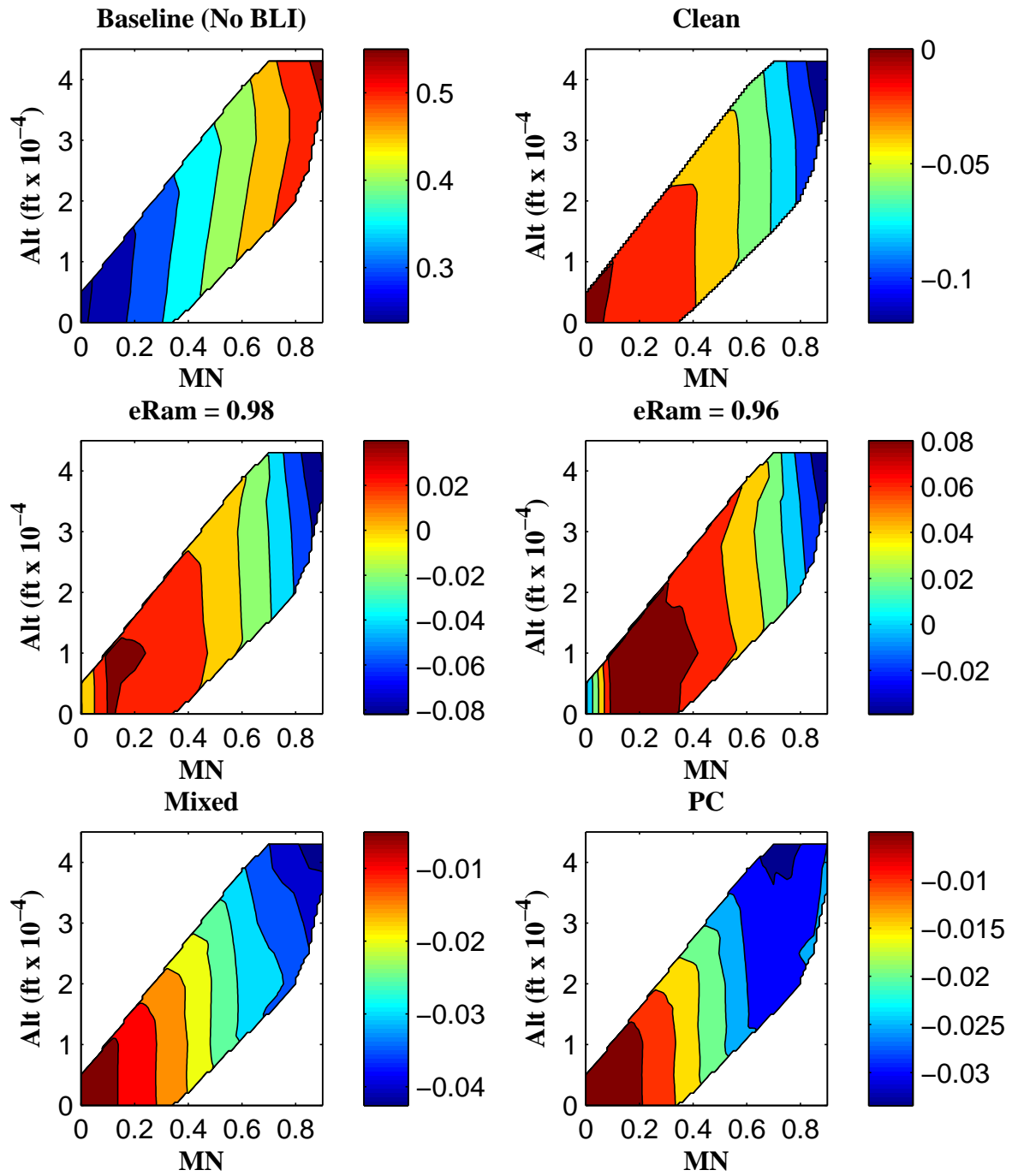


Figure 89: Plots of baseline TSFC variation over the flight envelope (top left) and difference between TSFC predicted by each of the models in the model hierarchy and the baseline

The picture for the TSFC is very similar as to that for thrust as shown in fig. 89. At low speeds, the TSFC approaches that of the baseline cycle, even though the engine is too small relative to the baseline requirement. However, at higher speeds, and with more TSC, the TSFC improves substantially relative to the baseline for low loss assumptions (10% for clean, 7% for 98% recovery), and less for the mixed/PC models (3-4%) and higher loss model with 96% recovery (2%).

Part Power Variation

The low pressure % speed variation for critical flight conditions is shown in fig. 90 for cruise, top of climb, and take-off. These plots are shown for the same angle of attack at all conditions (2 degrees). One trend identified from this data is that there is a more significant difference between the models at part power because of the pre-entry diffusion driven boundary layer growth (same as that as shown in experiment 1.b). Furthermore, the inlet recovery is significantly smaller at the low speed condition, and therefore the TSFC is significantly higher assuming a fixed loss. This highlights the importance of including the strong variation in inlet recovery with the Mach number and boundary layer change.

Finally, perhaps the most interesting trend is that BLI has the effect of flattening the power hook curve at flight speed. This happens because the thrust saving coefficient increases substantially at lower power since the thrust declines at a faster rate than the BLI benefit term. Felder [47] also identified this trend for a turbo-electric distributed propulsion system, in which the power hook is completely reversed and the system becomes more efficient at part power. Though the 2-engine BLI system shown below does not quite reach that point, an increase in the design point TSC (by increasing inlet AR, for example) produces substantially better efficiencies at part power in relation to the baseline model without including the part power losses as shown in figs. 91 and 92.

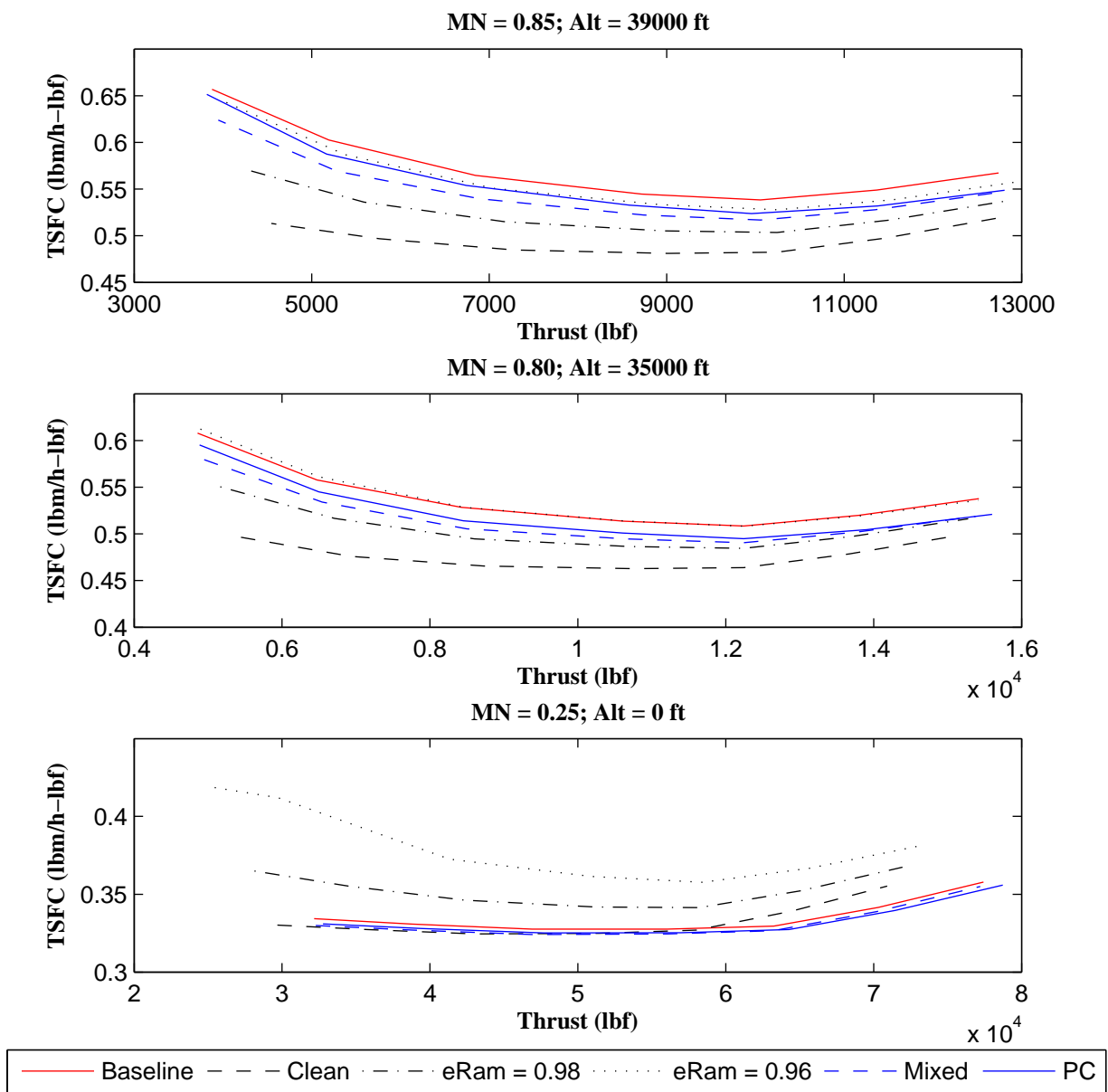


Figure 90: Throttle hooks for different models in the model hierarchy and for normal flight sizing conditions TOC (Top), cruise (middle), TKO (bottom)

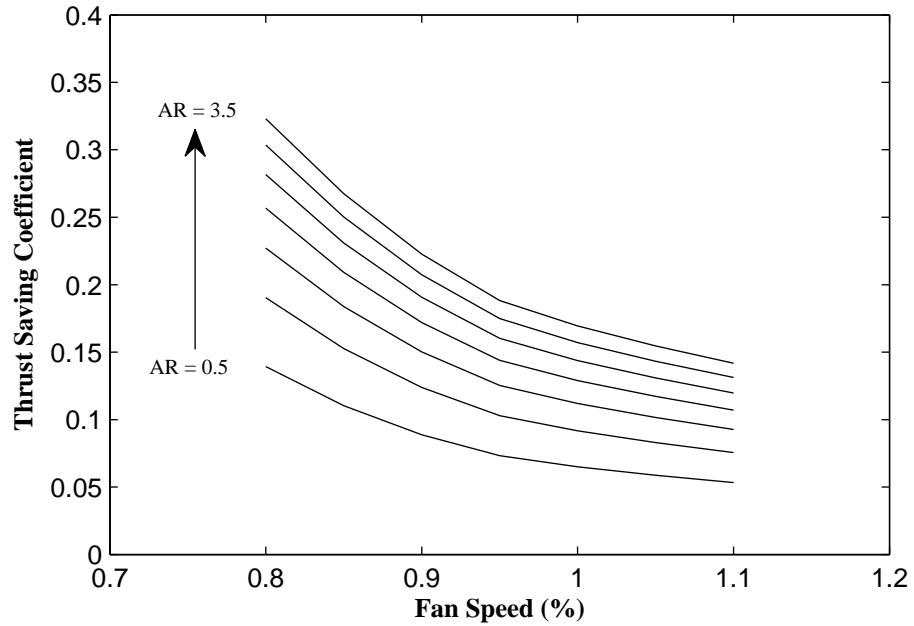


Figure 91: Variation in thrust saving coefficient at different speeds and for increasing inlet aspect ratio for the clean model (no losses)

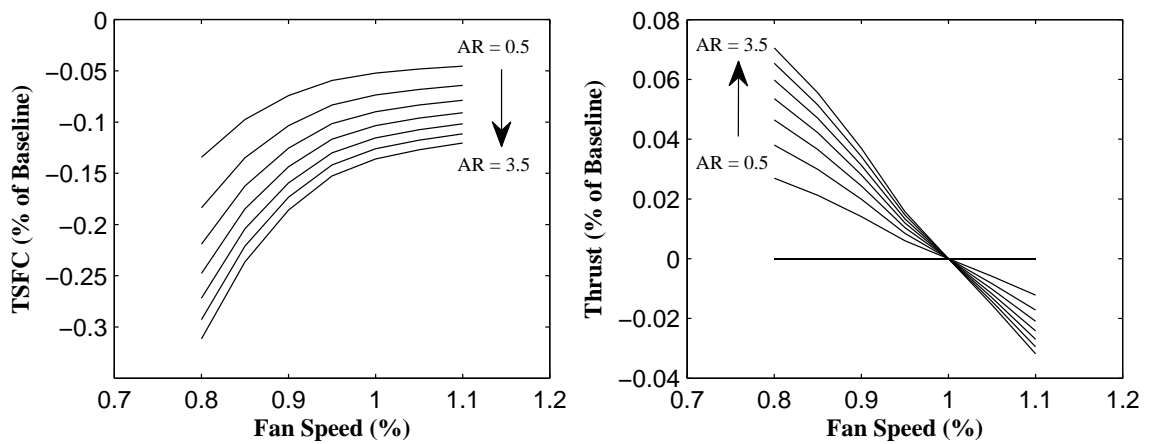


Figure 92: Variation of the deviation from baseline thrust and TSFC for the BLI system for a range of inlet aspect ratios for the clean model (no losses)

However, when the loss models are included, not only is the benefit at design point reduced significantly for increasing aspect ratio, but the trend is essentially reversed by the large non-linear increase in part power losses, as seen in fig. 93. Though it may be interesting to consider the prospect of having BLI improve part power performance significantly, the designer must consider the nature of the pre-entry stream-tube variation during part power operation and how that impacts both benefit and loss for the specific level of BLI chosen for a given vehicle. It must also be considered and properly modeled during engine deck formation and subsequent mission analysis routines for evaluating overall fuel burn performance, though the majority of the fuel will be burned at % speeds greater than 75%.

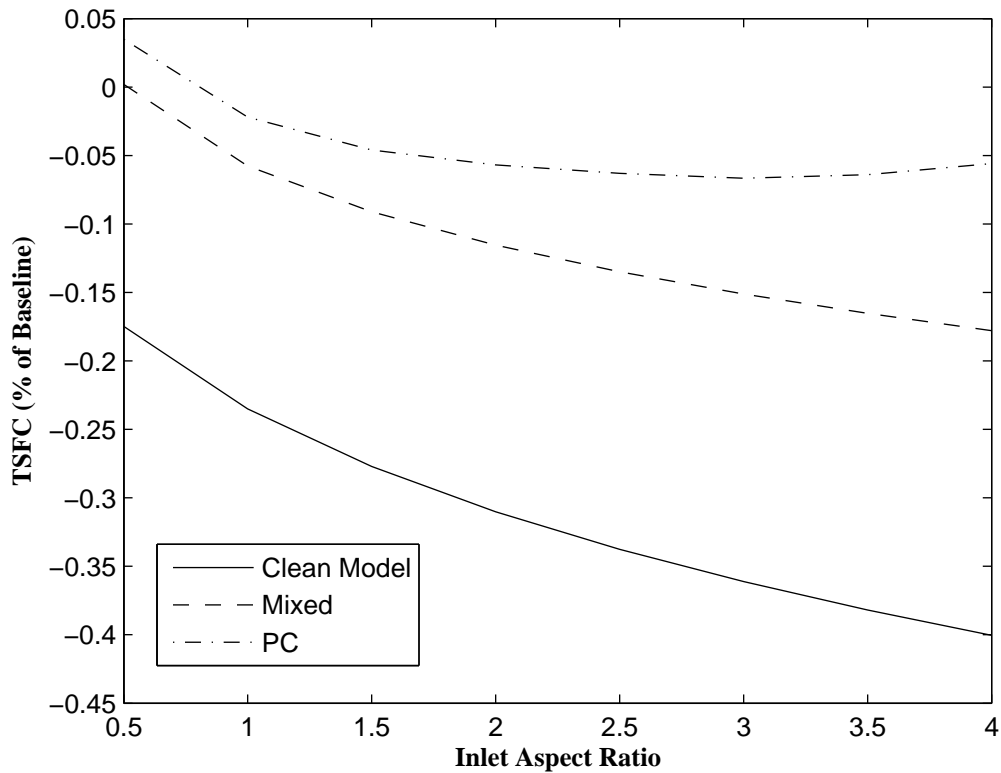


Figure 93: TSFC difference in percentage of the baseline at 75% speed for the clean, mixed, and parallel compressor models as a function of the inlet aspect ratio

Angle of Attack Variation

The angle of attack variation of the engine is an important aspect of a BLI system. The vehicle boundary layer, and indeed total drag, changes with the angle of attack, and therefore the thrust saving coefficient and inlet recovery tend to change with it as well. As such, this can impact the thrust and efficiency of the system in potentially harmful ways. The off-design angle of attack results for experiment 1 are shown in fig. 94 for the cruise flight condition. These results are for a system sized to a fixed thrust at an α of 2 degrees (which is why the thrusts all match for every model at 2 degrees). For the case of the clean model, the thrust saving coefficient once again drives the trends, and α increasing simply implies an increase in thrust and efficiency. For the mixed model, the TSC increases with α , but the inlet recovery decreases. This happens to keep thrust at approximately baseline levels with a small decrease in TSFC. For the PC model, which includes distortion related thrust and efficiency penalties, the thrust actually increases at lower angle of attack because of the decreased distortion, but decreases substantially at higher angles of attack for the same reasons. The TSFC curve exhibits an optimum value somewhere near the 2 degree point. The implication is that, for higher α than design, there may exist significant thrust loss for a BLI system due to distortion. There may even be thrust loss at lower angles of attack (in low loss scenarios) because of the decrease in thrust savings due to BLI.

At the takeoff condition (results shown in fig. 95), the difference is that the boundary layer thickness and TSC is very low for a much larger range of α . At higher speeds, the impact of α on the system is much more than at this low speed condition. Because of this, the system will be thrust deficient relative to the baseline if the cruise/TOC condition is the only one used to size it. As losses are added at high speed relative to low speed, this trend becomes more true, but when one considers losses at high α TKO then it may indicate a more critical condition to consider for

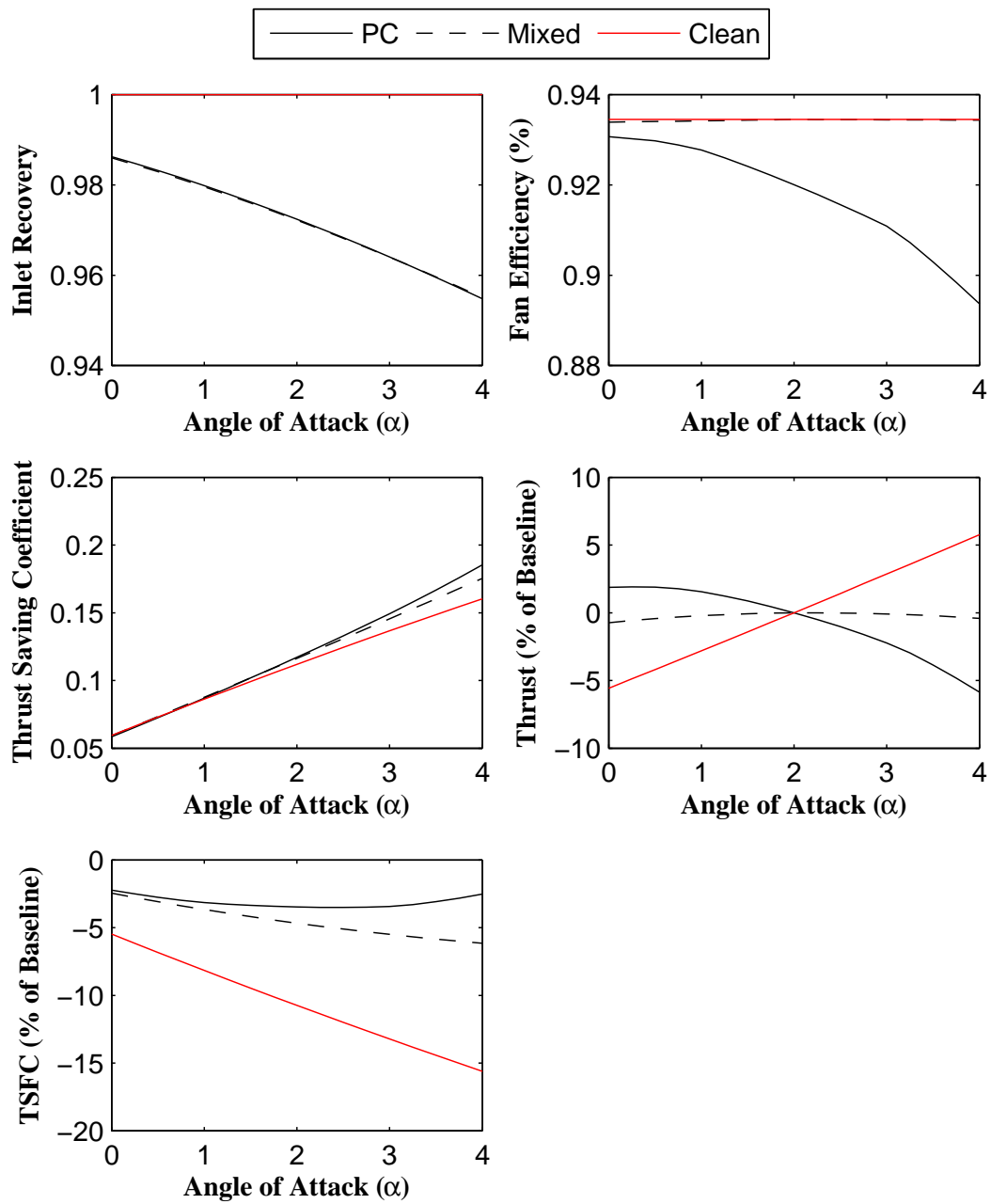


Figure 94: Trends of the system losses, thrust saving coefficient, and aggregate performance for a range of angle of attack at cruise with a design α of 2 degrees

thrust.

At a high enough α , the airfoil approaches boundary layer separation prior to entry. This massively increases the boundary layer thickness. For the clean and mixed models, this has the effect of increasing the thrust due to the TSC. However, for the parallel compressor model, the dirty sector stalls at an α of about 12 degrees for this case. The vehicle may need to have very high α at the take-off and landing conditions, possibly up to and beyond 16 degrees. For this reason, high α points should be considered likely candidates for a distortion constraint point when constructing the flight condition check vector in the vehicle matching phase. This will be discussed in more detail in chapter 6.

4.4.5 Experiment 1.d Results

Experiment 1-d is designed to investigate the influence of the boundary layer thickness and shape change on system off-design performance. To do this, a “Fixed Boundary Layer” model was created which assumes that all off-design conditions inherit the same boundary layer parameters for the wake recovery computation and the inlet model boundary condition as the design condition. However, the edge velocities are allowed to change with the free-stream conditions. Comparisons for Mach number and alpha changes are made using the parallel compressor model between the fixed and variable boundary layer model to ascertain the importance of BL property variability.

The difference between the fixed and variable boundary layer models in terms of thrust and efficiency are shown in fig. 97. The variation is on the order of +/- 1.5% for both thrust and TSFC with an increase in thrust at lower Mach/higher altitude and the opposite for high Mach. The angle of attack variation at cruise between constant boundary layer and fixed boundary layer is shown in fig. 97. The trends here are really just reflecting the overall change of performance with α since it only has the effect of changing the boundary layer and edge velocity. As such, the trends

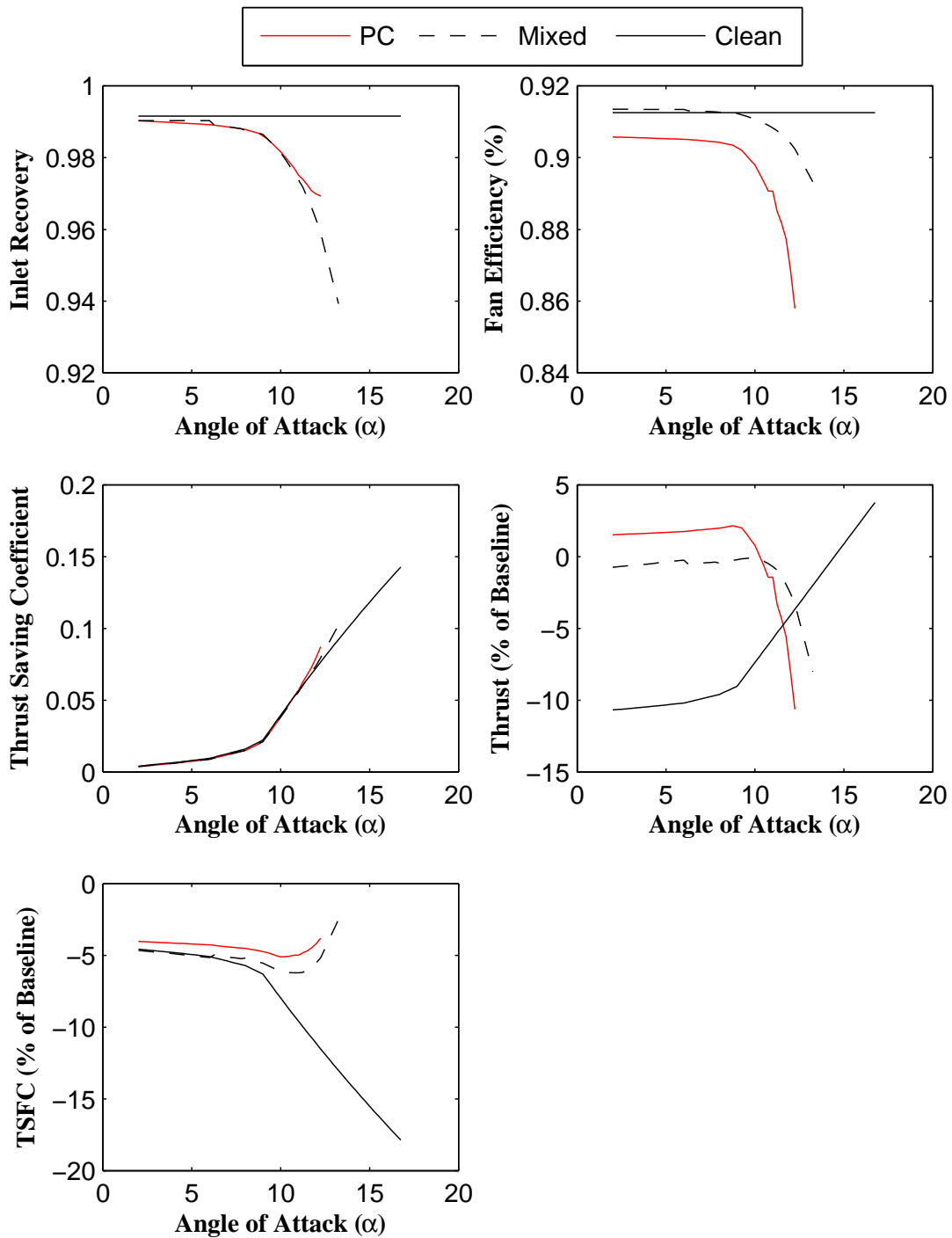


Figure 95: Trends of the system losses, thrust saving coefficient, and aggregate performance for a range of angle of attack at take-off (MN = 0.25, Altitude = 0 ft)

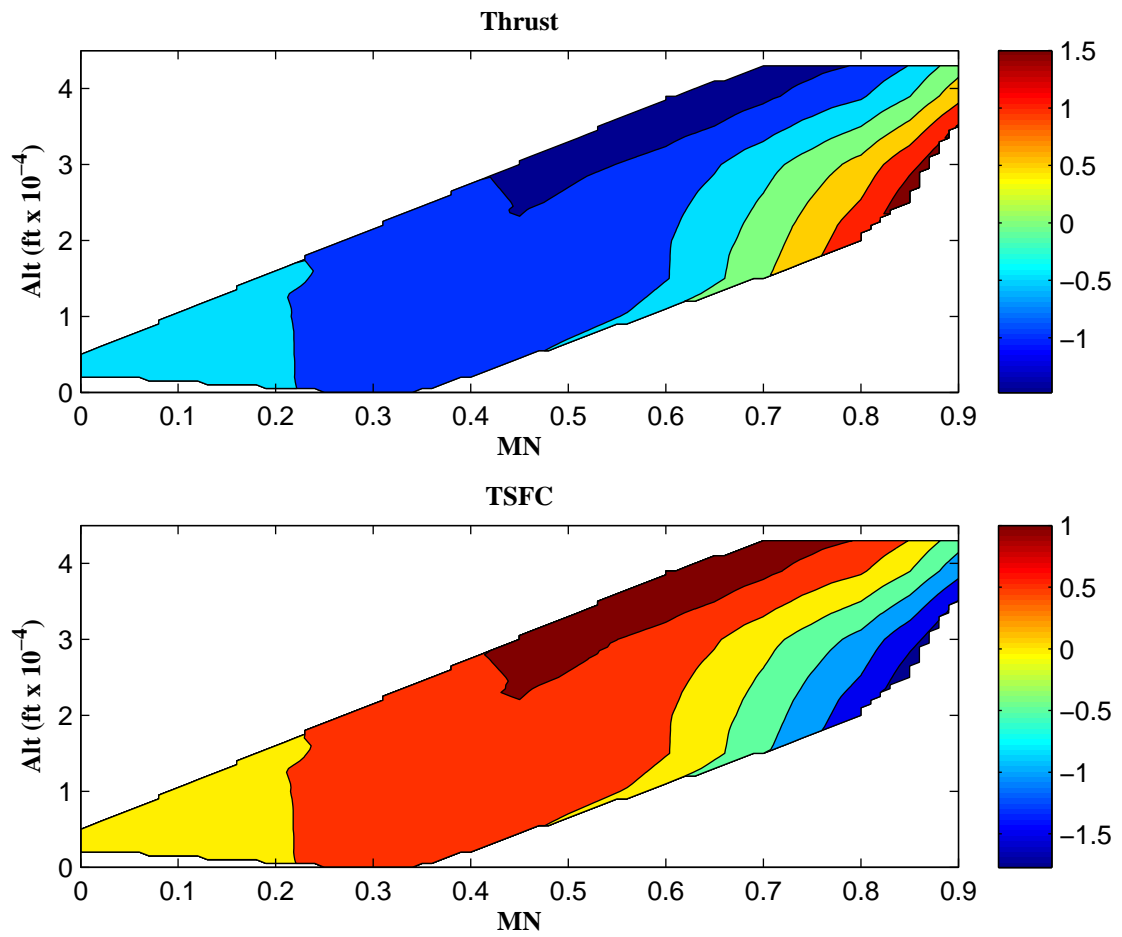


Figure 96: Percent difference of thrust (top) and TSFC (bottom) between the fixed and variable boundary layer models at different Mach numbers and a fixed angle of attack of 2 degrees

for TKO are not shown since they would be redundant with those shown previously for the α trends.

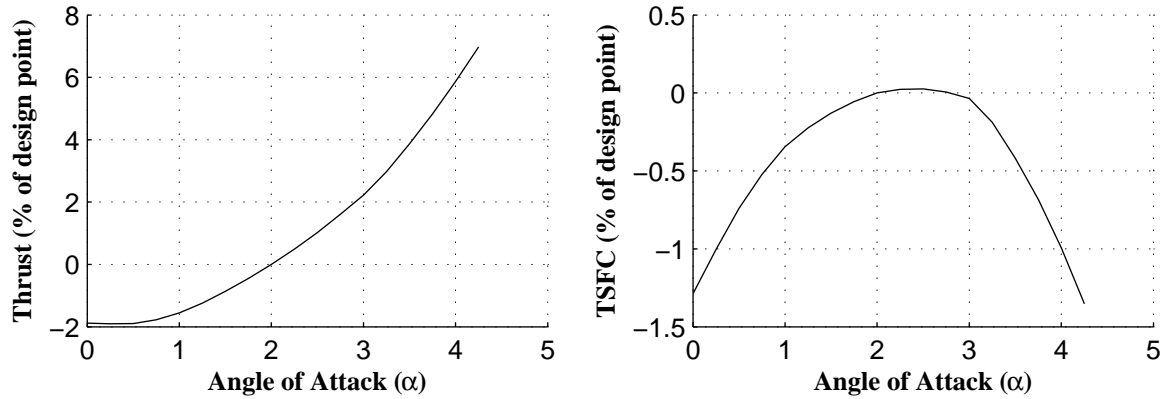


Figure 97: Percent difference of thrust (top) and TSFC (bottom) between the fixed and variable boundary layer models at different angles of attack at cruise

4.5 Experiment 2

The second experiment is designed to test hypothesis 2 which is repeated for the sake of the reader below:

Hypothesis 2: “The operability constraint limits the size of a propulsor in relation to the amount of boundary layer that it ingests.”

The experiment will therefore investigate the operability impact of BLI in relation to variations in fundamental propulsion system design variables that effect the engine/propulsor size. The results will show the propulsion system design space with stall margin constraints added to identify that this confirms the hypothesis.

A secondary aspect of experiment 2 is to determine the relative impact of compression system stabilizing actions on performance and operability. These measures include:

- Re-matching engine to a different operating line (higher design stall margin)

- Nozzle Area Trim
- HPC bleed flow re-circulation (inlet flow control)

4.5.1 Experimental Setup

The same model used in experiment 1 will be used for the second experiment. The operability measurement will be the stall margin of the fan. Stall margin can be measured in two ways: constant flow or constant speed. The equation for stall margin at constant flow is the following:

$$SMW = \frac{PR_{stall}(W_c) - PR(W_c, N_c)}{PR(W_c, N_c)} \cdot 100 \quad (116)$$

The equation for the stall margin at constant speed is the following:

$$SMN = \left(\frac{W_c/W_{c,stall}}{PR/PR_{stall}} - 1 \right) \cdot 100 \quad (117)$$

The main difference between these two measures is that the stall margin at constant speed takes into account the difference between current corrected flow and the stall point. This mainly matters if there is some curvature in the fan map speed lines such that pressure ratio declines relative to the stall line prior to reaching stall. This potentially creates a situation where the stall margin measure is not monotonically decreasing with operating line (R-line). Since this is the case for the baseline fan map for the lower speed lines, the stall margin at constant speed will be used. According to the classic parallel compressor model, the predicted stall point with distortion is the point at which the distorted sector reaches the stall line, therefore the dirty sector SMN will be used as the measure of operability.

The baseline design point stall margin is set to 27.92% SMN, which corresponds to about 15.45% SMW and is a standard quantity for a hi-bypass fan. The stall margin stack-up for a fan will include some substantial contribution for distortion depending on the application and flight requirements, but in general can be considered to be

about 5% SMW [77]. This would correspond to about 9-10% SMN available for distortion loss in the stack-up. As such, the constraint analysis which follows will start with a 10% allowable loss as a maximum allowable distortion loss and will be varied parametrically to determine how the design space constraint moves as the allowable is made more stringent.

Table 15: Table showing independent variables for experiments 2.a and 2.b

Experiment	Design Independents	Operational Independents
2.a	N_{eng} , Inlet AR, FPR/EXT	α , MN, altitude
2.b	Des SMN, Flow control bldfrac	α , MN, altitude, Byp Nozzle Area

4.5.2 Experiment 2.a Results

The first design space to be analyzed is the number of engines and the inlet aspect ratio design space, which fundamentally determines the design TSC. The results for this are shown in fig. 98 in the form of a design space constraint plot. The feasible space is constrained by the stall margin on the upper portion and on the right by the requirement to have at least 2 engines. The hypothesis is notionally confirmed by this plot by recognizing that the direction of decreasing engine capture height is towards lower thrust and higher aspect ratios. The hypothesis is more directly confirmed in figs. 99 and 100 where the engine capture height and thrust saving coefficient are plotted vs. SMN and showing a very nice collapse onto a consistent curve which confirms the hypothesis.

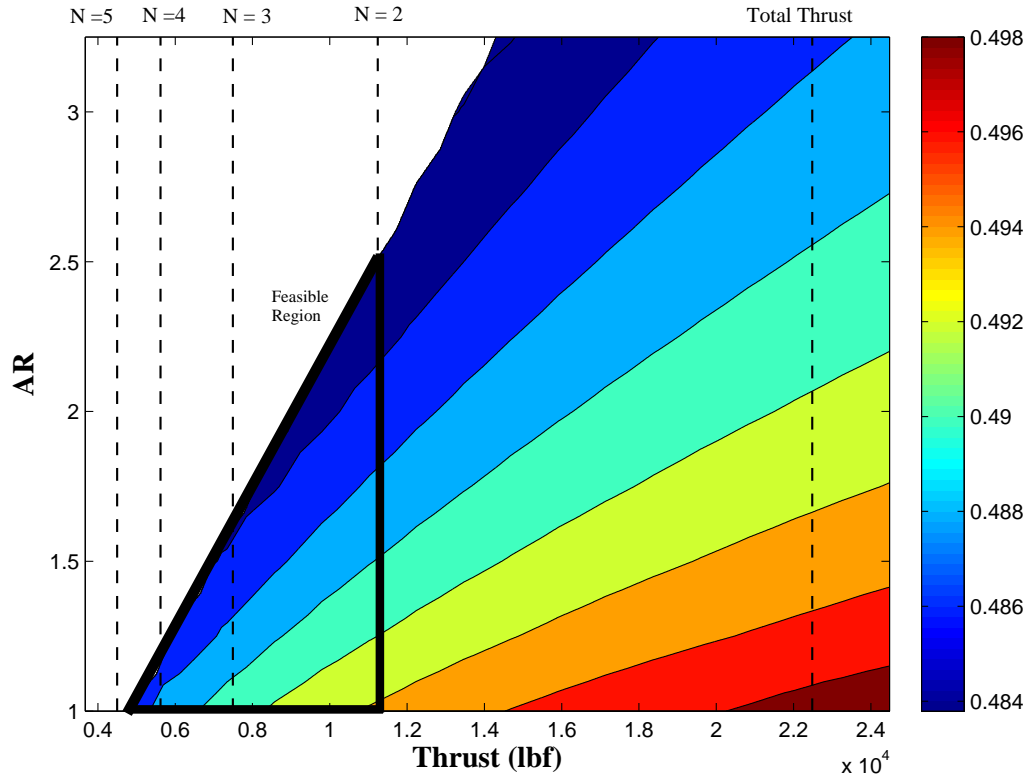


Figure 98: Contour plot of TSFC vs. thrust and AR with constraints shown assuming a minimum SMN loss of 9%

The usefulness of this hypothesis is that a 2-D constraint plot, such as that in fig. 98, can be collapsed to a scatter plot of TSFC and SMN vs. height to show trends. Fig. 101 shows this for increasing angle of attack with the infeasible inlet height regions highlighted. The minimum height which defines the feasible region is the point where the 18.9% SMN horizontal line intersects with the SMN vs. height curve (green points). As the α (and BL thickness increases, the constraining height level is increased, reducing the options available in terms of propulsion system architecture and the achievable TSC of the system.

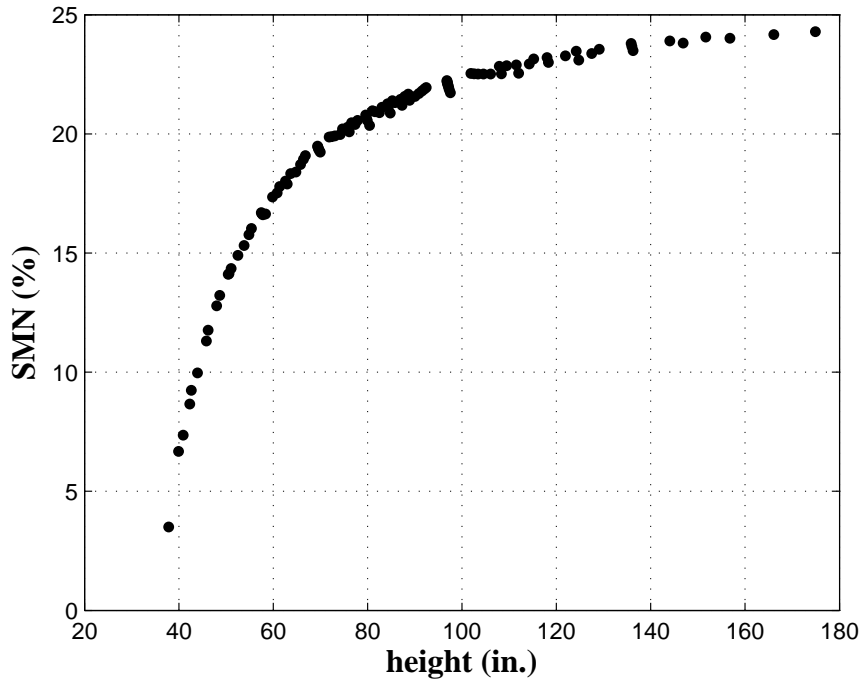


Figure 99: Plot of SMN vs. height for the data generated by varying inlet aspect ratio and the number of engines

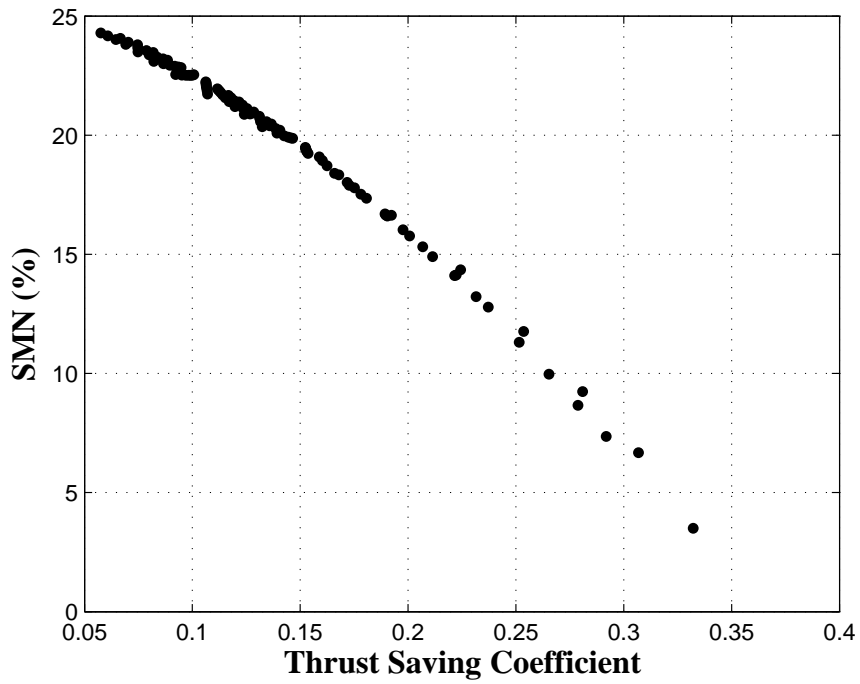


Figure 100: Plot of SMN vs. TSC for the data generated by varying inlet aspect ratio and the number of engines

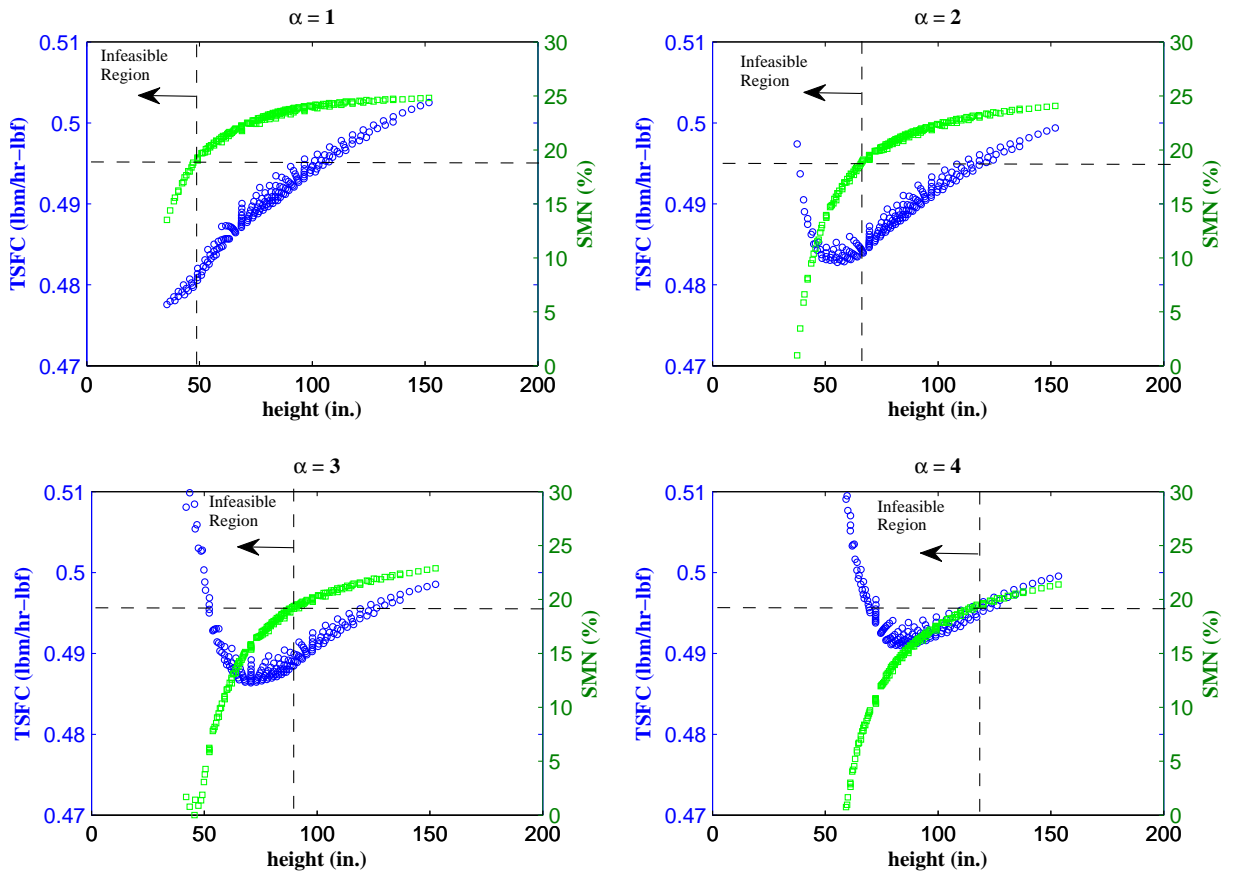


Figure 101: Constrained TSFC plot showing that the height/SMN relationship can be used to constrain the TSFC. Feasible space is shown for progressively thicker angles of attack.

The trends of the stall margin over the cycle design space are shown in fig. 102 for different aspect ratio values. The SMN doesn't change much within the space, but it is typically worse at lower fan pressure ratios and extraction ratios (smaller BPR/fan diameter). At higher aspect ratio values, the slope with respect to the fan pressure lines change and the SMN only declines slightly at lower FPR relative to high.

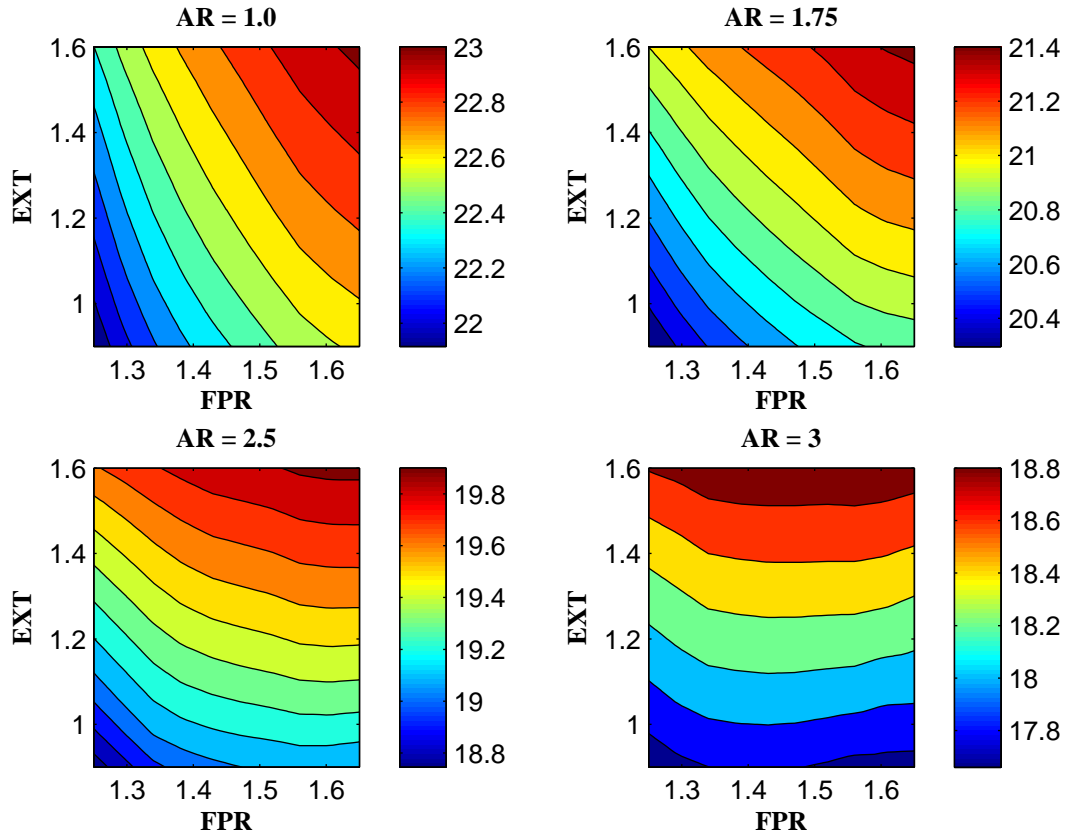


Figure 102: Contour plot of distorted sector stall margin for different inlet aspect ratio values

With FPR, the designer cannot completely collapse the constraint onto the single height variable since the design FPR impacts the stall margin loss significantly as lower FPR is more sensitive to the distortion in the PC model. This trend is illustrated in fig. 103. The lines of constant FPR seem to fall onto a single height vs. SMN correlation, but the change in FPR moves each of the lines to the left (higher FPR implies smaller engines and less distortion loss). In any case, it seems the changes in inlet aspect ratio and engine number have a much bigger impact on the size of the engine in relation to the boundary layer and therefore the stall margin. However, this does show that increasing the BPR (something that's generally desirable anyway) can be a good way to increase the operability by a small amount for high TSC designs. We

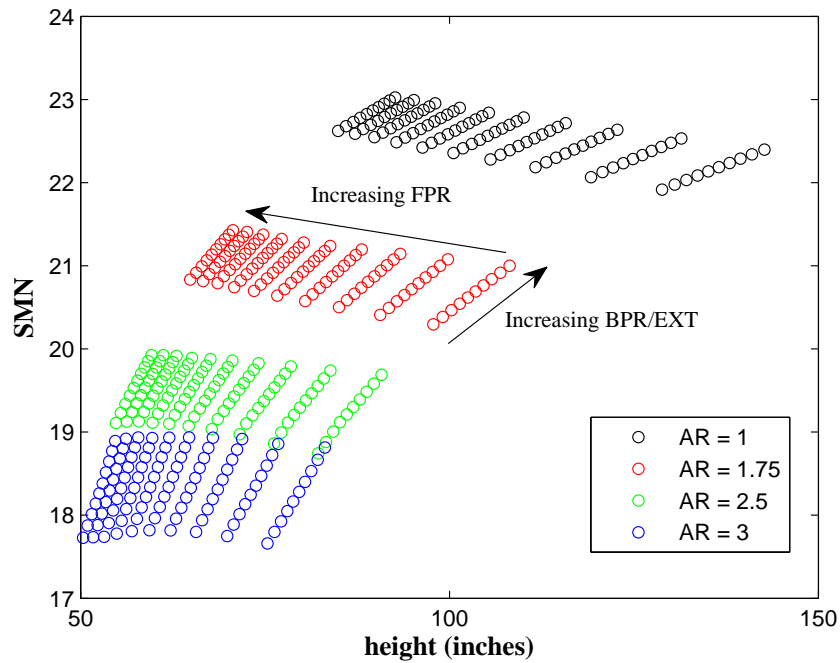


Figure 103: Contour plot of distorted sector stall margin for different inlet aspect ratio values

have thus far shown the impact of certain design choices which change the stream-tube height on the stall margin of the engine. We now look at how these changes might affect the TKO condition, given that this is typically a very critical stall point for UHB engines. Fig. 104 shows the take-off stall margin loss at the sea-level condition due to the BLI related distortion without the use of a variable area nozzle. Clearly as the angle of attack increases the SMN gets quite worse relative to the baseline. The data also shows that hypothesis 2 extends to the take-off condition because the higher inlet AR curves reach stall at lower angles of attack. If we impose an angle of attack requirement at that point, then the constraint becomes more stringent for increasing height. This implies that if the hypothesis applies at the design point condition (at high speed), then it should also apply to constraints at off-design conditions by constraining the possible angle of attack. However, the variable area nozzle may be an effective means of re-opening the design space for off-design conditions, especially at

the low altitude/low speed conditions which require higher lift coefficients and angle of attack. Chapter 5 will discuss the topic of the most critical conditions and sizing in a multi-design point framework with BLI including operability.

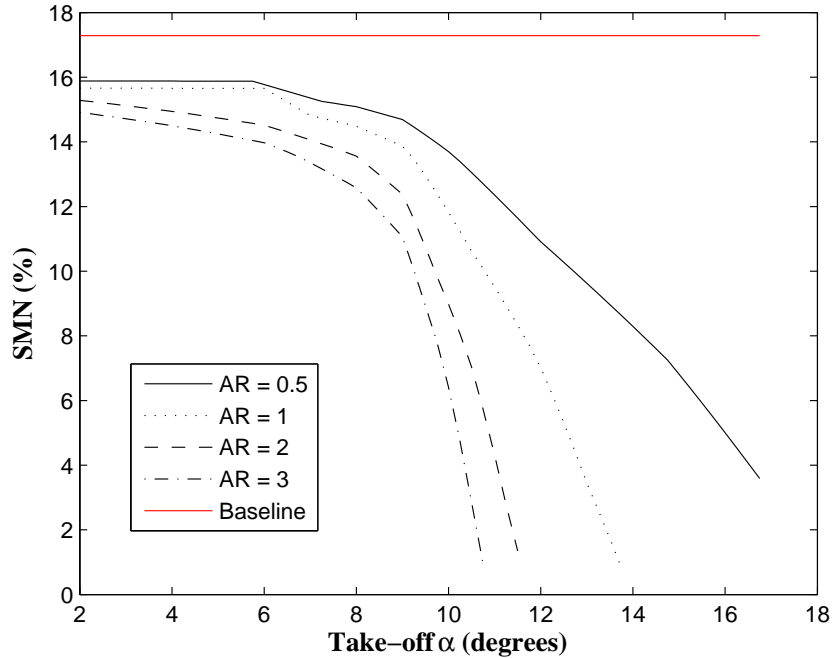


Figure 104: Take-off stall margin vs. vehicle angle of attack for several angles of attack (3 engine configuration)

4.5.3 Experiment 2.b Results

Experiment 2.b is designed to analyze the efficacy of different stabilizing mechanisms in opening up the design space. However, since these mechanisms penalize the cycle efficiency, the TSFC benefit design space closes. Therefore, this experiment will compare the un-stabilized design spaces from experiment 2.a with the design spaces including stabilization. The expectation from hypothesis 2 is that the cycle penalties required to satisfy the SMN constraint should increase when the SMN decreases with the engine stream-tube height. We would expect to therefore continue to see some height limitation within the TSFC space when stabilization is included.

Inlet Flow Control

Studies of inlet flow control with application to BLI have been conducted, with the major study being done by Owens and Gorton [68]. The purpose of the study was to determine the efficacy of using flow control for distortion reduction and also identify the flow requirements to achieve sufficient distortion mitigation. The study was conducted at large transonic Mach of 0.85 which represents a cruise or top-of-climb type flight condition. Fig. 105 shows a curve derived from the study data which correlates the amount of jet flow into the inlet with the circumferential distortion index. The

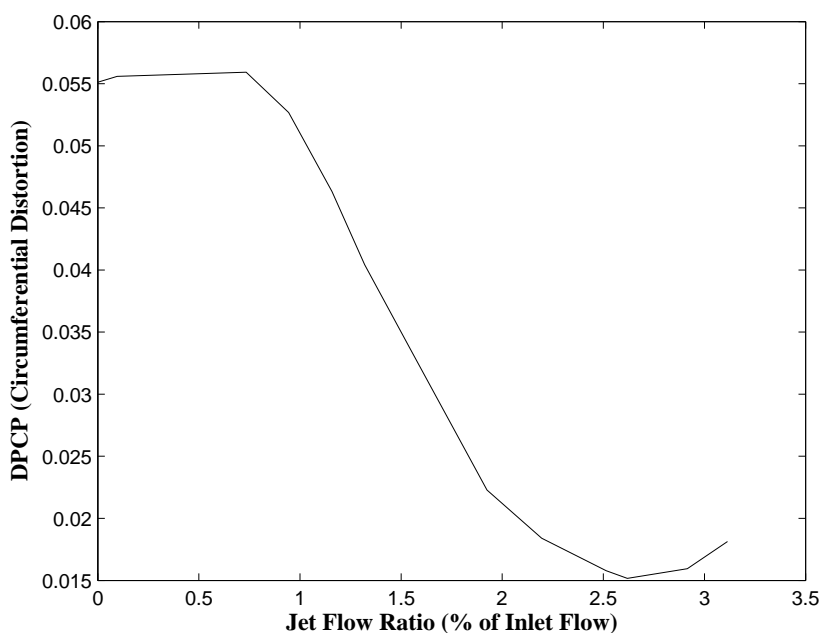


Figure 105: Correlation of circumferential distortion against inlet jet flow ratio (% of inlet flow)

required jet flow for significant distortion increase is a few % of the total inlet flow. However, the jet flow static pressure ratios required increase with the flow demand and were at a maximum of 3. This means that the flow will need to be taken off of (most likely) the first few stages of the HPC (or some other compression source depending on the architecture). Therefore, though the required flow demand is small in

terms of the inlet, for high bypass ratio designs the percentage of core flow extracted would be very large and the TSFC penalties would be significant.

To model this, an inlet flow control bleed was setup to connect an HPC bleed port to the inlet. This has the effect of moving the operating line farther out from the stall region. The results, shown in fig. 106, show the poor ability of the inlet flow control

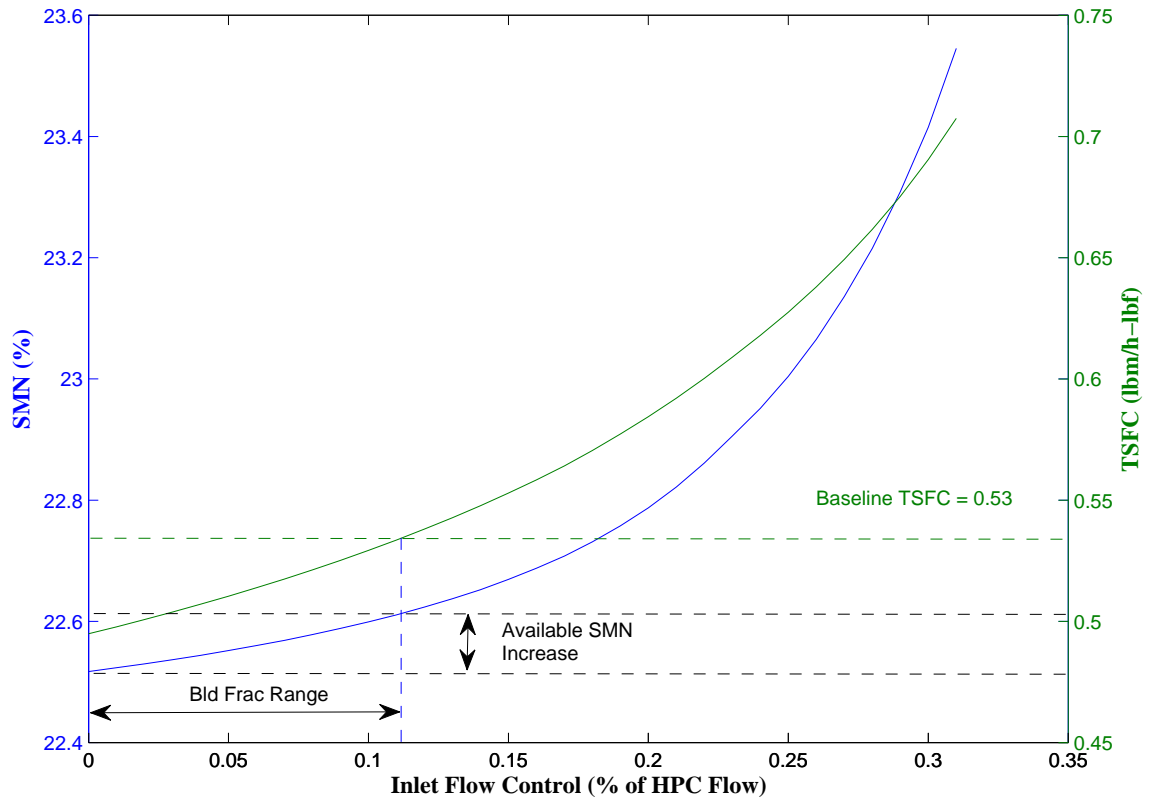


Figure 106: Plot of stall margin (primary y-axis) and TSFC (secondary y-axis) for increasing core bleed extraction ratio. FPR = 1.4, EXT = 1.21.

to reduce the distortion without increasing the fuel consumption substantially by reducing the core flow. This is consistent with the findings from the study of Owens and Gorton: namely that a substantial amount of inlet flow must be supplied to deal with the distortion (2-3% of inlet flow or 25-30% of core flow). Since the TSFC increase is so much larger than the SMN gain, because of the core flow requirement, it stands to reason that the constraint identified in hypothesis 2 is still active even

when flow control is used.

Fan Re-Match

The fan re-matching is essentially the ability to move the operating line on the fan map in order to provide more stability margin for the fan. This is tantamount to increasing the corrected flow and decreasing the pressure ratio at the design point for the clean sector. The dirty sector also moves outward as the design operating line is increased, since it moves to the point which balances the exit static pressure. The result is that the flow annulus area must increase to accommodate the increased flow, and the TSFC may be impacted depending on the relative changes in efficiency for the different sectors.

The re-match solver setup is somewhat complex but revolves around the idea of matching the average operating point as close to the desired clean map point as possible within a specified dirty sector stall constraint. As the distortion gets large, the dirty and clean sector operating points move farther apart while the average remains stationary (because the solver is setup to maintain it as such). When the stall constraint is reached, the average operating line (R-line in NPSS) must be increased to move both the dirty and clean sectors to higher stall margin values.

With this approach, a sufficient stall margin can be maintained for every design except for those which have sufficient distortion to drive the clean sector into the choked region (far right) of the speed line after the re-match. This is not to say that the clean sector would necessarily choke under such conditions, but only that the parallel compressor model can no longer be used. This is because, under choking conditions, perturbing the location of the clean sector operating point will have no impact on the flow and exit static pressure thus yielding a singular jacobian matrix in the solver solution procedure. The thrust/inlet AR design space is shown in fig. 107 with color contours of stall margin shown. In this case, a minimum stall constraint

of 22% is used. The gradient of stall margin is clearly seen in the bottom right corner where SMN is greater than the constraint. As the engines are made smaller and capture height is decreased (increasing the distortion), the SMN decreases and eventually hits the constraint line. Every point after that is maintained at a value of 22% using the re-match solution procedure. With this value of the SMN constraint, essentially every viable propulsion architecture (2-5 engines) requires some degree of rematch. The consequence of this rematch in the constrained region is shown in fig. 108 which shows color contours of the total fan inlet annulus area (a measure of fan diameter and inlet size).

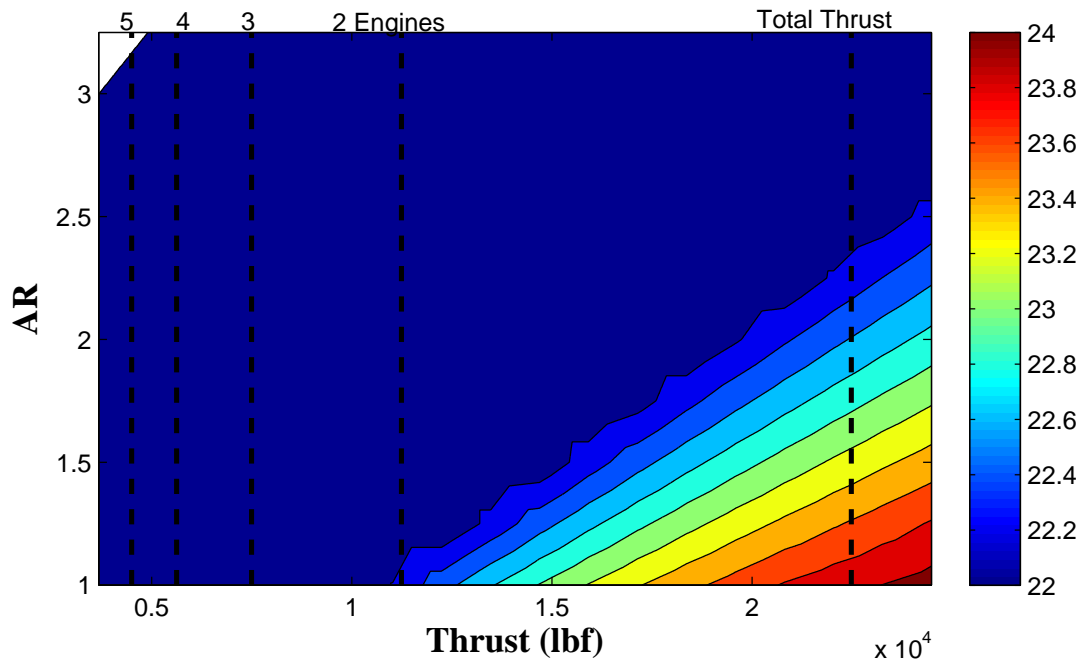


Figure 107: Contour plot showing the stall margin with a SMN constraint of 22 applied with the re-match solver logic

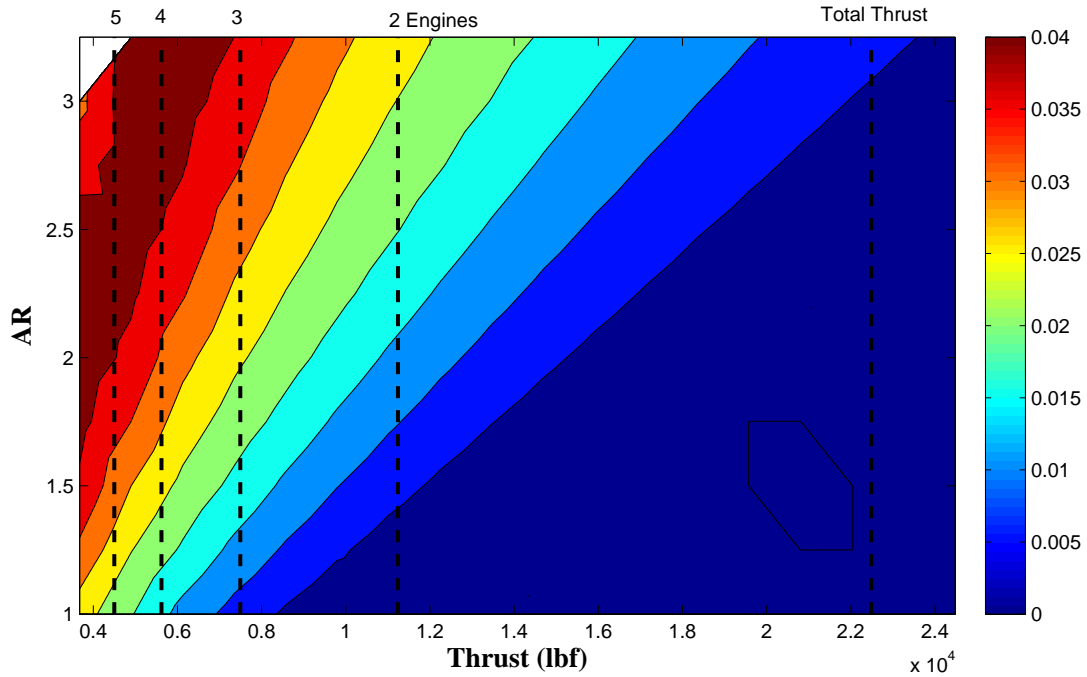


Figure 108: Contour plot showing the effect of engine rematch on area increase in the design space region which is height/stall constrained

The relation between this and hypothesis 2 is really illustrated in fig. 109 which shows the general penalty of doing the rematch. This is to say that an increase in the fan area of the propulsion system on the order 0-5% must accompany the increase in stall margin. An interesting feature of the parallel compressor model is that the TSFC tends to drop a little bit (though relatively constant) until the choking region. This is really a feature of how the fan map efficiency contours behave and is probably not a truly accurate representation of the efficiency at such extremes of the modeling space with very high distortion levels, small stream-tube to boundary layer ratios, and a compressor designed to operate near choke (something generally undesirable anyway). In any case, the point remains that, although the impact of hypothesis 2 can be mitigated using available design degrees of freedom, such as the operating line, it is clear that doing so would come at some cost and therefore place limits on how much could be done while still maintaining an overall performance benefit.

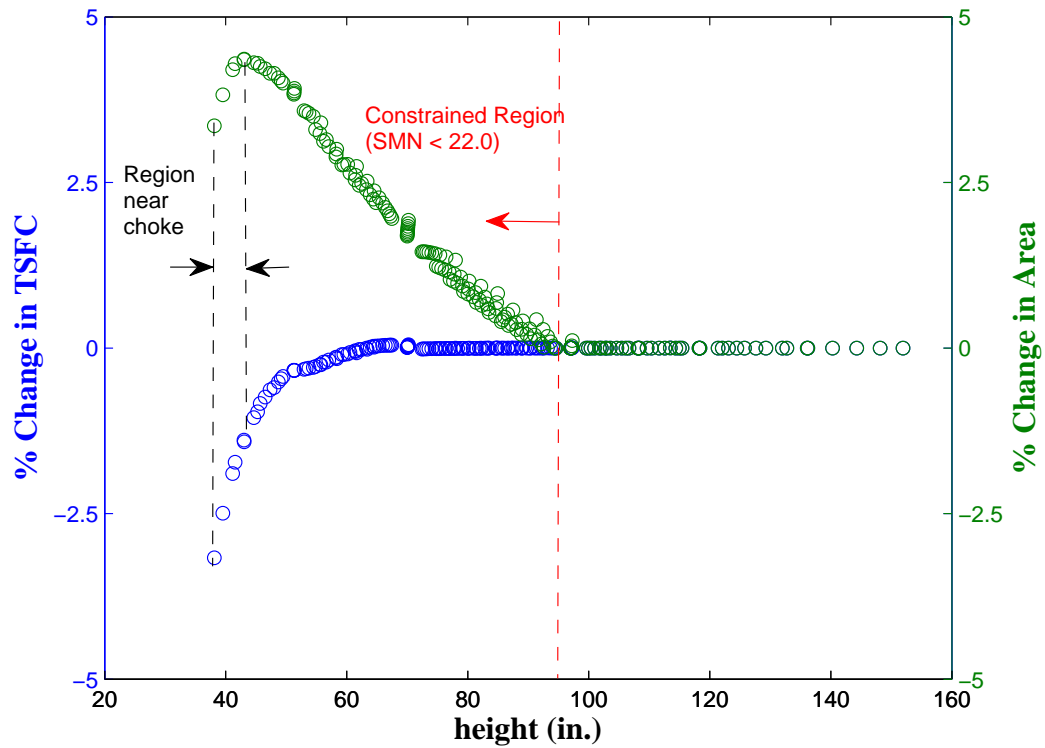


Figure 109: Plot showing the effect of engine rematch in the region which height/stall constrained. The relative change in area is shown (green) along with relative change in TSFC (blue).

4.6 Summary of Chapter 4

The preceding chapter demonstrated the BLI modeling phase of the BLIPSS methodology on a sample problem and attempted to validate hypotheses 1 and 2. Both hypotheses were confirmed, at least for the sample problem. Some of the main takeaways from experiment 1 and experiment 2 are listed in the sections below.

4.6.1 Experiment 1 Summary

- Hypothesis 1: There is a strong relationship between the size (and shape) of the stream-tube ingested, the thickness of the boundary layer, and system performance (losses and benefits)
- Failing to account for variation in the system losses with the stream-tube size can yield to improper choices for design variables which impact the BLI system and inaccuracy during performance estimation
- Generally increasing the thrust saving coefficient by means of widening the stream-tube or distributing the propulsors is accompanied with increasing losses and diminishing returns on performance
- BLI tends to increase performance at lower fan pressure ratios (larger fan diameter means more BLI), but lower FPR is also more sensitive to system losses
- The angle of attack of the vehicle has a strong impact on performance in both design and off-design. Designers should take special care to understand the interaction between the vehicle orientation and engine performance.
- The performance at off-design flight conditions depends crucially on how the vehicle boundary layer profile changes with Mach number (and to a lesser degree, altitude). Assuming a fixed boundary layer profile and scaling by free-stream velocity generally yields a few % error.
- Performance at part power tends to improve because of the increasing thrust saving coefficients, however the influence of the pre-entry zone on the inlet recovery and fan losses counteracts this effect significantly.

4.6.2 Experiment 2 Summary

- Hypothesis 2: The conceptual design space of a BLI propulsion system is limited by a stall margin (circumferential distortion) constraint which places limits on the height of the ingested stream-tube in relation to the boundary layer thickness.
- This additionally places limits on design choices such as the number of engines and the aspect ratio of the inlet (which in turn limits the amount of BLI which can be ingested)
- In general, lower FPR designs are more sensitive to distortion than higher FPR designs, though higher FPR designs tend to have worse distortion because they are smaller.
- The methods for mitigation were found to be capable of restoring a bit of stall margin, but also came with costs in terms of engine size/weight and TSFC (meaning that the constraint is still present in the form of a penalty function in the constrained region).

CHAPTER V

ARCHITECTURE INTEGRATION PHASE

The following chapter will demonstrate the “Architecture Integration Phase” on the HWB vehicle with turbofan BLI engines. Hypotheses 3 and 4 will be investigated with corresponding experiments and some conclusions will be drawn regarding the method, the hypothesis, and their general validity.

5.1 AI Phase Overview

All of the results from chapter 4 assume that each engine in the architecture experience the centerline boundary layer of the baseline HWB vehicle. The architecture integration phase is the procedure by which the MDP methodology is augmented to account for the difference between the BLI installation effects across the propulsion system architecture due to differences in the local airframe aerodynamics. The steps in the process are as follows, (as illustrated in fig. 11):

1. Specify number of propulsors
2. Specify inlet locations
3. Specify number of unique inlet conditions
4. Specify design rules
5. Specify power management rules

Each of these steps will be implemented in this chapter for a 3 engine architecture on the baseline aircraft.

5.2 Implementation

A crucial concept for implementing the process – and, in fact, which makes MDP possible – is the concept of engine “assemblies” [2]. The NPSS program is object oriented, and an “assembly” is an instantiation of a particular propulsion architecture or set of components. Each assembly has its own solver, and can additionally interact with the global NPSS solver which employ the Newton-Raphson solution procedure. In a standard MDP setup, each flight condition is instantiated within its own assembly. During each solver pass, the primary aerodynamic design point is executed first, and other assemblies which are considered to be in off-design have the design point engine passed to them and are run in sequence after the design point. With the architecture integration phase, each unique inlet/propulsor combination requires its own assembly, meaning that the total assemblies required is the multiplication of the number of flight conditions in the MDP and the number of unique inlet conditions. Another feature of the AI phase addition is that there can be multiple design points at a given flight condition, depending on the choice of the design rules (see chapter 3 for more detailed discussion). If a propulsor with a unique inlet condition is not an aerodynamic design point, according to the chosen design rule, then it must inherit the engine definition from one of the aerodynamic design points and a power management strategy which relates the operation of the two engines within the solver.

5.3 Experiment 3

5.3.1 Experiment 3 Design Specifications

The number of propulsors for this architecture is three (turbofans), with 2 engines at some “to be determined” outboard location and 1 at the inboard centerline of the vehicle. This means that there are 2 unique inlet conditions. Each of these inlet conditions will be represented by an assembly in the NPSS model. For this test, there

will only be a single flight condition, so the number of assemblies required is two.

Power Management and Control Rules

Experiment 3 is designed to compare the use of the AI phase in the BLIPSS design process with alternative approaches of modeling architectures. The comparison will be made between the “single inlet” standard assumption and the “single engine” model. The design mapping matrix is shown in tab. 16.

Table 16: Design point mapping matrix for the 3 engine architecture for experiment 3.

	X = Not used	D = On-Design	O = Off-Design		
Design Option		Core/HP Spool	Fan/LP Spool	Design Rule	PM Rule
Single Inlet	Inboard	D	D	None	None
	Outboard	X	X	None	None
	Inboard	X	X	None	None
	Outboard	D	D	None	None
Single Engine	Inboard	D	D	None	N1
	Outboard	O	O	None	N1
	Inboard	O	O	None	N1
	Outboard	D	D	None	N1

For the single inlet condition, there is no required design or power management rule (see eq. 75). For the single engine case, there is a consistent engine/propulsor designed but the difference between the inlet conditions is accounted for by having a separate assembly within the model. For this case, there is only a single ADP required, and therefore the number of power management rules is one. The PM rule used here is the assumption of constant fan speed (N1 is the low pressure spool corrected RPM).

Thrust Matching Relations

For the single inlet case, the thrust matching relations are the same as for a normal engine design, since there is only one engine. For the single engine case, the thrust matching relations need to be augmented to account for the inlet condition and BLI difference. The thrust matching relation is as follows:

$$F_n = F_{n,Inboard} + 2F_{n,Outboard} \quad (118)$$

and fuel flow is:

$$W_f = W_{f,Inboard} + 2W_{f,Outboard} \quad (119)$$

then the TSFC is the ratio of the total fuel flow between the three and engines and the total vehicle thrust, rather than the TSFC per engine as in the single inlet case.

5.3.2 Wake Correction Method

The wake correction method is another approach that can be used to account for differences in the BLI wake recovery across the upper surface of the vehicle. This was used, for instance, by Sato et. al. [79] in their HWB BLI design methodology. The approach essentially corrects the power savings of BLI based on the wake kinetic energy thickness variation as a function of the propulsor location. Their results showed a more conservative estimate of the power saving coefficient because the vehicle taper ratio causes a reduction in the viscous drag at the outboard sections. The primary difference between the BLIPSS methodology and the wake correction approach is that the BLIPSS method can also account for differences in the inlet recovery along the propulsor array and also sizes the propulsion system accounting for wake difference. The BLIPSS architecture integration approach will be compared to both the single inlet assumption and the wake correction method in experiment 3.

5.3.3 Experimental Setup

Experiment 3 is designed to demonstrate 2 primary features of the architecture integration method: first, that it can achieve the desired goal of quantifying architectural impacts on the BLI system through sizing; second, that the difference between this method and both the single inlet approach and the wake correction method are larger with increasing difference between the local boundary layer. This will be done by demonstrating the difference between the boundary layer at different lateral locations on the airframe and then implementing each of the methods and comparing the performance results of the different approaches. The expectation is that the single inlet approach will deviate the most from the proposed method, while wake correction will deviate somewhat less. The engine model and design approach is the same as that used for experiments 1 and 2 with a single design point at the cruise flight condition and the same total vehicle thrust value used.

5.3.4 Experiment 3 Results

Figs. 110 and 111 show the variation in boundary layer thickness parameters (displacement and momentum) as the outboard location of the engine increases. These values are predicted using the XFOIL tool by varying the vehicle chord as a function of the lateral location. It should be noted that, in these figures, a “y location” of unity represents the maximum allowable outboard position on the center body of the HWB and not the wing tip. The trends show very clearly that the boundary layer thickness decreases with the chord at the outboard locations. The momentum and displacement thicknesses decrease by roughly the same percentage, though they deviate somewhat at higher outboard locations as shown in the shape factor trends in fig. 114. The boundary layer edge velocity at the point where the pre-entry to the inlet begins also increases substantially. This is because of the requirement that the engine

maintain the same distance from the trailing edge, so that the axial location of the inlet hilite area must necessarily move forward on the airframe regions to higher local velocity. The amount of “wake recovery” (BLI thrust benefit term) also decreases as the boundary layer reduces in thickness at the outboard sections as shown in fig. 112. This is because the far downstream wake thickness at the “Trefftz” plane is decreased so that the total amount of thrust recovery from the BLI effect per unit stream-tube width is reduced. Finally, a change in angle of attack at the cruise point yields a substantial step change in the boundary layer thickness parameters and edge velocity.

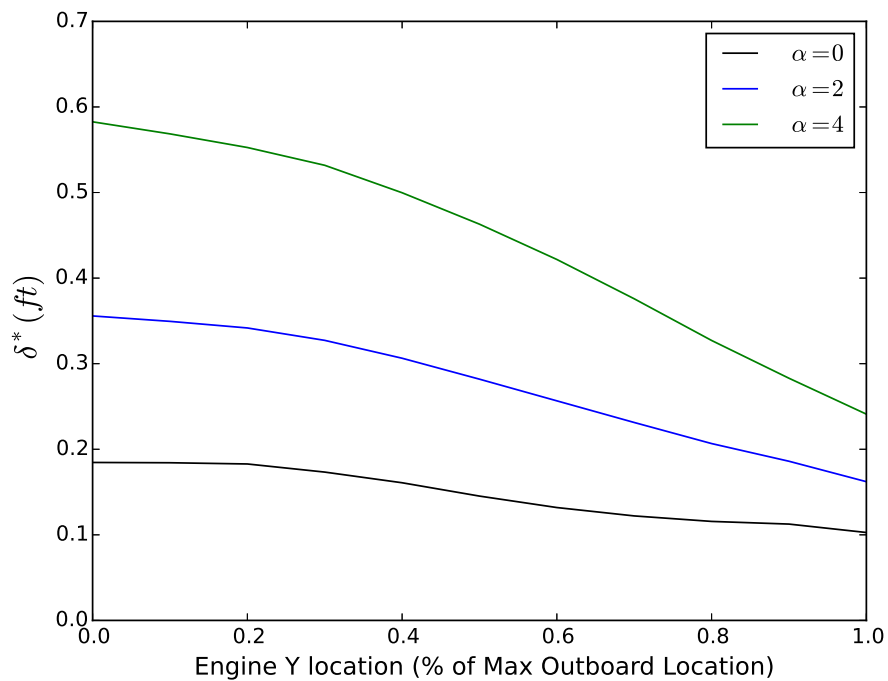


Figure 110: Boundary layer displacement thickness variation with engine outboard location.

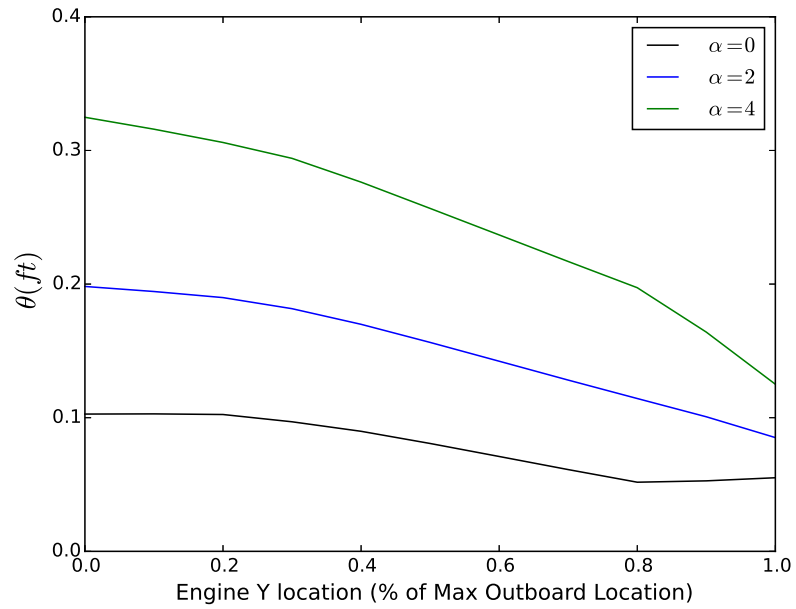


Figure 111: Boundary layer momentum thickness variation with engine outboard location.

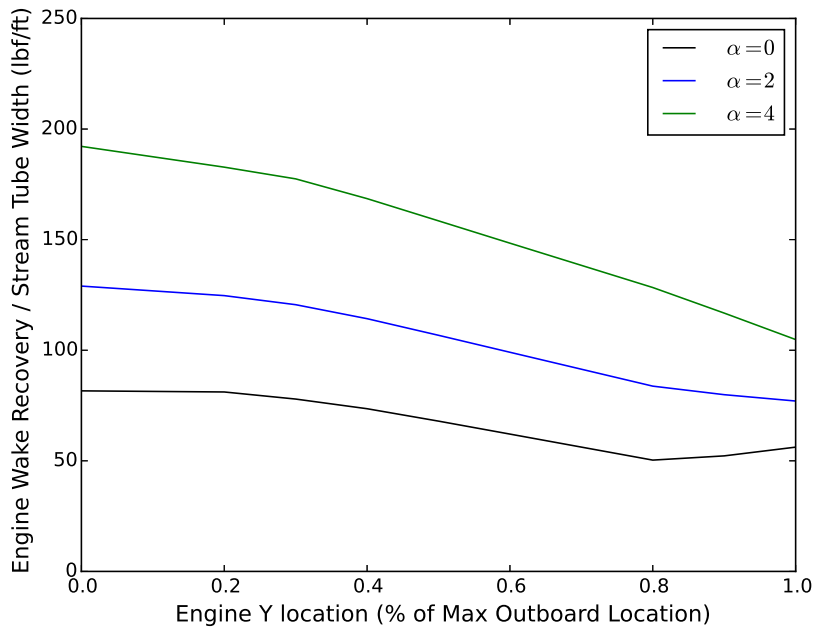


Figure 112: Engine BLI wake recovery per unit stream-tube width variation with engine outboard location.

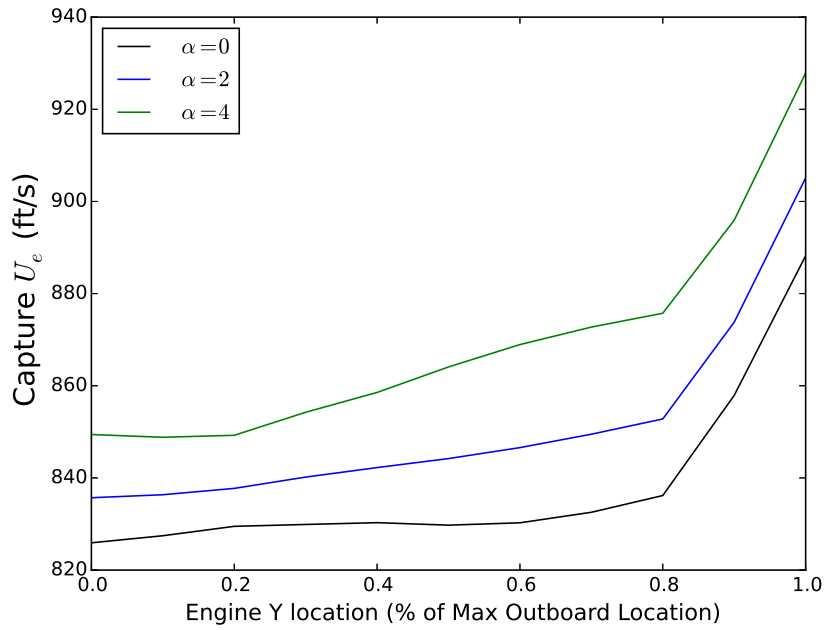


Figure 113: Boundary layer edge velocity variation with engine outboard location.

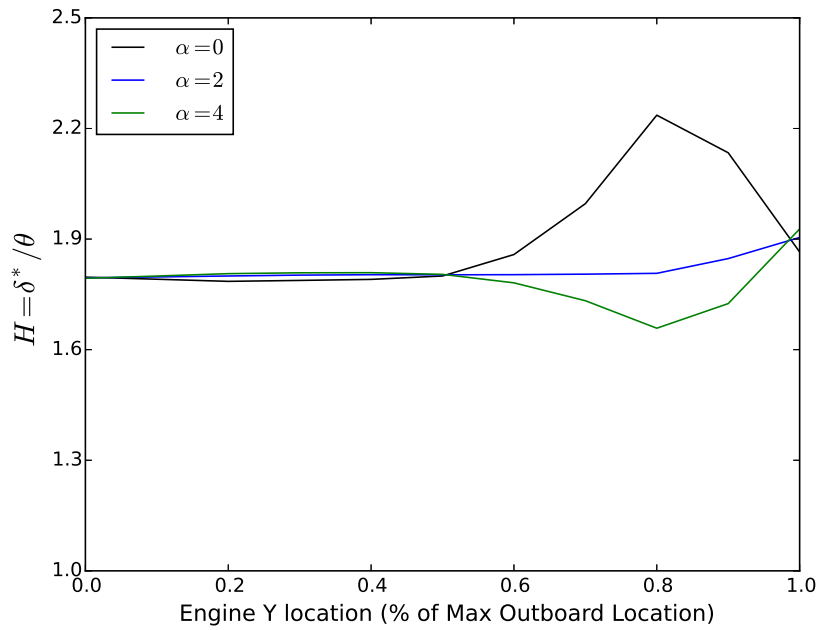


Figure 114: Boundary layer shape parameter variation with engine outboard location.

Single Inlet Evaluation

The next step in the experiment is to evaluate the single inlet design point model. This is the approach that was used for experiments 1 and 2 and in the majority of published BLI studies. The inlet location for the single inlet SDP sizing was varied to get a sensitivity of the inlet performance which is shown in figs. 115-118. Perhaps the most interesting aspect of these results – which is related to hypothesis 1 – is that there is a trade-off between the thrust saving coefficient and the inlet recovery/fan efficiency. The former depreciates as the engine is moved outboard, since less drag is ingested, but the situation with regard to the losses improves. This effect is more drastic for the higher design angle of attack scenarios (losses improve more while benefits degrade more).

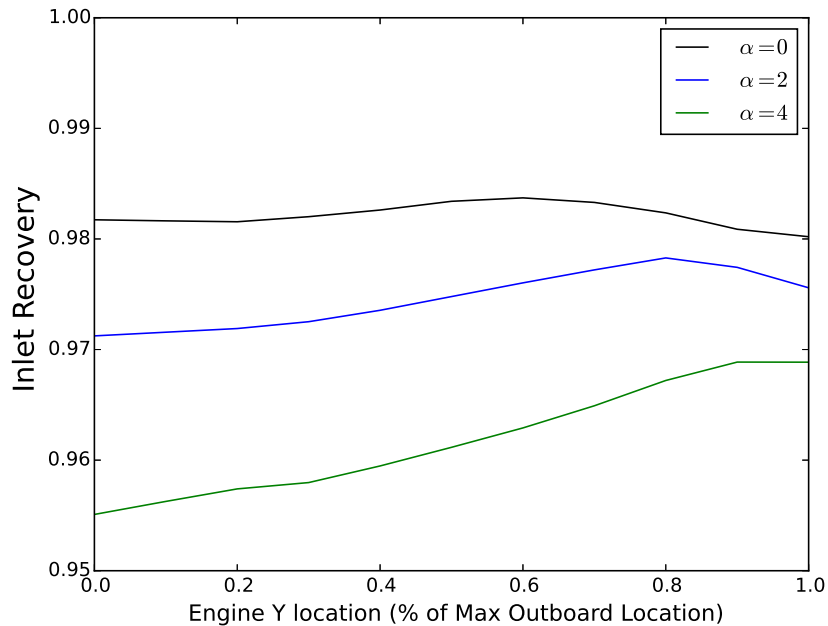


Figure 115: Inlet recovery for the single inlet case as the engine location is moved outboard.

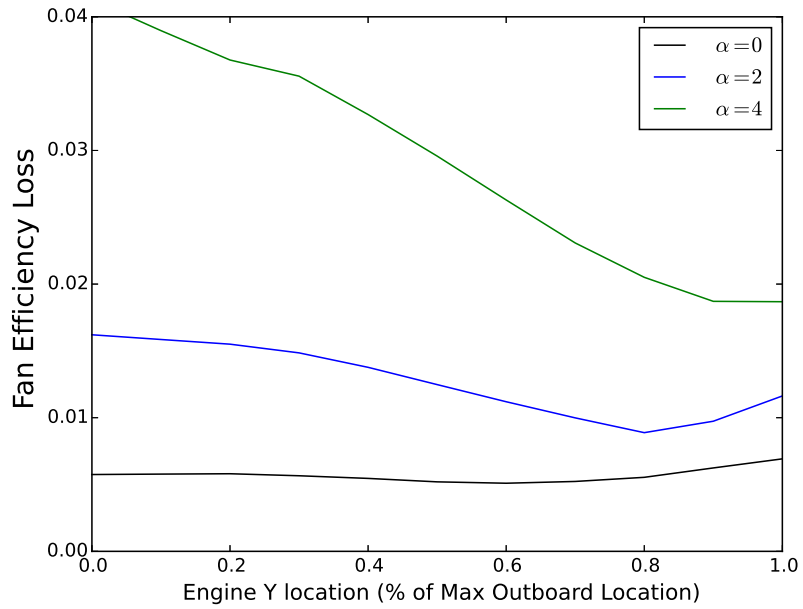


Figure 116: Fan efficiency loss for the single inlet case as the engine location is moved outboard.

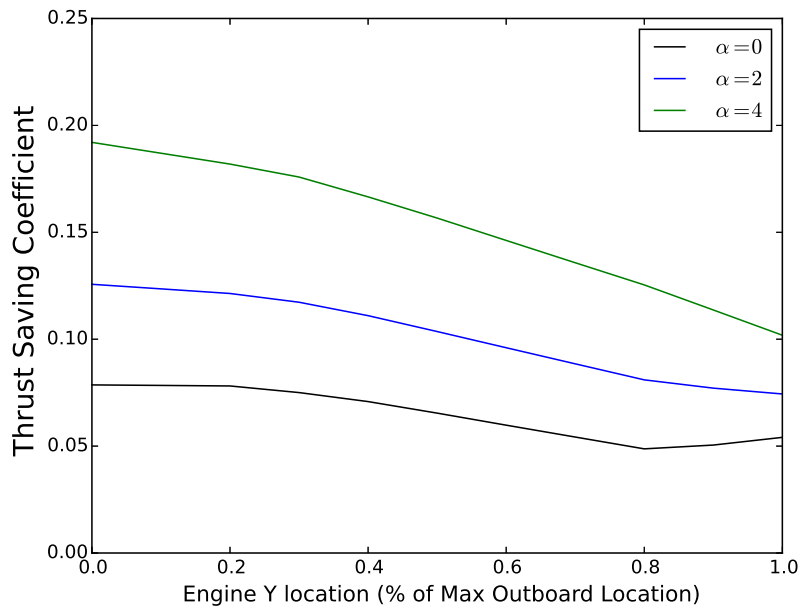


Figure 117: Thrust saving coefficient for the single inlet case as the engine location is moved outboard.

The thrust specific fuel consumption trend, in fig. 118, shows that the net effect of the BLI loss/benefit trade-off is to increase the TSFC by a few percentage points as the inlet condition for the single inlet case is moved outboard. This means that the loss in thrust saving coefficient impacts the engine relatively more than the improvement of the inlet recovery and fan efficiency. Another noteworthy point here is that choosing the inboard condition would be a less conservative approach from a performance perspective than the outboard, regardless of choice of angle of attack. If a designer therefore opts to use the standard single inlet approach, it may be prudent to pick an outboard location as the design point, since it is likely a bit more conservative in terms of prediction. Furthermore, most engine configurations for a turbofan architecture would have the majority of the thrust produced at an outboard location.

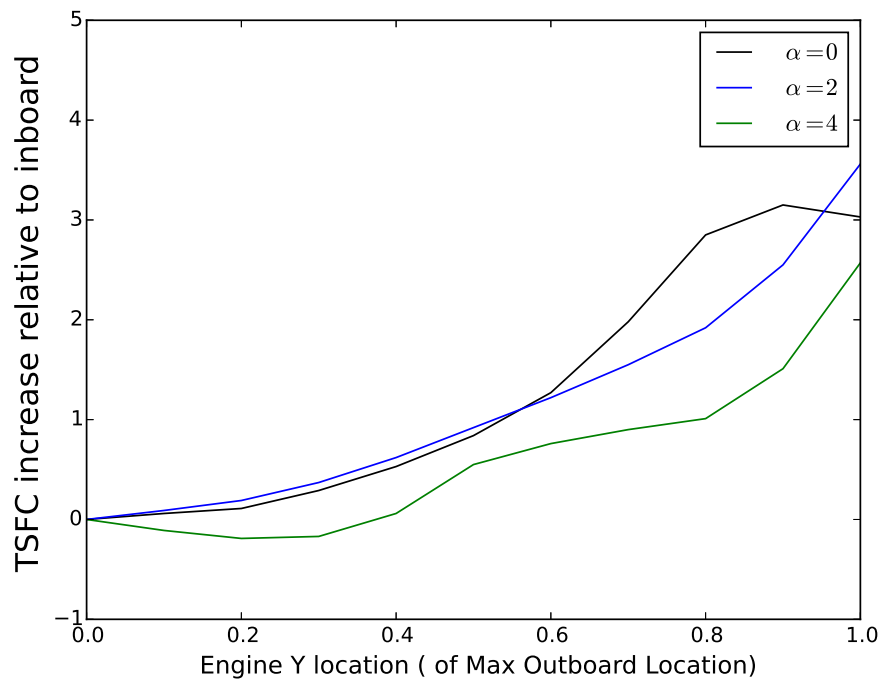


Figure 118: % Change in thrust specific fuel consumption for the single inlet case as the engine location is moved outboard.

Wake Correction Evaluation

The wake correction evaluation was implemented using a correction factor that impacts the wake recovery per unit ingested stream-tube width, as shown in fig. 112. The correction factor reduces the BLI drag recovery which is a function of how the kinetic energy defect varies over the upper surface due to the chord taper. The correction factor was created as a table in the NPSS program using the data from fig. 112 by creating a ratio of the outboard to inboard recovery as a function of the engine location. This is then applied to the BLI drag/thrust recovery term using a single assembly in NPSS. The drag reduction factor is computed as follows:

$$\xi_c = \frac{1 + 2 \frac{\theta_{out}^*}{\theta_{in}^*}}{3} \quad (120)$$

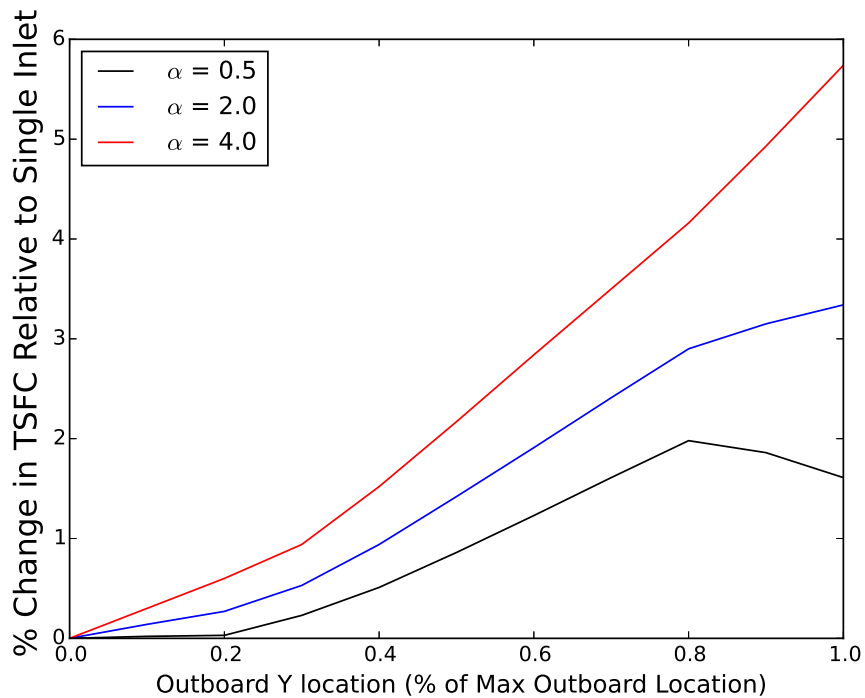


Figure 119: Difference between the wake correction and the single inlet TSFC.

This is then used to reduce the thrust saving coefficient of the engine. The difference between this method and the BLIPSS approach is that the impact of the changes in the losses as the engine moves is not included. The results show clearly that a single inlet assumption, in which the assumed location is the vehicle centerline, will over-predict the system TSFC by about 1-5% for this configuration. The important trends here are the general increase in the difference between the two approaches as the engines are moved to the far outboard location (because the wake is most significantly different there) and the increase with angle of attack or boundary layer thickness.

BLIPSS Method Evaluation

The BLIPSS implementation was evaluated in a similar manner. One assembly maintains the inboard inlet condition and boundary layer while the other represents the outboard location (2 engines). The thrust results for each engine (including the BLI term) from the implementation of the BLIPSS methodology is shown in fig. 120. As the outboard engine is moved farther from the centerline, the thrust saving coefficient of the outboard declines, requiring additional mass flow, as shown by the red curve. This has the effect of increasing the engine and therefore the thrust of the centerline inboard engine, as shown by the black curve. The total thrust is represented by the green line and is flat by the design of the method, since we are sizing the system to a constant thrust. For the case where α is 2 and the boundary layer is substantially thicker, a similar result occurs as shown in fig. 121. In this case, the overall thrust of the outboard engine remains relatively constant until the region where the chord begins to taper substantially and the thrust saving coefficient of the outboard engine declines. The trend is much flatter due to the fact that the change in the outboard recovery and fan losses are substantially larger with the thicker boundary layer, such that this trades more favorably with the loss in thrust saving coefficient, at least in

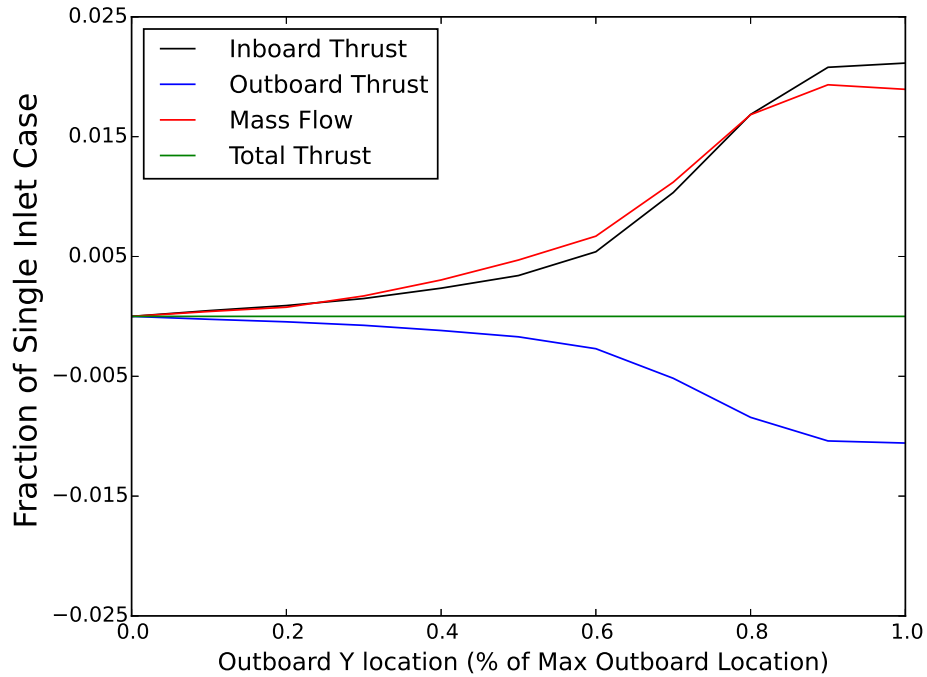


Figure 120: Change in thrust for the inboard, outboard, and total system and also total mass flow relative to the single inlet case for an $\alpha = 0.5^\circ$

terms of thrust when corrected for BLI. For the $\alpha = 4$ case (fig. 122), the loss improvement is so substantial as the engine moves outboard that the system requires a small reduction in required mass flow. This again highlights the importance of understanding how the fraction of ingested drag and the losses in the propulsion system are correlated in order to understand the best placement for the propulsors.

Figs. 123-125 show the fuel flow results for all three angles of attack. The fuel flow adjusts to match the mass flow required to maintain the burner fuel-to-air ratio for each engine. The fuel flow trends show the strong influence of the variation of the TSC with outboard location. Even for the case of the very thick boundary layer ($\alpha = 4$), the total fuel flow still increases even though the inboard engine fuel flow decreases relative to the single engine. Fig. 126 shows the TSFC results compared with the single inlet case assuming a design point inlet condition at the centerline, which interestingly reflects a similar trend to that of the single inlet case as the

outboard engine is moved. The maximum TSFC difference is on the order of 2-3% at the far outboard location and is actually on that order regardless of the angle of attack, though the different α curves exhibit unique shapes and trends in the intermediate locations because the benefit/loss trade-off evolves differently for the each angle of attack.

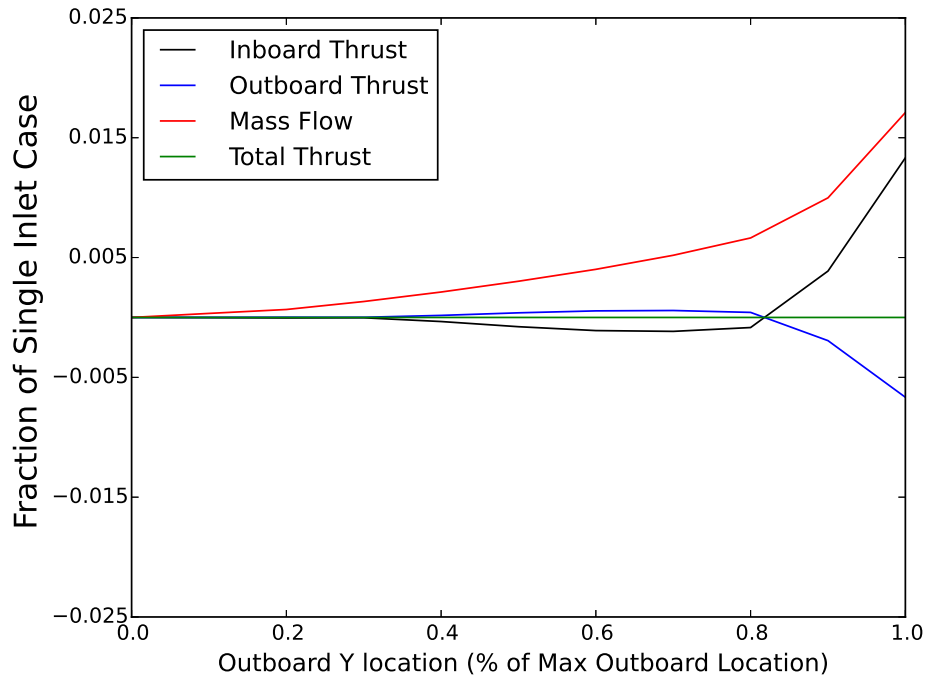


Figure 121: Change in thrust for the inboard, outboard, and total system and also total mass flow relative to the single inlet case for an $\alpha = 2^\circ$

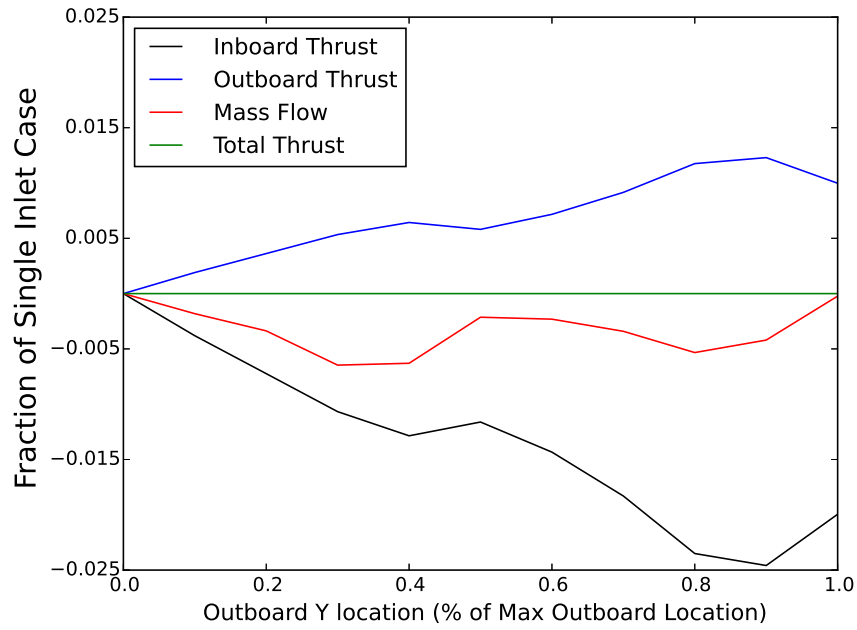


Figure 122: Change in thrust for the inboard, outboard, and total system and also total mass flow relative to the single inlet case for an $\alpha = 4^\circ$

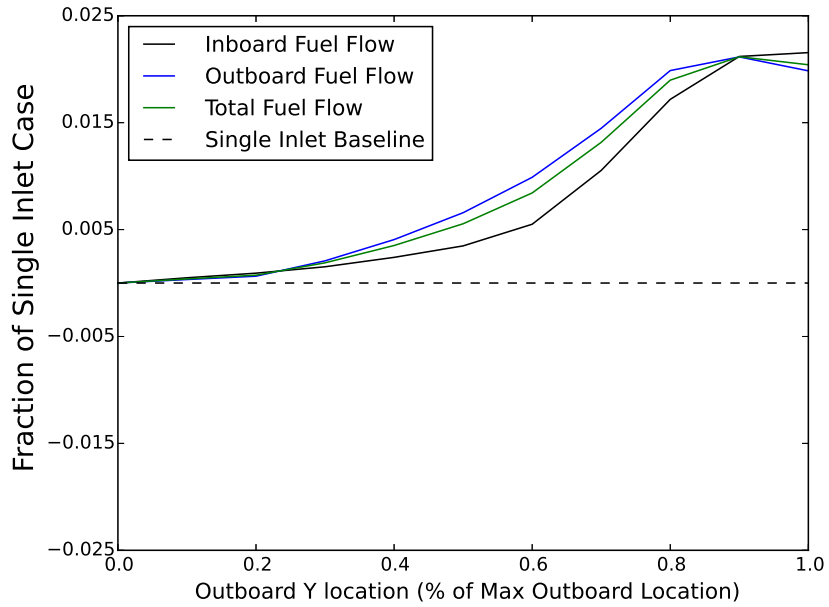


Figure 123: Change in fuel flow for the inboard, outboard, and total system for an $\alpha = 0.5^\circ$

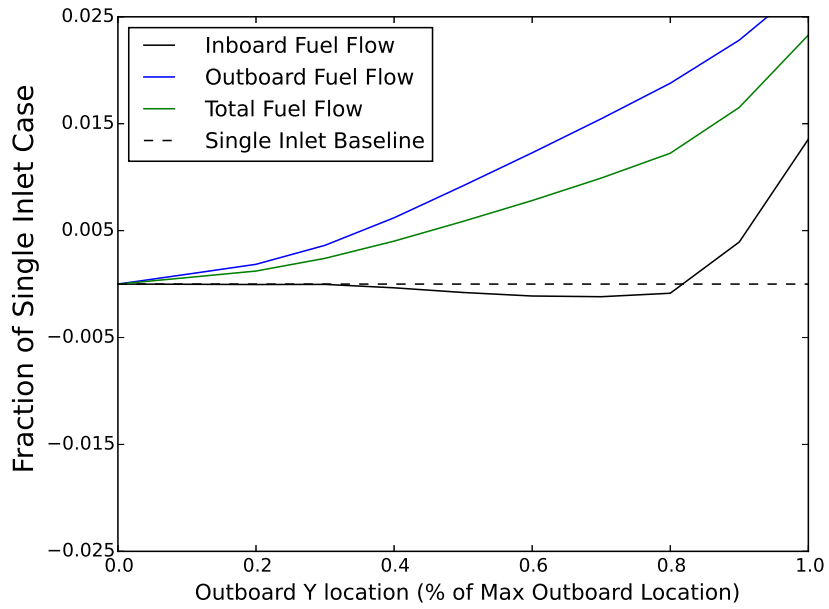


Figure 124: Change in fuel flow for the inboard, outboard, and total system for an $\alpha = 2^\circ$

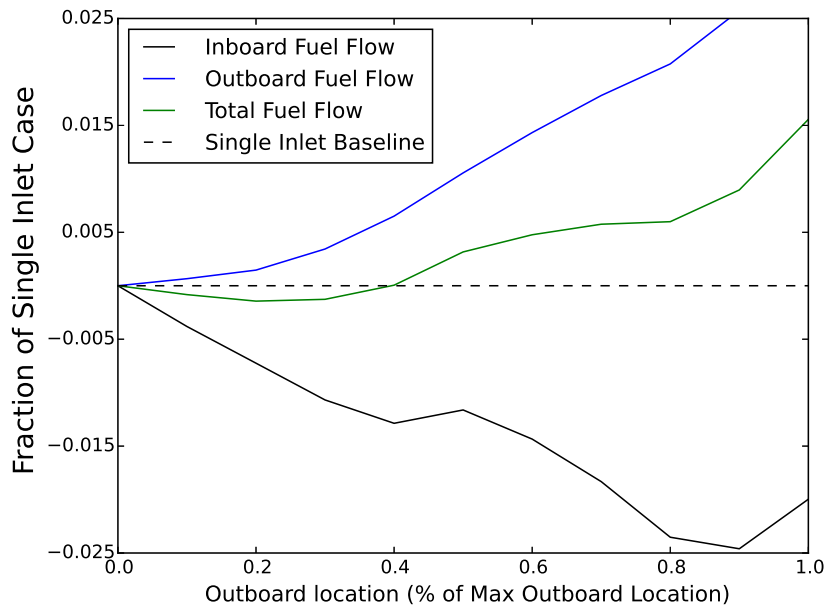


Figure 125: Change in fuel flow for the inboard, outboard, and total system for an $\alpha = 4^\circ$

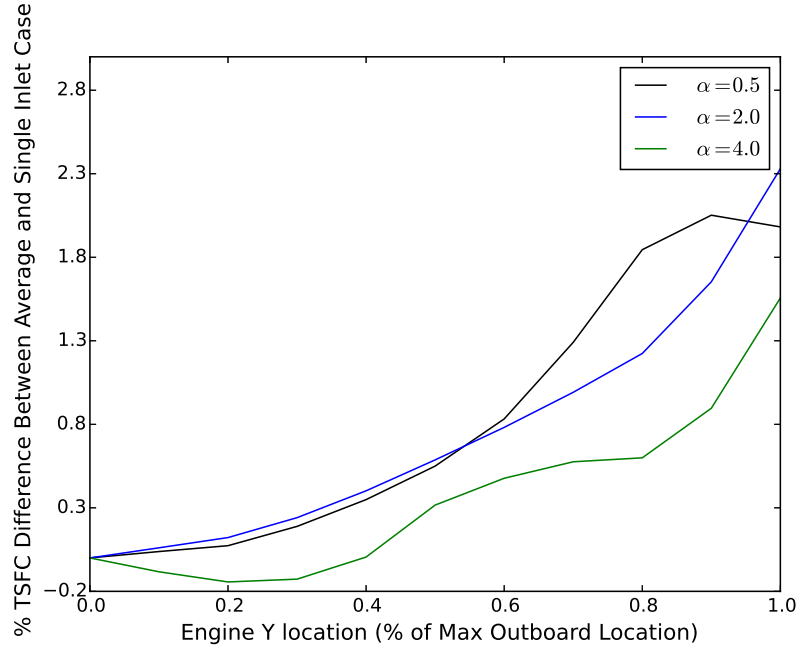


Figure 126: Change in TSFC for the inboard, outboard, and total system for several angles of attack.

5.3.5 Comparison of Wake Correction and BLIPSS

Now that it has been shown that the BLIPSS approach can be used for the BLI application, it is worth comparing the BLIPSS and the wake correction method for the purpose of knowing the most appropriate approach for the designers and the consequence of each assumption. Fig. 127 shows the TSFC trends for the two methods, normalized by the single inlet values. This data was generated by varying the inlet aspect ratio design variable to increase the thrust saving coefficient of the system. The outboard engine was assumed to be located at its maximum possible location for all cases. The comparison shows two relevant trends: first, that the single inlet prediction is progressively worse at higher levels of BLI, which is a trend seen for both models; second, that the wake correction will be generally less conservative for lower TSC but greater for higher. The latter trend is driven by the fact that the BLIPSS approach accounts for the change in inlet recovery as the engine moves to a thinner

boundary layer, which counteracts some of the reduction in the TSC.

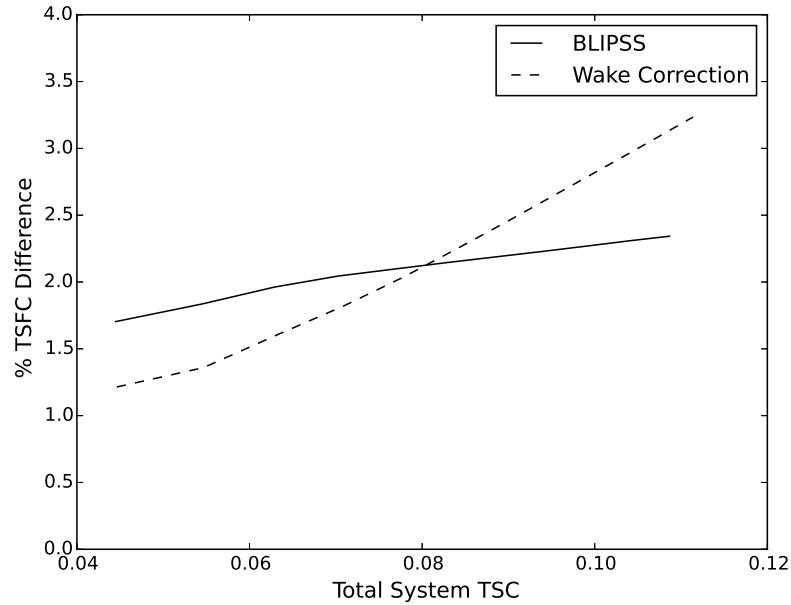


Figure 127: Difference between the single inlet case and the BLIPSS method vs. thrust saving coefficient of the system.

5.3.6 Off-Design Evaluation

An off-design analysis of this system can be conducted by running both engine assemblies according to the specified off-design power management rule. For this case, we look at the similar N1 case (constant fan corrected speed between engines). Fig. 128 shows the off-design variation at power settings different than the design point. At the 100% point, we see the 2% difference as shown in the design run trends previously. There is a sharp rise in the outboard TSFC as the system is throttled back because of the increased thrust saving coefficients at part power. That is to say that moving the engine to a thinner boundary layer location has a more significant impact at part power where the total thrust produced comprises a much more significant percentage of BLI savings.

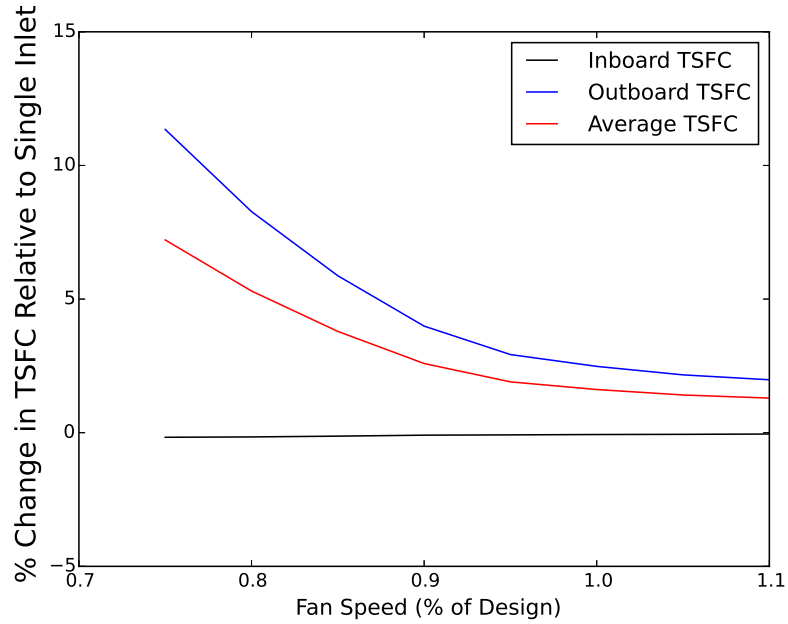


Figure 128: Difference between the BLIPSS method and the single inlet approach for different throttle settings in terms of TSFC. The data is shown for an $\alpha = 0.5^\circ$

5.4 Experiment 4

Now that the usefulness of the BLIPSS methodology has been demonstrated for different inlet conditions, we now consider the prospect of using this analytical framework to exploit potential degrees of freedoms which may be conducive to BLI systems. As discussed in chapter 3, the additional degree of freedom for the 3-Engine BLI propulsion system is essentially the ratio of the size of the outboard to the inboard engine. For a cycle analyst, the best way of measuring this is the mass flow ratio, defined as:

$$MFR = \frac{\dot{m}_{outboard}}{\dot{m}_{inboard}} \quad (121)$$

It is expected that the use of the mass flow ratio could allow the system to be better tailored to the local variation in flow field and boundary layer properties and therefore provide a fuel burn benefit, which is the basis for hypothesis 4. The following experiment will attempt to validate this and quantify how much benefit is available

for acceptable ranges of the mass flow ratio.

5.4.1 Implementation

There are two principal design options used for experiment 4 as shown in table 17. The first option is a fixed core, where the core has a single aerodynamic design point inlet condition, at either outboard or inboard (both will be examined) and the fan/LP spool is allowed to be re-designed/scaled to potentially better match the local flow conditions. The idea is that this would reduce design costs by utilizing a common core design and part numbers (see [74]). The outboard/inboard fans could then be designed independently to better match the level of BLI ingested and the particular distortion patterns located there. The design rule implemented here (there is only one required) is that the mass flow ratio is equal to some specific factor, which is now an additional design degree of freedom.

Table 17: Design point mapping matrix for the 3 engine architecture for experiment 4.

	X = Not used	D = On-Design	O = Off-Design		
Design Option		Core/HP Spool	Fan/LP Spool	Design Rule	PM Rule
Fixed Core	Inboard	D	D	MFR	None
	Outboard	O	D	MFR	None
	Inboard	O	D	MFR	None
	Outboard	D	D	MFR	None
Two Engine	Inboard	D	D	MFR	None
	Outboard	D	D	MFR	None

The second option is to have two different engines on the aircraft. This option, though perhaps more expensive in terms of development costs, might be plausible if existing engine designs could be used to give the differential size between inboard and

outboard. In any case, the design rule used is the same as that for the fixed core case, except that there are additional degrees of freedom since we could potentially utilize an entirely different cycle including the core design.

For implementation of the design rule, it is possible to either have the Newton-Raphson solver control the mass flows of both engines simultaneously to equalize them, or the mass flow of the first engine in the solver sequence (order in which the assemblies are executed) can be multiplied or divided by the MFR to give the mass flow for the second engine. Initial analyses showed that the first option made runs much less stable, with far more failed convergences than using the second option. Since the MFR is a user specified design variable, there is really no reason not to do this since it avoids unnecessary function calls to determine partial derivatives for equalizing the MFR equation.

5.4.2 Results

Inboard Core Design

The first question to ask is whether or not changing the fan size has some influence on the overall achievable level of ingested BLI (thrust saving coefficient). The results from experiment 4 for the fixed core option with the inboard inlet condition as the aerodynamic design point are shown in figure 129. Moving from smaller MFR to larger, the outboard engines increase relative to the inboard. The result is that, although the individual thrust saving coefficients of the inboard/outboard propulsors change substantially, the overall level of thrust saving coefficient (averaged among the three engine total thrust contribution) remains relatively constant. This is to say that increasing the thrust saving coefficient of the outboard engines by making them smaller will have the necessary effect of reducing the thrust saving coefficient of the inboard engine which is made larger. Since the wake thickness is roughly half at the outboard location, the net effect is the flattening of the overall MFR vs. TSC

sensitivity.

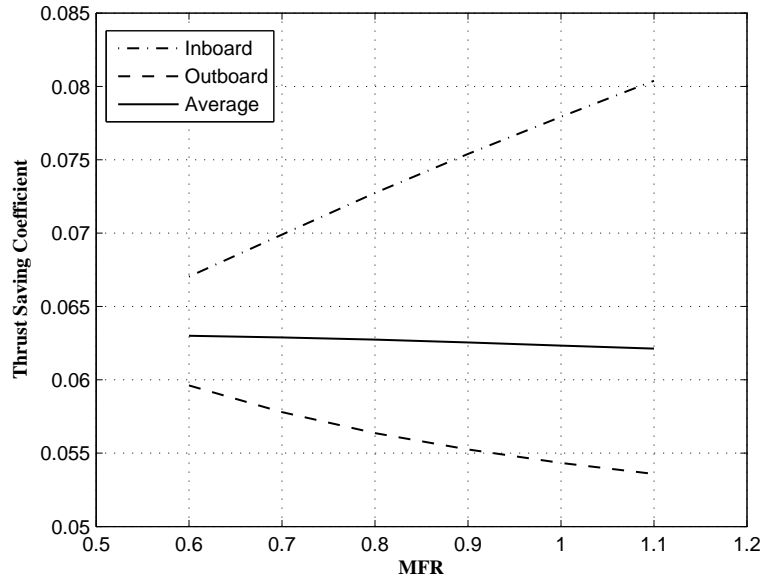


Figure 129: Inboard, outboard, and total system thrust saving coefficient vs. the mass flow ratio of the system. Results are for an α of 0.5 degrees.

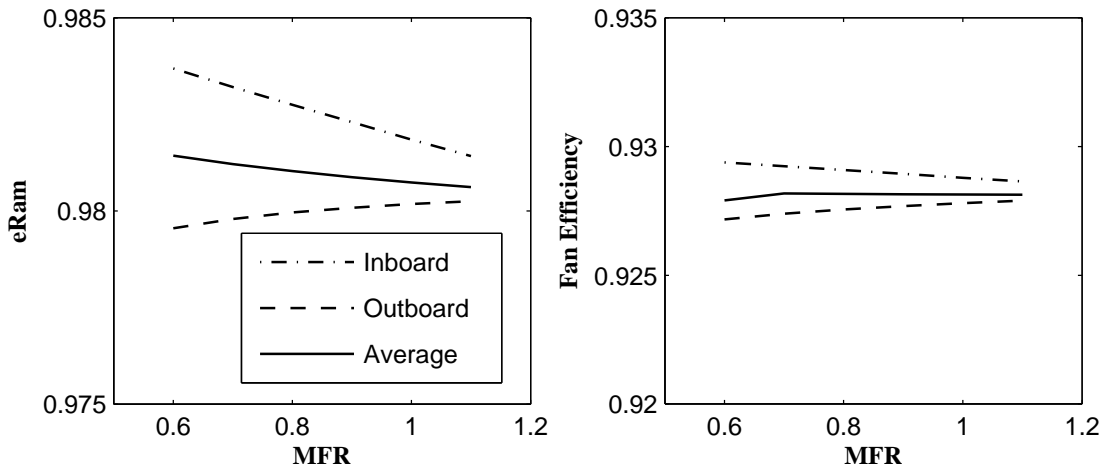


Figure 130: Inboard, outboard, and total system component efficiencies vs. the mass flow ratio of the system. Results are for an α of 0.5 degrees.

The story is very much the same when looking at the inlet and fan efficiencies as shown in fig. 130. The recovery slightly improves for the outboard configuration

as it becomes larger relative to the inboard and vice versa. The net result is a mass averaged recovery which produces a small decline in recovery as the MFR is increased. Finally, the TSFC results are shown in fig. 131 and a comparison with the baseline and other angle of attacks is shown in fig. 132. There is a small benefit at higher MFR, however, in this case, the core is over-spiced at the outboard location because of the increased flow. At some point, this pushes the core past its over-speed limit and therefore MFR beyond a value of about 1.1 is not possible. This set of data shows that, although there is a benefit for higher MFR, it is basically driven by the baseline improved efficiency at core over-speed (higher OPR). This suggests that this type of design is not really preferable because it doesn't offer much benefit vis a vis BLI.

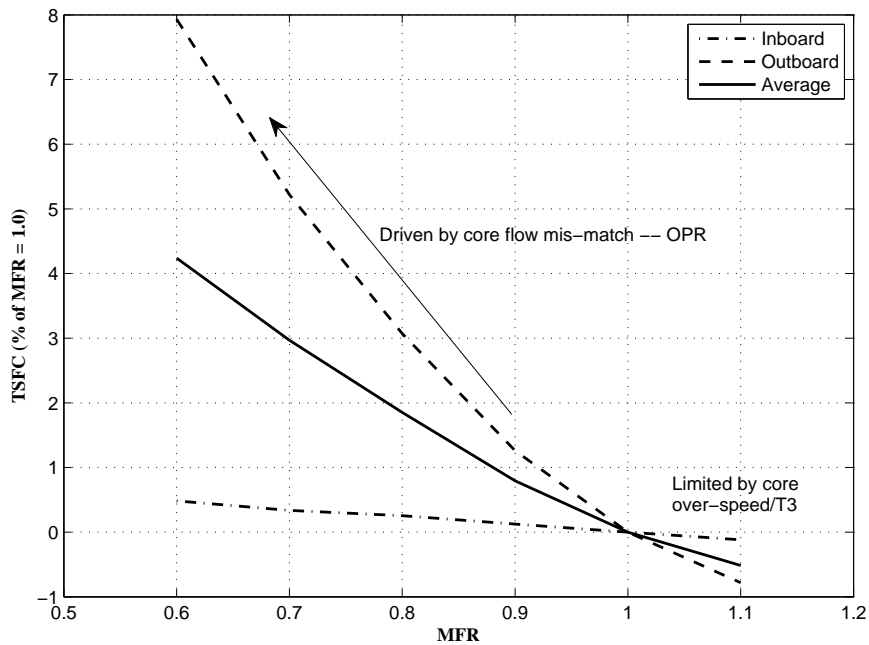


Figure 131: Inboard, outboard, and total system TSFC vs. the mass flow ratio of the system. Results are for an α of 0.5 degrees.

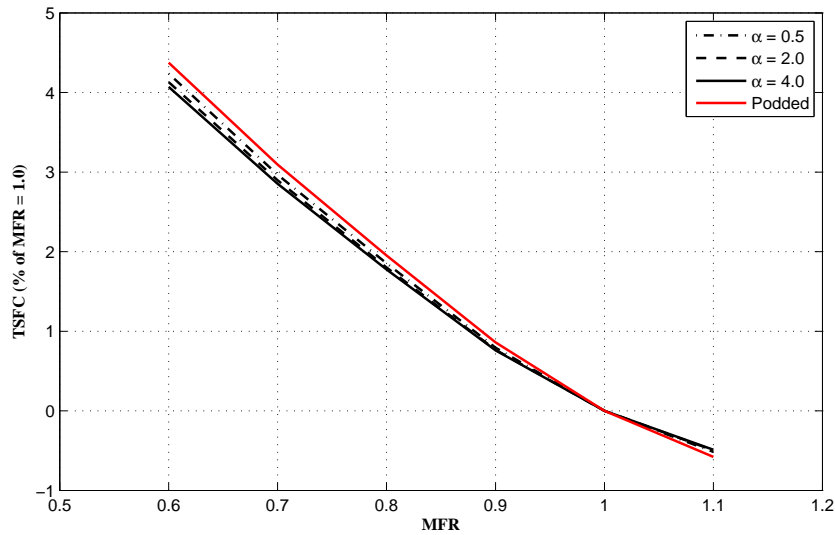


Figure 132: Inboard, outboard, and total system TSFC vs. the mass flow ratio of the system. Results are shown for the baseline and several BLI designs with different angles of attack.

Outboard Core Design

The outboard core design is similar to the inboard core except that the mass flow ratio is limited at low values, since the core flow mis-match will happen at the inboard engine so that values of MFR less than unity will yield a core over-speed scenario. The results for this design option are shown in figs. 133 and 134, with very similar results to the inboard core case. There is some substantial difference between the BLI case and the baseline case at high MFR, but in this scenario the baseline propulsion system is so much less efficient that the BLI effects are meaningless. At lower MFR, there is some negligible benefit for the BLI system relative to the baseline, but the overarching result for the fixed core scenario is that it does not offer much benefit in the way of maximizing BLI potential and that result does not seem to change much with the choice of the aerodynamic design point.

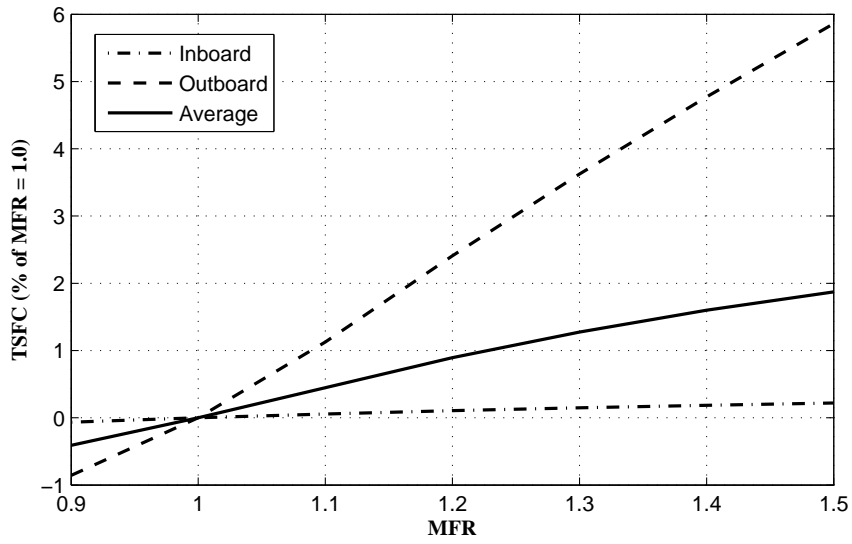


Figure 133: Inboard, outboard, and total system TSFC vs. the mass flow ratio of the system. Results are for an α of 0.5 degrees and for the outboard core aerodynamic design point.

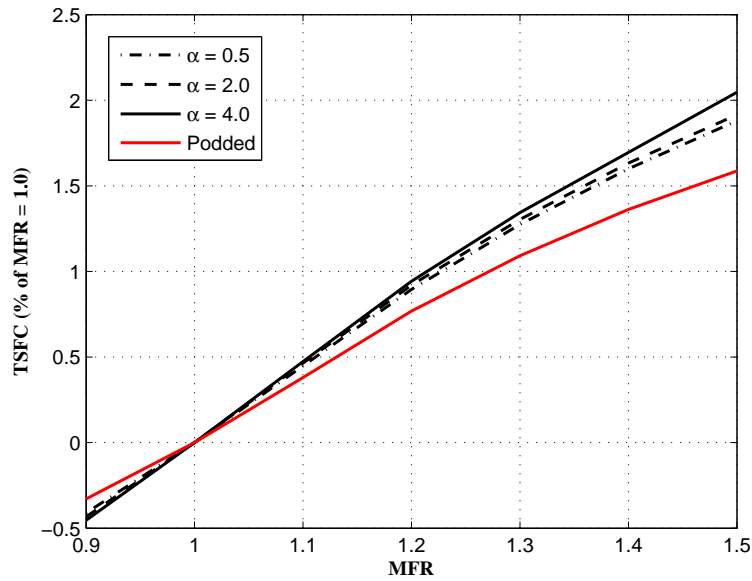


Figure 134: Inboard, outboard, and total system TSFC vs. the mass flow ratio of the system. Results are shown for the baseline and several BLI designs with different angles of attack.

Two Engine Design

The results for the fixed core analysis were shown to be somewhat discouraging. The small benefit available by changing the size of the BLI system and different inlet locations was completely over-ridden by trends of the baseline gas turbine model with flow and BPR variation or mis-match. The next design option is the two-engine problem, in which one engine of a particular size is used for the outboard and another unique engine is used for the inboard. For the time being, it will be assumed that the cycle designs for both engines will be exactly the same, but the size of the engines is allowed to vary. This will isolate the influence of BLI on the system, though it does ignore the fact that there will be a slightly different optimal FPR/BPR combination for unique boundary layer thicknesses. In any case, the above assumptions will be used to test the “two-engine” case.

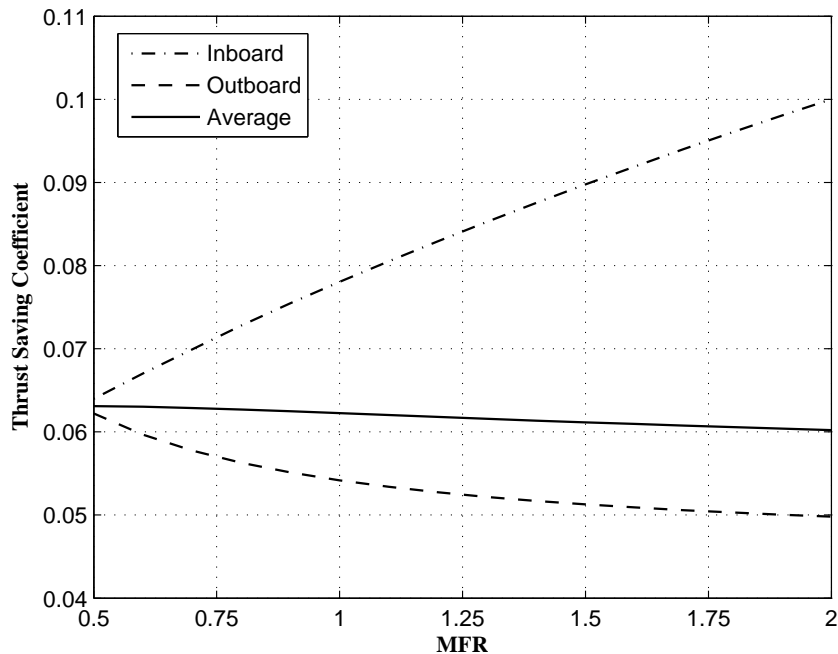


Figure 135: Inboard, outboard, and total system TSC vs. the mass flow ratio of the system with angle of attack of 0.5 degrees.

The situation with regard to the thrust saving coefficient is shown in fig. 135, with all cases having been run using the BLIPSS methodology. Both outboard and inboard thrust saving coefficients increase or decrease when the engine mass flows are decreased or increased respectively. The trends are very similar to that of the fixed core case in that the overall thrust saving coefficient of the system doesn't change much when the MFR is decreased. However, the difference between the two-engine and fixed-core case is that the bounds imposed by the fixed core assumption are not present, allowing for a wider range of allowable mass flow ratios. The component efficiency variation is also very similar to the trends for the fixed core case, with larger engines tending to have a better recovery and lower losses due to distortion as shown in fig. 136.

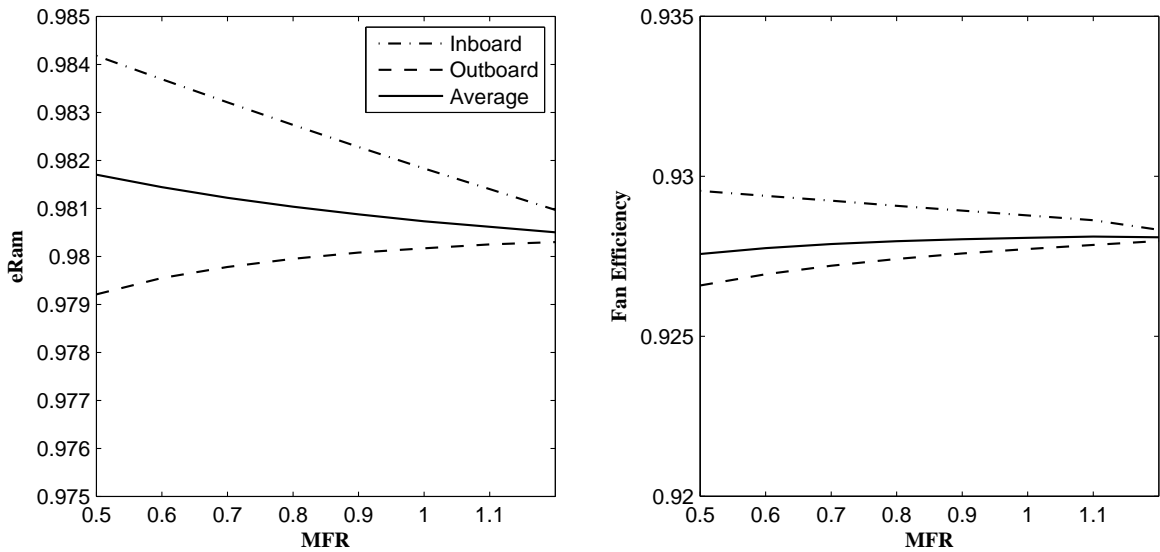


Figure 136: Inboard, outboard, and average system component efficiencies vs. the mass flow ratio of the system with angle of attack of 0.5 degrees.

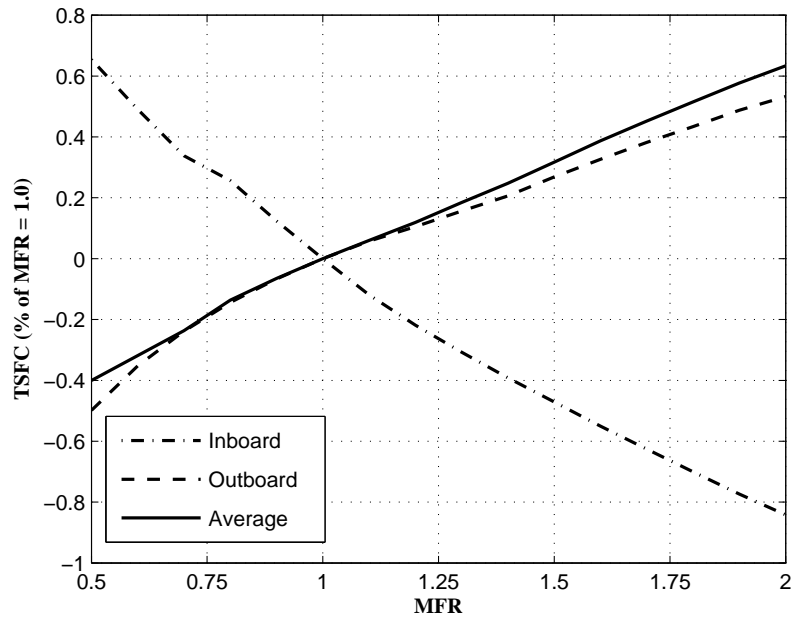


Figure 137: Inboard, outboard, and average system component TSFC vs. the mass flow ratio of the system with angle of attack of 0.5 degrees.

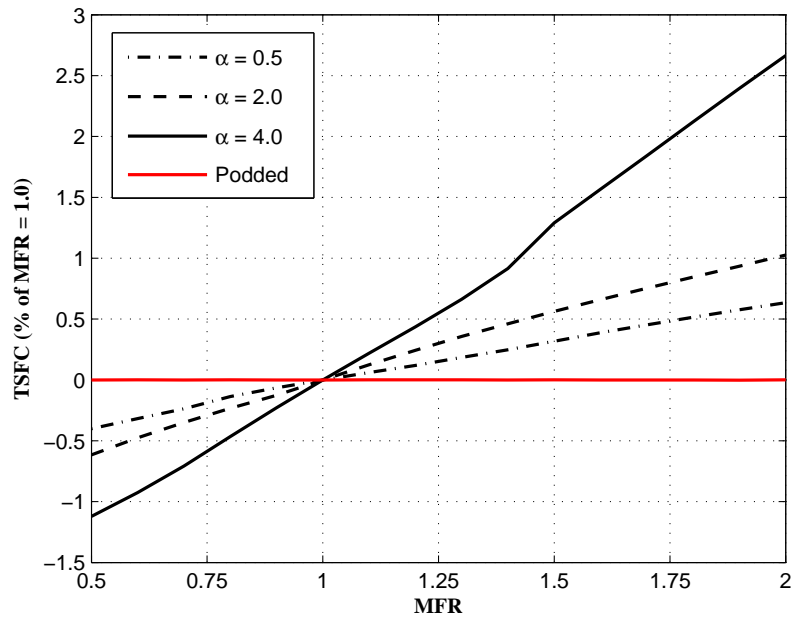


Figure 138: Inboard, outboard, and average system component TSFC vs. the mass flow ratio of the system with angles of attack of 0.5, 2, and 4 degrees.

The TSFC results are shown in fig. 137 with the result that the smaller outboard engines are somewhat better. This is further corroborated by looking at the TSFC benefit for different angles of attack. For the case of an α of 4 degrees, the boundary layer is very thick relative to the capture or hi-lite area and therefore increasing the recovery of the inboard engine by making it larger has a more substantial impact on the overall system fuel burn rate.

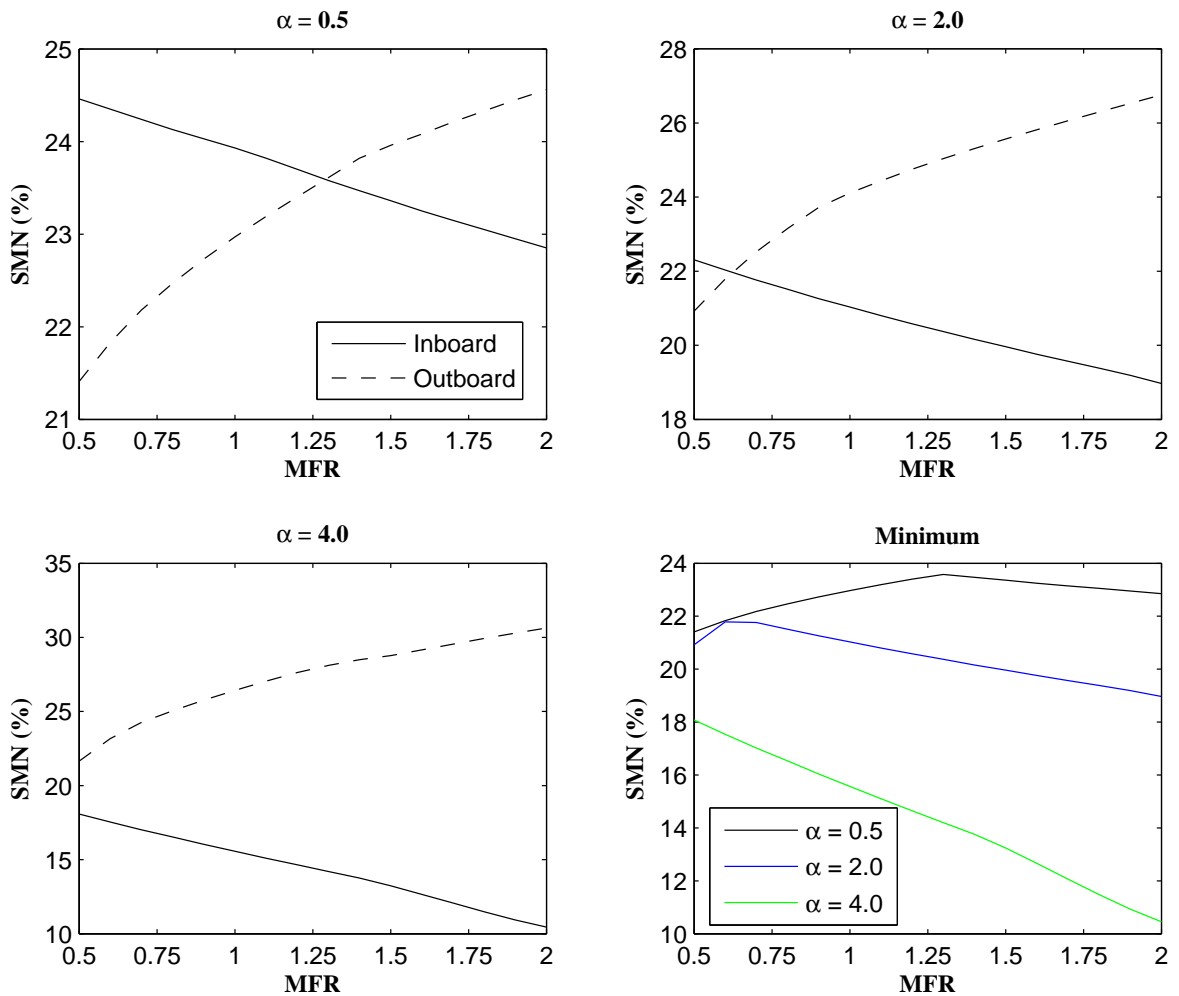


Figure 139: Stall margin variation for different angles of attack showing the inboard and outboard stall margin. Bottom right shows the minimum stall margin at each MFR for the 3 angles of attack.

The stall margin results in fig. 139 show that the stall margin of the system can be improved by designing at a lower MFR. This is to say that a few points of stall margin on the outboard engine can be traded to increase that of the inboard by increasing its size. This also has the additional benefit of bringing both engine stall margins closer into line perhaps making life and degradation estimates easier to conduct. The implication of the preceding analysis is, therefore, that a BLI system which allows the ratios of the thrusts or mass flows between the propulsors to be a free design variable will find its optimum at some unique value of the design rule parameter which best matches the way that the wake is distributed over the vehicle – assuming this design point satisfies operability and geometric constraints.

5.4.3 Geometric Compatibility

The final component of the architecture integration phase is to check the geometric compatibility of the design. This step can either be done off-line after the system has been sized by constraining the propulsion system design space according to the constraints or it can be included in the solver setup to ensure that certain design variables always fall into feasible regions. The following constraints are examples of those that could be implemented for conceptual level BLI systems, and especially for the HWB design: Fan diameter constraints; Inlet diffusion angle constraints; Inlet/propulsor spacing constraints.

Fan Diameter Constraints

There is generally a stringent fan diameter constraint for engines sized for under the wing mounting. These must fit in the space between the wing and the ground. For the HWB, there is no such constraint for top mounted engines. However, there is a limited amount of space within the vehicle to fit the engine, so larger engines means that there will be more of the engine nacelle and inlet exposed to the flow, increasing

the external drag profile.

For designs that are space limited on the upper surface, such as the double bubble [37], there will be very tight constraints on what values the fan diameter can take since the engines will be designed precisely to fit on the upper surface of the vehicle. In this case, it might make sense to actually constrain the solver to produce designs which precisely fit the geometric requirements. The fan diameter would be specified and the fan pressure ratio would be the design variable which precisely determines the bypass ratio of the engines.

Inlet diffusion angle constraints

From Shedon [84], the diffuser equivalent cone angle is defined as in eq. 122, where “f” is the fan station, “c” is the capture area station, and “g” is the circumference of the annulus at each location. The angle α_d is that which would be made by a cone with the same diffusion area ratio and length of the inlet.

$$\tan \frac{\alpha_d}{2} = \frac{2(g_c A_f - g_f A_c)}{g_c g_f (l_f - l_c)} \quad (122)$$

In general, the larger the diffusion angle, the more the skin friction loss (since the wall duct circumference is effectively increased) and the likelihood of flow separation additionally increases due to adverse pressure gradients. For a fixed diffusion ratio, such as that assumed in this thesis, a requirement can be imposed that the inlet length scales such as to maintain a reasonable value of the diffuser cone angle. For each case, the required inlet length would be computed to maintain the angle, and this would additionally impact the location of the engine capture area (x/c).

Inlet/Propulsor Spacing Constraints

The obvious spacing constraint for configurations like the HWB is that the engines have to be sufficiently spaced if they are housed in separate nacelles. The closer the

nacelles, the more likely it is that excessive interference drag will be produced (see for instance, Rodriguez [72]), and furthermore, there is a hard geometric limit that the engines have to not be overlapping when the choice of outboard location is made. This constraint actually works with the fan diameter computation since the size of the engine will obviously impact how much spacing there is between them as well as the chosen outboard location of the engines.

5.5 Summary of Chapter 5

The preceding chapter showed an implementation of the architecture integration phase for the BLIPSS methodology on a 3-Engine HWB vehicle. It was found that accounting for variations in performance and loss benefits due to engine location makes a fairly significant difference in the performance of the system at a high-speed cruise point. This difference tends to increase as the inlet condition disparity is increased between the engines. One key observation is that, though the thrust saving coefficient of the system declines as the engine is moved outboard, the inlet and fan losses tend to decrease. This led to the BLIPSS method capturing a trade-off that the wake-correction method cannot capture since it only accounts for variation in the benefit with engine location.

It was found that there was a very marginal benefit available by optimizing the size of the propulsors for different boundary layer thickness inlet values. The benefit may not be worth the additional design costs, but the BLIPSS methodology enables these kinds of trade-offs for other systems for which it may be more synergistic, such as distributed propulsion fan system with a tapering fan size in the array. The other added benefit of doing this is that the stall margin of the outboard engine which is generally higher can be traded to improve the stall margin of the inboard engine which would have thicker boundary layers generally. This concept helps add some viability to the idea of using the extra degree of freedom.

CHAPTER VI

VEHICLE MATCHING PHASE

The previous 2 chapters have presented the BLI modeling phase and architecture integration phase, and how they can improve design choices made during BLI conceptual design which determine the fundamental benefit of the system. In this chapter, the final piece of the BLIPSS methodology will be implemented and hypothesis 5 will be investigated and put to the test. The fundamental claim being made is really a two part claim: first, that there are unique critical design points in terms of thrust and stall margin which may differ from the normal podded design points; second, that out of all of the engine requirement points, there exists a subset which captures the critical design points for the majority of designs in the design space. This hypothesis, if verified, would justify the use of the proposed screening process in the BLIPSS design methodology as a means to efficiently discover critical flight conditions during conceptual design. This not only has use in the BLIPSS process itself, by identifying the proper sizing point, but also gives guidance to detailed aerodynamic designers for determining what flight conditions should be considered as candidates for their analyses. The purpose of this chapter is therefore to describe the “Vehicle Matching Phase” algorithm and its implementation on the canonical HWB with BLI problem, and to establish an experiment using this implementation which attempts to verify hypothesis 5.

6.1 Methodology Implementation

The “Vehicle Matching Phase” (VMP) methodology requires a few specific inputs from the vehicle design which relate to the engine requirements, aside from the original

MDP inputs. These are as follows:

1. Vehicle Flight Envelope – A list of MN, altitude, and angle of attack range over which the vehicle must fly with associated thrust required values
2. Distortion constraint schedule – A schedule of allowable stall margin loss as a function of flight condition
3. A set of screening cases which will determine the critical flight condition vector
4. A baseline set of design requirements to populate the initial MDP target and constraint point vectors

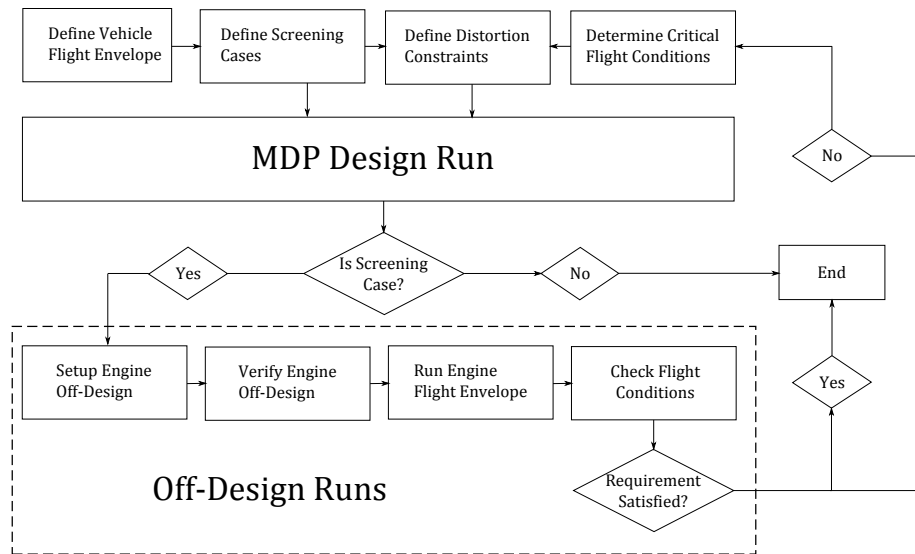


Figure 140: High level algorithm for the “Vehicle Matching Phase” methodology.

These inputs are fed into the initial MDP design setup which executes the design run of the engine for that specific set of propulsion system design variables. If the case at hand is a screening case, the engine is moved to the off-design runs. The off-design run is conducted and first verified with the initial design run to ensure that the assembly used to run the off-design cases produces the same result for the design condition within some numerical tolerance. The engine is then run throughout the entire flight

envelope and thrust/operability performance is compared with the original baseline engine requirement. The most critical deficit condition is used in the next iteration of the methodology as a constraint point within the MDP design run. This process is shown in fig. 140.

6.1.1 Baseline Flight Envelope Requirements

There may be many flight conditions to consider for specific aspects of the propulsion system design. For instance, the requirement for low cowl spillage drag during engine windmilling will, to a large extent, dictate the limitations on the external nacelle design. However, specific to the BLIPSS methodology is the inclusion of points which affect the overall size of the engine itself or its operating line, which is to say conditions for which the effect of BLI and embedding the engine near the airframe may cause a need for additional thrust or stall margin at that point relative to what the performance of the BLI system would be using the baseline sizing conditions. As such, the requirements points used for experiment 5 will consist of those at high angle take-off and all points during the cruise-climb portion of the vehicle flight as predicted by the baseline vehicle performance model. This is because that, at low speed, the high angle of attack condition is likely to contribute to stall margin loss (as shown in chapter 4), and at high speed, the lapse of the engine and the reduced inlet recovery due to BLI is likely to cause some thrust loss.

Take-off Requirements

The requirements for take-off are effectively the same as that for baseline engine prior to lift-off, rotation, and obstacle and avoidance. These are the points where the flight speed becomes substantial enough to produce installation effects due to BLI that would effect performance and operability. The angle of attack during take-off rotation from the baseline FLOPS model is shown in fig. 141 up to the point where

obstacle clearance is required at 16° . This assumes a flap (elevon) deflection of 15° .

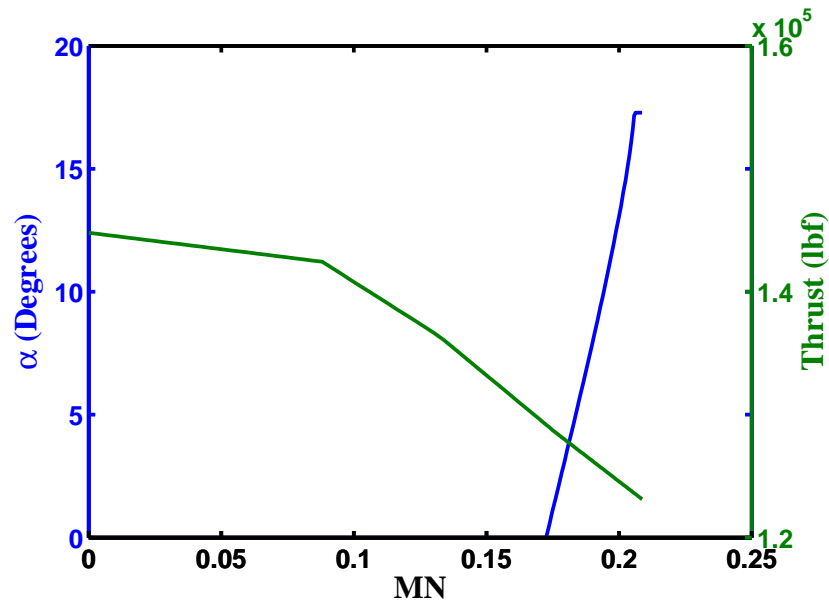


Figure 141: Take-off angle of attack and thrust requirements

These angles of attacks and lift coefficients are based on the FLOPS low speed aerodynamic model which is similar to that derived from the test data, which was conducted at a similar flight Mach and angle of attack regime. Though scalable drag polars are used in the FLOPS model, precise prediction of angle of attack is not used for the cruise and climb segments. It is therefore necessary to estimate the lift curve slope at low speed and project to other Mach numbers using compressibility corrections to determine the angle of attack during climb and cruise. The data in fig. 142 shows the lift curve of the test apparatus from [32] with no high lift devices used. This lift curve slope is approximately 0.049 per degree of AoA, which will be used as the incompressible lift curve slope of the vehicle.

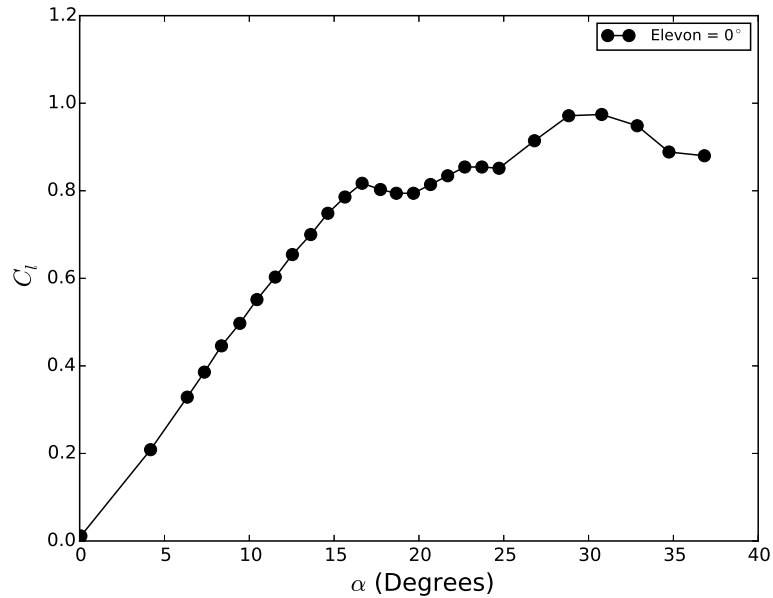


Figure 142: Lift coefficient vs. angle of attack take from the experiment of [32] at a Mach of 0.2 with zero elevon deflection (clean configuration).

Cruise-Climb Requirements

The requirements for the cruise and climb segments are based off of the baseline flight profile. The Mach number and altitude flight profile is shown in the top left of fig. 143. This profile is determined by the FLOPS baseline model and is the result of minimum energy path optimization. It is therefore indeed possible that a BLI system which differs from the baseline propulsion system due to the installation impacts may have a different resulting optimal flight path. Despite this, the flight path for the baseline system will be used here for testing hypothesis 5. The thrust requirement, also shown in the bottom right of the figure, will be used to define the thrust requirement of the propulsion system.

The lift coefficient during the flight of the vehicle is shown in the top right of fig. 143 and varies fairly significantly from climb-out to top-of-climb (implying significant angle of attack variation). Assuming the vehicle incompressible lift curve slope is 0.049

per degree, as described above, then α can be computed at each point by assuming a simple Prandtl-Glauert approximation and correcting the lift-curve slope by dividing by $\sqrt{1 - M^2}$. The zero-lift angle of attack is also assumed to be zero. The results of this approximation are shown in the bottom left chart in fig. 143. The angle of attack ranges from about 7-8° at the lower speed conditions and relaxes significantly as the vehicle approaches the TOC and cruise points to between 2 and 3 degrees.

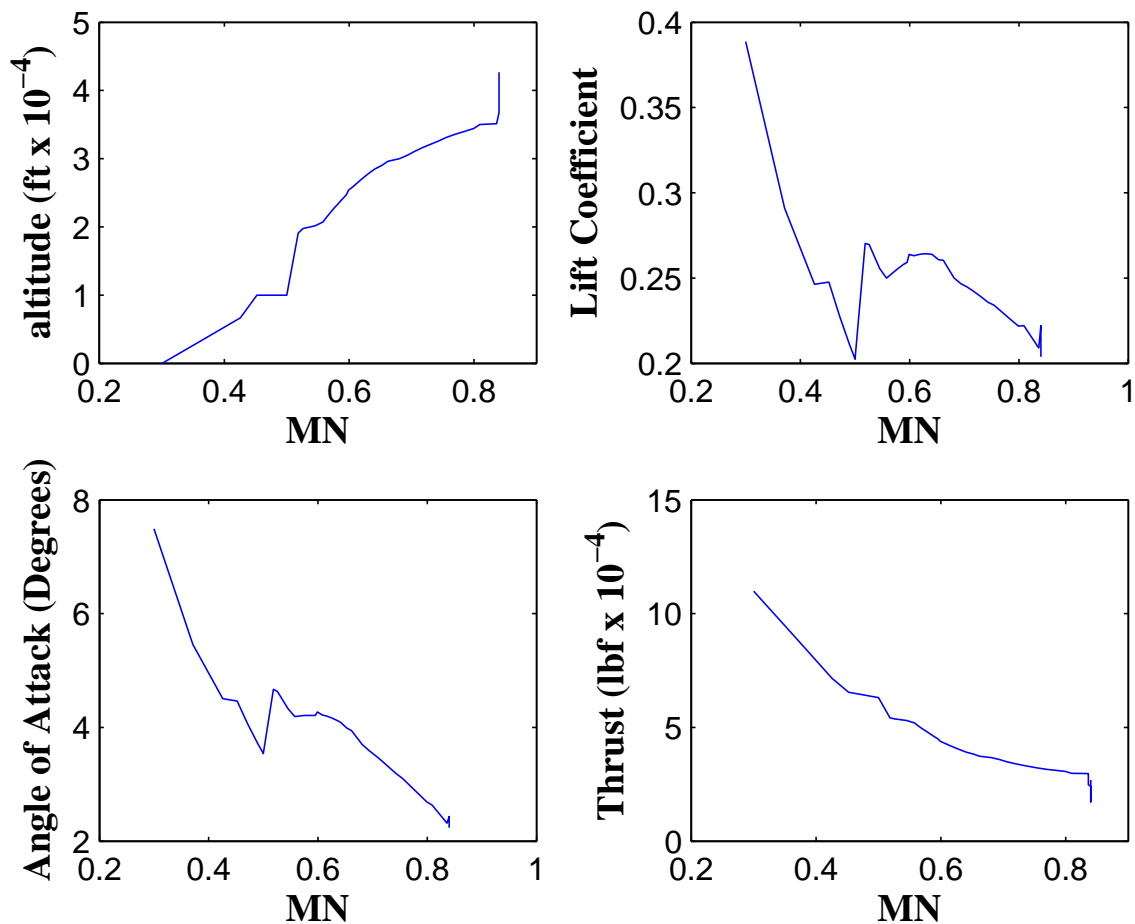


Figure 143: Climb envelope showing Mach number vs. altitude, lift coefficient, angle of attack and thrust requirement.

The sensitivity studies from chapter 4 showed that this is a reasonable value for the angle of attack, one in which the recovery is not so high that the engine stalls

unavoidably but also high enough to provide a reasonable thrust saving coefficient. Although the estimate of α here should be considered an approximation, it is therefore reasonable to assume this profile to demonstrate the method.

Requirements Scenarios

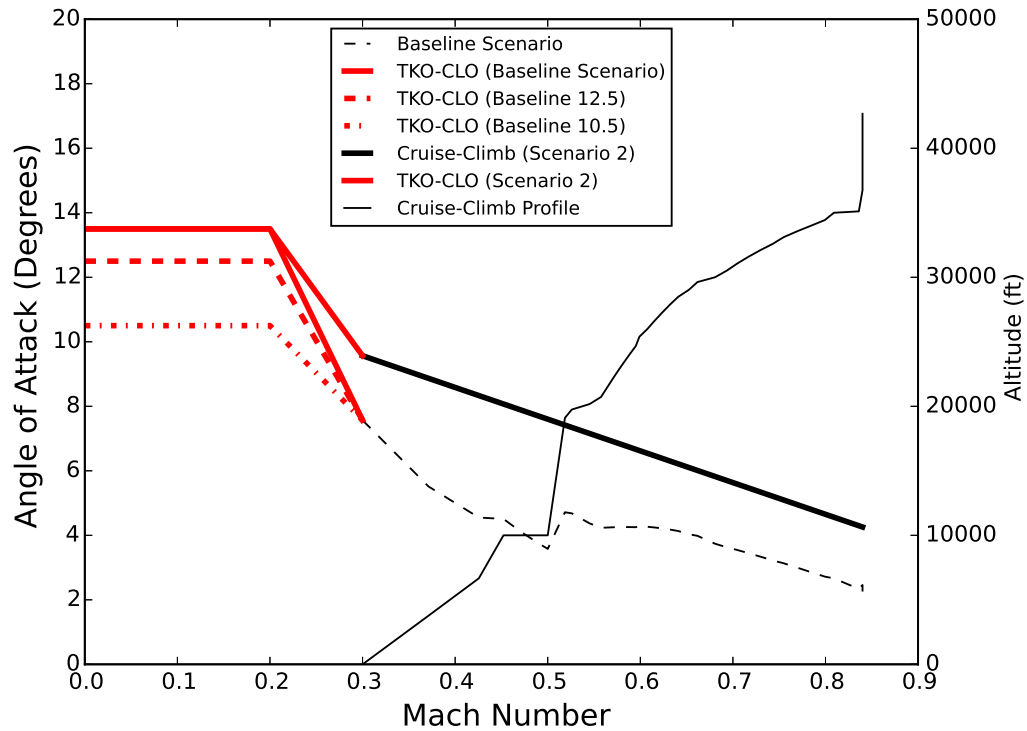


Figure 144: Alpha schedule of the baseline vehicle for take-off, climb-out, and cruise. Also shown are the alpha envelope scenarios to be tested.

Having defined the way in which the baseline vehicle traverses its mission through different flight conditions and vehicle orientation, the next definition which must be made is the limiting α requirements schedule. This is effectively a schedule of maximum required α vs. the Mach number and altitude of the vehicle. To test hypothesis 5 and demonstrate the BLIPSS methodology, there will be two scenarios used as inputs: first, an envelope scenario which adheres very closely to the baseline α schedule; second, an envelope scenario which allows for additional angle of attack beyond the

what the baseline mission schedule demands. These schedules are illustrated in fig. 144. The schedule is segregated into TKO/CLO and Cruise/Climb segments with the red and black lines respectively, and the transition line with large negative slope represents the climb-out reduction in α moving from the maximum of 19° . For lack of a better assumption, the transition line is assumed to be linear. For cases where the angle of attack constraint envelope is higher than the actual vehicle profile α schedule, the thrust requirement imposed is that the engine can continue to produce *at least* as much thrust as the baseline propulsion system.

The reason for using this requirement instead of the actual vehicle thrust required at that angle of attack is that the drag scales up significantly as the α and C_l are increased, much beyond what the baseline propulsion system could provide. Therefore, the requirement imposed is really that the propulsion system should be able to provide enough thrust for steady-level flight at the baseline (MN, alt, α) and must not *lose thrust or too much stall margin* if there are variations in vehicle orientation.

For the TKO/CLO segments, analysis will be conducted at a hot-day with $+27^\circ\text{F}$ ΔT from ISA since those are known to be more critical. Finally, the envelope schedule defines the “maximum” α the engine is required to operate successfully at. For the rolling take-off, it is necessary to consider both the SLS thrust requirement and the end of run-way thrust prior to take-off rotation, lift-off, and climb-out. This means the zero angle of attack point at take-off needs to be analyzed as well to ensure thrust production capability.

6.1.2 Propulsion System Schedules, Ratings, Limits, and Technology Parameters

As part of the BLIPSS process, MDP includes a requirements and technology definition phase. This phase consists of a step which establishes technology rules which

Table 18: Technology parameters which define the engine constraints at different design points.

Name	Description	Value/Range
Fan N_c Max	Maximum fan corrected speed	TOC N_c
T_4 (MTO)	Maximum take-off thrust T_4	3475°R
T_4 (MCT/MCL)	Maximum continuous thrust T_4	3304°R
$F_{n,max}$	Maximum Take-off rated thrust	72605 / Engine
$A_{19} / A_{19,Design}$	VAN area change	0.8-1.2
$M_t < M_{crit}$	Throat choke Mach number limit	$M_{crit} = 0.85$

feed into the cycle constraint points within the MDP. The distortion allowable schedule definition then feeds into this technology and requirements phase, but the phase also requires definition of certain technology parameters which define how the engine components are limited in their operation. The set of required design parameters and their limits are shown in table 18. These constraints are implemented in the NPSS solver for both the MDP design runs and the off-design checking runs in the vehicle matching phase. It is assumed that max continuous thrust begins above a Mach number of 0.4 (which typically represents the allotted time for MTO thrust).

Define Distortion Constraints

The distortion constraint is the next requirement set to be input to the BLIPSS methodology. The approach here will be to use a constant distortion constraint requirement of no more than 5% SMW reduction from the design point SMW (15%), which are typical numbers recommended in both Saravanamuttoo [77] and Walsh and Fletcher [89]. This means that the SMN equivalent constraint is then a minimum of 18.6%. In reality, this would most likely be put in as a function of the fan corrected speed for the desired operating line, since the stall margin stack-up varies in its

components at different speed. This would mean the amount that is book-kept for distortion varies during the operation of the engine. In any case, the approach here is to assume that for each design, the BLI engine does not drop below the lower bound of 18.6% SMN (10% SMW).

6.1.3 Initial MDP Setup

Table 19: Initial baseline design points for the MDP setup

Design Point	Mach	Altitude	Delta Temp.	α	Specification
ADP (Cruise)	0.84	36749 ft	0	2.45°	Fan $N_c = 100\%$
TOC	0.8091	35,000 ft	0	2.66°	$F_n = 30700$ lbs, $W_c/W_{cDes} = 103\%$
TKO	0.2	0 ft	+27 ° F	0	$F_n = 123,496$ lbs, $T_4 = T_{4-Max}$
SLSU	0	0 ft	0	N/A	$F_n = 145,000$ lbs, No customer bleed, installation effects or HPX
SLSI	0	0 ft	+27 ° F	N/A	$F_n =$ SLSU thrust, Includes customer bleed, installation effects and HPX, $T_4 < T_{4-Max}$

Taking all of the preceding setup into account, an initial MDP setup case can be established that is very similar to the baseline MDP case, shown in fig. 19. First, the TOC and cruise point setups are exactly the same as the baseline, except that the angles of attack for the BLI system are also included. Finally, the angle of attack at the TKO condition is input as zero, since this is the ground-roll AoA prior to lift-off and rotation. This is chosen since it is the point at which the thrust saving coefficient (BLI effect) is smallest and is a likely candidate for critical thrust condition at TKO. The high alpha take-off and an additional TOC point are included

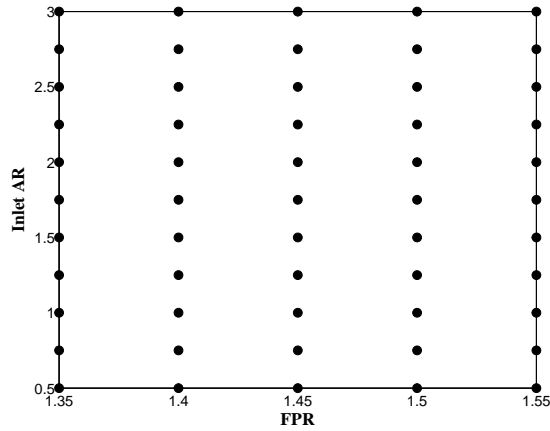
for iteration purposes, but there are no requirements imposed for these conditions in the vehicle matching relations.

6.2 Experiment 5

Experiment 5 is designed to test hypothesis 5, which essentially postulates that there are a limited number of flight conditions out of the total set of conditions which are critical. To determine these, a set of screening cases are used to determine the critical flight conditions and then the design evaluation is carried out after the fact once the flight conditions are known. The experiment will consist of testing a small set of screening cases to determine if this is, in fact, true under the assumptions of the design problem at hand and with the modeling assumptions made. The screening cases will be carried out for a few different sets of angle of attack requirements scenarios. The results of the screening cases will then be compared to a larger set of cases to determine a rough guideline for the number of required screening cases. Finally, an analysis of the design variables chosen will be conducted to determine their influence on the critical flight conditions.

6.2.1 Screening Test Setup

The initial screening test will be done on a 2 engine configuration on the baseline HWB vehicle. Some of the assumed design parameters and the screening case ranges are shown in fig. 145b. These cases will be run with and without the variable area nozzle to determine the efficacy of nozzle trim on improving the stability margin for these systems, and to determine whether or not the critical thrust points change when the VAN system is used.



(a) Screening design of experiments points.

Parameter	Value
FPR	1.35-1.55
Inlet AR	0.5-3.0
y/b_{center}	0
x/c	0.81

(b) Screening DoE design parameters and ranges.

Figure 145: Screening DoE Case Description

6.2.2 Baseline MDP Results

Each of the screening DoE cases above was run through the baseline model to size the engine to meet those criteria. The results for the MDP convergence rates are shown in fig. 146. A constant first initial iterate was used during these runs, and the majority of the runs at low inlet aspect ratio converged, while the higher AR cases had more difficulty finding a solution within the 500 iterations allowed for the Newton Raphson solver. This is because these cases have dirty sectors very close to the stall line, and are also farther away from the design used to generate the initial iterate. The failure rates for the case without the VAN was 17.2% while the failure rates with the VAN was 21%, so the VAN did not seem to affect convergence rates much. ‘

The results in fig. 147 shows some of the primary cycle differences between the solutions for the podded engine and the BLI engine with this MDP setup. The TOC fan over-speed is reduced as the inlet aspect ratio and thrust saving coefficient are increased. The result of this is that the speed at TKO is also reduced by an even more significant amount and the engine is burning a good bit cooler at altitude, because of the increased BLI benefit there relative to the TKO point. The BLI can therefore

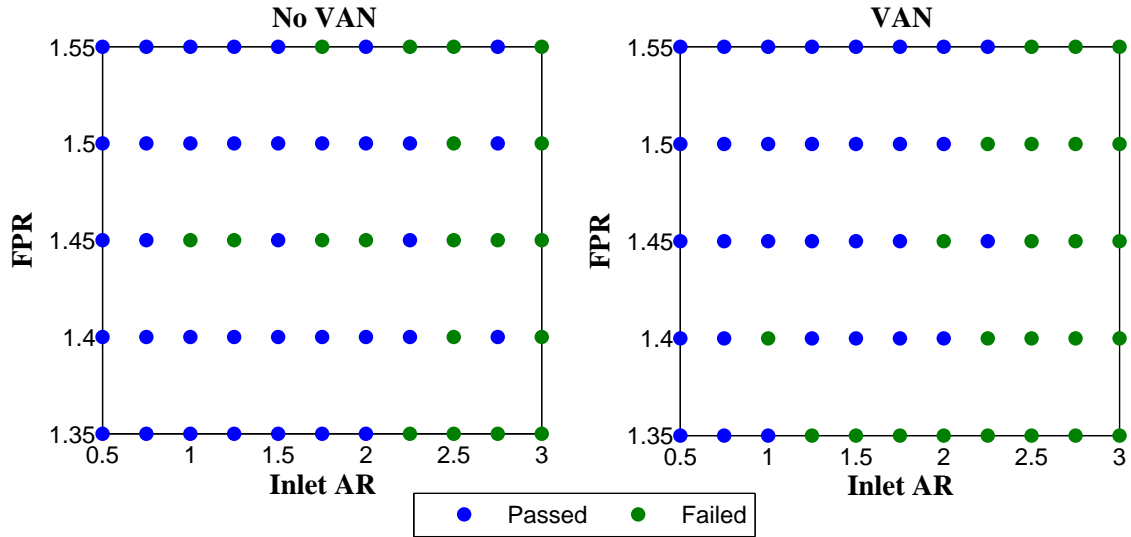


Figure 146: Figure showing the converged and failed cases in the screening doe for the initial BLI MDP setup.

be viewed as a kind of adverse lapse, tending to make the engine want a little more innate thrust at TKO and a little less at TOC where BLI is more active. If only the TOC point was used for sizing, the proper T4 to assume would not be known, and a constant T4 would yield either too little thrust at take-off or too much.

6.2.3 Off-Design Screening Test Results

We know depart to the actual results of the screening exercise. The way these results will be presented is to first describe the impact of the engine on the boundary layer in off-design by giving a sub-set of cases with increasing inlet aspect ratio to show off-design trends. Then, different scenarios will be investigated along those lines to show the impact of the requirements imposed. Finally, a summary is provided at the end to discuss the overall trends and conclusions from the screening exercise.

Baseline Scenario – No VAN

The baseline scenario without variable area nozzle was run for the 55 screening cases. The essential story for this case is illustrated below in figs. 148 and 149, where the

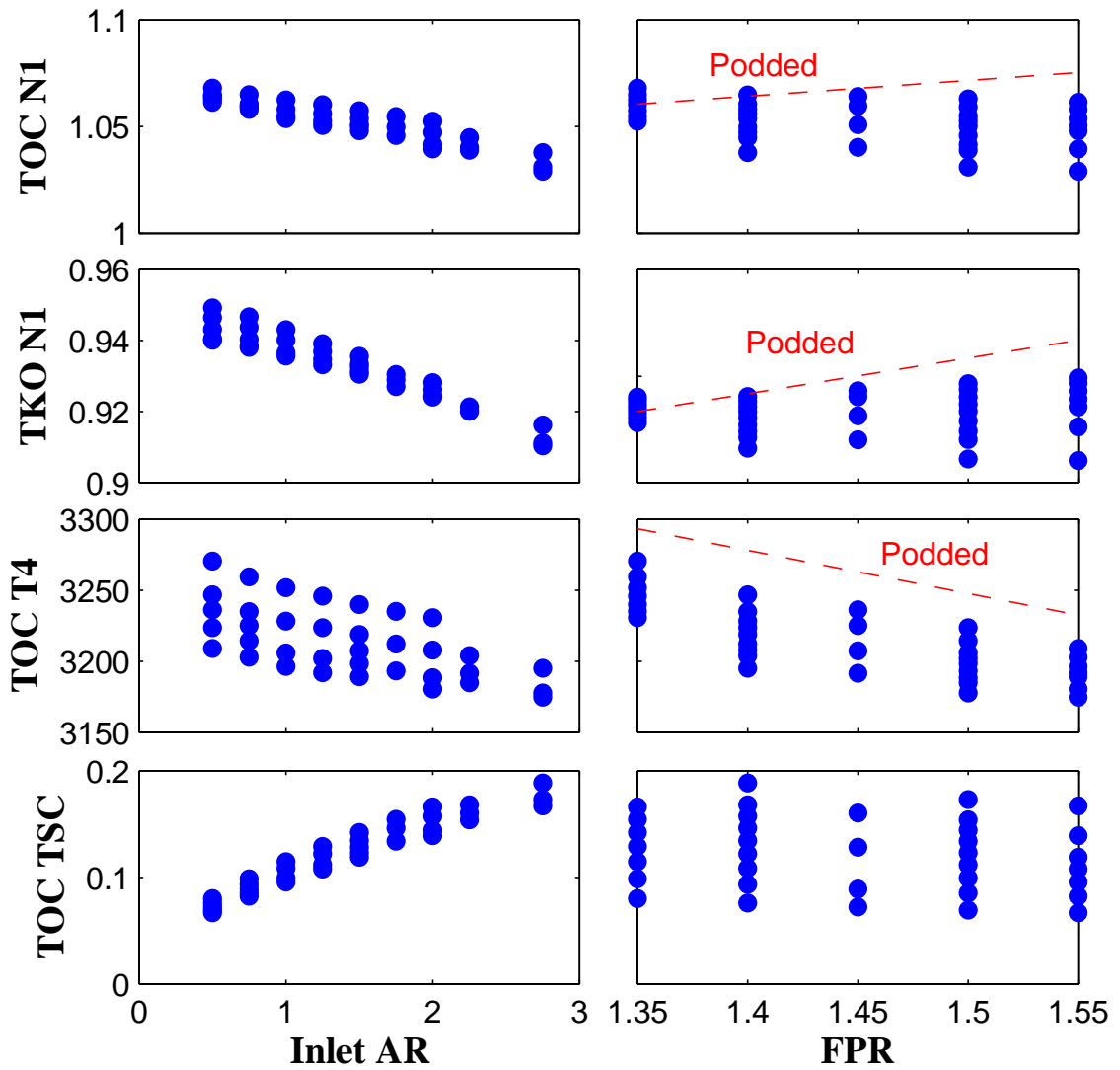


Figure 147: Figure showing effect of increasing the thrust saving coefficient on the MDP design solutions with BLI.

high α HD-TKO and TOC points are seen to be critical in terms of both thrust and stall margin. The stall margin constraint is increasingly prohibitive as the inlet height is lowered by increasing the AR. The same story goes for the choking of the inlet, which tends reduce the thrust at the TKO point significantly when the engine is effectively being starved by the boundary layer blockage.. A zoom in of the thrusts at

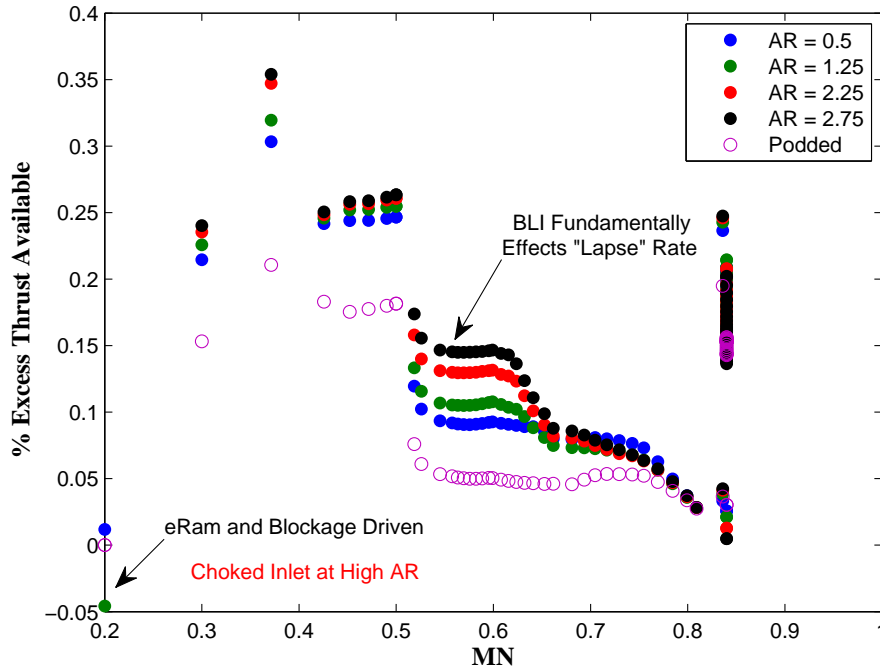


Figure 148: Excess thrust vs. flight Mach number for the baseline scenario without the variable area nozzle and a constant ADP FPR of 1.4.

TOC show one more additional interesting point (fig. 150), which is that the critical TOC sizing point has moved from the initial TOC point selected which was minimum for the baseline case and moved to the higher altitude climb. This is because the inlet recovery losses at the higher altitude/Mach are more significant at that point with the loss in ambient pressure, but the thrust saving coefficient doesn't add much additional benefit so the benefit to loss variation favors the lower altitude point (less thrust at high altitude/Mach). The influence of the inlet AR design variable is shown in figs. 149 and 152. Again, the story is fairly consistent with the previous analysis that was

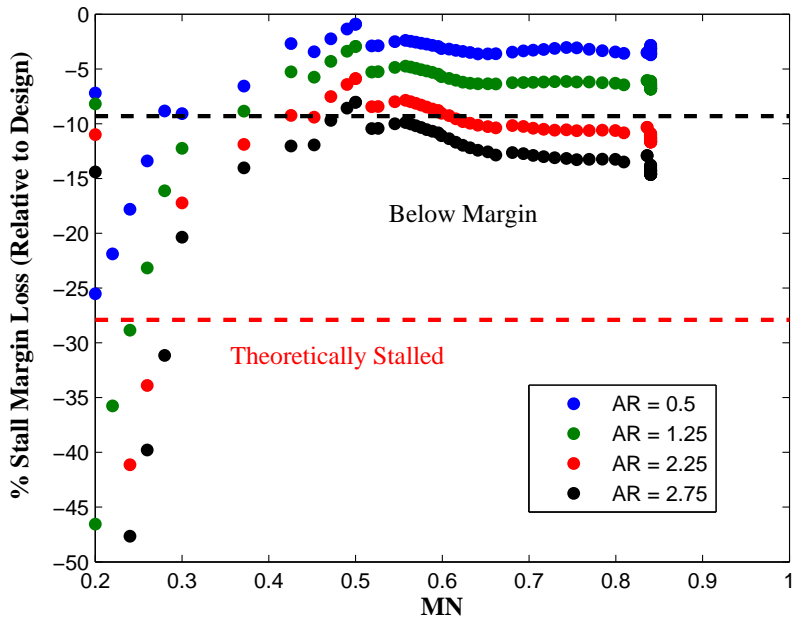


Figure 149: Distortion related stall margin loss vs. flight Mach number for the baseline scenario without the variable area nozzle and a constant ADP FPR of 1.4.

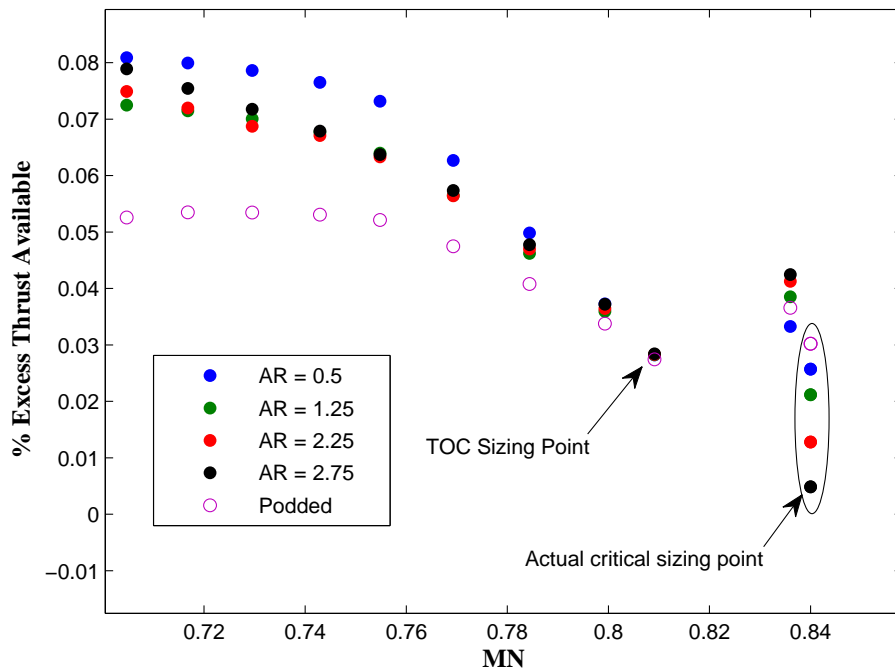
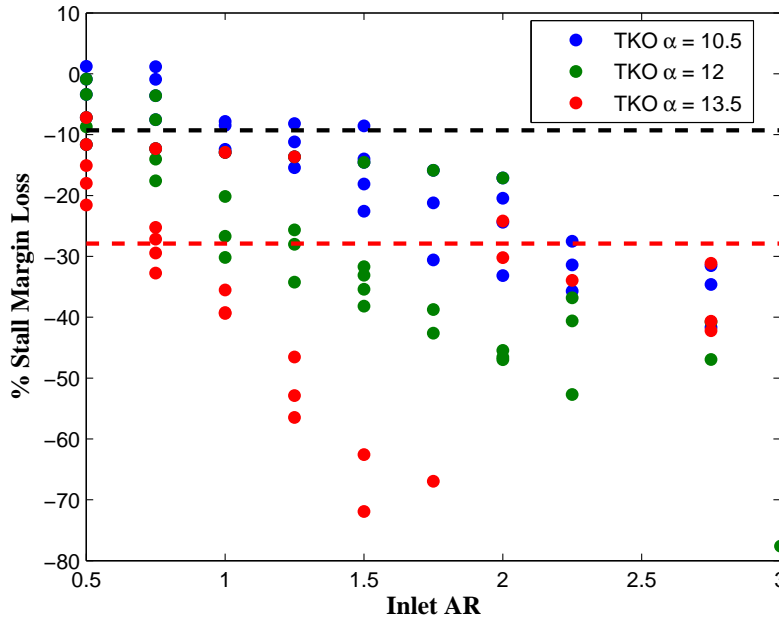


Figure 150: Excess thrust near TOC vs. flight Mach number for the baseline scenario without the variable area nozzle and a constant ADP FPR of 1.4.

done at constant FPR. The higher inlet aspect ratios have an increasing propensity to fail in either the MDP design run or in the off-design case runs. Furthermore, a single failure in the off-design cases can put the solver into an initial iterate for the next run which again produces another failure. This produces the lower density of points in the high AR region. The influence of the TKO α is also shown starkly in fig. 151, where the TKO 10° produces many stall feasible designs, whereas the additional few degrees above that moves the local airfoil into separation and a massively decreased inlet recovery region with higher blockage. The story is precisely the same for the thrust in this case, which is totally dominated by the choking of the inlet at sea-level for many of the high α cases. The higher inlet heights and lower α designs tend to have much less thrust loss or none, which is to say that some of the designs are more critical at the low α TKO point.



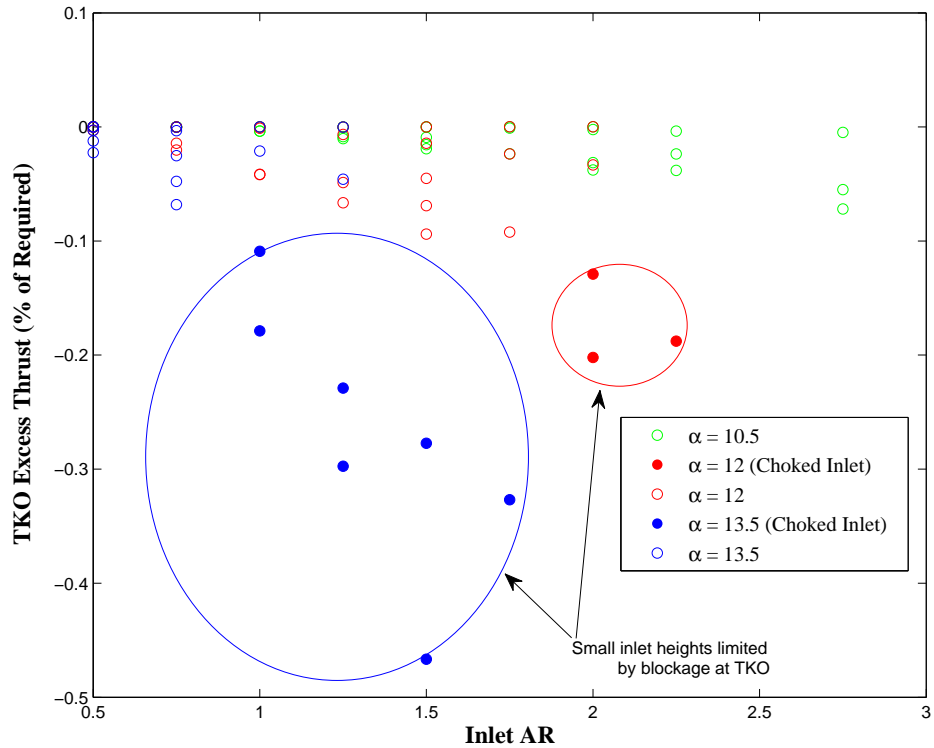


Figure 152: Take-off excess thrust (negative means thrust loss) vs. inlet capture area aspect ratio at different TKO angles of attack.

Baseline Scenario – With VAN

With the addition of the variable area nozzle into the mix, there are two expectations: first, that a few additional cases will fail in the design run because they are being constrained to a stall margin requirement; second, that the frequency of feasible cases should increase and that the stall constraint should be alleviated for some design. A glance at tab. 20 in the summary part of this section will show that this is the case. In general, we expect that the low altitude point would significantly improve their stall margin, which is again confirmed by the results in fig. 154. The downside to this is that opening the nozzle area and moving to a lower FPR op-line reduces thrust. Fig. 153 shows that this reduces the excess thrust during climb relative to the non-VAN case. Nonetheless, this is desirable since it keeps the op-line of the fan in a favorable

region. The VAN schedule in fig. 155 shows that the relative increase in the bypass

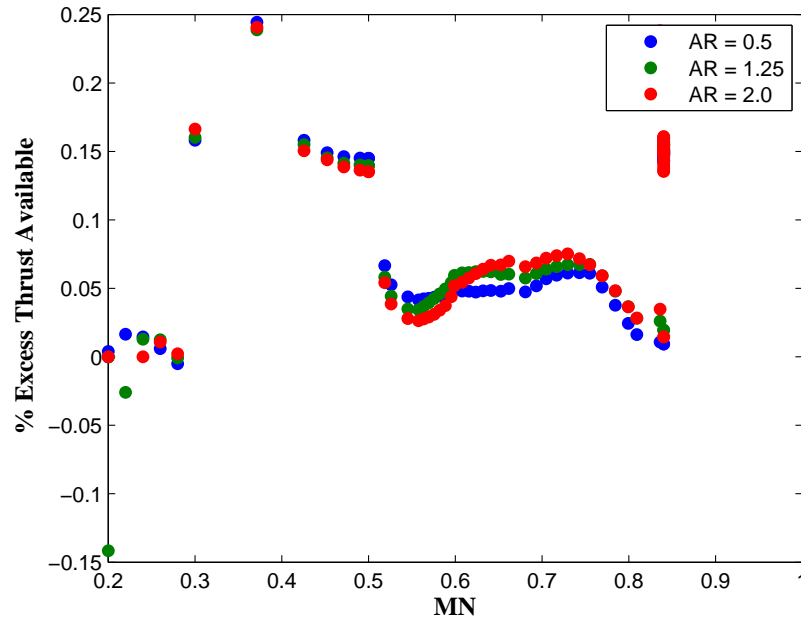


Figure 153: Excess thrust vs. flight Mach number for the baseline scenario with the variable area nozzle and a constant ADP FPR of 1.4.

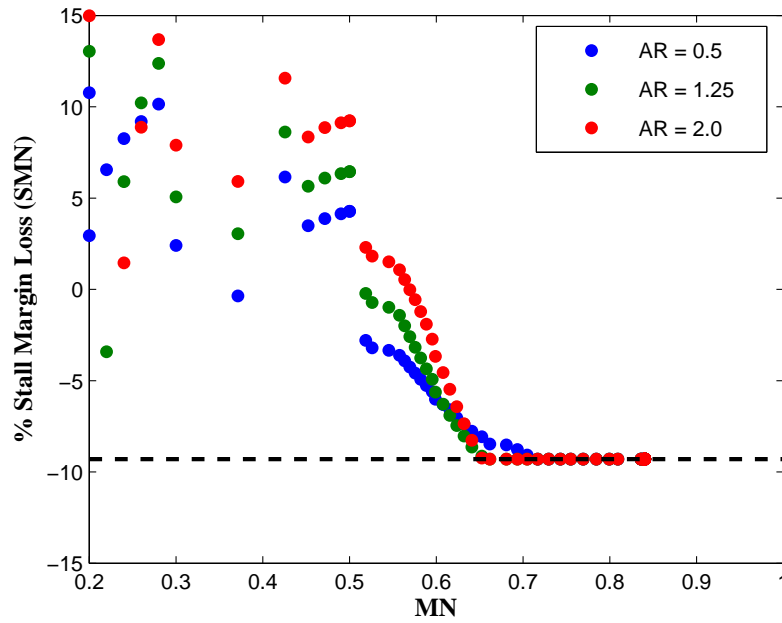


Figure 154: Distortion related stall margin loss vs. flight Mach number for the baseline scenario with the variable area nozzle and a constant ADP FPR of 1.4.

area at the high α TKO point is much higher (in fact tat its limit for many high AR cases). This tends for the fan compressor to require additional flow, shown in fig. 156, and thus chokes a higher percentage of the intakes for these designs. This brings to light the true nature of the problem, that re-matching through whatever means is available essentially costs something in the way of mass flow, engine size, and possibly efficiency.

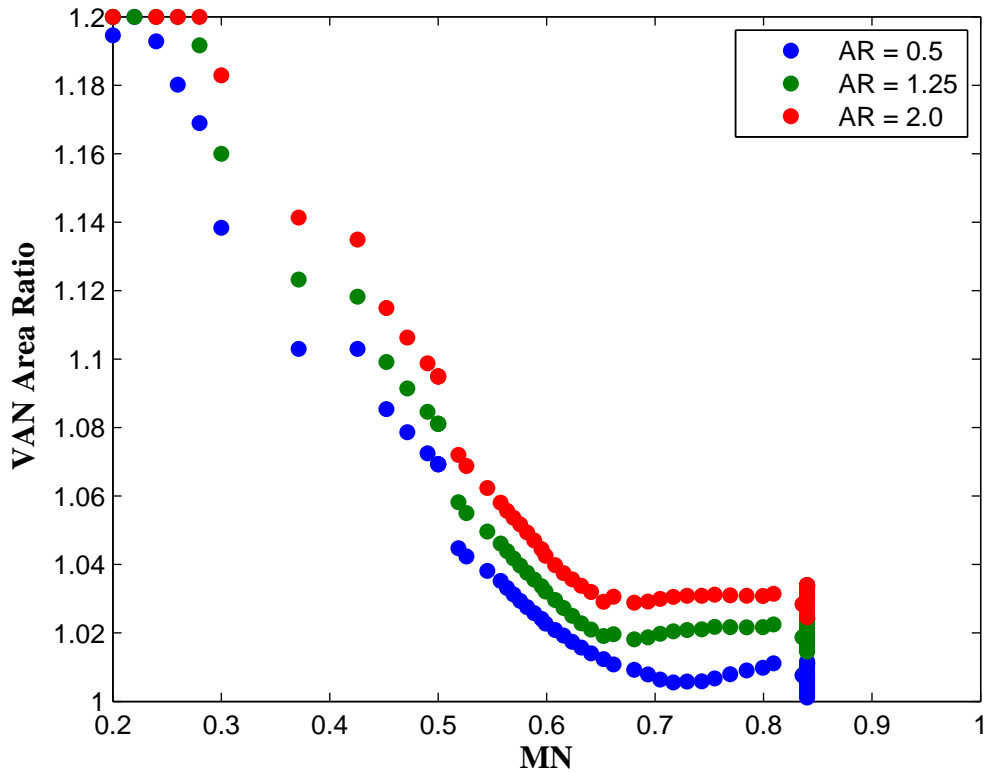


Figure 155: Van area schedule for the baseline flight envelope scenario.

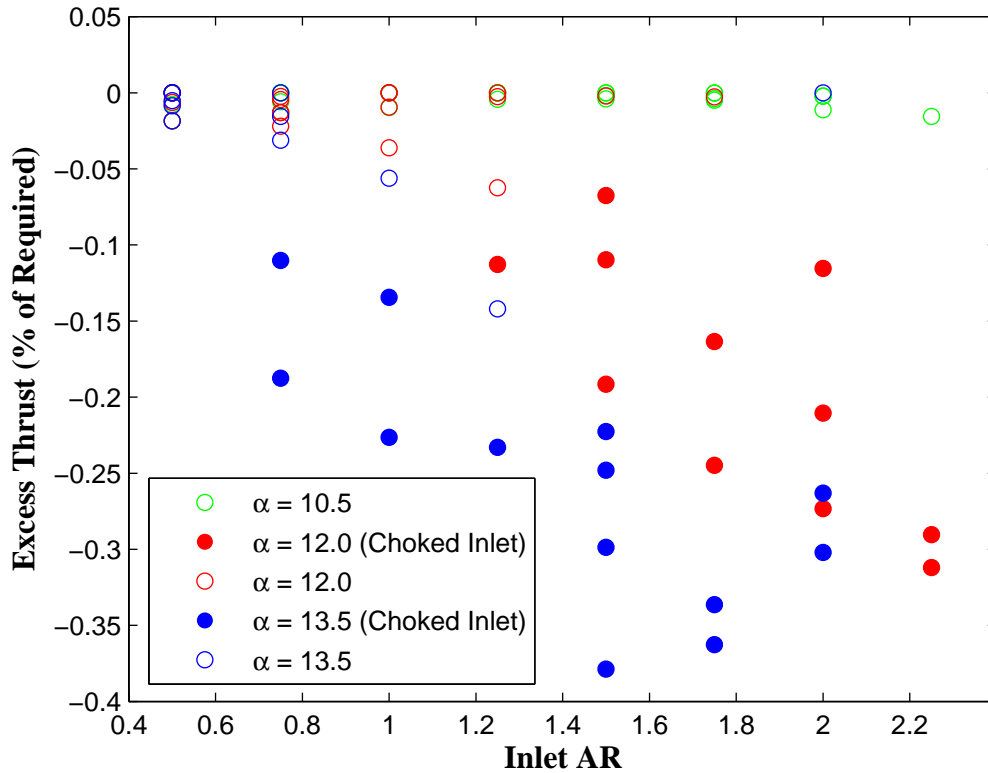


Figure 156: Take-off excess thrust (negative means thrust loss) vs. inlet capture area aspect ratio at different TKO angles of attack with VAN.

Scenario 2

The second scenario is one in which a margin of 2 degrees is added to the angle of attack during the cruise-climb portions. The expectation is that the percentage of cases which are critical in terms of both thrust and stall margin at the high altitude points would increase, which again is observed (tab. 20). Fig. 157 highlights this by comparing the baseline and scenario 2 with the α margin scenario. Many of the climb points are now thrust deficit, though none of them more than the TOC point. This is a function of the fact that a constant $\Delta\alpha$ margin is used. A scenario with increased α requirement during climb but minimal required excess α during TOC may have a different result. Regardless, the point is that the requirements set by the vehicle, in

conjunction with the installation impacts on the propulsion system, are driving the required sizing conditions. There may be certain requirements sets where the critical point is not necessarily known *a-priori*, thus requiring the vehicle matching phase.

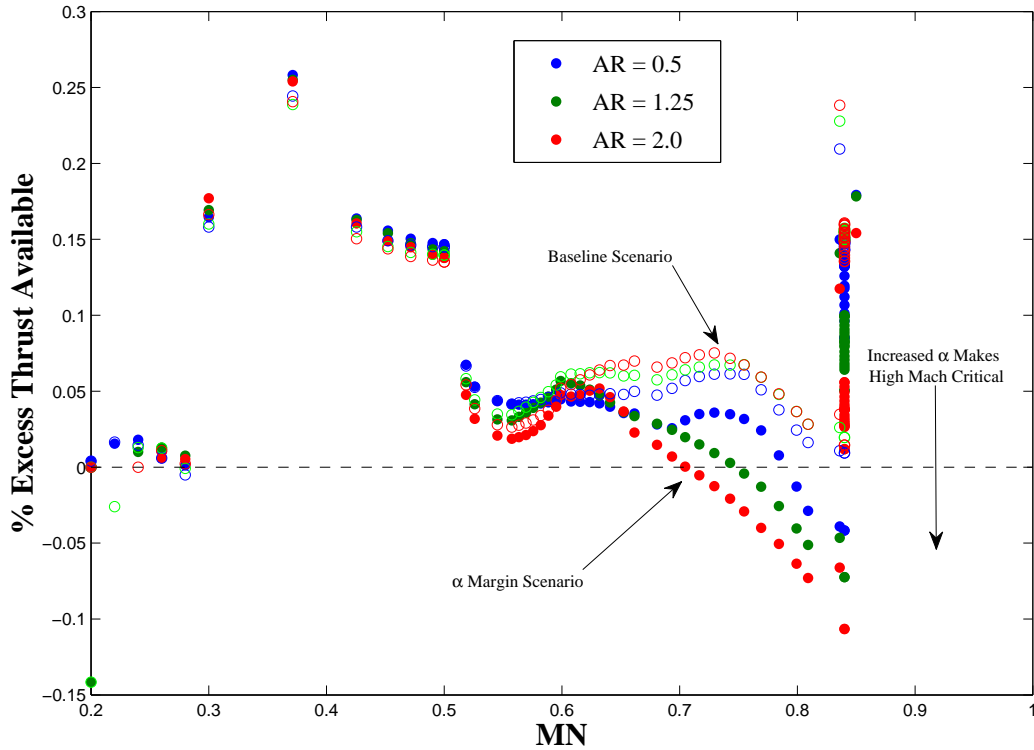


Figure 157: Distortion related stall margin loss vs. flight Mach number for the baseline scenario without the variable area nozzle and a constant ADP FPR of 1.4.

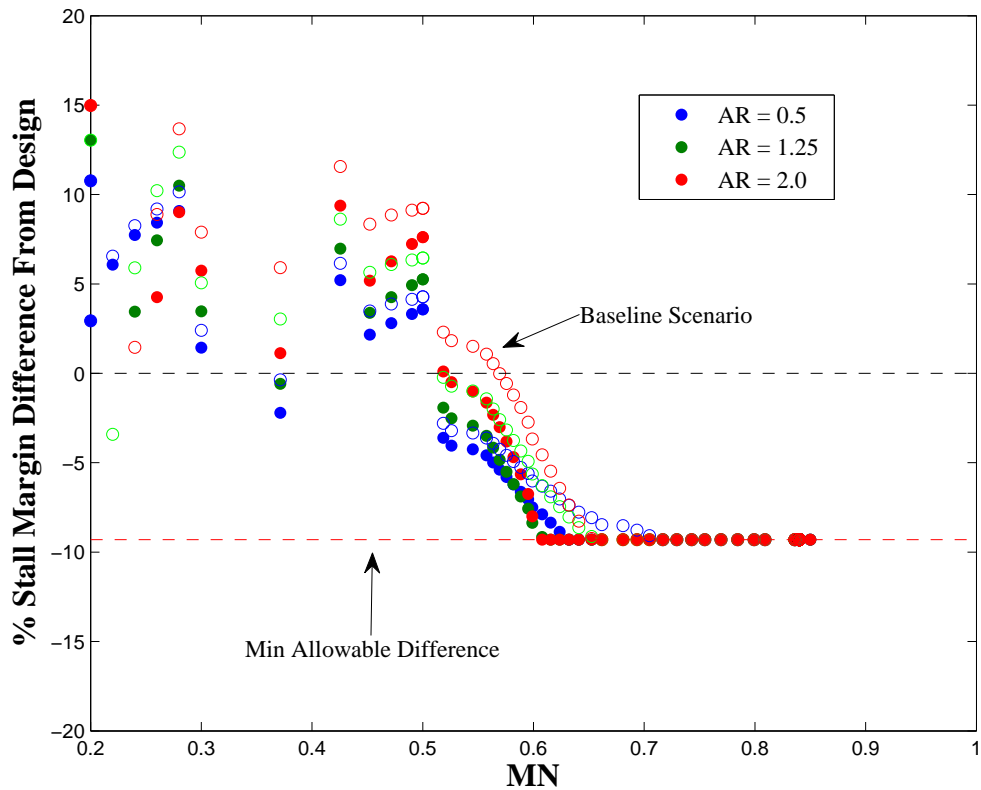


Figure 158: Distortion related stall margin loss vs. flight Mach number for the baseline scenario without the variable area nozzle and a constant ADP FPR of 1.4.

6.2.4 Screening Case Summary

A final summary of the results of the above experiments is shown below in tab. 20 and highlights some of the key differences between the designs with or without VAN and the influence of the angle of attack envelope requirements. The first point is that, generally speaking, going to higher angle of attacks than that at which the engine and inlet capture area were sized is – to put it mildly – very bad, both from a model convergence and performance/operability perspective (since they are related). The logical corollary is that these points should be included in the sizing process to ensure reasonable operation should the vehicle need to experience this condition.

The second point is that reducing the inlet height and increasing the width tends to make it much more difficult to achieve feasible designs at high α . The combination of low fan pressure ratio and high inlet aspect ratio, or high fan pressure ratio and high inlet aspect ratio tend to fail. On one side it's being driven by the increased sensitivity to distortion at low FPR; on the other by the small inlet capture height and the reduced distortion. These are the sorts of factors that designers need to begin to consider in the cycle analysis and early planning phases for BLI systems.

Table 20: Summary of the cases run for experiment 5.

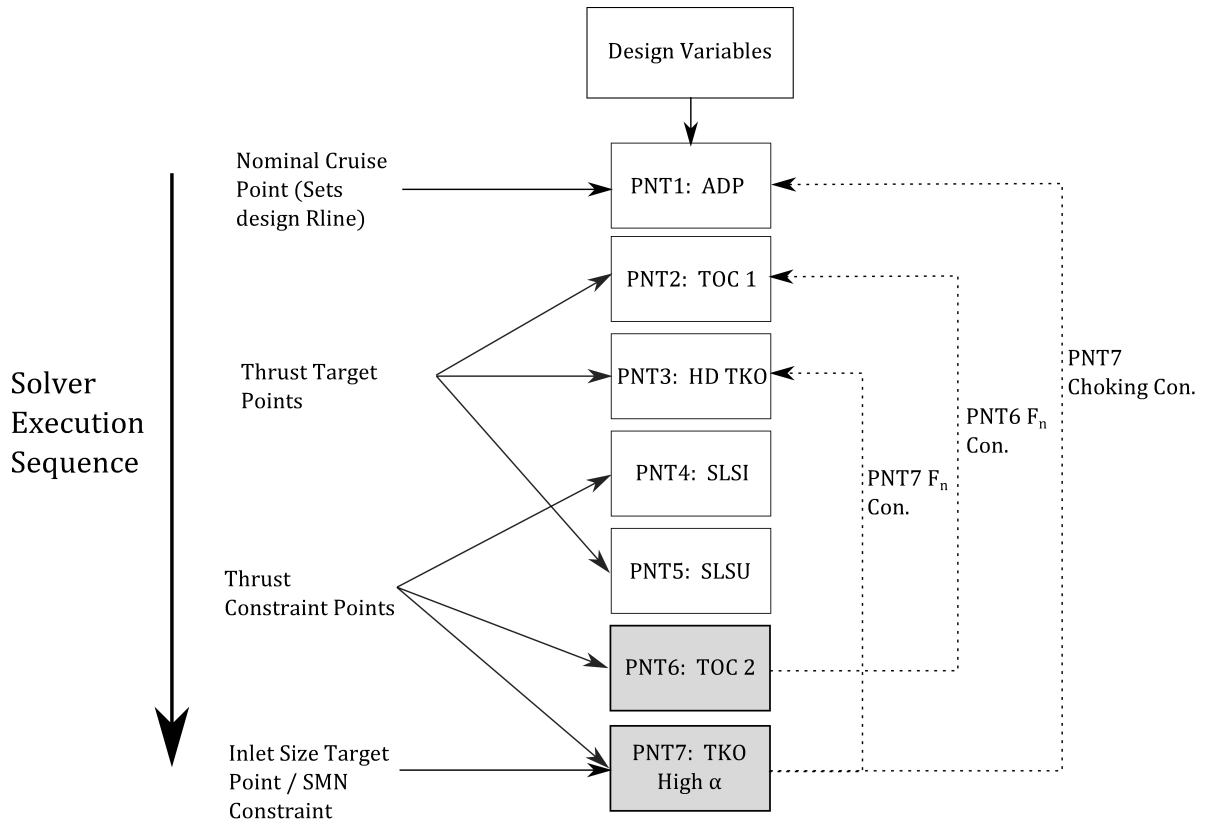
	Case	No. Of Failed Runs	No. of Feasible Designs	Crit. F_n Points (MN,alt, α)	Crit SMN Points	No. Choked Inlets
No VAN	Baseline $\alpha_{TO} = 10.5^\circ$	19	2	(0.2,0,10.5)	(0.2,0,10.5)	0
	Baseline $\alpha_{TO} = 12^\circ$	19	0	(0.2,0,12)	(0.2,0,12)	4
	Baseline $\alpha_{TO} = 13.5^\circ$	27	0	(0.2,0,13.5)	(0.2,0,13.5)	7
	Scenario 2 $\alpha_{TO} = 13.5^\circ$	37	0	(0.2,0,13.5) (0.84,37k,4.5)	(0.2,0,13.5)	4
VAN	Baseline $\alpha_{TO} = 10.5^\circ$	25	16	(0.2,0,10.5) (0.84,37k,2.5)	(0.2,0,10.5)	0
	Baseline $\alpha_{TO} = 12^\circ$	25	6	(0.2,0,12) (0.84,37k,2.5)	(0.2,0,12)	9
	Baseline $\alpha_{TO} = 13.5^\circ$	27	4	(0.2,0,13.5) (0.84,37k,2.5)	(0.2,0,13.5)	18
	Scenario 2 $\alpha_{TO} = 13.5^\circ$	29	0	(0.2,0,13.5) (0.84,37k,4.5)	(0.2,0,13.5)	17

6.2.5 Vehicle Re-match

The next step in the experiment is to conduct the rest of the algorithmic process in fig. 140. This could be done programatically, but it is recommended that this process take place by manually iterating the MDP process with the new design conditions. This is because the new initial iterate can be much different if the minimum SMN and the thrust condition change around. The process, then, is to simply add new assemblies which represent the new critical flight conditions and a new set of solver independent and dependent cycle and thrust matching relations for these points. The new design points and their specifications are shown in tab. 21. Essentially, the new additional TOC thrust point and the high α TKO point are added to the MDP. The specifications are that the net thrust for each point is greater than the vehicle requirement at that point and that the inlet is not choked at the high angle of attack TKO point. These are implemented as cycle constraint relations in the solver independent and dependent list. This process is illustrated in fig. 159, and shows how the constraint points are related to each other point. The detailed solver setup is shown in appendix A. The same screening cases will be run to compare the off-design results from the initial and vehicle re-match MDP.

Table 21: Initial baseline design points for the MDP setup

Design Point	Mach	Altitude	Delta Temp.	α	Specification
TOC 2	0.84	37024 ft	0	2.45°	$F_n = 13452 \text{ lbf}$
High α TKO	0.2	0 ft	0	2.66°	$F_n = F_n@TKO ;$ $A_o/A_c < (A_o/A_c)_{choke}$



** With VAN -- All Points are constrained by their min SMN (Bypass area changed until satisfied)
 * Without VAN -- The design Rline is moved to match the PNT7 Requirement

Figure 159: Diagram of the re-matching procedure for the baseline scenario.

The screening cases were rerun for the VAN case with the re-match MDP setup. The results from the re-match for the baseline scenario showed that the re-matching iteration rematches the system for each of the screening cases for which the solver converges. The results for both thrust (fig. 160) and stall margin (fig. 161) are shown and corroborate that the chosen additional design conditions resolve the issues at the critical design points. This is, essentially, verification of the critical conditions shown for the baseline scenario which further corroborates hypothesis 5.

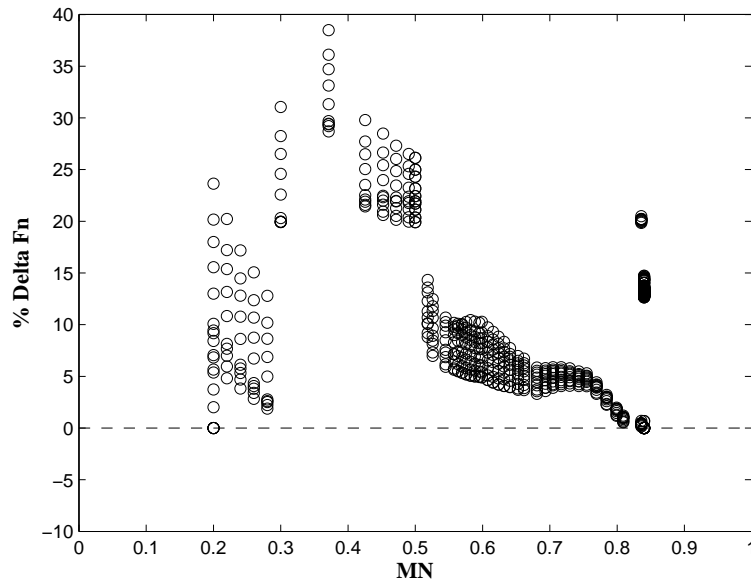


Figure 160: Plot showing the % excess thrust at each point in the flight envelope for all of the converged cases using the re-match process

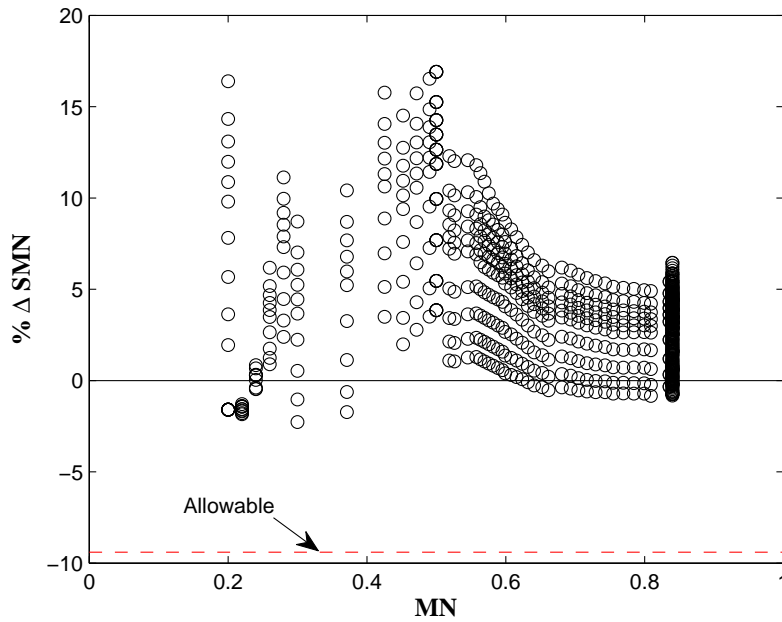


Figure 161: Plot showing the excess SMN at each point in the flight envelope for all of the converged cases using the re-match process.

shows a clear inflection point which represents the trade-off between the TKO choking condition and additional inlet and fan losses during cruise due to the larger capture area and increased pre-entry pressure expansion.

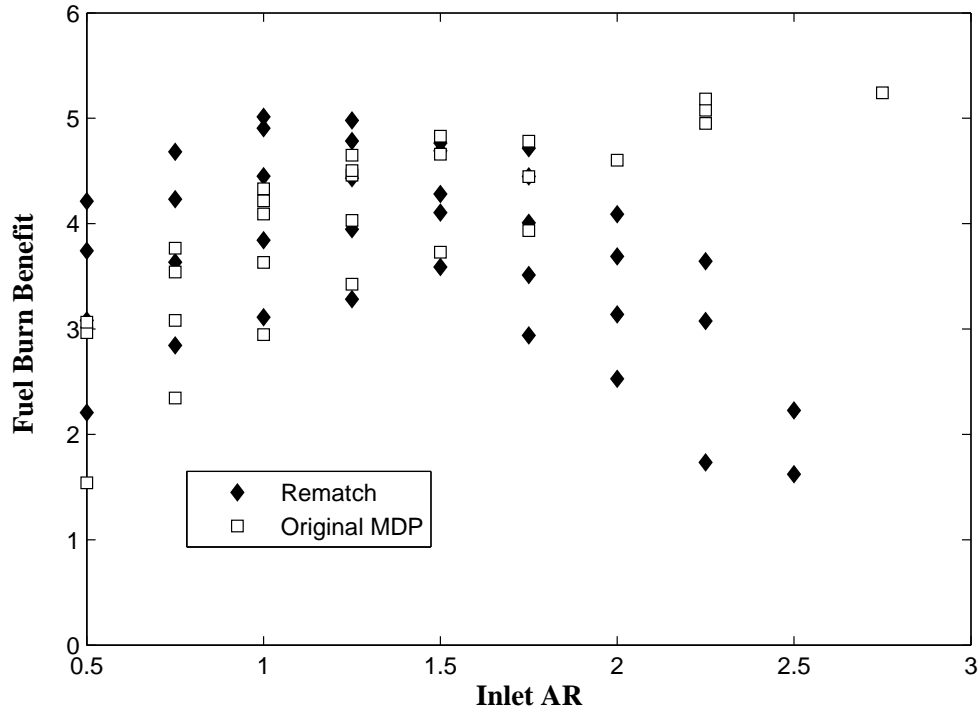


Figure 163: Plot showing the inlet aspect ratio vs. fuel burn trends and comparing the rematch MDP with the original setup.

6.2.6 On Hypothesis 5

Finally, the result of the investigation into hypothesis 5 is confirmed by the data. The total number of additional critical conditions necessary to include for the BLI system (relative to baseline)– in these screening cases, under these assumptions, and with the precise requirements set input to the method – is two. Furthermore, additional design aspects of the system, such as the extraction ratio are not likely to change the actual critical conditions sub-set, though they may perturb which condition is actually critical, and in which mode. This is, at least, strong evidence that the hypothesis

is correct, though far from a mathematical proof that it will always be. The more conditions that are added to a system requirements envelope, the more likely that the sub-set might expand, depending on the design variables which affect the performance of the system. This author does not wish to speculate on the universal validity of the hypothesis, but only to say that accepting it as true is probably a good starting point for departing into the investigation. If it is found that the number of potential critical flight conditions is so large within the design space that it would be infeasible to construct an MDP design around them, then the vehicle matching phase screening process should be abandoned and every design case should be checked in off-design.

6.3 Summary of Chapter 6

This chapter demonstrated the tentative validity of hypothesis 5, and justified the construction of the vehicle matching phase in its current form. The implementation showed that, for the canonical HWB with turbo-fan BLI system, the high α HD TKO point was generally the most critical in terms of thrust and stall margin without a variable area nozzle, except for very low inlet aspect ratio designs (which don't ingest much BLI). With the VAN, the stall margin is able to be recovered, but the choking of the inlet becomes a problem with a fixed inlet capture ratio at the ADP point. Many points are therefore thrust deficit when the VAN is used, requiring a rematching process to satisfy both thrust and SMN constraints.

CHAPTER VII

SUMMARY AND CONCLUSIONS

The thesis presented in the preceding chapters is that the method developed herein – the BLIPSS methodology – improves upon existing BLI system analysis methodologies in the following ways: it allows for better estimates of performance and operability at design and off-design conditions, takes into account multiple propulsion system architectures, and determines the critical flight conditions required to include in a simultaneous multi-design point solution procedure for both thrust and stall margin requirements. The methodology comprises the original 3 MDP phases and 3 additional phases developed as part of this research: the BLI modeling phase, the architecture integration phase, and the vehicle matching phase. The BLI modeling phase established a process for mapping performance and operability at design and off-design conditions. Experiments 1 and 2 established the importance of this for truly defining the BLI design space in terms of the fuel consumption objective and the stall margin constraint. The architecture integration phase provides a way of using the MDP framework for analyzing systems with asymmetric configurations. Experiments 3 and 4 investigated the effects of doing this on a sample HWB architecture to establish the relative importance of the approach for the test case. The vehicle matching phase defined a process for determining a set of critical flight conditions which should be included in the MDP setup. Experiment 5 showed that this was a useful process because an initial set of potential conditions can be reduced to a critical sub-set, making the MDP setup phase much more tractable and numerically stable. The rest of this chapter will provide a summary of the detailed hypotheses explored in the preceding chapters, the contributions of this thesis, and finally a series

of recommendations for future related work.

7.1 Review of Hypotheses

The initial theoretical investigation in chapter 3 demonstrated the physical relationships of importance for BLI systems and established hypothesis 1:

***Research Question 1:** What are the minimum requirements for conceptual level modeling of a boundary layer ingesting cycle model in order to reasonably construct the architecture and cycle design space of a BLI propulsion system?*

***Hypothesis 1:** BLI propulsion system cycle models need to include the physical coupling between the vehicle boundary layer profile, the ingested stream-tube, and system powerbalance and losses at critical sizing conditions. Without these effects, the model will not properly characterize performance trends at design and off-design conditions.*

This hypothesis was tested on an HWB vehicle similar to the Boeing N2A-EXTE with turbofan engines. The hypothesis was shown to be valid for this system by constructing a set of boundary layer ingestion component models which capture the relationship between the level of BLI (or thrust saving coefficient), the engine mass flow (stream-tube ratio), and the inlet and fan losses. The experiment compared the impact of including each of the loss components in the analysis by looking at sensitivities of performance to variations in the design variables. Additional assumptions for off-design conditions were tested, including whether to assume fixed aspect ratio or fixed width stream-tube projection, and the impact of using a fixed boundary layer in off-design performance.

Perhaps one of the most important insights which arose from this investigation is in understanding a fundamental trade-off of BLI systems: thrust/propulsive efficiency benefit vs. inlet/fan losses. In the case of the HWB with turbo-fan engines, the

designer may attempt to increase the amount of BLI by changing the width of the stream-tube or by increasing the number of engines. Doing so causes the stream-tube height to decline and the losses to increase to a point where the trade-off becomes unfavorable. The design angle of attack was further found to have a strong influence on this trade-off by changing the boundary layer thickness.

In off-design, the importance of the stream-tube and boundary layer thickness (or angle of attack) interaction were emphasized within the model. The take-off point was found to have very low TSC at a 0° angle of attack, but to have higher TSC near the actual lift-off angle. This high level of BLI was also accompanied with higher losses and a tendency to choke the inlet because of the vastly increased blockage. This emphasizes the need to consider the high angle of attack point as a potential inlet sizing point.

The second research question and hypothesis has to do with the impact of the operability constraint on the propulsion system design space, and was formulated as follows:

Research Question 2: *How does the stall margin constraint affect the BLI propulsion system design space?*

Hypothesis 2: *The stall margin constraint limits the size of a propulsor in relation to the amount of boundary layer that it ingests.*

This hypothesis was tested in experiment 2, which was performed on a single design point model. The capture height was varied by changing the number of engines (or thrust per engine) and the inlet aspect ratio. The stall margin was found to be strongly correlated with the physical capture height of the inlet, thus confirming the hypothesis. Hypothesis 2 was also further confirmed by the later MDP model, which was evaluated over the entire mission envelope in experiment 5. The implication

of hypothesis 2 is that higher inlet AR designs (lower capture height) will tend to have more distortion and lower inlet recovery, though they also ingest more boundary layer. To accommodate the reduced stall margin at the higher levels of BLI, distortion mitigation actions must be used and their penalty must be low enough to be useful. Design point re-match and inlet flow control were explored as options in experiment 2.b, neither of which were as good as the variable area nozzle explored in experiment 5, which proved necessary to handle the TKO high AoA condition.

Research question and hypothesis 3 were in relation the architecture integration phase, and are as follows:

***Research Question 3:** How can multiple design points, different BLI propulsion system architectures, and variations in inlet properties between propulsors/engines at a given flight condition be accounted for in BLI propulsion system conceptual design?*

***Hypothesis 3:** Differing inlet conditions for BLI propulsion systems can be accounted for by using a modified simultaneous MDP approach where design points are considered on a “per-propulsor” basis and sizing to a total vehicle thrust. If the difference in the local inlet properties are large, this approach will yield increasingly different performance predictions than if the traditional single engine or the wake correction method is used.*

This hypothesis essentially argues that the MDP approach can be made more general by considering design points on a “per-propulsor” basis. The procedure then matches the system to a total thrust rather than a single engine thrust. This allows the simultaneous solution to be found for the entire system while still maintaining the traditional concepts of engine “on-design” and “aerodynamic design points”. A process for implementing this was defined in the BLIPSS methodology and implemented

on a 3-Engine HWB vehicle. The vehicle taper produced differences in the ingested boundary layer between the engines. Experiment 3 showed that by increasing the outboard location and the difference between the ingested boundary layer, that the solution between the BLIPSS methodology differs from the single inlet approach on the order of a few percent, depending on the angle of attack. This is a key motivation for the use of the BLIPSS methodology.

The fourth research question and hypothesis pertains to the use of the new degree of freedom that the BLIPSS methodology enables for the HWB design problem, namely the mass flow ratio between outboard and inboard engines. They are stated as follows:

***Research Question 4:** For BLI propulsion systems, which design options provides the largest benefit?*

***Hypothesis 4:** The mass flow ratio degree of freedom can improve the performance benefit of the canonical BLI propulsion system.*

Experiment 4 confirmed that, in fact, lower MFR systems are preferable, but only if the size reduction of the outboard engine does not significantly impact the gas turbine core, as was the case with the fixed core design. The chosen aerodynamic design point did not significantly impact efficiency, but the smaller outboard engine case seems to always provide a more optimal efficiency. This is because the smaller inlet heights better match to the reduced boundary layer thicknesses at the outboard location. Based on this observation, this author believes it is fair to speculate that other system architectures may have this same feature, where the individual propulsor size can be tailored to the size and shape of the boundary layer it is ingesting.

Finally, the fifth research question and hypothesis for the BLIPSS methodology is formulated in relation to the vehicle matching phase:

Research Question 5: *What flight conditions are necessary to include for sizing BLI systems in a MDP cycle analysis?*

Hypothesis 5: *A sub-set of all thrust/stall margin flight conditions can be found that contain the most critical conditions for a large majority of the BLI conceptual design space.*

The hypothesis was confirmed by doing a screening experiment on a 2-Engine configuration, assuming several different α requirements scenarios. For every case in the design space, the critical flight condition was either the high α hot-day TKO point or one of the two TOC points. It was also found that it was necessary to include the low α HD TKO point since the BLI benefit at this α is very low. This acts as an inverse lapsing effect, since the BLI benefit is higher at altitude, enabling lower speeds at TKO and TOC and lower burn temperatures at altitude.

7.2 Summary of Contributions

The principal contributions of this thesis are as follows:

- The development of a method for BLI propulsion systems sizing and analysis (BLIPSS) which combines three things: proper component modeling of BLI benefits, losses, and operability estimates over the design space and in off-design conditions; an enhanced multi-engine MDP based method that accounts for architecture types with different size propulsors and inlet conditions; and finally a screening process for determining which flight conditions are critical for a BLI system based on the required flight envelope and angle of attack requirements. This method allows designers to properly size an a propulsion system with more accurate estimates of performance during the conceptual design phase and enables trade space studies of BLI benefits vs. potential losses and distortion or operability issues. It further allows the designer to establish cycle models

to provide to CFD experts when performing the higher fidelity analyses and serves to give some guidance on the flight conditions where critical detailed aerodynamic information is required for propulsion system design refinement.

- Some insights were made into the general BLI problem. First, that there is generally a trade-off for class 2 BLI problems between the amount of BLI that can be ingested and the height of the inlet stream-tube in relation to the boundary layer. This implies a critical trade-off between the % BLI or thrust saving coefficient achievable and the system performance and operability losses. Second, that accounting for variation in the boundary layer at different inlet locations on the vehicle can have a substantial impact on the performance results, and that tuning the size of each propulsor according to the size of the local boundary layer may give some additional benefit to a BLI system. Finally, the critical flight conditions for the HWB with turbo-fan engines is likely the high angle of attack or lowest angle of attack HDTKO point for the max T4 sizing point and the highest altitude/MN TOC is the likely candidate for the max corrected flow sizing point.
- Finally, the development of a unique means for using the parallel compressor method in steady-state gas turbine models for engine On-Design was developed. This method employed a two step process which uses a uniformly distributed design run to set the pressure and efficiency scalars, and another design run to match the required flow capacity. It was found that this process gave good results in terms of convergence.

7.3 Notes on the Methodology

7.3.1 On Convergence and Initial Iterates

The practitioner of the BLIPSS methodology should be warned that it is a method which requires deep understanding of the concept of object oriented programming and specifically the use of engine assemblies such as those in NPSS. Without this toolset, or something very much like it, the methodology will be very difficult to implement. Furthermore, even with this toolset, adding more assemblies to the solver increases the number of non-linear equations which must be solved, the function calls which must be made to the cycle model, and the likelihood of non-convergence based on a bad initial guess. This is further motivation for use of the screening process to eliminate unnecessary design conditions, and becomes especially perilous if the architecture integration phase is used and there are multiple inlet conditions present. Finally, special care should be taken when implementing the vehicle matching phase process. It is tempting to automate this process, but the current authors attempt to do so yielded non-convergence or failure for a significant amount of cases due to the fact that the critical design points may jump from high altitude to low. This makes it very difficult to setup initial iterates which are robust enough to find solutions. The use of the MDP correction algorithm (see [83]) may be a solution to this problem, but the current author has not attempted an implementation of this with the BLIPSS method.

7.3.2 Regarding Other Architectures

While the BLIPSS method was developed for a general BLI system architecture, many of the steps in the architecture integration phase may take some additional developments or investigation. For instance, the power management and design rules may be substantially different for the distributed propulsion case which has the problem

of coupling a gas turbine generator, an electrical distribution system, electric motors, and ducted BLI fans. How this system is power managed is a thesis problem in and of itself, but the hope is that if some relationship between the gas turbine core power and the speeds of the fans is established, then the AIP process should be able to provide the converged thrust solution with the proper BLI accounting and variation in inlet recovery.

It should also be mentioned that some architectures will have very different trends in their performance than the HWB with turbo-fan engines. For instance, both the double bubble and distributed propulsion HWB architectures have a much more constraining geometrical problem of fitting all of the propulsors into an exact width. This means the level of BLI ingested is more or less set, but still hypothesis 1 of this thesis applies when investigating the loss mechanisms which result from, for instance, the fan pressure ratio (see also Felder [47] for an example of this).

7.3.3 Other Use Cases

Finally, other applications for this methodology seem relevant. Military systems sometimes have non-uniform inlet conditions and have much wider angle of attack envelopes and flight conditions that they operate under. There are even other types of civil aircraft that are non-BLI which have these types, such as tri-jets which have a third engine placed in the tail (often with a lower inlet recovery S-duct). The AIP process used in BLIPSS could easily be used for sizing systems with these variations. With some work, the BLIPSS methodology may be generalized further to include all highly integrated vehicle/propulsion system sizing. Perhaps one day someone will take on the task.

7.4 Recommendations for Future Work

While the author of thesis believes that the methodologies used in this thesis are sufficient to show the usefulness of the method and to substantiate the contributions of the thesis, it is clear that the system level BLI modeling is not yet where it needs to be. The physics of BLI inlets is very complex, geometry dependent, and filled with traps for the system level engineer to set for himself, either by positioning the inlets incorrectly such that it interferes negatively with the airframe or by causing separation in the inlet diffuser etc. Furthermore, any study at this level will have some level of uncertainty in them. For this reason, the current author recommends future work be devoted to primarily two areas: additional high-fidelity modeling of the physics in a way which can be mapped to system studies; development of uncertainty based BLI methods to assist in decision making.

7.4.1 Higher Fidelity Component Modeling

The following items are recommended for future research, to attempt to map their affects to the system level:

- TKO and climb high α detailed aerodynamic data
- Cruise and TOC detailed aerodynamic maps (multiple points on vehicle airframe and many MN, alt, α combinations)
- Better estimates for inlet recovery and performance at mass flow ratio, including lip losses, pre-entry flow separation losses
- Methods for treatment of radial and swirl distortion effects and how engine size/scaling and inlet choices during sizing effect their impact.
- Estimates of external cowl, spillage, and interference drags for different inlets and parameterized for multiple configurations etc.

7.4.2 Integrated Vehicle Design Tools

Clearly the BLI engine, as shown in experiment 5, operates in a slightly different way than a normal podded engine, especially in terms of its effective lapse rate. The system is so dependent on the angle of attack that designers now have the problem of needing an α dependent engine deck. Then, of course, the engine can effect the lift distribution of the airplane – an aspect totally ignored thus far in this thesis. We therefore have a situation in which the integrated designs of the systems must be considered at all levels. How to approach this in the context of current design tools is a very difficult challenge. For instance, the NASA vehicle tool FLOPS does not account for the angle of attack in the engine deck (why would it). Therefore, the architecture of the design code would need to change to make these compatible.

If the tool integration problem could be solved, it would be interesting to investigate the true impacts of BLI on the way that the vehicle flies, and ultimately how it is sized. Though in this thesis we looked at primarily TSFC as a metric of performance, the reduction in fuel burn could loop back to a vehicle weight benefit as well when done in the sizing loop. Initial attempts at looking at this were conducted by this author and a few others, showing that BLI had some impact on the chosen cycle, in terms of fuel burn, but the models at that point did not take into account the angle of attack or variations in inlet recovery. The application of this in the full conceptual vehicle design process would be an interesting next step.

7.4.3 Robust Design Methods

Finally, the use of uncertainty based methods and specifically robust design may have application for the BLI problem. For instance, a recent thesis by Wilson [91] developed a methodology for doing robust design optimization under uncertainty with mitigation actions. His test case was an aircraft design problem, but further developments of this

work are underway for the engine design problem as well. Aspects of the BLI problem are amenable to this kind of thinking, since there are inherent distortion related constraints, but also the opportunity to use mitigation technologies such as vortex generators, distortion tolerant fan, inlet flow control, and others that may improve the designs after the fact. Integrating the BLIPSS sizing method with uncertainty based modeling for unknown physical components and distortion mitigation actions would be a very interesting academic task.

7.5 Final Thoughts

Finally, this problem has been a very intellectually stimulating one to take on for a thesis topic. The topic is rich with work spanning multiple disciplines; the field is highly active and the literature ever changing, and there always seems to be some new aspect of the problem arising as the details unfold. My hope is that those involved in decision making and resource allocation will continue to take the application seriously enough to carry it through to fruition on an actual commercial vehicle, and that the humble findings and methodologies contained in this thesis – contingent as they may be – might inform the embattled engine designers as they attempt to tread that path.

APPENDIX A

MODEL SOLVER SETUP

Table 22: Table showing flow area ratio-MN solver independents and dependents for experiments 1-4 (SDP)

Independent	Dependent	Description
ATD_Out_MN	ATD_MN_err	Used to keep ATD area ratio fixed
Burner_Out_MN	HPT_Flow_Coef	Used to keep a consistent HPT inlet flow coefficient
BypBld_Out_MN	BypBld_Area_Out	Used to keep Bypass bld area ratio fixed
Duct11_Out_MN	Duct15_Area_Out	Used to keep Duct 15 area ratio
Duct13_Out_MN	Duct13_Area_Out	Used to keep Duct 13 area ratio
Duct15_Out_MN	LPT_Flow_Coef	Used to keep the LPT flow coefficient constant
FanCln_Out_MN	Fan_Area_Out	Used to keep a consistent fan area ratio at design
HPC_Out_MN	HPC_Area_Out	Used to keep a consistent HPC area ratio at design
LPC_Out_MN	LPC_Area_Out	Used to keep a consistent LPC area ratio at design

Table 23: Table showing design point solver independents and dependents for all experiments

Independent	Dependent	Description
FanDst.S_map.ind_RlineMap	FanDst.S_map.dep_errWc	Conserves fan distorted sector flow continuity
HPT.S_map.ind_parmMap	HP_Shaft.integrate_Nmech	Balances shaft work for the HP shaft
Inlet.ind_Weng	Inlet.dep_inletFlowErr	Used to keep inlet flow continuity
LPT.S_map.ind_parmMap	LP_Shaft.integrate_Nmech	Balances shaft work for the LP shaft
PCsplitter.ind_BPR	MixExh.dep_errPs	Used to fix the exhaust static pressure of the PC model
PNT1_BPR	PNT1_Extraction_Ratio	Used to keep a fixed input extraction ratio
PNT1_Byp_Nozz	PNT1_BypassThroat	Used to vary the bypass throat area at design
PNT1_FAR	PNT1_T4	Used to keep a constant T4 at design
PNT1_HPC_InletMN	PNT1_HPC_Spec_Flow	Used to keep a constant HPC specific flow value
PNT1_LPCPRD	PNT1.OPRD	Used to keep a constant OPR
PNT1_LPC_InletMN	PNT1_LPC_Spec_Flow	Used to keep a constant LPC specific flow value
PNT1.W	PNT1_Thrust	Used to balance the thrust requirement
SPL_Byp_MN	SPL_Byp_Area	Used to keep bypass duct area ratio fixed
SPL_Core_MN	SPL_Core_Area	Used to keep core area ratio fixed

Table 24: Solver independents and dependents for general “off-design” continuity point

Independent	Dependent	Description
Ambient.ind_W	Core_Nozz.dep_Area	Continuity for core nozzle
Inlet.ind_Weng	Inlet.dep_inletFlowErr	Continuity for inlet
PCsplitter.ind_BPR	MixExh.dep_errPs	Constant exit static pressure for fan
FanCln.S_map.ind_RlineMap	FanCln.S_map.dep_errWc	Clean sector flow continuity
FanDst.S_map.ind_RlineMap	FanDst.S_map.dep_errWc	Dirty sector flow continuity
Splitter.ind_BPR	Byp_Nozz.dep_Area	Bypass nozzle flow continuity
LPC.S_map.ind_RlineMap	LPC.S_map.dep_errWc	LPC flow continuity
HPC.S_map.ind_RlineMap	HPC.S_map.dep_errWc	HPC flow continuity
HPT.S_map.ind_parmMap	HPT.S_map.dep_errWp	HPT flow continuity
LPT.S_map.ind_parmMap	LPT.S_map.dep_errWp	LPT flow continuity
HP_Shaft.ind_Nmech	HP_Shaft.integrate_Nmech	HP shaft power balance
LP_Shaft.ind_Nmech	LP_Shaft.integrate_Nmech	LP shaft power balance

Table 25: Solver independents and dependents for the thrust matching and cycle design relations in experiments 3 and 4.

Independent	Dependent	Description
PNT1.BPR	PNT1.Extraction_Ratio	Extraction ratio match to cycle
PNT1.FAR	PNT1.T4	Vary FAR to hit the max T4
PNT1.W	PNT1.Thrust	Vary the flow at design to hit thrust
PNT6.Burner.FAR	PNT6.FanCln.NcqNcDes	Vary the outboard engine FAR to match PM rule

Table 26: Solver independents and dependents for the thrust matching and cycle design relations in experiments 3 and 4.

Independent	Dependent	Description
PNT1.W	PNT3.Thrust	Vary ADP mass flow to reach thrust at TKO
PNT1.BPR	PNT1.Extraction_Ratio	Vary BPR to meet cycle design relation
PNT1.FAR	PNT2.Wc	Vary fuel to air at ADP to match fixed TOC flow ratio
PNT2.FAR	PNT2.Thrust	Vary fuel to air at TOC to match TOC thrust
PNT3.FAR	PNT3.T4max	Vary fuel to air at TKO to match T4max
PNT4.FAR	PNT5.Thrust	Vary fuel to air at SLSU to match SLS thrust
PNT4.FAR	con.T4max_SLS	Keep both SLSI and SLSU constrained by T4 max

Table 27: Solver independents and dependents for the cooling flow relations in experiments 5.

Independent	Dependent	Description
PNT1.HPT_Cool1	PNT3.HPT.Cool.dep.BleedFlow1	HPT Cooling Flow 1 to meet HPT TKO temperature
PNT1.HPT_Cool2	PNT3.HPT.Cool.dep.BleedFlow2	HPT Cooling Flow 2 to meet HPT TKO temperature
PNT1.LPT_Cool1	PNT3.LPT.Cool.dep.BleedFlow1	LPT Cooling Flow 1 to meet LPT TKO requirement
PNT1.LPT_Cool2	PNT3.LPT.Cool.dep.BleedFlow2	LPT Cooling Flow 2 to meet LPT TKO requirements

Table 28: Solver independents and dependents for the thrust matching relations and constraint relations for the rematch runs in experiments 5.

Independent	Dependent	Description
PNT6_FAR	PNT6_Fan_Speed	Vary TOC2 FAR to match TOC over-speed
PNT7_FAR	PNT7_Fan_Speed	Vary high α TKO to match TKO speed
PNT7_FAR	con_PNT7_T4max	Constrain high α TKO over-speed by TKO T4max
PNT1_Acapture	PNT1_Min_Acapture	Vary design point capture area ratio to meet the minimum
PNT2_FAR	con_PNT6_Thrust	Constrain TOC thrust by TOC2 minimum Thrust
PNT3_FAR	con_PNT7_Thrust	Constrain TKO thrust by high α TKO Thrust

APPENDIX B

INTEGRAL BOUNDARY LAYER INLET MODEL

The integral boundary layer model is designed to model the variation of the boundary and its interaction with the inviscid flow through the pre-entry region and until the fan face at station 2 for a quasi one-dimensional inlet duct. The dominant features captured here are changes in external inviscid flow velocity and associated pressure gradients which promote boundary layer growth, reduced total pressure, and tendency towards flow separation in the inlet. Also the effect of the wall skin friction is included in the boundary layer growth terms. The results from this model are presented in chapter 4, but below the aerodynamic theory is presented in full along with a solution procedure for the coupled viscous/inviscid problem. In the final section, the code is presented in detail and each piece is described for the purposes of replication by the user.

B.1 Integral Boundary Layer Equations

The derivation of the equations for the boundary layer are taken from the lecture notes of Drela [20] and Plas [69]. The conservation of mass and momentum for the boundary layer are:

$$\frac{\partial \rho u}{\partial x} + \frac{\partial \rho v}{\partial y} = 0 \quad (123)$$

$$\rho u \frac{\partial u}{\partial x} + \rho v \frac{\partial u}{\partial y} - \rho_E u_E \frac{du_E}{dx} - \frac{\partial \tau}{\partial y} = 0 \quad (124)$$

These are combined and integrated to produce a dimensionless system of equations in terms of the boundary layer integral properties as follows:

$$\frac{d\theta}{dx} = \frac{C_f}{2} - (H + 2 - M_E^2) \frac{\theta}{u_E} \frac{du_E}{dx} \quad (125)$$

$$\frac{d\theta^*}{dx} = 2C_D - \left(\frac{2H^{**}}{H^*} + 3 - M_E^2\right) \frac{\theta}{u_E} \frac{du_E}{dx} \quad (126)$$

The above two equations are, respectively, the Von-Karman integral momentum equation and the integral kinetic energy equation. Combining them, the KE equation can be replaced by the following:

$$\frac{\theta}{H^*} \frac{dH^*}{dx} = \frac{2C_D}{H^*} - \frac{C_f}{2} + \left(H - 1 - \frac{2H^{**}}{H^*}\right) \frac{\theta}{u_E} \frac{du_E}{dx} \quad (127)$$

The continuity equation for the duct is:

$$\rho_E u_E = \frac{\dot{m}}{\rho(A - \delta^*)} \quad (128)$$

Differentiating with respect to x leads to:

$$\frac{du_E}{dx} = \frac{u_E}{A - \delta^*} \left(\frac{d\delta^*}{dx} - \frac{dA}{dx} \right) \frac{1}{1 - M_E^2} \quad (129)$$

This finally gives a 3x3 system of ODEs in (θ, δ^*, u_E) which must be solved for each point along the x-axis in the model domain.

B.2 Solution Procedure

For this purpose, first define the following relation:

$$\beta_{(\cdot)} = \frac{x}{(\cdot)} \frac{d(\cdot)}{dx} \quad (130)$$

Here, the (\cdot) represents any quantity in the system of equations. Eq. 127 can be rewritten by multiplying the whole equation by x/θ and using the definition in 130:

$$\beta_H \left(\frac{H}{H^*} \frac{dH^*}{dH} \right) - \left(H - 1 - \frac{2H^{**}}{H^*} \right) \beta_{u_E} = \frac{x}{\theta} \left(\frac{2C_D}{H^*} - \frac{C_f}{2} \right) \quad (131)$$

Now, β_H can be re-written as follows:

$$\beta_H = \frac{x}{\delta^*/\theta} \frac{d(\delta^*/\theta)}{dx} = \frac{\theta}{\delta^*} x \left[\frac{d\delta^*}{dx} \frac{1}{\theta} - \frac{\delta^*}{\theta^2} \frac{d\theta}{dx} \right] = \frac{x}{\delta^*} \frac{\delta^*}{dx} - \frac{x}{\theta} \frac{d\theta}{dx} = \beta_{\delta^*} - \beta_{\theta} \quad (132)$$

which can be used to substitute into Eq. 131. The Von Karman integral momentum equation can be similarly re-written as:

$$\beta_{\theta} + \left(H + 2 - M_E^2 \right) \beta_{u_E} = \frac{C_f x}{2 \theta} \quad (133)$$

and the continuity can be re-written as:

$$\beta_{u_E} - \frac{\delta^*}{(A - \delta^*)} \beta_{\delta^*} = \frac{-x}{(A - \delta^*)} \left(\frac{dA}{dx} \right) \frac{1}{1 - M_E^2} \quad (134)$$

This gives a 3x3 system of ODEs to be solved within the inlet model domain:

$$\begin{pmatrix} 1 & 0 & H + 2 - M_E^2 \\ -\frac{H}{H^*} \frac{dH^*}{dH} & \frac{H}{H^*} \frac{dH^*}{dH} & \left(1 - H + 2\frac{H^{**}}{H^*}\right) \\ 0 & -\frac{\delta^*(1 - M_E^2)}{(A - \delta^*)} & 1 - M_E^2 \end{pmatrix} \begin{pmatrix} \beta_\theta \\ \beta_{\delta^*} \\ \beta_{u_E} \end{pmatrix} = \begin{pmatrix} \frac{C_f x}{2\theta} \\ \frac{x}{\theta} \left(\frac{2C_D}{H^*} - \frac{C_f}{2} \right) \\ \frac{-x \left(\frac{dA}{dx} \right)}{(A - \delta^*)} \end{pmatrix} \quad (135)$$

The above system allows for the computation of a state-matrix on the left hand side of the equation and the forcing vector on the right hand side at some initial x_i with given boundary conditions $(\theta, \delta^*, u_E)_i$. Then the BL properties and edge velocity at some point x_{i+1} is computed using a forward Euler scheme as follows for any of the three BL properties and this solution is carried forth until the inlet domain ends.

$$(\cdot)_{i+1} = (\cdot)_i \left(1 + \beta_{(\cdot)} \frac{x_{i+1} - x_i}{x_i} \right) \quad (136)$$

The only things that remains is to describe the computation of the parameters H^* , H^{**} , dH^*/dH , C_f , C_d , M_E , and dA/dx .

B.3 Turbulent Closure Relations

The Reynolds number with respect to the momentum thickness Re_θ is:

$$Re_\theta = \frac{\theta u_E}{\nu} \quad (137)$$

The definitions of the BL shape factor H and the kinematic shape factor H_k are:

$$H = \frac{\delta^*}{\theta} \quad (138)$$

$$H_k = \frac{H - 0.29M_E^2}{1 + 0.113M_E^2} \quad (139)$$

From [21], F_c is defined as:

$$F_c = \sqrt{1 + \frac{\gamma - 1}{2} M_E^2} \quad (140)$$

and the skin friction coefficient can be computed as follows:

$$F_c C_f = \frac{0.3e^{-1.33H_k}}{\left[\log_{10}(Re_\theta/F_c)\right]^{1.74+0.31H_k}} + 1.1 \times 10^{-4} \left[\tanh\left(4 - \frac{H_k}{0.875}\right) - 1\right] \quad (141)$$

The energy factor for the boundary layer comes from [69] by first defining H_o as:

$$H_o = \begin{cases} 3 + \frac{400}{Re_\theta} & Re_\theta > 400 \\ 4 & Re_\theta < 400 \end{cases} \quad (142)$$

and computing the kinematic energy factor, H_k based on the kinematic shape factor H .

$$H_k^* = \begin{cases} \left(0.5 - \frac{4}{Re_\theta}\right) \left(\frac{H_o - H_k}{H_o - 1}\right)^2 \frac{1.5}{H_k + 0.5} + 1.5 + \frac{4}{Re_\theta} & , \text{if } H_k < H_o \\ (H_k - H_o)^2 \left(0.007 \frac{\log(Re_\theta)}{\left(H_k - H_o + \frac{4}{\log(Re_\theta)}\right)^2} + \frac{0.55}{H_k}\right) + 1.5 + \frac{4}{Re_\theta} & , \text{else} \end{cases} \quad (143)$$

From the above, the energy factor is then:

$$H^* = \frac{H_k^* + 0.028M_E^2}{1.0 + 0.014M_E^2} \quad (144)$$

and the dissipation coefficient can be computed from the following relationship:

$$\frac{2C_D}{H^*} = \frac{0.5}{3} C_f \left(\frac{4}{H_k} - 1\right) + 0.03 \left(1 - \frac{1}{H_k}\right)^3 \quad (145)$$

Finally, the density thickness factor H^{**} is computed from:

$$H^{**} = \left(\frac{0.064}{H_k - 0.8} + 0.251\right) M_E^2 \quad (146)$$

The only thing that remains are the derivative terms dH^*/dH and dA/dx . The area derivative is computed by taking a finite difference of the input area distribution based

on a forward differencing technique. The other derivative term is computed as follows by recognizing that $dH^*/dH = (dH^*/dH_k^*)(dH_k^*/dH_k)(dH_k/dH)$ and computing the necessary derivatives from Eqs. 144, 143, and 139. These are as follows:

$$\frac{dH^*}{dH_k^*} = \frac{1}{1 + 0.014M_E^2} \quad (147)$$

$$\frac{dH_k}{dH} = \frac{1}{1 + 0.113M_E^2} \quad (148)$$

$$\frac{dH_k^*}{dH_k} = \begin{cases} \left(.165 - \frac{1.6}{\sqrt{Re_\theta}} \right) \frac{(-1.6H_k(H_o - H_k)^{0.6} - (H_o - H_k)^{1.6})}{H_k^2} & , \text{if } H_k < H_o \\ 2(H_k - H_o) \left(\frac{.04}{H_k} + \frac{.007 \log(Re_\theta)}{\left(H_k - H_o + \frac{4}{\log(Re_\theta)} \right)^2} \right) \\ + (H_k - H_o)^2 \left(\frac{-.04}{H_k^2} + \frac{-.014 * \log(Re_\theta)}{\left(H_k - H_o + \frac{4}{\log(Re_\theta)} \right)^3} \right) & , \text{else} \end{cases} \quad (149)$$

B.4 Computation of Inlet Recovery

We now proceed with a derivation for approximating inlet total pressure recovery as a function of the boundary layer parameters computed by the IBLT tool. This is used to estimate the inlet recovery at the fan face and other locations. The mass averaged total pressure is as follows:

$$\bar{P}_t \dot{m} = \int_A \left[P_s + \frac{1}{2} \rho u^2 \right] d\dot{m} = \int_A P_s d\dot{m} + \int_A q d\dot{m} \quad (150)$$

Assuming uniform static pressure over the fan face, we get:

$$\bar{P}_t \dot{m} = P_s \dot{m} + q_e \int_A \frac{\rho u^2}{\rho_e u_e^2} d\dot{m} = P_s \dot{m} + q_e \int_A \frac{\rho u^2}{\rho_e u_e^2} \rho u dA \quad (151)$$

Dividing by the mass flow, and recognizing the $\dot{m} = \rho_e u_e (A - \delta^*)$:

$$\bar{P}_t = P_s + \frac{q_e}{A - \delta^*} \int_A \left(\frac{\rho}{\rho_e} \right) \frac{\rho u^3}{\rho_e u_e^3} dA \quad (152)$$

Again, assuming that the density defect is negligible (tantamount to assuming uniform static pressure as done earlier), then the density ratio can be pulled out of the integral and set to unity. Finally, recognize the following relation from the definition of the kinetic energy defect:

$$\int_A \frac{\rho u^3}{\rho_e u_e^3} dA = \int_A \frac{\rho u_e^2 u}{\rho_e u_e^3} dA - \theta^* = \int_A \frac{\rho u dA}{\rho_e u_e} - \theta^* = \frac{\dot{m}}{\rho_e u_e} - \theta^* = (A - \delta^* - \theta^*) \quad (153)$$

Putting this all together, we get a relation for the mass averaged total pressure:

$$\bar{P}_t = P_s + q_e \frac{A - \delta^* - \theta^*}{A - \delta^*} \quad (154)$$

This equation essentially describes the relationship between the kinetic energy and mass flow defects and the dynamic pressure loss in the diffuser annulus.

B.5 Inlet Code

```
//===== Inlet class file =====//
// Written by: Jonathan Gladin
//=====//
```

```
#include "stdafx.h"
#include "Point.h"
#include "Mesh.h"
#include "State.h"
#include "Inlet.h"
```

```
//Constructor
```

```

Inlet::Inlet()
{
    parse_inputs();
    create_mesh();
    calc_mesh();
    output_data();

}

// Destructor
Inlet::~~Inlet()
{
}

void Inlet:: parse_inputs() {

    FILE* file_id = fopen("InletData.input", "r");

    double initUe, initTheta, initDeltaStar, Acapture, UeqUinf, AcqA
    int numPoints;
    double x, y;

    if( file_id )
    {
        char buff[256];

        fgets(buff, 256, file_id);  sscanf( buff, "%d", &numNo

```

```

fgets(buff, 256, file_id); sscanf( buff, "%lf", &xLoca
fgets(buff, 256, file_id); sscanf( buff, "%lf", &length
fgets(buff, 256, file_id); sscanf( buff, "%lf", &nu );
fgets(buff, 256, file_id); sscanf( buff, "%lf", &Me );
fgets(buff, 256, file_id); sscanf( buff, "%lf", &Tt );
fgets(buff, 256, file_id); sscanf( buff, "%lf", &Pt );
fgets(buff, 256, file_id); sscanf(buff, "%lf", &AcqAh);
fgets(buff, 256, file_id); sscanf(buff, "%lf", &UeqUinf);
fgets(buff, 256, file_id); sscanf( buff, "%lf", &initD
fgets(buff, 256, file_id); sscanf( buff, "%lf", &initT
fgets(buff, 256, file_id); sscanf( buff, "%ld", &numP
fgets(buff, 256, file_id); sscanf(buff, "%lf", &Acaptu
fgets(buff, 256, file_id); sscanf(buff, "%lf", &s_preE

```

```

initState = new State();

```

```

double Ts = Tt / (1 + .2 * pow(Me, 2));

```

```

double a = sqrt(1.4*1716.54*Ts);

```

```

double Ps = Pt / pow(1 + 0.2 * pow(Me, 2), 1.4 / 0.4);

```

```

double Ho = initDeltaStar / initTheta;

```

```

//These values are at the capture area after diffusion

```

```

initUe = Me * a * UeqUinf;

```

```

initDeltaStar = initDeltaStar * Acapture;

```

```

initTheta = initTheta * Acapture;

```

```

Ts = Tt - pow(initUe, 2) / 2.0 / (1716.54*1.4 / .4);

```

```

a = sqrt(1.4 * 1716.54 * Ts);

initState->set_state(initUe, initDeltaStar, initTheta, n
initState->set_Mach(initUe / a);

Lp = s_preEntry*sqrt(4.0 * Acapture / 3.14159); //Length
double AoqAc = 1.0 / (AcqAh)*(1.0 / UeqUinf + AcqAh*init
double m = (AoqAc - 1) / Lp;

for(int i = 0; i < 2*numPoints; i++) {
    if (i > numPoints-1) {
        fgets(buff, 256, file_id);
        sscanf(buff, "%lf %lf\n", &x, &y);

        x = length * x;  y = Acapture * abs(y);

        vec2d* tempVec2d = new vec2d(x, y);

        areaVec.push_back(tempVec2d);

        if (i == 2 * numPoints - 1)
            length = x;
    }
    else {
        x = ((double)i - (double)numPoints)* Lp
        y = Acapture * (-m * x + 1.0);
    }
}

```

```

        vec2d* tempVec2d = new vec2d(x, y);

        areaVec.push_back(tempVec2d);
    }
}
double g = (1 + 0.2 * pow(initUe / a, 2.0));
double mdot = Ps / 1716.54 / Ts * initUe * (areaVec[0]->get_y());
mesh.set_mdot(mdot);
}
}

```

```

void Inlet::create_mesh() {
    int numPoints = numNodes;

    for(int i = 0; i < 2*numPoints; i++) {
        Point* pnt = new Point;
        mesh.push_pnt(pnt);

        double tempLoc = (double)i * (length + Lp) / (double)(2*numPoints);
        pnt->set_x(tempLoc);

        double tempArea;

        if(i == 0)
            tempArea = areaVec[0]->get_y();
        else

```



```

        tempArea = interp_area_array(tempLoc-xLocation);

        pnt->set_area(tempArea);
        pnt->set_Pt(Pt);
        pnt->set_Tt(Tt);

    }
    mesh.calc_dA_dX();
    mesh.get_pnt(0)->set_state_pntr(initState);

}

void Inlet::calc_mesh() {

    int numPoints = mesh.get_pnt_vec()->size();

    for(int i = 0; i < numPoints-1; i++) {
        Point* tempPnt = mesh.get_pnt(i);
        tempPnt->calc_state();
        mesh.calc_next_point(i);
    }

}

double Inlet::interp_area_array(double x) {
    int i = 0;
    while((i < areaVec.size()-1) && (x > areaVec[i]->get_x())) {
        i++;
    }
}

```

```

    }

    double returnHeight = areaVec[i-1]->get_y() + (areaVec[i]->get_y() - areaVec[i-1]->get_y());
    return returnHeight;
}

void Inlet::output_data() {

    FILE* file_id = fopen("InletData.output", "w+");

    double tempUe, tempTheta, tempDeltaStar, tempX, tempH, tempHstar;

    if (file_id)
    {
        char buff[1000000];
        fprintf(file_id, "%s %s %s %s %s %s %s\n", "s", "Ue", "T", "theta", "deltaStar", "H", "Hstar");

        for (int i = 0; i < mesh.get_pnt_vec()->size() - 1; i++)
        {
            tempUe = mesh.get_pnt(i)->get_state()->get_edge_Ue();
            tempTheta = mesh.get_pnt(i)->get_state()->get_theta();
            tempDeltaStar = mesh.get_pnt(i)->get_state()->get_deltaStar();
            tempHstar = mesh.get_pnt(i)->get_state()->get_hStar();
            tempH = mesh.get_pnt(i)->get_state()->get_H();
            tempArea = mesh.get_pnt(i)->get_area();
            fprintf(file_id, "%f %f %f %f %f %f %f\n", mesh.get_pnt(i)->get_x(), mesh.get_pnt(i)->get_y(),
                mesh.get_pnt(i)->get_x(), mesh.get_pnt(i)->get_y(), tempUe, tempTheta, tempDeltaStar, tempHstar, tempH, tempArea);
        }
    }
}

```

```

int lastpnt = mesh.get_pnt_vec()->size() - 1;

double area = mesh.get_pnt(lastpnt)->get_area();
double PsFan = mesh.get_pnt(lastpnt)->get_Pt() / (1 + 1.4 / 2.0
double PtInf = mesh.get_pnt(0)->get_Pt();
double AFan = mesh.get_pnt(lastpnt)->get_area();
double rhoFan = mesh.get_mdot() / mesh.get_pnt(lastpnt)->get_sta
double QFan = 0.5 * rhoFan * pow(tempUe, 2.0);
double TsFan = mesh.get_pnt(lastpnt)->get_Tt() / (1 + .2* pow(m
double Ai = mesh.get_pnt(0)->get_area();
double Pti = mesh.get_pnt(0)->get_Pt();
double Psi = mesh.get_pnt(0)->get_Pt() / (1 + 1.4 / 2.0 * pow(m
double Qi = Pti - Psi;
double dstari = mesh.get_pnt(0)->get_state()->get_delta_star();
double thetai = mesh.get_pnt(0)->get_state()->get_theta();
double Mei = mesh.get_pnt(0)->get_state()->get_Me();
double hstari = mesh.get_pnt(0)->get_state()->get_hStar();

PsFan = mesh.get_pnt(lastpnt)->get_Pt() / pow(1 + 0.2 * pow(mesh
QFan = PtInf - PsFan;
double pressureRecovery = (PsFan + QFan * (AFan - tempDeltaStar
double inletRecovery = (Psi + Qi * (Ai - dstari - thetai*hstari)
inletRecovery = pressureRecovery / inletRecovery;
double testUeMax = 0;

for (int i = numNodes; i < 2 * numNodes; i++) {

```

```

        double checkUe = mesh.get_pnt(i)->get_state()->get_edge-velocity();

        if (checkUe>testUeMax) {
            testUeMax = checkUe;
        }
    }

    double Wc2Afan = testUeMax * .002377;

    FILE* file_id2 = fopen("Recovery.output", "w+");

    Ai = mesh.get_pnt(numNodes)->get_area();
    double Wc2AfanMetric = Wc2Afan / 0.0685217659 * 10.7639;

    fprintf(file_id2, "%s %s %s %s %s %s\n", "Recovery", "Wc2Afan", "Wc2AfanMetric", "Ai", "Wc2AfanMetric/Ai", "Wc2AfanMetric/Ai");
    fprintf(file_id2, "%f %f %f %f %f %f\n", pressureRecovery, Wc2Afan, Wc2AfanMetric, Ai, Wc2AfanMetric/Ai, Wc2AfanMetric/Ai);

    double tempThetaStar, tempRho, Phi, tempMe;
    double tempBetaTheta, tempBetaU, tempBetaDeltaStar, tempCf;
    double tempdHstarDh, tempHdoubleStar, tempCd;
    double tempDaDx;
    double tempPt, tempTt;

    for (int i = 0; i < mesh.get_pnt_vec()->size() - 1; i++) {
        tempUe = mesh.get_pnt(i)->get_state()->get_edge-velocity();
        tempTheta = mesh.get_pnt(i)->get_state()->get_theta();
        tempDeltaStar = mesh.get_pnt(i)->get_state()->get_deltaStar();
        tempHstar = mesh.get_pnt(i)->get_state()->get_hStar();
    }

```

```

tempH = mesh.get_pnt(i)->get_state()->get_H();
tempBetaTheta = mesh.get_pnt(i)->get_state()->get_betaTheta();
tempBetaU = mesh.get_pnt(i)->get_state()->get_betaU();
tempBetaDeltaStar = mesh.get_pnt(i)->get_state()->get_betaDeltaStar();
tempX = mesh.get_pnt(i)->get_x();
tempCf = mesh.get_pnt(i)->get_state()->get_cF();
tempMe = mesh.get_pnt(i)->get_state()->get_Me();
tempdHstarDh = mesh.get_pnt(i)->get_state()->get_dHstarDh();
tempHdoubleStar = mesh.get_pnt(i)->get_state()->get_hDoubleStar();
tempCd = mesh.get_pnt(i)->get_state()->get_cD();
tempArea = mesh.get_pnt(i)->get_area();
tempDaDx = mesh.get_pnt(i)->get_dAdX();
tempPt = mesh.get_pnt(i)->get_Pt();
tempTt = mesh.get_pnt(i)->get_Tt();

double g = (1 + .2*pow(tempMe, 2));
double mdot_test = tempPt / sqrt(1716.54 * tempTt / g) /

double diameter = sqrt(tempArea * 4.0 / 3.14159);
double deltaStarThickEq = diameter - sqrt(pow(diameter, 2) - 4.0 * tempArea);
double checkCalc = 3.14159 / 4.0 * (pow(diameter, 2) - 4.0 * tempArea);

    }
}

//===== Mesh class file =====//
// Written by: Jonathan Gladin

```

```

//=====//

#include "stdafx.h"
#include "Mesh.h"

Mesh::Mesh() {}

Mesh::~Mesh() {}

void Mesh::calc_dA_dX () {

    for (int i = 0; i < pntVec.size (); i++) {
        if (i==0)
            pntVec [ i ]->set_dAdX (( pntVec [ i+1 ]->get_area () - pntVec [ i ]->
            else if ( i==pntVec.size ()-1)
            pntVec [ i ]->set_dAdX (( pntVec [ i ]->get_area () - pntVec [ i-1 ]->
            else
            pntVec [ i ]->set_dAdX (( pntVec [ i+1 ]->get_area () - pntVec [ i-1 ]->
    }
}

void Mesh::calc_next_point (int i) {
    double nextTheta, nextU, nextDeltaStar;
    Point* currPnt = pntVec [ i ];
    Point* nextPnt = pntVec [ i+1 ];
    State* currState = currPnt->get_state ();
    State* nextState = nextPnt->get_state ();
}

```

```

        nextTheta = currState->get_theta() * (1 + currState->get_betaThe
currPnt->get_x());
        nextU = currState->get_edge_velocity() * (1 + currState->get_beta
currPnt->get_x());
        nextDeltaStar = currState->get_delta_star() * (1 + currState->ge
currPnt->get_x());

        nextState->set_state(nextU, nextDeltaStar, nextTheta, currState-

double Cp = 1716.54 * 1.4 / (1.4 - 1);
double aStar = sqrt(1716.54 * nextPnt->get_Tt()) / nextPnt->get_
double nextTs = nextPnt->get_Tt() - 0.5 * pow(nextU, 2) / Cp;
double nextMe = nextU / sqrt(1.4 * 1716.54 * nextTs);

        nextState->set_Mach(nextMe);
        currState->get_betaU() / currPnt->get_x() << endl;
        currState->get_betaU() / currPnt->get_x() << endl;
    }

//===== Point class file =====//
// Written by: Jonathan Gladin
//=====//

#include "stdafx.h"
#include "Point.h"
#include "State.h"

```

```

Point::Point() {
    coordVec = vec2d(area, dAdX);
    state = new State();
}

Point::~~Point(){}

void Point::calc_state() {
    double stateDiameter = sqrt(4 / 3.14159 * area);
    state->calculate_closure(stateDiameter);
    state->calculate_state_matrix(area);
    state->calculate_state_vector(area, dAdX, xLoc);
    state->calculate_beta();
}

double Point::calc_Me(double Pt, double Tt, double arear, double Mguess)

    double mo, dm, delm, mr, ml, dadm;
    mo = Mguess;
    dm = 1/1000.;
    delm = 1.0;

    while (abs(delm) > .0001) {
        mr = mo+dm;
        ml = mo-dm;
        dadm = ( calc_area(mr) - calc_area(ml) )/(2*dm);

```



```

        delm = -(calc_area(mo)-arear)/dadm;
        mo = mo + delm;
    }

    return mo;
}

```

```

double Point::calc_area(double Me) {
    double gamma = 1.4;
    double term = 1.0 + .5*(gamma-1)*pow(Me, 2);
    double arear = 2/( gamma+1)*term;
    arear = pow(arear ,((gamma+1)/(gamma-1)));
    arear = arear/( pow(Me,2));
    arear = sqrt(arear);
    return arear;
}

```

```

//===== State class file =====//
// Written by: Jonathan Gladin
//=====//

```

```

#include "stdafx.h"
#include "State.h"

```

```

State::State()
{

```

```

std::vector <double> rowOne;    rowOne.resize (3);
std::vector <double> rowTwo;    rowTwo.resize (3);
std::vector <double> rowThree;  rowThree.resize (3);

stateMatrix.push_back(rowOne);
stateMatrix.push_back(rowTwo);
stateMatrix.push_back(rowThree);

stateVector.resize (3);
}

State::~~State()
{
}

void State::calculate_closure(double diameter) {

    //Skin Friction Calc
    double theta = diameter - sqrt(pow(diameter,2) - 4/3.14159*momen
    ReTheta = theta * edgeVelocity / nu ;
    H = displThick / momentumThick;
    double Fc = pow((1 + 0.2 * pow(Me, 2)), 0.5);
    double Hk = (H - 0.290 * pow(Me, 2)) / (1 + .113 * pow(Me, 2));
    cF = 1.0 / Fc * ( (0.3 * exp(-1.33 * Hk)) / ( pow((log10(ReTheta

    //Shape Parameter Calc
    double HkStar, Ho, dHstardHkStar, dHkdH, dHkStardHk;

```

```

if (ReTheta > 400.)
    Ho = 3.0 + (400.0 / ReTheta);
else
    Ho = 4;

dHstardHkStar = 1.0 / (1 + .014 * pow(Me, 2));
dHkdH = 1.0 / (1 + .113 * pow(Me, 2));

if(Hk < Ho) {
    HkStar = 1.505 + 4.0 / ReTheta + (0.165 - 1.6 / sqrt(ReTheta));
    dHkStardHk = (.165 - 1.6 / sqrt(ReTheta)) * (1.6 * Hk *
} else {
    HkStar = 1.505 + 4.0 / ReTheta + pow((Hk - Ho), 2) * (.0
    dHkStardHk = (2 * (Hk - Ho) * (.04 / Hk + .007 * log(Re
        + pow(Hk - Ho, 2) * ( -.04 / pow
}

dHstarDh = dHkStardHk * dHkdH * dHstardHkStar;

hStar = (HkStar + 0.028 * pow(Me, 2)) / (1 + .014 * pow(Me, 2));

//Dissipation Calculation
cD = hStar / 2.0 * ( cF / 2.0 * ( 4.0 / Hk - 1) * (1. / 3.) + .0
HdoubleStar = (.064 / (Hk - 0.8) + 0.251 ) * pow(Me, 2);
}

void State::calculate_state_matrix(double A) {

```

```

//Calculate row 1
stateMatrix[0][0] = 1.0;  stateMatrix[0][1] = 0.0; stateMatrix[0][2] = 0.0;

//Calculate row 2
stateMatrix[1][0] = (-H/hStar * dHstarDh);  stateMatrix[1][1] = 0.0;
stateMatrix[1][2] = 0.0;

//Calculate row 3
stateMatrix[2][0] = ( 0.0 );  stateMatrix[2][1] = ( -displThick );
stateMatrix[2][2] = ( 1.0 );
}

void State::calculate_state_vector(double A, double dAdX, double x) {
    stateVector[0] = x / momentumThick * cF / 2.0;
    stateVector[1] = x / momentumThick * (2 * cD / hStar - cF / 2.0);
    stateVector[2] = -x / (A - displThick) * dAdX * 1 / (1 - pow(Me, 2));
}

void State::calculate_beta() {

    double det = stateMatrix[0][0] * ( stateMatrix[1][1] * stateMatrix[2][2] -
    - stateMatrix[0][1] * ( stateMatrix[1][0] * stateMatrix[2][2] -
    + stateMatrix[0][2] * ( stateMatrix[1][0] * stateMatrix[2][1] -
    - stateMatrix[1][1] * stateMatrix[2][0] ) ) ) -
    - stateMatrix[0][2] * ( stateMatrix[1][0] * stateMatrix[2][1] -
    + stateMatrix[1][1] * stateMatrix[2][0] ) ) -
    + stateMatrix[0][1] * ( stateMatrix[1][0] * stateMatrix[2][2] -
    - stateMatrix[1][1] * stateMatrix[2][0] ) ) ;

    std::vector<std::vector<double>> inverse;

    inverse.resize(3);

    for (int i=0;i<3;i++) {

```

```

        inverse[i].resize(3);
    }

    std::vector<std::vector<double>> a = stateMatrix;

    //Row 1
    inverse[0][0] = (a[1][1]*a[2][2] - a[1][2]*a[2][1]);
    inverse[0][1] = (a[0][2]*a[2][1] - a[0][1]*a[2][2]);
    inverse[0][2] = (a[0][1]*a[1][2] - a[1][1]*a[0][2]);

    //Row 2
    inverse[1][0] = (a[1][2]*a[2][0] - a[1][0]*a[2][2]);
    inverse[1][1] = (a[0][0]*a[2][2] - a[2][0]*a[0][2]);
    inverse[1][2] = (a[0][2]*a[1][0] - a[1][2]*a[0][0]);

    //Row 3
    inverse[2][0] = (a[1][0]*a[2][1] - a[2][0]*a[1][1]);
    inverse[2][1] = (a[0][1]*a[2][0] - a[2][1]*a[0][0]);
    inverse[2][2] = (a[0][0]*a[1][1] - a[1][0]*a[0][1]);

    betaTheta = 1.0 / det * ( inverse[0][0] * stateVector[0] + inver
    betaDeltaStar = 1.0 / det * ( inverse[1][0] * stateVector[0] + i
    betaU = 1.0 / det * ( inverse[2][0]*stateVector[0] + inverse[2][
}

```

REFERENCES

- [1] *N.P.S.S Developer's guide, software release: N.P.S.S 1.6.4., rev: Q. 2006, NASA.*
- [2] *N.P.S.S reference sheets, software release: N.P.S.S 1.6.4., rev: Q. 2007, NASA.*
- [3] ALLAN, B. G. and OWENS, L. R., "Numerical modeling of flow control in a boundary layer ingesting offset inlet diffuser at transonic mach numbers," in *44th AIAA Aerospace Sciences Meeting and Exhibit*, 2006.
- [4] ALLAN, B. G., OWENS, L. R., and BERRIER, B. L., "Numerical modeling of active flow control in a boundary layer ingesting offset inlet," in *2nd AIAA Flow Control Conference*, 2004.
- [5] ALLAN, B. G., OWENS, L. R., and LIN, J. C., "Optimal design of passive flow control for a boundary- layer-ingesting offset inlet using design-of-experiments," in *44th AIAA Aerospace Sciences Meeting and Exhibit*, 2006.
- [6] ANDERSON, J. D., *Fundamentals of Aerodynamics*. McGraw-Hill, 2001.
- [7] BERRIER, B. L. and ALLAN, B. G., "Experimental and computational evaluation of flush-mounted, s-duct inlets," in *42nd AIAA Aerospace Sciences Meeting and Exhibit*, 2004.
- [8] BERRIER, B. L. and MOREHOUSE, M. B., "Evaluation of flush-mounted, s-duct inlets with large amounts of boundary layer ingestion."
- [9] BERTIN, J. J., *Aerodynamics for Engineers (Fourth Edition)*. Prentice Hall, 2002.
- [10] BRADLEY, M. K. and DRONEY, C. K., "Subsonic ultra green aircraft research phase ii: N+4 advanced concept development," tech. rep., NASA, 2012.
- [11] CAMPBELL, R. L., CARTER, M. B., PENDERGRAFT, O. C., FRIEDMAN, D. M., and SERRANO, L., "Design and testing of a blended wing body with boundary layer ingestion nacelles at high reynolds numbers," in *43rd AIAA Aerospace Sciences Meeting and Exhibit*, 2005.
- [12] CARTER, M. B., CAMPBELL, R. L., PENDERGRAFT, O. C., FRIEDMAN, D. M., and SERRANO, L., "Designing and testing a blended wing body with boundary-layer ingestion nacelles," *Journal of Aircraft*, vol. 43, pp. 1479–1489, 2006.
- [13] COMMITTEE, S. S.-., "Gas turbine inlet flow distortion guidelines," Tech. Rep. ARP 1420, Revision B, Society of Automotive Engineers, 2002.

- [14] CONVERSE, G. and GIFFIN, R., “Extended parametric representation of compressor fans and turbines. volume 1: Cmpgen user’s manual,” tech. rep., NASA CR 174645, 1984.
- [15] COUSINS, W. T., “History, philosophy, physics, and future directions of aircraft propulsion system / inlet integration,” in *Proceedings of ASME Turbo Expo*, June 14-17, 2004.
- [16] COUSINS, W. T. and DAVIS, M. W., “Evaluating complex inlet distortion with a parallel compressor model: Part 1 – concepts, theory, extensions, and limitations,” in *Proceedings of ASME Turbo Expo 2011*, 2011.
- [17] COUSINS, W. T. and DAVIS, M. W., “Evaluating complex inlet distortion with a parallel compressor model: Part 2 applications to complex patterns,” in *Proceedings of ASME Turbo Expo 2011*, June 6-10, 2011, British Columbia, Canada.
- [18] CUMPSTY, N. and HORLOCK, J., “Averaging non-uniform flow for a purpose,” *Journal of Turbomachinery*, vol. 128, January 2006.
- [19] DOUGLASS, W., “Propulsive efficiency with boundary layer ingestion,” tech. rep., McDonnell Douglas, 1970.
- [20] DRELA, M., “Lecture notes on iiblt solutions.” Online, Fall 2003.
- [21] DRELA, M., *Two-dimensional transonic aerodynamic design and analysis using the euler equations*. PhD thesis, Massachusetts Institute of Technology, 1985.
- [22] DRELA, M., “Xfoil: An analysis and design system for low reynolds number airfoils,” in *Low Reynolds Number Aerodynamics* (MUELLER, T., ed.), vol. 54 of *Lecture Notes in Engineering*, pp. 1–12, Springer Berlin Heidelberg, 1989.
- [23] DRELA, M., “Power balance in aerodynamic flows,” *AIAA Journal*, vol. 47, July 2009.
- [24] FERRAR, A. M., O’BRIEN, W. F., and NG, W. F., “Active control of flow in serpentine inlets for blended wing-body aircraft,” in *45th AIAA/ASME/SAE/ASEE Joint Propulsion Conference & Exhibit*, August 2009.
- [25] FERRAR, ANTHONY M., O. W. F., “Flow in boundary layer ingesting serpentine inlets,” in *47th AIAA/ASME/SAE/ASEE Joint Propulsion Conference & Exhibit*, 2011.
- [26] FERRAR, ANTHONY M., O. W. F., “Progress in boundary layer ingesting embedded engine research,” in *48th AIAA/ASME/SAE/ASEE Joint Propulsion Conference & Exhibit*, 2012.
- [27] FLEMING, J., ANDERSON, J., NG, W., and HARRISON, N., “Sensing and active flow control for advanced bwb propulsion-airframe integration concepts,” tech. rep., NASA, 2005.

- [28] FLOREA, R. V., MATALANIS, C., HARDIN, L. W., STUCKY, M., and SHAB-BIR, A., “Parametric analysis and design for embedded engine inlets,” in *48th AIAA/ASME/SAE/ASEE Joint Propulsion Conference & Exhibit*, 2012.
- [29] FLOREA, R. V., VOYTOVYCH, D., TILLMAN, G., STUCKY, M., SHABBIR, A., SHARMA, O. P., and AREND, D. J., “Aerodynamic analysis of a boundary layer ingesting distortion-tolerant fan,” in *Proceedings of ASME Turbo Expo 2013: Turbine Technical Conference and Exposition*, 2013.
- [30] FREULER, P. N., “Boundary layer ingesting inlet design for a silent aircraft,” Master’s thesis, Massachusetts Institute of Technology, 2005.
- [31] GARG, M., CHOUDHARY, S., and KALLA, S. L., “On the sum of two triangular random variables,” *International Journal of Optimization: Theory, Methods, and Applications*, vol. 1, pp. 279–290, 2009.
- [32] GATLIN, G. M., VICROY, D. D., and CARTER, M. B., “Experimental investigation of the low-speed aerodynamic characteristics of a 5.8 percent scale hybrid wing body,” in *30th AIAA Applied Aerodynamics Meeting*, 25-258 June 2012.
- [33] GEARHART, W. S. and HENDERSON, R. E., “Selection of a propulsor for a submersible system,” *Journal of Aircraft*, Jan.-Feb. 1966.
- [34] GLADIN, J., SANDS, J. S., KESTNER, B. K., and MAVRIS, D. N., “Effects of boundary layer ingesting (bli) propulsion systems on engine cycle selection and hwb vehicle sizing,” in *48th AIAA/ASME/SAE/ASEE Joint Propulsion Conference & Exhibit*, 2012.
- [35] GLADIN, J. C., KESTNER, B., SCHUTTE, J. S., and MAVRIS, D. N., “Engine design strategy for boundary layer ingesting propulsion systems with multiple non-symmetric engine inlet conditions,” in *Proceedings of ASME Turbo Expo 2013*, June 3-7, 2013.
- [36] GOLDSCHMIED, F. R., “Integrated hull design, boundary-layer control, and propulsion of submerged bodies,” *Journal of Hydronautics*, July 1967.
- [37] GREITZER, E., “Mit n+3 final report, volume 2: Appendices design methodologies for aerodynamics, structures, weight, and thermodynamic cycles,” tech. rep., Massachusetts Institute of Technology, 2010.
- [38] GUO, J., JULIEN, P. Y., and MERONEY, R. N., “Modified log-wake law for zero-pressure-gradient turbulent boundary layers,” *Journal of Hydraulic Research*, vol. 41, no. 5, p. pp. 493, 2003.
- [39] GUYNN, M. D., BEBERTON, J., TONG, M. T., and HALLER, W. J., “Advanced single-aisle transport propulsion design options revisited,” in *2013 Aviation Technology, Integration, and Operations Conference*, August 12-14, 2013.

- [40] HARDIN, L. W., TILLMAN, G., SHARMA, O. P., BERTON, J., and AREND, D. J., “Aircraft system study of boundary layer ingesting propulsion,” in *48th AIAA/ASME/SAE/ASEE Joint Propulsion Conference & Exhibit*, 2012.
- [41] JONES, S., “An introduction to thermodynamic performance analysis of aircraft gas turbine engine cycles using the numerical propulsion system simulation code,” tech. rep., NASA TM 2007-214690, 2007.
- [42] KAWAI, R. T., FRIEDMAN, D. M., and SERRANO, L., *Blended Wing Body(BWB) Boundary Layer Ingestion (BLI) Inlet Configuration and System Studies*. NASA. CR-2006-214534.
- [43] KESTNER, B. K., SCHUTTE, J. S., GLADIN, J. C., and MAVRIS, D. N., “Ultra high bypass ratio engine sizing and cycle selection study for a subsonic commercial aircraft in the n+2 timeframe,” in *ASME Gas Turbine Exposition*, (Vancouver, Canada), 2011.
- [44] KIM, H. and LIOU, M.-S., “Flow simulation of n3-x hybrid wing-body configuration,” in *51st AIAA Aerospace Sciences Meeting*, 2013.
- [45] KIM, H. and LIOU, “Optimal inlet shape design of n2b hybrid wing body configuration,” in *48th AIAA/ASME/SAE/ASEE Joint Propulsion Conference & Exhibit*, 2012.
- [46] KIM, H. D. and FELDER, J. L., “Control volume analysis of boundary layer ingesting propulsion systems with or without shock wave ahead of the inlet,” in *AIAA Aerospace Sciences Meeting Including the New Horizons Forum and Aerospace Exposition*, (Orlando, Florida), 2011.
- [47] KIM, H. D., FELDER, J. L., and BROWN, G. V., “An examination of the effect of boundary layer ingestion on turboelectric distributed propulsion systems,” in *Proc. AIAA Aerospace Sciences Meeting Including the New Horizons Forum and Aerospace Exposition*, (Orland, Florida), 2011.
- [48] KIM, H. D., “Distributed propulsion vehicles,” in *27TH INTERNATIONAL CONGRESS OF THE AERONAUTICAL SCIENCES*, 2010.
- [49] KO, Y.-Y. A., *The Multidisciplinary Design Optimization of a Distributed Propulsion Blended-Wing-Body Aircraft*. PhD thesis, Virginia Polytechnic Institute and State University, 2003.
- [50] KOK, H., VOSKUIJL, M., and VAN TOOREN J.L., M., “Distributed propulsion featuring boundary layer ingestion engines for the blended wing body subsonic transport,” in *51st AIAA/ASME/ASCE/AHS/ASC Structures, Structural Dynamics, and Materials Conference; BRç 18th*, 2010.
- [51] KULFAN, B. M., “A universal parametric geometry representation method – ”cst”,” in *45th AIAA Aerospace Sciences Meeting and Exhibit*, 9-11 Jan 2007.

- [52] KURZKE, J., “Effects of inlet flow distortion on the performance of aircraft gas turbines,” *Journal of Engineering for Gas Turbines and Power*, 2008.
- [53] LEE, C. H., *Bayesian Collaborative Sampling: Adaptive Learning for Multi-Disciplinary Design*. PhD thesis, Georgia Institute of Technology, 2011.
- [54] LIEBECK, R., “Design of the blended-wing-body subsonic transport,” in *40th AIAA Aerospace Sciences Meeting & Exhibit*, 2002.
- [55] LIEBECK, R., “Blended wing body design challenges,” in *AIAA/ICAS International Air and Space Symposium and Exposition: The Next 100 Years*, 2003.
- [56] LIOU, M.-S. and JOON LEE, B., “Minimizing inlet distortion for hybrid wing body aircraft,” *Journal of Turbomachinery*, vol. 134, May 2012.
- [57] LONGLEY, J. and GREITZER, E., “Inlet distortion effects in aircraft propulsion system integration,” 1993.
- [58] LUCAS, J. R., “Effect of bli-type inlet distortion on turbofan engine performance,” Master’s thesis, Virginia Polytechnic Institute and State University, 2013.
- [59] LYLTE, J., “The numerical propulsion system simulation: An overview,” tech. rep., NASA TM 2000-209915, 2000.
- [60] LYNCH, F., “A theoretical investigation of the effect of ingesting airframe boundary layer air on turbofan engine fuel consumption,” tech. rep., Douglas Aircraft Company, 1960.
- [61] MANKINS, J., “Technology readiness levels,” tech. rep., NASA Office of Space Access and Technology, 1995.
- [62] MATTINGLY, J., *Element of Gas Turbine Propulsion*. McGraw-Hill, 1996.
- [63] MATTINGLY, J., HEISER, W., and DALEY, D., *Aircraft Engine Design*. AIAA Education Series, second ed., 2002.
- [64] NICKOL, C. L., “Silent aircraft initiative concept risk assessment,” tech. rep., NASA, 2008.
- [65] NICKOL, C. L. and MCCULLERS, L. A., “Hybrid wing body configuration system studies,” in *47th AIAA Aerospace Sciences Meeting Including The New Horizons Forum and Aerospace Exposition*, 2009.
- [66] OATES, G. C., *The Aerothermodynamics of aircraft gas turbine engines*. AFAPL-TR-78-52, 1978.
- [67] OATES, G., *Aircraft Propulsion Systems Technology and Design*. American Institute of Aeronautics and Astronautics, 1989.

- [68] OWENS, L. R., ALLAN, B. G., and GORTON, S. A., “Boundary-layer-ingesting inlet flow control,” *Journal of Aircraft*, vol. 45, p. 100, July-August 2008.
- [69] PLAS, A., “Peraircraft of a boundary layer ingesting propulsion system,” Master’s thesis, Massachusetts Institute of Technology, 2006.
- [70] PLAS, A., SARGEANT, M., MADANI, V., CRICHTON, D., GREITZER, E., HYNES, T., and HALL, C., “Performance of a boundary layer ingesting (bli) propulsion system,” in *AIAA Aerospace Sciences Meeting and Exhibit*, (Reno, Nevada), 2007.
- [71] QIAN, M., “Application of modified log-wake law in nonzero-pressure-gradient turbulent boundary layers,” Master’s thesis, National University of Singapore, 2004.
- [72] RODRIGUEZ, D. L., *A Multidisciplinary Optimization Method for Designing Boundary Layer Ingesting Inlets*. PhD thesis, Stanford University, 2001.
- [73] RODRIGUEZ, D. L., “Multi-disciplinary optimization method for designing boundary-layer-ingesting inlets,” *Journal of Aircraft*, vol. 46, no. 3, 2009.
- [74] SANDS, J. S., *Robust Design Methodology For Common Core Gas Turbine Engines*. PhD thesis, Georgia Institute of Technology, 2015.
- [75] SANDS, J., GLADIN, J., KESTNER, B., and MAVRIS, D. N., “Effects of boundary layer ingesting (bli) propulsion systems on engine cycle selection and hwb vehicle sizing,” in *AIAA Aerospace Sciences Meeting Including the New Horizons Forum and Aerospace Exposition*, (Nashville, TN), 2011.
- [76] SANDS, J. S., “Modeling the effects of boundary layer ingesting (bli) propulsion systems on vehicle sizing.” AE 8900 Special Problems, School of Aerospace Engineering, 2010.
- [77] SARAVANAMUTTOO, H., ROGERS, G., COHEN, H., and STRAZNICKY, P., *Propulsion Theory (6th Edition)*. Pearson Education Limited, 2009.
- [78] SATO, S., *The Power Balance Method for Aerodynamic Performance Assessment*. PhD thesis, Massachusetts Institute of Technology, June 2012.
- [79] SATO, S., PRITESH, M. C., HALL, D. K., DE LA ROSA BLANCO, E., and HILEMAN, J. I., “Assessment of propulsion system configuration and fuel composition on hybrid wing body fuel efficiency,” in *49th AIAA Aerospace Sciences Meeting including the New Horizons Forum and Aerospace Exposition*, 2011.
- [80] SCHUTTE, J. S., SANDS, J. S., TAI, J., and MAVRIS, D. N., “Cycle design exploration using multi-design point approach,” in *Proceedings of ASME Turbo Expo 2012*, 2012.

- [81] SCHUTTE, J. S., TAI, J., and MAVRIS, D. N., “Multi-design point cycle design incorporation into the environmental design space,” in *48th AIAA/ASME/SAE/ASEE Joint Propulsion Conference & Exhibit*, July 2012.
- [82] SCHUTTE, J., S.HERNANDO, J., and MAVRIS, D. N., “Technology assessment of nasa environmentally responsible aviation advanced vehicle concepts,” in *AIAA Aerospace Sciences Meeting Including the New Horizons Forum and Aerospace Exposition*, (Orlando, Florida), 2011.
- [83] SCHUTTE, J. S., *Simultaneous Multi-Design Point Approach to Gas Turbine On-Design Cycle Analysis for Aircraft Engines*. PhD thesis, Georgia Institute of Technology, 2009.
- [84] SHEDON, J., *Intake aerodynamics. 2nd ed.* Oxford: Blackwell Science., 1999.
- [85] SMITH, A. and ROBERTS, H., “The jet airplane utilizing boundary layer air for propulsion,” *Journal of the Aeronautical Sciences*, vol. 14, pp. 97–109, 1947.
- [86] SMITH, L. H., “Wake ingestion propulsion benefit,” *Journal of Propulsion and Power*, vol. 9, pp. 74–82, 1993.
- [87] SPANG, A. H., “Control of jet engines,” *Control Engineering Practice* 7, 1043-1059, 1999.
- [88] THURSTON, S. and EVANBAR, M., “Efficiency of a propulsor on a body of revolution-inducting boundary-layer fluid,” *Journal of Aircraft*, May-June 1966.
- [89] WALSH, P. P. and FLETCHER, P., *Gas Turbine Performance*. Blackwell Science, 1998.
- [90] WEED, P. A., “Hybrid wing-body aircraft noise and performance assessment,” Master’s thesis, Massachusetts Institute of Technology, June 2010.
- [91] WILSON, J. S., *Uncertainty Quantification with Mitigation Actions for Aircraft ConConcept Design*. PhD thesis, Georgia Institute of Technology, 2015.

VITA

Jonathan Gladin received his undergraduate degree in Aerospace Engineering from the Georgia Institute of Technology in 2006. He worked as a structural analyst for Sikorsky Helicopters for three years on the Black Hawk program before returning to Georgia Tech to pursue his graduate studies in 2009. He received his Master's degree in Aerospace Engineering with Prof. Mavris as his advisor in 2011 and continue his work for the Ph.D program. During graduate school, his area of interest has been in propulsion system cycle modeling and design, component design, airframe/propulsion integration, and recently hybrid electric propulsion for UAVs. He has several publications in conferences such as the AIAA JPC conference (now propulsion and energy), the Gas Turbine Exposition (Turbo-Expo).